TECH LIBRARY KAFB, NM
0143022

6258

NATIONAL ADVISORY COMMITTEE FOR AERONAUTICS

REPORT 1368

SYSTEMATIC TWO-DIMENSIONAL CASCADE TESTS OF NACA 65-SERIES COMPRESSOR BLADES AT LOW SPEEDS

By JAMES C. EMERY, L. JOSEPH HERRIG,
JOHN R. ERWIN, and A. RICHARD FELIX

DAR
TECHNICAL LIBRARY
AFL 2291

1958

For sale by the Superintendent of Documents, U. S. Government Printing Office, Washington 25, D. C. Yearly subscription, $10; foreign, $13; single copy price varies according to size - - - - - - - - - Price 70 cents

TECH LIBRARY KAFB, NM
0143022

REPORT 1368

SYSTEMATIC TWO-DIMENSIONAL CASCADE TESTS OF NACA 65-SERIES COMPRESSOR BLADES AT LOW SPEEDS

By JAMES C. EMERY, L. JOSEPH HERRIG,
JOHN R. ERWIN, and A. RICHARD FELIX

Langley Aeronautical Laboratory
Langley Field, Va.

National Advisory Committee for Aeronautics

Headquarters, 1512 H Street NW., Washington 25, D. C.

Created by act of Congress approved March 3, 1915, for the supervision and direction of the scientific study of the problems of flight (U. S. Code, title 50, sec. 151). Its membership was increased from 12 to 15 by act approved March 2, 1929, and to 17 by act approved May 25, 1948. The members are appointed by the President, and serve as such without compensation.

JAMES H. DOOLITTLE, Sc. D., Shell Oil Company, *Chairman*

LEONARD CARMICHAEL, PH. D., Secretary, Smithsonian Institution, *Vice Chairman*

ALLEN V. ASTIN, Ph. D., Director, National Bureau of Standards.
PRESTON R. BASSETT, D. Sc.
DETLEV W. BRONK, Ph. D., President, Rockefeller Institute for Medical Research.
FREDERICK C. CRAWFORD, Sc. D., Chairman of the Board, Thompson Products, Inc.
WILLIAM V. DAVIS, JR., Vice Admiral, United States Navy, Deputy Chief of Naval Operations (Air).
PAUL D. FOOTE, Ph. D., Assistant Secretary of Defense, Research and Engineering.
WELLINGTON T. HINES, Rear Admiral, United States Navy, Assistant Chief for Procurement, Bureau of Aeronautics.
JEROME C. HUNSAKER, Sc. D., Massachusetts Institute of Technology.
CHARLES J. MCCARTHY, S. B., Chairman of the Board, Chance Vought Aircraft, Inc.
DONALD L. PUTT, Lieutenant General, United States Air Force, Deputy Chief of Staff, Development.
JAMES T. PYLE. A. B., Administrator of Civil Aeronautics.
FRANCIS W. REICHELDERFER, Sc. D., Chief, United States Weather Bureau.
EDWARD V. RICKENBACKER, Sc. D., Chairman of the Board, Eastern Air Lines, Inc.
LOUIS S. ROTHSCHILD, Ph. B., Under Secretary of Commerce for Transportation.
THOMAS D. WHITE, General, United States Air Force, Chief of Staff.

HUGH L. DRYDEN, PH. D., *Director*

JOHN W. CROWLEY, JR., B. S., *Associate Director for Research*

JOHN F. VICTORY, LL. D., *Executive Secretary*

EDWARD H. CHAMBERLIN, *Executive Officer*

HENRY J. E. REID, D. Eng., Director, Langley Aeronautical Laboratory, Langley Field, Va.

SMITH J. DEFRANCE, D. Eng., Director, Ames Aeronautical Laboratory, Moffett Field, Calif.

EDWARD R. SHARP, Sc. D., Director, Lewis Flight Propulsion Laboratory, Cleveland, Ohio

WALTER C. WILLIAMS, B. S., Chief, High-Speed Flight Station, Edwards, Calif.

REPORT 1368

SYSTEMATIC TWO-DIMENSIONAL CASCADE TESTS OF NACA 65-SERIES COMPRESSOR BLADES AT LOW SPEEDS [1]

By James C. Emery, L. Joseph Herrig, John R. Erwin, and A. Richard Felix

SUMMARY

The performance of NACA 65-series compressor blade sections in cascade has been investigated systematically in a low-speed cascade tunnel. Porous test-section side walls and, for high-pressure-rise conditions, porous flexible end walls were employed to establish conditions closely simulating two-dimensional flow. Blade sections of design lift coefficients from 0 to 2.7 were tested over the usable angle-of-attack range for various combinations of inlet-flow angle β_1 of 30°, 45°, 60°, and 70°, and solidity σ of 0.50, 0.75, 1.00, 1.25, and 1.50. Design points were chosen on the basis of optimum high-speed operation. A sufficient number of combinations were tested to permit interpolation and extrapolation of the data to all conditions within the usual range of application.

The results of this investigation indicate a continuous variation of blade-section performance as the major cascade parameters, blade camber, inlet angle, and solidity were varied over the test range. Summary curves of the results have been prepared to enable compressor designers to select the proper blade camber and angle of attack when the compressor velocity diagram and desired solidity have been determined.

At a few test conditions, an upper limit to the design lift coefficient that could provide satisfactory performance was found. These results provide information as to the maximum value of the loading parameter, expressed as the product of solidity and section lift coefficient based on the vector mean velocity, that can be used effectively in compressor design. Analysis of the trends indicated that the common practice of employing a constant maximum value of the loading parameter for all inlet angles and solidities fails to define the observed performance of the compressor blades studied in this investigation.

An index that the positive and negative limits of useful angle-of-attack range occurred when the section drag coefficient reached twice the minimum value was used to estimate the operating range of the compressor blade sections studied. A broad operating range for these sections was observed, except for conditions of highest pressure rise across the cascade corresponding to high cambers at high inlet angles. These conditions are not typical of usual design practice and no difficulty should ordinarily be encountered in employing these blade sections. In general, the observed performance of NACA 65-series compressor blades in cascade is considered to be very satisfactory.

INTRODUCTION

The design of an axial-flow compressor of high performance involves three-dimensional high-speed flow of compressible viscous gases through successive rows of closely spaced blades. No adequate theoretical solution for this complete problem has yet appeared nor, from consideration of the complexity of the problem, does it seem likely that complete relationships will be established for some time. Various aspects of the problem have been treated theoretically, and the results of those studies are quite useful in design calculations. All such studies, however, have been based on idealized flow, with effects of one or more such physical realities as compressibility, finite blade spacing, and viscosity neglected. Consideration of viscosity effects has been particularly difficult. It appears, therefore, that in spite of advances in theoretical methods, theory must be supplemented by experimental data for some time to come.

Some of the information required can be obtained only by experiment in single-stage and multistage compressors. Much of the information, however, can be obtained more easily by isolating the effects of each parameter for detailed measurement. The effects of inlet angle, blade shape, angle of attack, and solidity on the turning angle and drag produced can be studied by tests of compressor blades in two-dimensional cascade tunnels. Cascade tests can provide many basic data concerning the performance of compressors under widely varying conditions of operation with relative ease, rapidity, and low cost. A number of successful high-speed axial-flow compressors have been designed by using low-speed cascade data directly. A more refined procedure, however, would use cascade data, not as the final answer, but as a broad base from which to work out the three-dimensional relations.

Data from a large number of two-dimensional cascade tests have been available in this and other countries for

[1] Supersedes NACA Technical Note 3916 (formerly NACA RM L51G31) by L. Joseph Herrig, James C. Emery, and John R. Erwin, 1957, and NACA Technical Note 3913 (formerly NACA RM L54H18a) by A. Richard Felix, 1957.

some years. Although the cascade configurations used in these investigations were geometrically two dimensional, in no case except that of the porous-wall cascade of reference 1 was the flow believed to be two dimensional. This situation is ordinarily accepted on the grounds that the flow in the compressor is also subject to three-dimensional end effects. That similar end conditions would exist in stationary cascades and rotating blade rows seems unlikely. As discussed in reference 1, there is evidence, however, that the flow through typical axial compressor blades is more nearly like that in aerodynamically two-dimensional cascades than like that in cascades which are only geometrically two dimensional. Excellent correlation between porous-wall cascade and rotor-blade pressure-distribution and turning-angle values is shown for the design conditions of the compressor investigation reported in reference 2. The proper basic approach to the compressor design problem, therefore, would seem to be to separate the two-dimensional effects from the three-dimensional. This approach should also aid in the evaluation of the separate effects of tip clearance and secondary flow in axial compressors. Therefore, a systematic series of low-speed cascade tests of the NACA 65-series compressor blade sections were made by means of the porous-wall technique to insure two dimensionality of the flow. These results and an analysis of the data are presented, as well as summarized data in the form of carpet plots for use in specific design problems.

SYMBOLS

a	mean-line loading designation
b	blade height or span, feet
c	blade chord, feet
c_d	section drag coefficient
c_F	resultant-force coefficient
c_l	section lift coefficient
$c_{l,o}$	camber, expressed as design lift coefficient of isolated airfoil
c_N	section normal-force coefficient
$c_{N,M}$	section normal-force coefficient obtained by calculation of momentum and pressure changes across blade row
$c_{N,P}$	section normal-force coefficient obtained by integration of blade-surface pressure distribution
c_w	wake momentum difference coefficient
F	force on blades, pounds
F_M	force on blades due to momentum change through blade row, pounds
F_p	force on blades due to pressure change through blade row, pounds
F_w	force on blades due to momentum difference in wake, pounds
g	tangential spacing between blades, feet
l/d	ratio of section lift to section drag
M	Mach number
P	total pressure, pounds per square foot
p	static pressure, pounds per square foot
Δp	static pressure rise across cascade, pounds per square foot
q	dynamic pressure, pounds per square foot
$\Delta p/q_1$	nondimensional static-pressure-rise parameter
R	Reynolds number based on blade chord
S	pressure coefficient $\left(\frac{P-p_l}{q_1}\right)$
U	rotor-blade rotational speed, feet per second
V	flow velocity, feet per second
W	flow velocity relative to blades, feet per second
x	chordwise distance from blade leading edge, feet
Y	scaled value substituted for θ, $\theta+50(c_{l,o}-0.4)$
y	perpendicular distance from blade chord line, feet
α	angle between flow direction and blade chord, degrees
β	angle between flow direction and a perpendicular to the cascade axis, degrees
θ	flow turning angle, degrees $(\beta_2-\beta_1)$
γ	angle between resultant-force direction and tangential direction, degrees
ρ	mass density of flow, slugs per cubic foot
σ	solidity, c/g

Subscripts:

a	component in axial direction
d	design value, except in drag coefficient
l	local
m	referred to vector-mean velocity, W_m
s	flow outside wake
u	component in tangential direction
1	upstream of blade row
2	downstream of blade row

APPARATUS, TEST PROGRAM, AND PROCEDURE

DESCRIPTION OF TEST EQUIPMENT

The test facility used in this investigation was the Langley 5-inch low-speed, porous-wall cascade tunnel described in reference 1 and shown in figures 1 and 2. During the course of this program some further improvements were required to establish proper testing conditions at higher pressure rise conditions. In particular, the boundary-layer buildup behind the slot on the convex flexible end wall with high pressure rise cascades was sufficient to cause separation and destroy simulation of the infinite cascade even though the blade flow was not separated. This condition was corrected by replacing the end wall with a porous flexible wall and suction chamber. In addition the large difference in flow length from the entrance cone to the side-wall slots between the tunnel ends at the higher inlet air angles gave quite different boundary-layer thickness along the length of the side-wall slots and made uniform flow entering the test section difficult to obtain. This condition was improved by making the changeable side plates porous and drawing a small amount of air through them. The concave flexible end wall was made porous to provide a further control of flow conditions through the test section.

The porous material found to be most satisfactory is commercial woven monel filter cloth. This cloth is available in various meshes in widths up to 36 inches and can be calendered at the factory to reduce porosity and improve surface smoothness. The combination found most suitable for the present work was a Dutch twill double weave of 30

by 250 mesh with warp wire diameter of 0.010 inch and fill wire diameter of 0.008 inch. The original thickness of about 0.026 inch was reduced to 0.018 inch by calendering. The resulting material has the porosity characteristics shown in figure 3. The primary advantages of this material over others tried previously are its uniformity, flexibility, strength, surface smoothness, and relatively low cost.

DESCRIPTION OF AIRFOILS

The blade family used in this investigation is formed by combining a basic thickness form with cambered mean lines. The basic thickness form used is the NACA 65(216)-010 thickness form with the ordinates increased by 0.0015 times the chordwise stations to provide slightly increased thickness toward the trailing edge. This thickness form has been designated the 65-010 blower blade section in references 3 and 4. It was not derived for 10-percent thickness but was scaled down from the NACA 65,2-016 airfoil given in reference 5. As discussed in reference 5, the scaling procedure gives the best results when it is restricted to maximum thickness changes of a few percent. Subsequent to the cascade studies of reference 3, in which the NACA 65-010 blower blade was first introduced, the basic thickness form for the NACA 65-010 airfoil section was derived and included in reference 5. The ordinates for the basic thickness form of the blower blade in reference 3 differ slightly from the airfoil ordinates in reference 5 but are considered interchangeable within the accuracy of the results reported herein. Ordinates for both the scaled thickness form (ref. 3) and derived thickness form (ref. 5) are given in table I.

TABLE I

ORDINATES FOR NACA 65-010 BASIC THICKNESS FORMS

[Stations and ordinates in percent chord]

Station, x	Ordinates, $\pm y$	
	65(216)-010 airfoil combined with $y=0.0015x$	Derived 65-010 airfoil
0	0	0
.5	.752	.772
.75	.890	.932
1.25	1.124	1.169
2.5	1.571	1.574
5.0	2.222	2.177
7.5	2.709	2.647
10	3.111	3.040
15	3.746	3.666
20	4.218	4.143
25	4.570	4.503
30	4.824	4.760
35	4.982	4.924
40	5.057	4.996
45	5.029	4.963
50	4.870	4.812
55	4.570	4.530
60	4.151	4.146
65	3.627	3.682
70	3.038	3.156
75	2.451	2.584
80	1.847	1.987
85	1.251	1.385
90	.749	.810
95	.354	.306
100	.150	0
L. E. radius	.666	.687

The basic mean line used is the $a=1.0$ mean line given on page 97 of reference 5. The amount of camber is expressed in reference 5 as design lift coefficient $c_{l,o}$ for the isolated airfoil, and that system has been retained. Ordinates and slopes for the $a=1.0$ mean line are given in table II for $c_{l,o}=1.0$. Both ordinates and slopes are scaled directly to obtain other cambers. Cambered blade sections are obtained by applying the thickness perpendicular to the mean line at stations laid out along the chord line. The blade sections tested are shown in figure 4. In the designation the camber $c_{l,o}$ is given by the first number after the dash in tenths. For example, the NACA 65-810 and NACA 65-(12)10 blade sections are cambered for $c_{l,o}=0.8$ and $c_{l,o}=1.2$, respectively.

TEST PROGRAM AND PROCEDURE

Test program.—The test program was planned to provide sufficient information to satisfy any conventional vector diagram of the type shown in figure 5. Tests of seven-blade cascades were run with various combinations of inlet air angle β_1 of 30°, 45°, 60°, and 70°, solidity σ of 0.50, 0.75, 1.00, 1.25, and 1.50, and cambers from $c_{l,o}$ of 0 to 2.7 over the useful angle-of-attack range. The most complete test series were run at solidities of 1.00 and 1.50; sufficient tests were made at the other solidities to guide interpolation and extrapolation. The combinations of β_1, σ, and blade section which were tested are tabulated in table III. The camber range covered at solidities of 1.00 and 1.50 was determined by one of two limitations. At the higher inlet angles progressively higher cambers were used until the limit loading had been reached, that is, until the design condition coincided with stall; at lower inlet angles, however, design turning angle exceeded inlet angle before the limit loading had been reached and the tests were terminated

TABLE II

ORDINATES FOR THE NACA $a=1.0$ MEAN LINE, $c_{l,o}=1.0$

[Stations and ordinates in percent chord]

Station, x	Ordinate, y	Slope, dy/dx
0	0	-------
.5	.250	0.42120
.75	.350	.38875
1.25	.535	.34770
2.5	.930	.29155
5.0	1.580	.23430
7.5	2.120	.19995
10	2.585	.17485
15	3.365	.13805
20	3.980	.11030
25	4.475	.08745
30	4.860	.06745
35	5.150	.04925
40	5.355	.03225
45	5.475	.01595
50	5.515	0
55	5.475	−.01595
60	5.355	−.03225
65	5.150	−.04925
70	4.860	−.06745
75	4.475	−.08745
80	3.980	−.11030
85	3.365	−.13805
90	2.585	−.17485
95	1.580	−.23430
100	0	-------

TABLE III

CASCADE COMBINATIONS TESTED

σ	NACA airfoil			
	$\beta_1=30°$	$\beta_1=45°$	$\beta_1=60°$	$\beta_1=70°$
0.50		65-410 65-(12)10 65-(18)10	65-410 65-(12)10 65-(18)10	
.75		65-410 65-(12)10 65-(18)10	65-410 65-(12)10 65-(18)10	
1.00	65-010 65-410 65-810 65-(12)10 65-(15)10 65-(18)10	65-010 65-410 65-810 65-(12)10 65-(15)10 65-(18)10 65-(21)10 65-(24)10 65-(27)10	65-010 65-410 65-810 65-(12)10 65-(15)10 65-(18)10 65-(21)10	65-010 65-410 65-810 65-(12)10 [a] 65-(15)10
1.25	65-410 65-(12)10 65-(18)10	65-410 65-(12)10 65-(18)10	65-410 65-(12)10 65-(18)10	65-410 65-810 65-(12)10 65-(15)10
1.50	65-010 65-410 65-810 65-(12)10 65-(15)10 65-(18)10	65-010 65-410 65-810 65-(12)10 65-(15)10 65-(18)10 65-(21)10 65-(24)10	65-010 65-410 65-810 65-(12)10 65-(15)10 65-(18)10 65-(21)10 65-(24)10	65-010 65-410 65-810 65-(12)10 65-(15)10

[a] No design point was obtained for this combination.

there. Limit conditions were attained at $\beta_1=70°$, $\sigma=1.00$, 1.25, and 1.50, and at $\beta_1=60°$, $\sigma=1.00$ and 1.50.

Test procedure.—It was shown in reference 1 that two-dimensional flow can be achieved by controlling the removal of boundary-layer air through porous test-section side walls so that the downstream static pressure equals the ideal value, corresponding to the turning angle, corrected for the blocking effect of the wake. This criterion was accordingly used in these tests. In addition, the flexible end-wall shapes and suction-flow quantities were adjusted to obtain uniform upstream flow direction and wall static pressures, criteria of two-dimensional flow simulating an infinite cascade. This procedure necessitated an approximate measurement of turning angle and wake size and an estimate of the correct pressure rise before the final settings could be made. Initially, this system required some cut-and-try procedure but after the initial tests at each combination of β_1 and σ a chart similar to figure 5 of reference 1 could be drawn to assist in estimating the pressure rise. An experienced operator could make the required estimates and settings very quickly by this procedure. Spot calculations of the correct pressure rises were made after completion of tests to check the accuracy of the values used.

Tests were made at each cascade combination shown in table III over a range of angles of attack at intervals of 2° to 3°. In general, the tests covered the interval from negative to positive stall, where stall was determined by a large increase in wake size. The principal exceptions occurred for low cambered blades where negative stall would have occurred at negative turning. It was found that the small wall boundary-layer buildup for negative turning angles and hence negative pressure rises would have required a less porous material than that normally used, to avoid excess air removal while maintaining sufficient suction pressure differential to avoid local reverse flow through the porous material. It was not deemed worthwhile to change the porous material to obtain data in this relatively uninteresting range. For the NACA 65-010 section at $\beta_1=30°$, however, the difficulty persisted well above 0° turning, and this combination was tested with both porous and solid walls.

The tests were entirely within a speed range considered incompressible. The bulk of the tests at solidities of 1.00 and 1.50 were run at an entering velocity of 95 feet per second. For the usual 5-inch blade chord, the Reynolds number was 245,000. Some information near the design point was obtained at higher effective Reynolds number for most cascade combinations by adding roughness to the blade leading edges in the form of ¼-inch-wide strips of masking tape draped around the leading edges from wall to wall. In addition, some tests near design conditions were run at a speed of 135 feet per second and a Reynolds number of 346,000 with and without roughness. Two cascade combinations were tested at design conditions over a range of Reynolds numbers from 160,000 to 470,000 to assist in estimating performance at Reynolds numbers other than the usual test value. In order to provide further information on scale effects, two cascade combinations were tested through the α range with leading-edge roughness at the standard Reynolds number and in the smooth conditions at a Reynolds number of 445,000. For solidities of 0.50 and 0.75 the tunnel could not accommodate seven blades of 5-inch chord; the blade chord was reduced to 2.5 inches and the Reynolds number to approximately 200,000 for those tests. Tests with roughness were made near the design point for solidities below 1.00, but Reynolds numbers higher than 200,000 could not be obtained with the existing equipment.

Test measurements.—The blade pressure distribution was measured at the midspan position of the central airfoil at each angle of attack. In addition, surveys of wake total-pressure loss and turning angle were made downstream of the cascade. The total-pressure surveys were made with a non-integrating multitube rake approximately 1 chord downstream of the blade trailing edges. Turning angle surveys were made by the "null method" with a claw-type yaw head; since the yaw device was mounted on a track at the rear of the tunnel the distance from the blades varied from about 1 to 3 chords in the flow direction depending upon the inlet- and turning-angle combination. Flow discharge angle readings were taken at a number of points downstream of several blade passages along the tunnel center line. These readings were averaged to obtain the final value. Since the angle readings in the wake deviated several degrees from the average reading, and the direction of the deviation varied consistently with the direction of the total pressure gradient, the accuracy of readings in the wake was questioned. Therefore, the values obtained when the wake readings were included and excluded in the averaging process were compared for a number of tests. The resulting turning-angle

curves compared very well, but scatter was considerably less when only the readings outside the wake were used to obtain the turning-angle value. This latter procedure has been adopted as the standard method of measuring the flow discharge direction. Static pressure and upstream flow angles were measured approximately 1 chord upstream of the blade row. Total pressure was measured in the settling chamber. Pressures were obtained by orifices with pressure leads to manometer boards. Angles of flow were again obtained by use of a claw-type yaw head by the null method.

Calculations.—Pressure distribution and wake-survey data were recorded and force values calculated nondimensionally as coefficients based numerically on the upstream dynamic pressure q_1. This choice was dictated partly for convenience in reducing the data (standardization of q_1 permits use of manometer scales which give nondimensional values directly) and partly because information based on entering flow was considered most convenient for design use, particularly when critical speed is important.

All forces due to pressure and momentum changes across the blade row were summed to obtain the resultant blade force coefficient $c_{F,1}$. In this process the wake total-pressure deficit was converted to an integrated momentum difference by the method given for the drag calculation in the appendix of reference 5. This wake momentum difference, expressed nondimensionally, is designated the wake coefficient $c_{w,1}$; it represents the momentum difference between the wake and the stream outside the wake, and is based on q_1 numerically. The wake coefficient is not considered to be a true drag coefficient, but is used merely for convenience in assessing the contribution of the wake in the summation of forces.

The resultant-force coefficient was resolved into components perpendicular and parallel to the vector mean velocity W_m (see fig. 5) to obtain the lift coefficient $c_{l,1}$ and the drag coefficient $c_{d,1}$, respectively. The mean velocity was calculated as the vector average of the velocities far upstream and far downstream. The velocity far downstream was obtained from measurements just behind the blades by using a momentum-weighted average of the velocity just behind the blades. This rather detailed method was found necessary to give consistent drag values. Since the resultant force is very nearly perpendicular to the mean velocity, the value of the component parallel to the mean velocity is quite sensitive to mean-velocity direction. Attempts at using the downstream velocity outside the wake for averaging rather than the momentum-average velocity gave very erratic drag results and indicated that mean velocity directions obtained in that manner were not reliable. In addition to the lift and drag, the section normal-force coefficient $c_{N,M,1}$ was obtained by computing the component of the resultant-force coefficient perpendicular to the blade chord line. This normal-force coefficient was compared with the normal-force coefficient $c_{N,P,1}$ obtained by integration of the blade surface pressure distribution as a check on the accuracy of individual tests. A detailed derivation of the method of calculating the force coefficients is given in appendix A.

Accuracy of results.—In general the turning-angle values measured are believed to be accurate within $\pm 0.5°$ near the design values. The correlation procedure used is believed to have improved further the accuracy of the design values in the final results. For tests far from design, that is, near positive or negative stall, the accuracy was reduced somewhat. In addition, at an inlet angle of 70° with sections of zero camber, satisfactory measurements were very difficult to obtain and the accuracy was reduced.

As noted in the section describing calculation methods, the blade normal-force coefficient $c_{N,M,1}$ calculated from pressure-rise and momentum considerations was compared with the normal-force coefficient $c_{N,P,1}$ obtained from the pressure distribution as a check on the overall accuracy of individual tests. Since these values would be affected by error in turning-angle, surface pressure or wake-survey readings, or by failure to achieve two dimensionality of the flow, this comparison is a check on the overall acceptability of the results. A difference of 5 percent between the two normal-force coefficients was set as the outside limit for acceptance of individual tests for lift coefficients above 0.2; below lift coefficients of 0.2 a direct numerical comparison was made using a limit of ± 0.01. The agreement was well within the 5-percent limit for most of the tests as originally run, and only a few conditions had to be repeated. The accuracy of the lift coefficients is directly comparable to that of the normal-force coefficients. The accuracy of wake-coefficient and drag-coefficient values will be discussed later under Reynolds number effects.

PRESENTATION OF RESULTS

Detailed blade-performance data for all cascade combinations tested are presented in the form of surface-pressure distributions and blade-section-characteristic plots in figures 6 to 84. The representative pressure distributions presented have been selected to illustrate the variation through the angle-of-attack range for each combination. The section characteristics presented through the angle-of-attack range are turning angle θ, lift coefficient $c_{l,1}$, wake coefficient $c_{w,1}$, drag coefficient $c_{d,1}$, and lift-drag ratio l/d. The effects of changes in Reynolds number and blade-surface condition on section characteristics are given in figure 85.

Trends of section operating range, in terms of angle-of-attack range, with camber for the four inlet angles of the tests are presented in figure 86. Variation of ideal and actual dynamic-pressure ratio across the cascade with turning angle and inlet angle is presented in figure 87. Figure 88 gives the relation between inlet dynamic pressure and mean dynamic pressure for convenience in converting coefficients from one reference velocity to the other. Limit loading information is summarized in figure 89. Comparison of the present porous-wall-cascade turning-angle data with those of the solid-wall cascade of reference 3 is made in figure 90 for a typical inlet angle and solidity combination.

The information which is most useful for choosing the blade sections to fulfill compressor design vector diagrams is summarized in figures 91 to 111. The variation of turning angle with angle of attack for the blade sections tested is presented for one combination of inlet angle and solidity in each of the figures 91 to 106. Trends of the slopes of the curves of turning angle against angle of attack near design are given in figure 107. Figures 108 to 111 are design and correlation charts; the variation of design turning angle and

design angle of attack with the parameters, camber, inlet angle, and solidity, is presented for several combinations of the parameters so that interpolation to the conditions of a design velocity diagram is relatively easy.

The selection of the blade section and the blade setting required to fulfill a given velocity diagram at design conditions requires several interpolations and cross plots of the data presented in figures 6 to 84. In order to facilitate these interpolations, a carpet plotting technique described in reference 6 has been used to correlate the data. This technique, for which details are explained in appendix B, permits a function of several variables to be presented on a single graph and such a graph lends itself readily to interpolations for intermediate values of the variables plotted. Carpet plots summarizing the present data are presented in figures 112 to 116, and an example illustrating their use is included in appendix B.

DISCUSSION

DESIGN CONDITIONS

The values and shape of the blade-surface pressure distribution are important criteria for predicting the conditions of best operation at high Mach numbers. Velocity peaks occurring on either surface in low-speed tests would be accentuated at high speeds, and supersonic velocities with attendant shock losses would occur at relatively low entering Mach numbers. The selection of the angle of attack designated as "design" for each combination of inlet angle, solidity, and camber is based on the premise that the blade section will be required to operate at Mach numbers near the critical value. The trend of pressure-distribution shape over the angle-of-attack range was examined for each cascade combination, and the angle for which no velocity peaks occurred on either surface was selected as being optimum from the standpoint of high-speed usage. In general, the design angle so selected is near the middle of the low-drag range thus indicating efficient section operation for angles a few degrees higher or lower than the design condition. The choices of design angle of attack are indicated by an arrow on the blade-section-characteristic plots of figures 6 to 84. The design angles are also shown by cross bars on the turning-angle summary curves in figures 91 to 106.

Correlation of the design angles of attack and design turning angles over the range of camber, solidity, and inlet angle is given by figures 108 to 111 in a manner convenient for design use. The correlation is excellent; smooth curves result when any two of the three parameters are used as independent variables.

The section-characteristic curves of figures 6 to 84 indicate that, in general, the design points chosen do not give maximum lift-drag ratios for low- and medium-speed operation. For designs which will not operate near critical speed, therefore, higher efficiency could be obtained by using angles of attack several degrees higher than the design points presented. This procedure must be used with caution, however, at the higher camber and inlet-angle combinations since the section operating range becomes quite narrow for combinations of highest camber and inlet angle corresponding to the highest values of $\Delta p/q_1$. It is recommended that the individual pressure distributions and section-characteristic curves be examined before departure from the specified design points is made.

REYNOLDS NUMBER EFFECTS

Pressure distribution and boundary layers.—For many of the tests at angles of attack near and below design, there is evidence that a region of laminar separation of the boundary-layer flow occurred on the convex blade surface; this separated boundary layer then became turbulent and reattached to the blade surface as a relatively thick turbulent boundary layer. The mechanism of such a flow sequence is described for the isolated airfoil in reference 7. The laminar separation is indicated by a relatively flat region in the pressure distribution on the convex surface and the turbulent reattachment is characterized by a rapid pressure recovery just downstream of the separated region. This flow pattern can be seen clearly in many of the figures but is particularly evident in figures 42 (a), 42 (c), 56 (b) to 56 (d), and 66 (a) to 66 (e). For some tests, laminar separation appeared to occur on the concave surface as well. This is noticeable in figures 42 (b), 42 (d), 42 (e), 66 (c), and 66 (d).

The extent of laminar boundary-layer flow which occurs on an airfoil surface is affected by Reynolds number, stream turbulence level, airfoil surface condition, and surface pressure gradient. Increases in Reynolds number, stream turbulence, and surface roughness would promote earlier transition. Qualitatively a gradient of decreasing surface pressure would be required to maintain laminar flow if the Reynolds number, stream turbulence, surface roughness, or the combination of these, which might be referred to as "effective Reynolds number," were high enough to favor transition. At the turbulence level of the 5-inch cascade tunnel, however, laminar flow and laminar separation on the convex surface persisted to Reynolds numbers up to 245,000 even when the surface pressure gradient was slightly unfavorable. The addition of leading-edge roughness, as described in the section "Test Procedure" reduced the extent of the laminar separation region, but did not eliminate it in some cases. In view of the thick boundary layer which results from laminar separation and reattachment, it appears that the minimum final boundary-layer thickness and section drag coefficient would result if the Reynolds number and turbulence values were such as to cause transition before laminar separation occurred. Use of leading-edge roughness to reduce an extended laminar separation region would probably result in a thinner final boundary layer than that for the smooth blade at the same Reynolds number but would probably result in a thicker boundary layer than that for the smooth blade at high Reynolds number. A thick turbulent boundary layer would be expected to promote turbulent separation near the trailing edge of compressor blades which produce a significant pressure rise.

Wake coefficient and drag coefficient.—As noted previously, the wake coefficient $c_{w,1}$ expresses the momentum difference between the wake flow and the downstream flow outside the wake in a manner convenient for use in summing blade forces. The wake coefficient is, of course, directly

dependent upon boundary-layer thickness and shape, and changes in the boundary layer with changes in effective Reynolds number are reflected in the wake-coefficient values. Furthermore, if the effective Reynolds number is near the condition where laminar separation may or may not occur, the change in surface pressure gradient with change in angle of attack would control the presence and extent of laminar separation on either blade surface. Obviously erratic variations in the value of the wake coefficients would result under those circumstances. The blade-section-characteristic curves of figures 6 to 84 show that in most cases the wake-coefficient values were irregular as the angle of attack was varied in the region near design at the usual test Reynolds number of 245,000. With either higher Reynolds number or leading-edge roughness, or both, the rapid local pressure recovery associated with boundary-layer reattachment was less evident in the surface pressure distributions and the wake coefficient usually was reduced. For a few cases, notably those of figures 34 (g), 35 (g), 68 (g), and 84 (g), leading-edge roughness increased the wake coefficient, however; in those cases the roughness apparently produced a more severe turbulent boundary layer than laminar separation and reattachment did.

The trend of drag coefficient $c_{d,1}$, defined as the component of resultant force parallel to the mean velocity, was similar to that of wake coefficient. The drag curves were quite irregular near design angle of attack and the values measured varied as much as 30 percent with Reynolds number and roughness. Obviously the values of both drag coefficient and lift-drag ratio near design are not sufficiently reliable to use directly in a design analysis. These values should be of some use for comparison purposes, however. The large drag rise associated with positive and negative stall should be relatively insensitive to Reynolds number effects, because the pressure gradients on the critical surfaces are then unfavorable to laminar flow and therefore should be useful for determining effective operating range.

The trend of drag coefficient with Reynolds number near the design condition for the NACA 65–(12)10 blade section at β_1 of 60°, σ of 1.00, and β_1 of 45°, σ of 1.50 shown in figure 85 (a) serves to indicate the magnitude of the Reynolds number effect. Increasing the stream turbulence by the use of a ½-inch-mesh screen upstream of the test section lowered the drag coefficients at low Reynolds number, and reduced the Reynolds number at which the drag coefficients become essentially constant with Reynolds number. The comparison of $c_{d,1}$ values through the angle-of-attack range for the same cascade combinations at two Reynolds numbers in figures 85 (b) and 85 (c) gives some further indication of Reynolds number effect. For R of 445,000, the drag coefficients are lower and the curves are smoother than for R of 245,000. The addition of leading-edge roughness in figure 85 (b) smoothed the drag curve but did not give the same decrease in drag that the high R did. There appears to be some effect on the angle of attack at which the drag rises rapidly in figure 85 (c) but since the effect was not the same in figure 85 (b) no conclusions can be drawn.

Turning angle and lift.—Figure 85 (a) shows that the effect of Reynolds number on turning angle near design α_1 is almost insignificant for R between 220,000 and 470,000. This is borne out by the fact that throughout figures 6 to 84 changes in θ with Reynolds number and roughness were, in general, within the limits of measuring accuracy. Below R of 220,000 a decrease of design turning angle can be expected. Reynolds number appears to have some effect on turning angle near stall in figure 85 (c), but again the effect has not been definitely established. It can be concluded that the design turning angles presented are correct for R above 220,000, but that the effect of R near stall is unknown.

Laminar separation had no appreciable effect on the measured lift. The lift-coefficient values for a given test agreed well at low and high Reynolds numbers and with and without roughness. The normal-force coefficients obtained by integration of the pressure distributions also changed very little with changes in Reynolds number and roughness.

OPERATING RANGE

In order to estimate the useful operating angle-of-attack range of the various sections at the several solidity and inlet angle conditions tested, Howell's index of twice the minimum drag (ref. 8) was used to select the upper and lower limits of angle of attack. As discussed previously in the section concerning Reynolds number effects, the accuracy of the measured values of drag coefficient near design angle of attack suffered due to laminar-flow separation. The minimum value of drag coefficient could not be determined exactly and an approximate value was used to determine the operating range. For most of the test configurations, the drag coefficient changed rapidly with angle of attack near the ends of the useful range, so an error in the value of minimum drag used would have only a small effect on the operating range value. Some scatter in the results was evident, however.

No significant effect of solidity was observed. Most values at constant camber and inlet angle fell within the scatter of the points. A tendency for the range to increase slightly as the solidity was increased was detectable at $\beta_1=45°$, but this was not evident for other inlet angles. The results plotted in figure 86 indicate that the major determinant of the operating range is inlet angle. As the inlet angle is increased, the usable range of angle of attack is decreased, with greater changes indicated for angles above design than for angles below design. The camber of the section affects the operating range in the following manner for angles of attack above design: at an inlet angle of 30°, the range increased with increasing camber; at inlet angles of 45°, 60°, and 70°, the opposite trend occurred. For values of α_1 less than design, little change in range with camber was indicated for $\beta_1=30°$; at higher inlet angles, the range decreased as the section camber increased.

With high entering velocities, the section operating range would be reduced because of a more rapid increase of drag at angles of attack well above or below design. Further, the comparison between sections of different camber, at constant inlet angle and solidity, would be altered as the flow velocities relative to the blade surfaces exceed the local velocity of sound.

PRESSURE RISE

The ideal, nondimensional pressure rise $\Delta p/q_1$ across a two-dimensional cascade is specified when the inlet angle and turning angle are known, since the ratio of the flow areas determines the pressure rise. Since the mass flow is constant, the actual pressure rise is less than the ideal because of the "blocking" effect of the wake on the downstream flow area. For given inlet and turning angles, the blocking effect would be more severe for higher solidity, since the unaffected flow area is reduced. For incompressible flow the nondimensional pressure rise is equal to one minus the dynamic-pressure ratio, that is, $\frac{\Delta p}{q_1}=1-\frac{q_2}{q_1}$. The actual dynamic-pressure ratio becomes higher than the ideal because of the wake blocking effect. The ideal dynamic-pressure ratios, and the actual ratios at design turning angles for two solidities, are summarized in figure 87 for the range of inlet and turning angles of the tests. The dynamic-pressure ratios for individual tests are given by the short bars at the 100-percent points of the pressure-distribution plots in figures 6 to 84. Wake blocking effects would be changed by the same Reynolds number and roughness factors which change the wake coefficient; however, the percentage change in dynamic-pressure ratio would be small.

LIMIT LOADING

Information on the maximum loading which can be achieved in a compressor blade row is important in the design of high performance axial-flow compressors. As noted previously, the high pressure rise associated with large turning at high inlet angles promotes turbulent separation so that at inlet angles of 60° and 70° the stall angle of attack moved progressively closer to the design value with increasing section camber. The limit turning is reached when the maximum turning angle is no greater than design turning angle. The practical limit would be somewhat lower to give a reasonable operating range.

Approximate limit turning was reached at β_1 of 60°, σ of 1.00 and 1.50, and at β_1 of 70°, σ of 1.00, 1.25, and 1.50. Information from those tests is given in terms of a commonly used loading parameter, $\sigma c_{l,m}$, in figure 89. Both the actual test values of the parameter, and the ideal values calculated using the test inlet and turning angles are presented. Note that the lift coefficient is here based, numerically, on the mean velocity, to conform to the usual form of the parameter.

Arbitrarily chosen constant values of $\sigma c_{l,m}$ have often been used as maximum allowable values in design analyses. The fallacy of using any constant value as a limit is clearly shown in figure 89; the true limiting value increases with increasing solidity and decreases with increasing inlet angle. Since no limits were reached for inlet angles of 45° and 30°, it is clear that the limitation has very little significance there except, perhaps, at very low solidities. The phenomenon is not yet well enough understood to permit the choice of a parameter which could define the overall limitation as a single value.

COMPARISON WITH SOLID-WALL CASCADE DATA

The comparison between pressure-distribution and turning-angle data for a solid-wall cascade tunnel and for the present porous-wall cascade tunnel is given in reference 1 for the NACA 65–(12)10 blade section at β_1 of 60° and σ of 1.00. The comparison has been extended in figure 90 to include turning-angle data for all the cambers reported for β_1 of 60° and σ of 1.00 in reference 3. The turning-angle curves compare fairly well for cambers up to $c_{l,o}$ of 0.8, but for the airfoils of higher camber the data of reference 3 deviate significantly from the present results. Comparisons at other conditions would show similar trends.

RELATIONSHIPS BETWEEN TURNING ANGLE AND ANGLE OF ATTACK

Summaries of the relationships between turning angle and angle of attack through the camber range are given for each inlet angle and solidity in figures 91 to 106. The variations are quite consistent for most of the range. Some inconsistency in the shape of the curves at stall is a result of reduced accuracy of measurement there. For combinations giving moderate pressure rises straight-line relationships are indicated for considerable portions of the curves. For the highest pressure rises, however, no definite straight-line relationships exist. The variation of the slopes near design is given in figure 107 to assist in estimating relationships at conditions other than those tested. These slopes are average slopes for the camber range, and do not apply for the highest cambers. They must be used with particular caution for inlet angles near 70°, since very narrow straight-line regions are prevalent there.

CARPET PLOTS

The usual procedure in blade-section selection is to determine the camber $c_{l,o}$, which is required for a given design velocity diagram at a selected solidity. Figure 112 gives carpet plots of the data at five solidity conditions. The carpet plots indicate the variation of camber $c_{l,o}$, at design angle of attack $\alpha_{1,d}$ with required values of inlet-air angle β_1 and design turning angle θ_d. Each carpet plot is spaced from the next by a number of grid units proportional to the difference in solidities. Since design angle of attack is independent of inlet-air angle, it is possible to present a carpet plot (fig. 113) showing design angle of attack $\alpha_{1,d}$ as a function of camber $c_{l,o}$ and solidity σ.

The tests were made at fixed inlet-air angles with the angle-of-attack variation produced by changing the blade setting. Although data of this type facilitated the determination of design conditions for the various combinations of inlet-air angle, solidity, and camber, it does not lend itself easily, as presented, to obtaining off-design performance of a blade section as regards operation of this section in a compressor in which blade setting is fixed and the angle of attack varied by changing the inlet-air angle. However, if the data are plotted as an off-design carpet, it is a simple matter to draw in curves of constant blade setting and thus to predict the

variation in turning angle with angle of attack for all intermediate conditions of solidity, camber, and blade setting. Such off-design carpet plots showing turning angle as a function of solidity, inlet-air angle, angle of attack, and camber are presented in figure 114. Off-design data are presented for the following sections:

NACA 65–(4)10
NACA 65–(8)10
NACA 65–(12)10
NACA 65–(15)10
NACA 65–(18)10

Pressure rise as a percentage of inlet dynamic pressure $\Delta p/q_1$, called pressure-rise coefficient, has been used as a cascade loading-limit parameter. It is known that cascade losses increase rapidly above certain limiting values of $\Delta p/q_1$. However, in view of the physical meaning of the pressure-rise coefficient, particularly in reference to the inner and outer casings, it is considered to be a useful parameter. If the inlet-air angle, the turning angle, and the entering Mach number are known, calculations of an isentropic pressure-rise coefficient is possible, provided some relationship is assumed between the entering and leaving stream-tube areas. Therefore, two carpet plots were made in order to show the variation of the pressure-rise coefficient with inlet-air angle β_1, turning angle θ, and entering Mach number M_1. The first of these plots (fig. 116 (a)) was calculated by assuming constant stream-tube area; the second (fig. 116 (b)) was calculated by assuming that the stream-tube area varied so that constant axial velocity would be produced across the blade passage. Pressure-rise coefficients obtained from these two plots very often bracket the value associated with the actual three-dimensional condition being examined.

SUMMARY OF RESULTS

The systematic investigation of NACA 65-series compressor blade sections in a low-speed cascade tunnel has provided design data for all conditions within the usual range of application. The results of this investigation indicate a continuous variation of blade-section performance as the important cascade parameters blade camber, inlet angle, and solidity are varied over the useful range. Summary curves have been prepared to facilitate selection of blade sections and settings for compressor-design velocity diagrams for optimum high-speed operation.

Upper limits for the loading parameter $\sigma c_{l,m}$ have been established for some conditions, and the invalidity of using a constant value of the parameter has been shown.

The variation of the useful section operating range with camber, inlet angle, and solidity has been shown. The operating range was found to be broad except for the highest pressure-rise conditions.

Compressor-blade cascade data have been presented in the form of design carpet plots, which greatly facilitate the selection of compressor blade sections required to fulfill velocity diagrams. Plots of this type also are shown to increase greatly the usefulness of available cascade data by providing a simple method of obtaining the off-design variation in turning angle with angle of attack.

Langley Aeronautical Laboratory,
National Advisory Committee for Aeronautics,
Langley Field, Va., *January 31, 1958.*

APPENDIX A

CALCULATION OF BLADE FORCE COEFFICIENTS

The two-dimensional resultant force on a blade in cascade is the vector sum of all the pressure and momentum forces exerted by the fluid. At any appreciable distance behind the blade row the static pressure is constant along a line parallel to the blade row, since any prior pressure gradients would have been converted to momentum changes. On the assumption that a pressure force acting in the upstream direction is positive,

$$F_p=(p_2-p_1)bg \tag{1}$$

sum the momentum forces in the axial and tangential directions. Assume that the axial momentum forces are positive if the force on the blade is in the upstream direction and that the tangential momentum forces are positive if the tangential velocity change is in the usual direction shown in figure 5. The axial momentum force then is

$$F_{M,a}=\int_g \rho_2 V_{a,2,l}(V_{a,2,l}-V_{a,1})b\,dg \tag{2}$$

and the tangential momentum force is

$$F_{M,u}=\int_g \rho_2 V_{a,2,l}(W_{u,1}-W_{u,2,l})b\,dg \tag{3}$$

Since momentum values in the wake can be obtained most easily as differences between the wake values and the downstream value outside the wake, it is convenient to rewrite equations (2) and (3)

$$F_{M,a}=\rho_1 V_{a,1}(V_{a,2,s}-V_{a,1})bg+\int_g \rho_2 V_{a,2,l}(V_{a,2,l}-V_{a,2,s})b\,dg \tag{4}$$

$$F_{M,u}=\rho_1 V_{a,1}(W_{u,1}-W_{u,2,s})bg+\int_g \rho_2 V_{a,2,l}(W_{u,2,s}-W_{u,2,l})b\,dg \tag{5}$$

However, the wake momentum force, as calculated from wake surveys, is

$$F_w=\int_g \rho_2 V_{a,2}(W_{2,s}-W_{2,l})b\,dg \tag{6}$$

If, now, the flow direction in the wake can be assumed to be the same as the average downstream flow direction, the wake force can be resolved into components in the axial and tangential directions. Using the same sign convention as before

$$F_{w,a}=-F_w\cos\beta_2=\int_g \rho_2 V_{a,2,l}(V_{a,2,l}-V_{a,2,s})b\,dg \tag{7}$$

$$F_{w,u}=F_w\sin\beta_2=\int_g \rho_2 V_{a,2,l}(W_{u,2,s}-W_{u,2,l})b\,dg \tag{8}$$

These are the integral terms in equations (4) and (5). Substituting equation (7) in equation (4) and equation (8) in equation (5) yields the axial and tangential force components, as follows:

$$F_a=F_p+F_{M,a}=(p_2-p_1)\,bg+\rho_1 V_{a,1}(V_{a,2,s}-V_{a,1})bg-F_w\cos\beta_2$$

$$F_u=F_{M,u}=\rho_1 V_{a,1}(W_{u,1}-W_{u,2,s})bg+F_w\sin\beta_2$$

For convenience coefficients based on q_1 are used and

$$c_{F,a,1}=\frac{F_a}{\frac{1}{2}\rho_1 W_1^2 bc}=\frac{1}{\sigma}\left[\frac{\Delta p}{q_1}+\frac{2V_{a,1}(V_{a,2,s}-V_{a,1})}{W_1^2}\right]-c_{w,1}\cos\beta_2$$

$$c_{F,u,1}=\frac{F_u}{\frac{1}{2}\rho_1 W_1^2 bc}=\frac{1}{\sigma}\left[\frac{2V_{a,1}(W_{u,1}-W_{u,2,s})}{W_1^2}\right]+c_{w,1}\sin\beta_2$$

The resultant-force coefficient is given by

$$c_{F,1}=\sqrt{c_{F,a,1}^2+c_{F,u,1}^2}$$

If γ is used to denote the angle between the resultant force and the tangential direction

$$\gamma=\tan^{-1}\frac{c_{F,a,1}}{c_{F,u,1}}$$

The lift coefficient $c_{l,1}$ and drag coefficient $c_{d,1}$ are the components of $c_{F,1}$ perpendicular and parallel, respectively, to the vector mean velocity W_m, where W_m is the vector average of the velocities far upstream and far downstream. The upstream velocity can be easily measured. The velocity far downstream is obtained by proper averaging of the velocities just behind the blades. Since the axial area controls the axial velocity, conservation of mass determines the axial component of the velocity far downstream. Inasmuch as there are no physical boundaries in the tangential direction to support pressure gradients, conservation of momentum controls the tangential component far downstream. The discussion up to this point applies to compressible as well as incompressible flow.

For compressible flow the effect of wake mixing on pressures and densities makes accurate determination of the axial velocity far downstream rather tedious. In the incompressible, two-dimensional case the downstream axial component is $V_{a,1}$, and the downstream tangential component is the momentum-weighted average of $W_{u,2}$. This tangential component can be obtained by adding to the tangential momentum of the discharge free stream the integrated tangential momentum of the wake. The integrated tangential momentum of the wake can be determined from the tangential component of the wake coefficient. Having the correct velocity far downstream, the vector mean-velocity direction W_m can be easily obtained. The direction of W_m should be determined accurately since $c_{F,1}$ is very nearly perpendicular to W_m, and the value of the drag component $c_{d,1}$ is sensitive to small changes in the direction of W_m.

APPENDIX B

CARPET-PLOTTING TECHNIQUE

CONSTRUCTION

Since the carpet-plotting technique is not too well known, a description of this technique will be helpful. Examine first figure 114 (a). It will be noted that this figure is composed of five similar and separate plots. Each of these plots shows the variation of the turning angle θ with the angle of attack α_1 and the inlet-air angle β_1 for a given solidity σ and a camber $c_{l,o}$ of 0.40. It might be here pointed out that the tests were made at four inlet-air angles, 30°, 45°, 60°, and 70°. The leftmost plot, which represents a solidity of 1.50, is constructed by plotting turning angle θ as ordinate against angle of attack α_1 as abscissa for $\beta_1=30°$. Then, for a β_1 of 45°, the α_1 scale is shifted to the right a number of grid units proportional to the 15° increment in β_1 and the turning angles are plotted as before. This procedure of shifting the α_1 scale is followed until the range of β_1 values for which test data are available has been completed. Curves of constant angle of attack may then be drawn between the several curves of α against θ, so that the removal of the α_1 abscissa scales is possible. At this point, curves of α_1 against θ may be filled in at 5° intervals of β_1 by using the proper abscissa increment. The plot thus constructed is called a θ,α_1,β_1 carpet.

A θ,α_1,β_1 carpet is constructed for the next solidity of 1.25 by shifting the angle-of-attack scales to the right a number of grid units proportional to the solidity increment of 0.25 and sufficient to keep any overlapping of the θ,α_1,β_1 carpets to a minimum. This procedure previously described in constructing the first θ,α_1,β_1 carpet is then repeated. The full range of solidities for which test data are available (0.50 to 1.50) may be presented by spacing and constructing the θ,α_1,β_1 carpets on this plot called a $\theta,\alpha_1,\beta_1,\sigma$ carpet plot. Similar $\theta,\alpha_1,\beta_1,\sigma$ carpet plots are then made for each of the other cambers, namely, $c_{l,o}=0.8$, 1.2, 1.5, and 1.8 shown in figures 114 (b), 114 (c), 114 (d), and 114 (e), respectively.

For intermediate camber conditions, linear interpolations between $\theta,\alpha_1,\beta_1,\sigma$ carpets could be used or these $\theta,\alpha_1,\beta_1,\sigma$ plots could be combined into a single carpet plot to make possible a single graphical interpolation. For example, figure 114 (a) may be combined with figure 114 (b) by again shifting the angle-of-attack scales to the right a number of grid units proportional to the camber increment of 0.40. Overlapping of the $\theta,\alpha_1,\beta_1,\sigma$ carpets can be avoided by shifting also the θ ordinate scale vertically a number of grid units proportional to the camber increment of 0.40. This combination of a vertical and a horizontal shift is facilitated by the use of register points labeled "AB" on both plots 114 (a) and 114 (b). The AB register points can be superimposed and the grids alined. In like manner, if all of the register points are used, figures 114 (a), 114 (b), 114 (c), 114 (d), and 114 (e) may be assembled into a single carpet plot. Figure 115 was made by combining plots 114 (a), 114 (c), and 114 (e) representing cambers $c_{l,o}$ of 0.4, 1.2, and 1.8, respectively. On this carpet, the design angle of attack is indicated by a dotted line and the approximate occurrence of twice minimum drag is indicated by a dashed line. Since the origins of the θ scales for cambers of 1.2 and 1.8 are shifted vertically a number of grid units proportional to the camber increment, the ordinate scale is no longer a true θ scale for these higher cambers and is called Y. When an interpolation is made for any camber above 0.4, the θ value may be obtained by substituting Y in the following expression:

$$\theta=Y-50(c_{l,o}-0.4)$$

Figures 114 (b) and 114 (d) representing cambers of 0.8 and 1.5 were omitted from figure 115 in order to reduce the size of the plot. It will also be noted that data are available for cambers of 0.8 and 1.5 at only two solidities, 1.00 and 1.50.

In view of the necessity for shifting the separate plots to provide for combinations of the several variables, as illustrated in figure 115, the carpet plots assembled in the present bound copy are useful only as a means of demonstrating this technique. For this reason, larger separate plots for use in compressor design have been prepared and are obtainable on request from NACA Headquarters, Washington, D. C.

ILLUSTRATIVE EXAMPLE

The use of the carpet plots presented can be shown best by use of an example. Generally, from a velocity-diagram calculation, the inlet-air angle, turning angle, and inlet Mach number are known, and some value of solidity has been decided upon. The problem is to find the camber $c_{l,o}$, the design angle of attack $\alpha_{1,d}$, the pressure-rise coefficient $\Delta p/q_1$ (one-dimensional flow being assumed), and the off-design variation in θ with α_1 at a constant blade setting. The following design conditions are assumed:

$$\beta_1=55°$$
$$\theta_d=15°$$
$$\sigma=1.10$$
$$M_1=0.65$$

Figure 112 is used to locate first the intersection of the curves for $\beta_1=55°$ and $\theta_d=15°$ on each of the four carpets representing solidities of 1.25, 1.00, 0.75, and 0.50; then a smooth curve is drawn connecting these four points which are labeled "A," "B," "C," and "D." If the β_1 and θ values had fallen between those represented on the curves, these intermediate values could be located by measuring the increments along the abscissa. Although the design solidity

of 1.10 falls between points A and B representing solidities of 1.25 and 1.00, respectively, points C and D for solidities of 0.75 and 0.50 are included to define more accurately the shape of the curve between points A and B. Since the horizontal interval from A to B represents a solidity increment of 0.25 from 1.25 to 1.00, the point corresponding to a solidity of 1.10 may be obtained by locating on the ABCD curve the point E, which has a horizontal distance from point B equal to a solidity increment of 0.10. Point E thus located indicates a camber $c_{l,o}$ of 0.87 on the ordinate scale.

Next, the solidity of 1.10 and the newly found camber $c_{l,o}$ of 0.87 are used in conjunction with figure 113 to find the design angle of attack. The point for a camber of 0.87 is located on the $\sigma=1.10$ curve between the camber of 0.8 and 0.9 curves by reading the proper horizontal increment of 0.07. This point indicates on the ordinate scale a design angle of attack of 10.5°.

The pressure-rise coefficient $\Delta p/q_1$ is found from figure 116 (a) by using the values $M_1=0.65$, $\beta_1=55°$, and $\theta=15°$. In figure 116 (a), the $\Delta p/q_1$ was calculated on a one-dimensional basis, whereas in figure 116 (b) the $\Delta p/q_1$ was calculated for a constant axial velocity. Since one-dimensional flow was assumed in this example, figure 116 (a) should be used. Employing the proper horizontal β_1 increment of 10° and starting at the $\beta_1=45°$ curve, locate the $\beta_1=55°$ point on the $\theta=15°$ curve for each of the carpet plots representing Mach numbers of 0.50, 0.60, 0.70, and 0.80. The four points thus located are designated "F," "G," "H," and "I" and are connected by a smooth curve. Next, locate on this curve point J whose horizontal distance from point G is equal to a Mach number increment of 0.05. Point J indicates on the ordinate scale a pressure-rise coefficient of 0.590.

The last step in this sample problem is the prediction of an α_1,θ curve at a constant blade setting. The off-design carpet (fig. 115) is used to predict this α_1,θ curve for the blade section having a camber $c_{l,o}$ of 0.87, a solidity σ of 1.10 and a blade setting of 44.5°. The blade setting is the difference between the inlet-air angle and the angle of attack, or 55°−10.5°=44.5° at the design condition. In figure 115, curves labeled "a" and "b" representing this constant blade setting of 44.5° are drawn on the θ,α_1,β_1 plots for $c_{l,o}$ of 0.4 at the solidities of 1.25 and 1.00, respectively. Curve c is then interpolated for the solidity of 1.10 by the use of the correct solidity increment along the abscissa. As can be seen in the example, this interpolation is aided by drawing between curves a and b lines of constant angle of attack at values of 6°, 8°, 10°, 12°, and 14°. A similar interpolation is then accomplished for a camber of 1.2, which produces curves d, e, and f. A linear interpolation for the intermediate camber of 0.87 is made between curves c and f to obtain curve g, which shows the variation of Y with α_1 for the design camber and solidity. The Y values may be converted to θ values by using the relationship

$$\theta=Y-50(c_{l,o}-0.4)$$

It has been found that linear interpolations between any two cambers of figure 115 produce design turning angles which agree with the design carpet plot within 1.0°. If greater accuracy is desired, a faired curve between the three cambers should be used. In figure 115, the design angle of attack is indicated by a short-dashed line and the approximate occurrence of twice minimum drag is indicated by a long-dashed line.

REFERENCES

1. Erwin, John R., and Emery, James C.: Effect of Tunnel Configuration and Testing Technique on Cascade Performance. NACA Rep. 1016, 1951. (Supersedes NACA TN 2028.)
2. Westphal, Willard R., and Godwin, William R.: Comparison of NACA 65-Series Compressor-Blade Pressure Distributions and Performance in a Rotor and in Cascade. NACA TN 3806, 1956. (Supersedes NACA RM L51H20.)
3. Bogdonoff, Seymour M., and Bogdonoff, Harriet E.: Blade Design Data for Axial-Flow Fans and Compressors. NACA WR L-635, 1945. (Formerly NACA ACR L5F07a.)
4. Bogdonoff, Seymour M., and Hess, Eugene E.: Axial-Flow Fan and Compressor Blade Design Data at 52.5° Stagger and Further Verification of Cascade Data by Rotor Tests. NACA TN 1271, 1947.
5. Abbott, Ira H., von Doenhoff, Albert E., and Stivers, Louis S., Jr.: Summary of Airfoil Data. NACA Rep. 824, 1945. (Supersedes NACA WR L-560.)
6. Yates, A. H.: 'Carpets' and 'Lattices.' Aircraft Engineering, vol. XVIII, no. 203, Jan. 1946, pp. 8–9.
7. Bursnall, William J., and Loftin, Laurence K., Jr.: Experimental Investigation of Localized Regions of Laminar-Boundary-Layer Separation. NACA TN 2338, 1951.
8. Howell, A. R.: Design of Axial Compressors. Lectures on the Development of the British Gas Turbine Jet Unit Published in War Emergency Issue No. 12 of the Institution of Mechanical Engineers. A.S.M.E. Reprint, Jan. 1947, pp. 452–462.

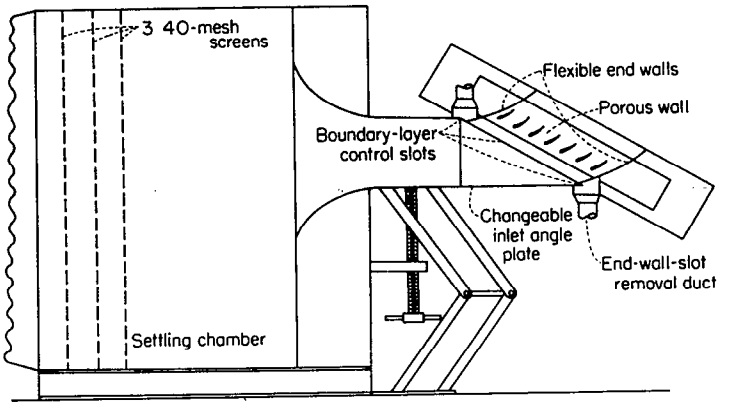

FIGURE 1.—Vertical cross section of two-dimensional low-speed cascade tunnel.

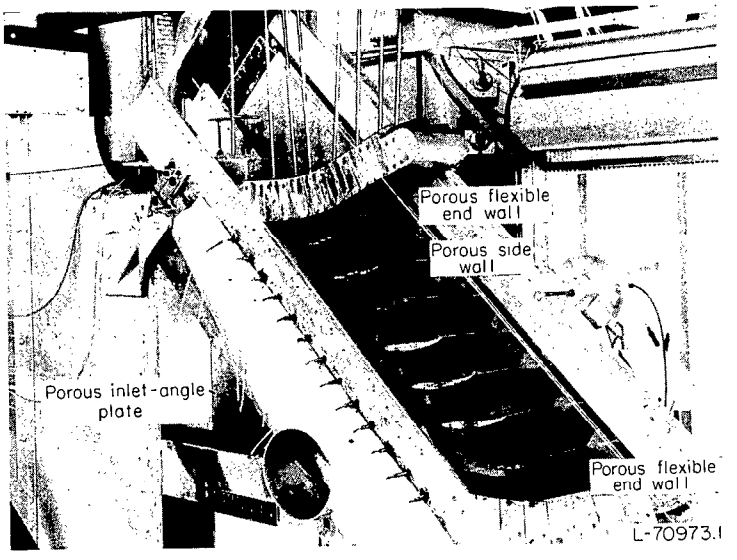

FIGURE 2.—Photograph of Langley 5-inch cascade tunnel with portions of one side removed to show porous surfaces.

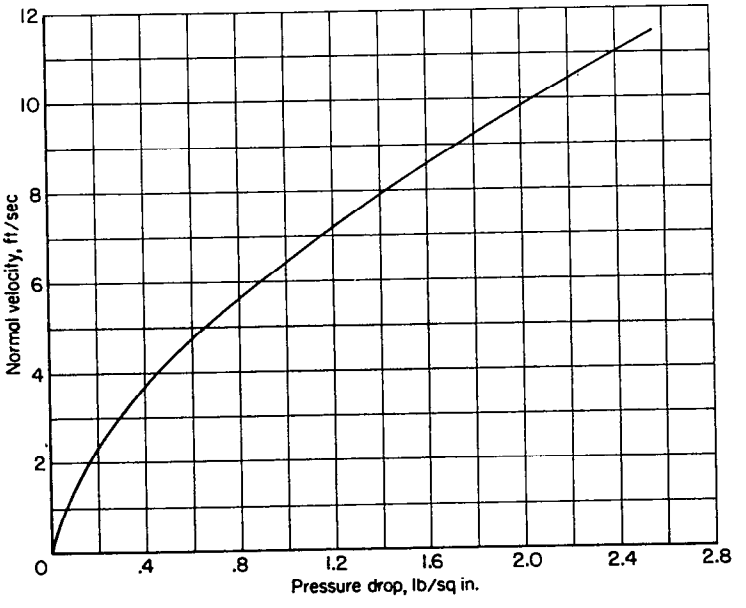

FIGURE 3.—Porosity characteristics of the calendered monel filter cloth used in this investigation.

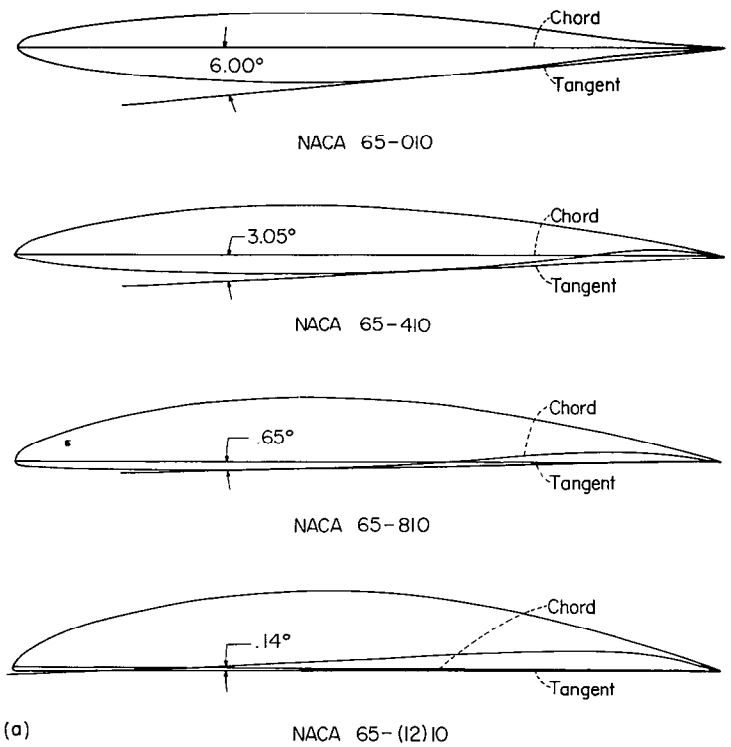

(a) Lower cambered sections. Angle between chord line and tangent to lower surface as shown for the various sections.

FIGURE 4.—Blade sections tested in this investigation.

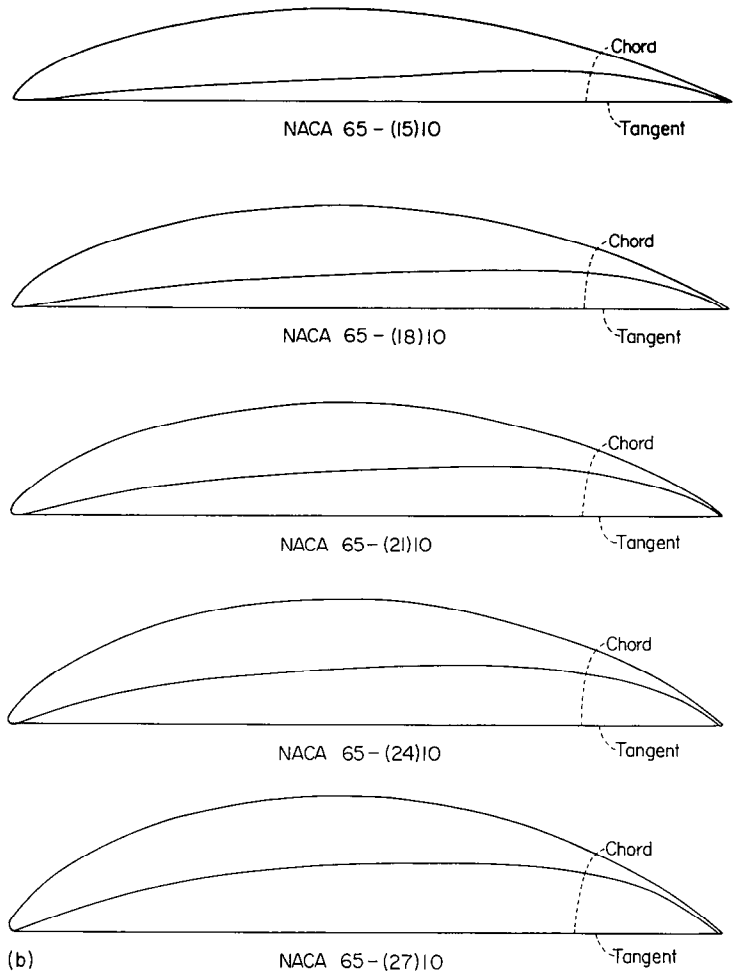

(b) Higher cambered sections. Chord line and tangent line coincident.

FIGURE 4.—Concluded.

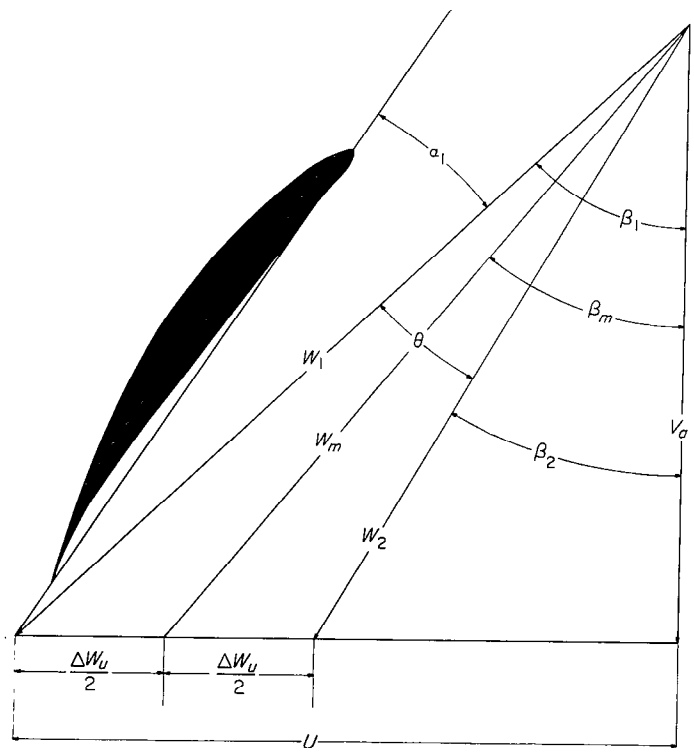

FIGURE 5.—Typical vector diagram for a compressor rotor.

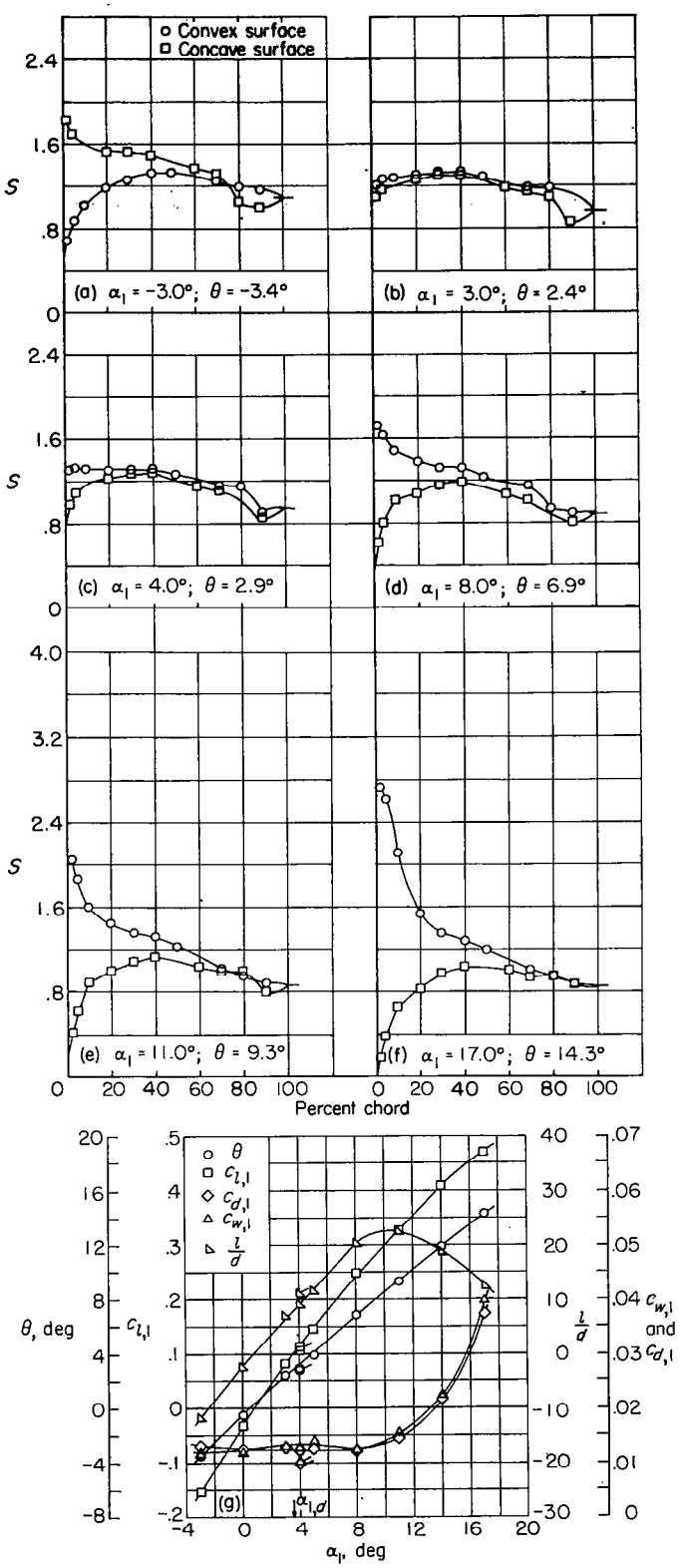

(g) Section characteristics; flagged symbol indicates leading-edge roughness.

FIGURE 6.—Blade-surface pressure distributions and blade section characteristics for the cascade combination, $\beta_1=30°$, $\sigma=1.00$, and blade section, NACA 65–010.

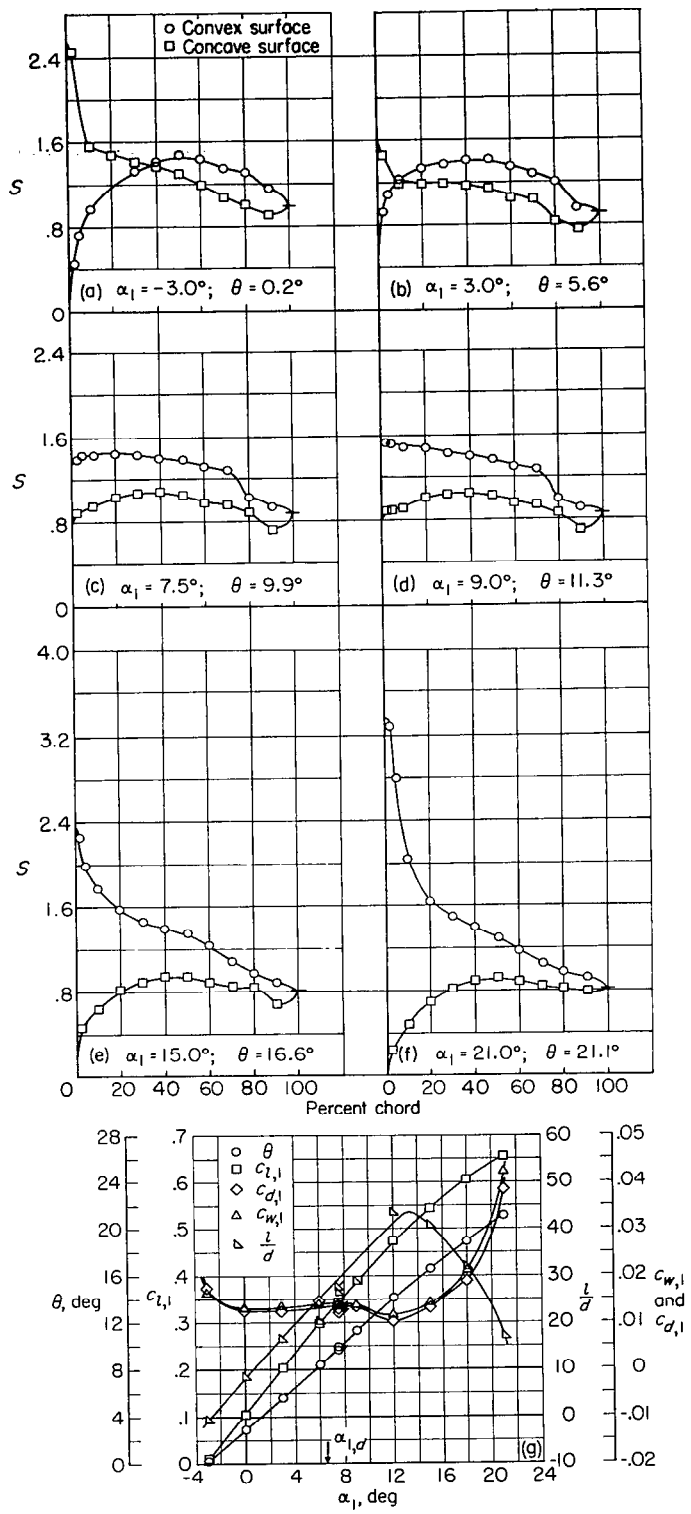

(g) Section characteristics; flagged symbol indicates leading-edge roughness.

FIGURE 7.—Blade-surface pressure distributions and blade section characteristics for the cascade combination, $\beta_1=30°$, $\sigma=1.00$, and blade section, NACA 65–410.

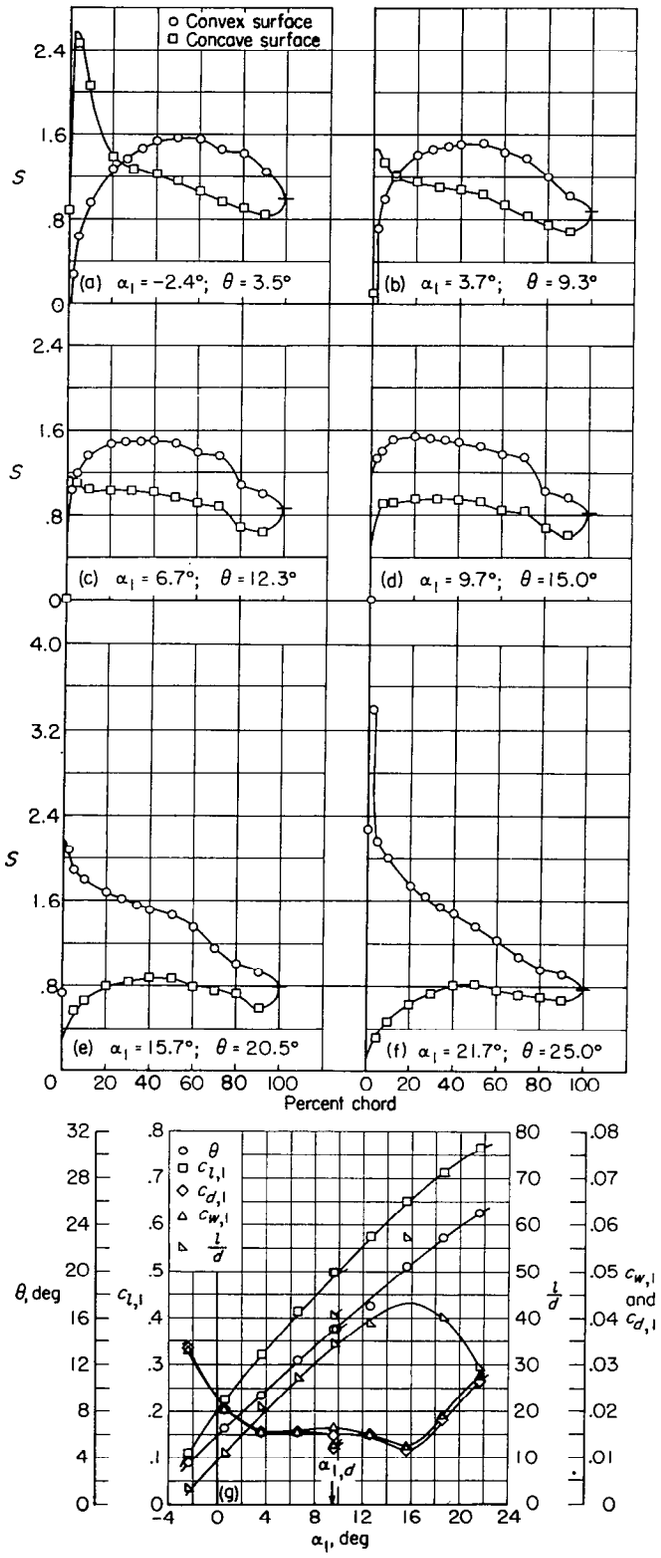

(g) Section characteristics; flagged symbol indicates leading-edge roughness.

FIGURE 8.—Blade-surface pressure distributions and blade section characteristics for the cascade combination, $\beta_1=30°$, $\sigma=1.00$, and blade section, NACA 65–810.

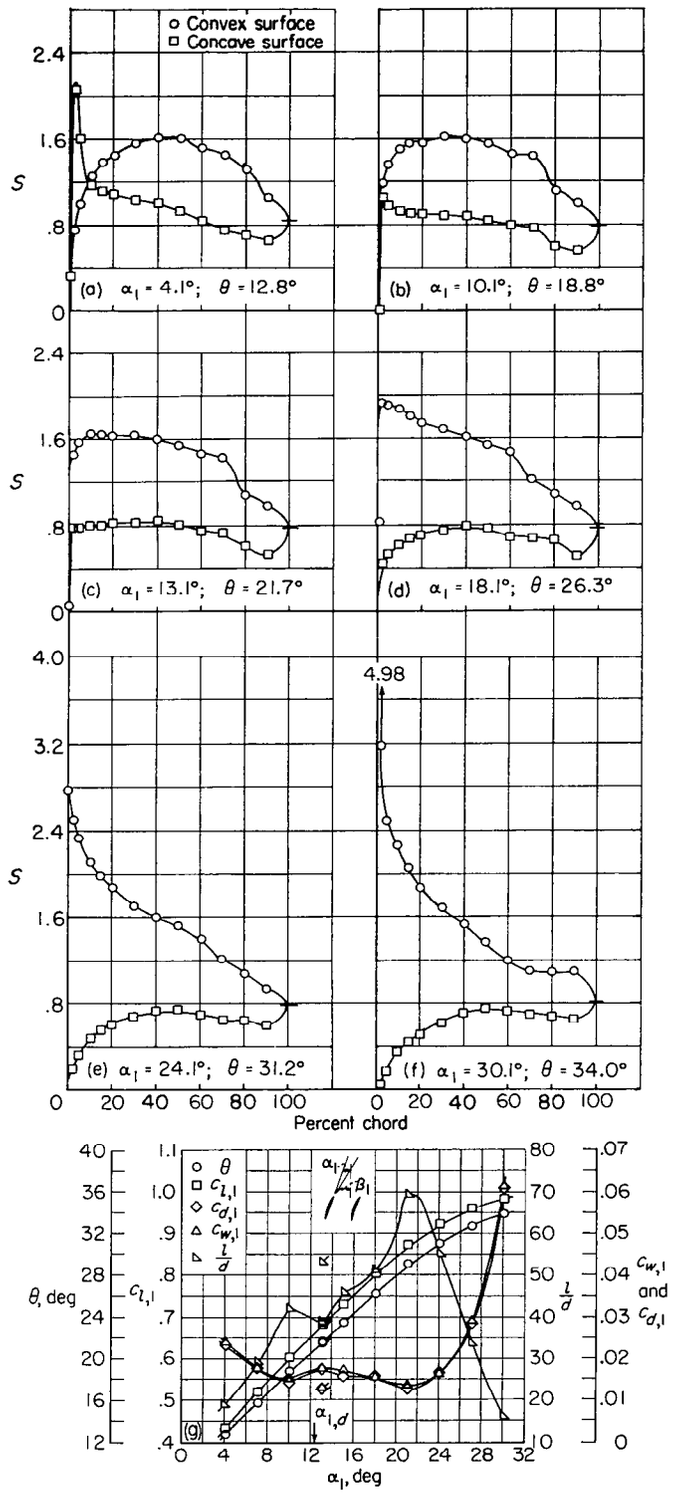

(g) Section characteristics; flagged symbol indicates leading-edge roughness.

FIGURE 9.—Blade-surface pressure distributions and blade section characteristics for the cascade combination, $\beta_1=30°$, $\sigma=1.00$, and blade section, NACA 65–(12)10.

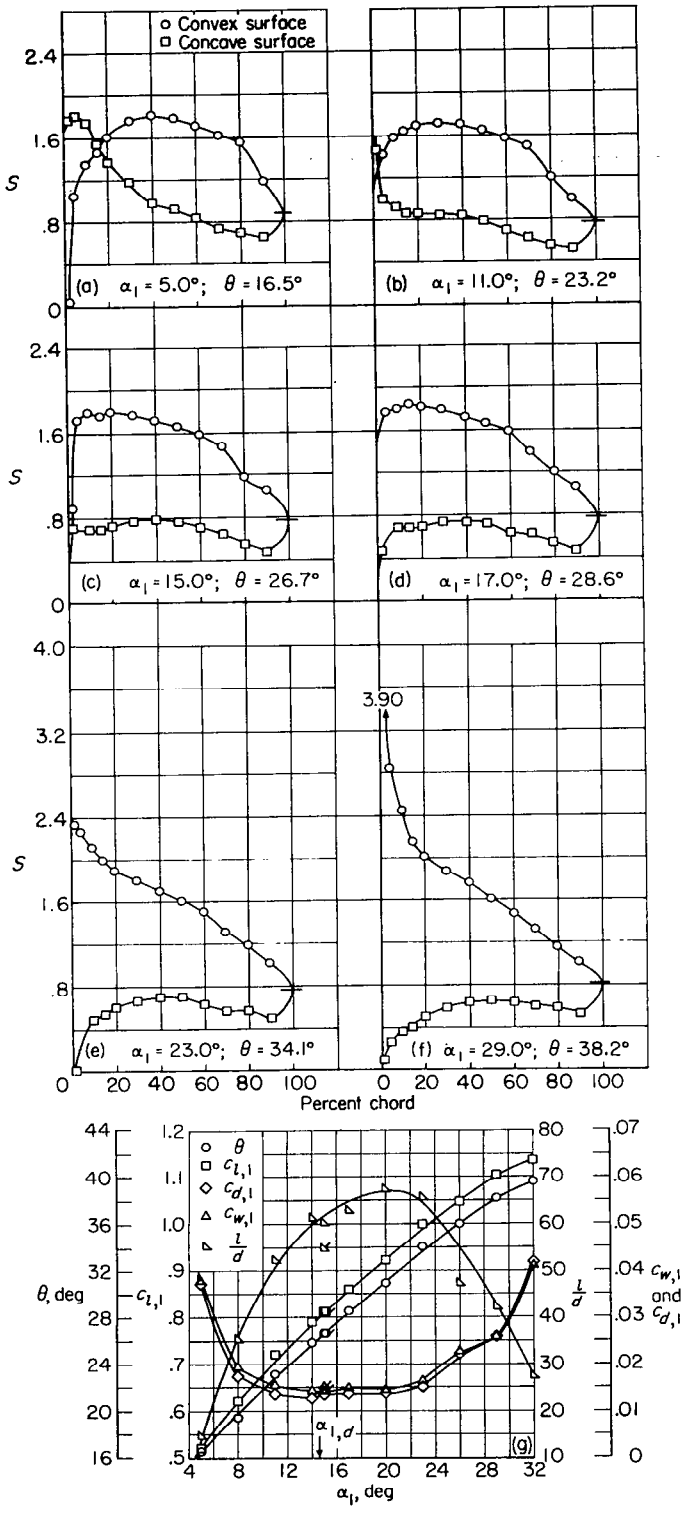

(g) Section characteristics; flagged symbol indicates leading-edge roughness.

FIGURE 10.—Blade-surface pressure distributions and blade section characteristics for the cascade combination, $\beta_1=30°$, $\sigma=1.00$, and blade section, NACA 65–(15)10.

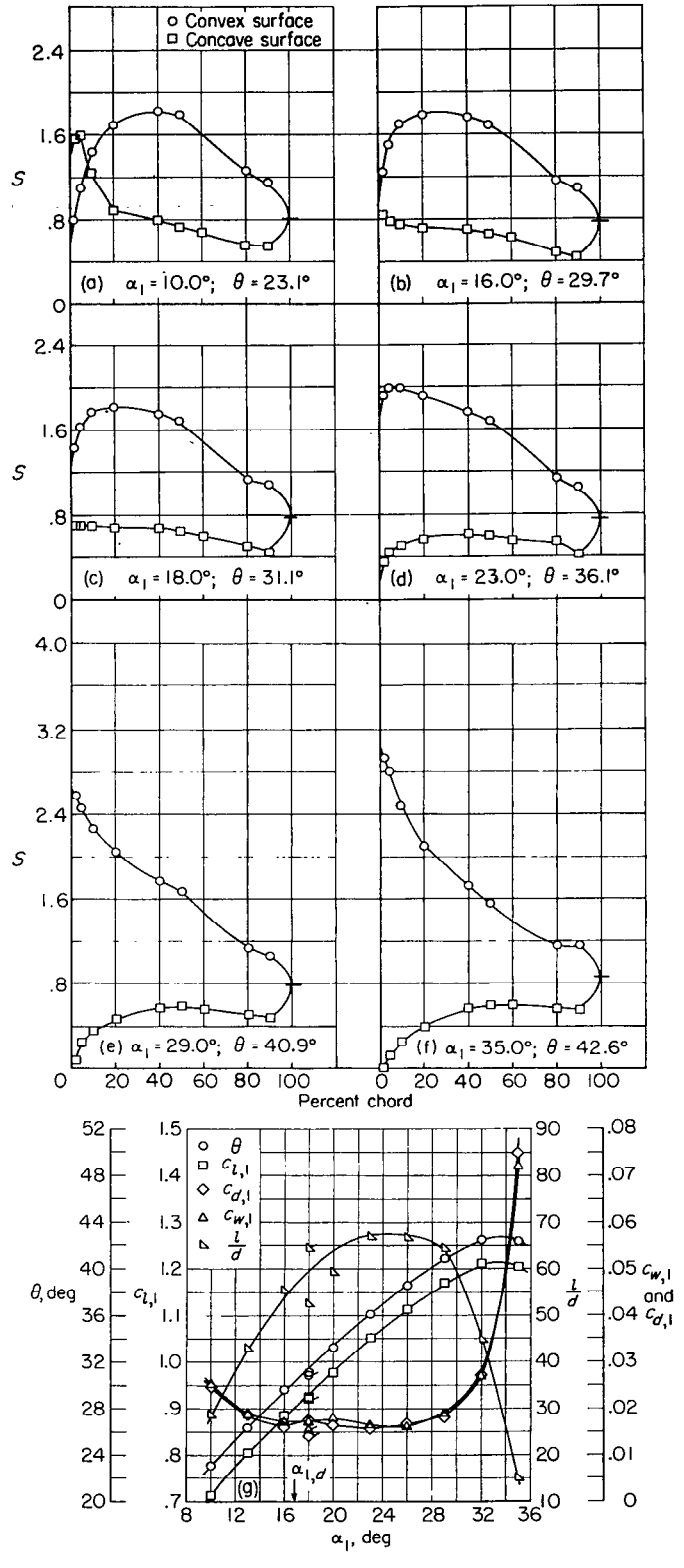

(g) Section characteristics; flagged symbol indicates leading-edge roughness.

FIGURE 11.—Blade-surface pressure distributions and blade section characteristics for the cascade combination, $\beta_1=30°$, $\sigma=1.00$, and blade section, NACA 65–(18)10.

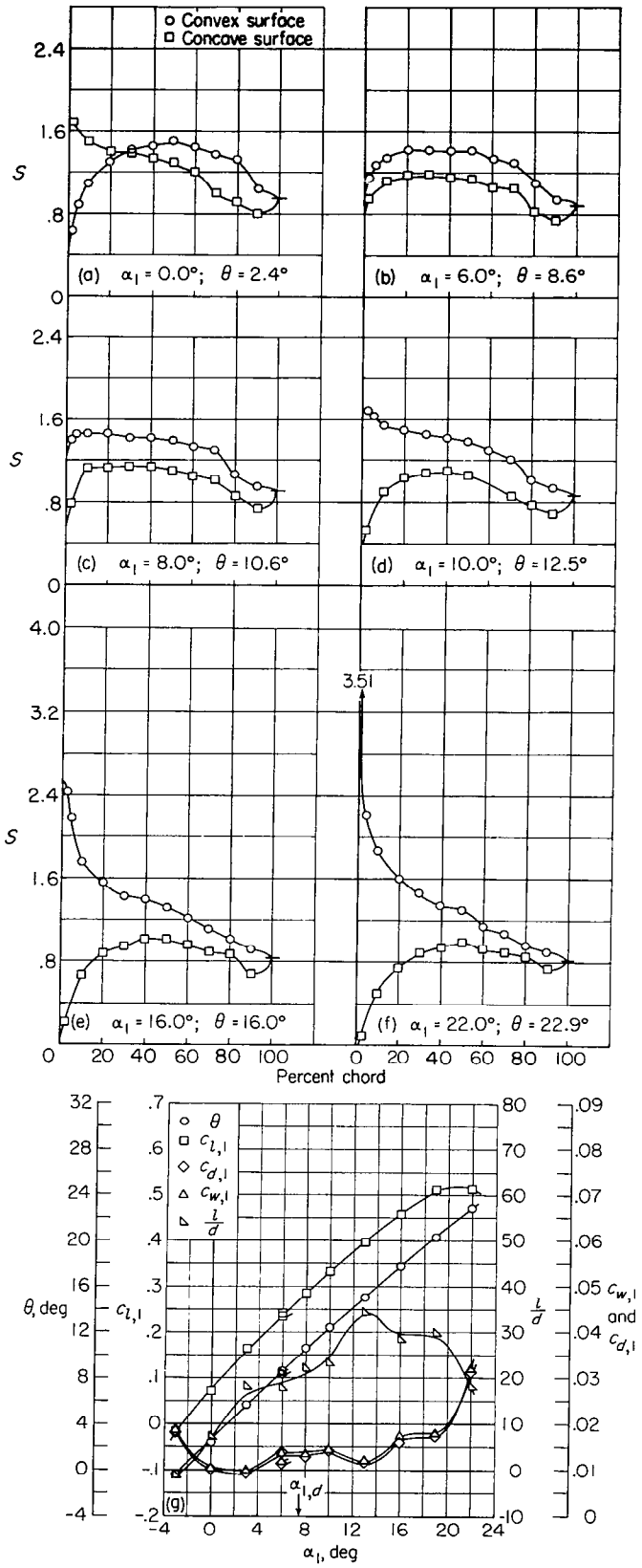

(g) Section characteristics; flagged symbol indicates leading-edge roughness.

FIGURE 12.—Blade-surface pressure distributions and blade section characteristics for the cascade combination, $\beta_1=30°$, $\sigma=1.25$, and blade section, NACA 65–410.

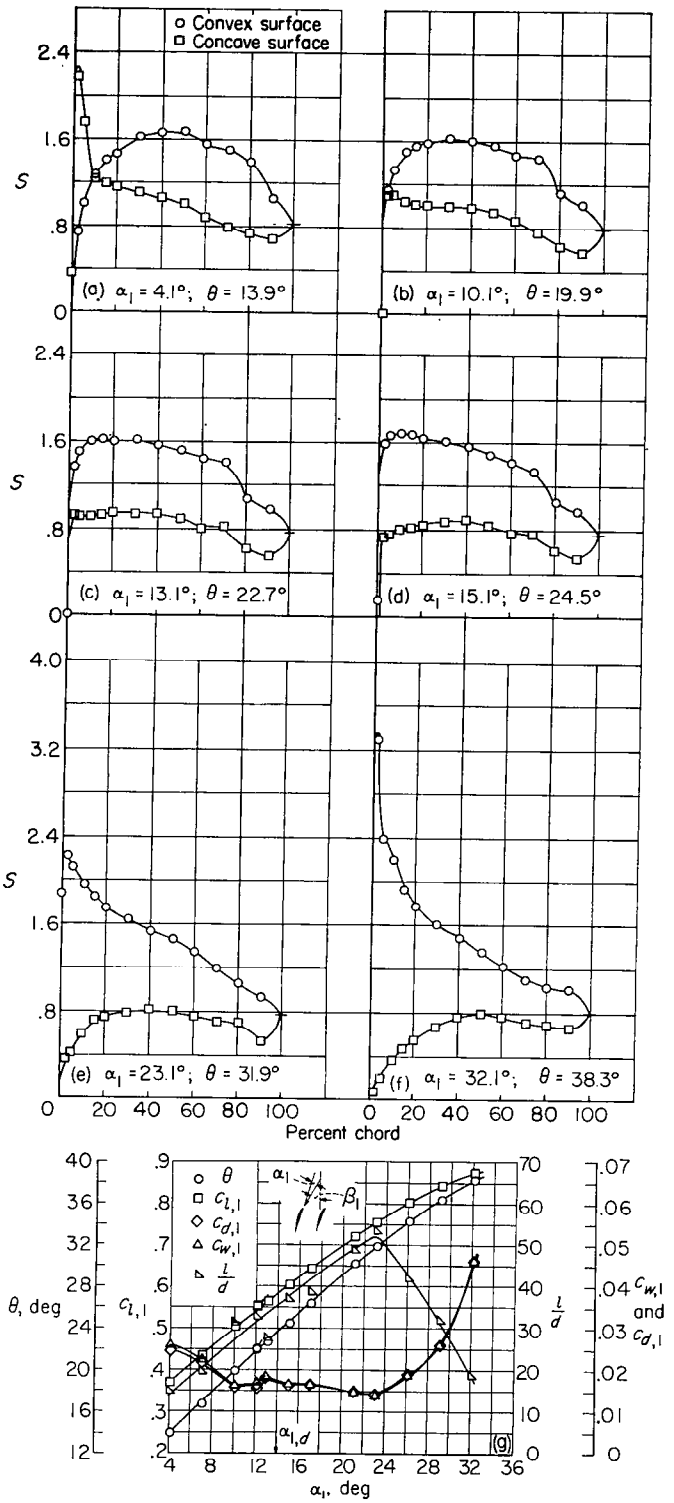

(g) Section characteristics; flagged symbol indicates leading-edge roughness.

FIGURE 13.—Blade-surface pressure distributions and blade section characteristics for the cascade combination, $\beta_1=30°$, $\sigma=1.25$, and blade section, NACA 65–(12)10.

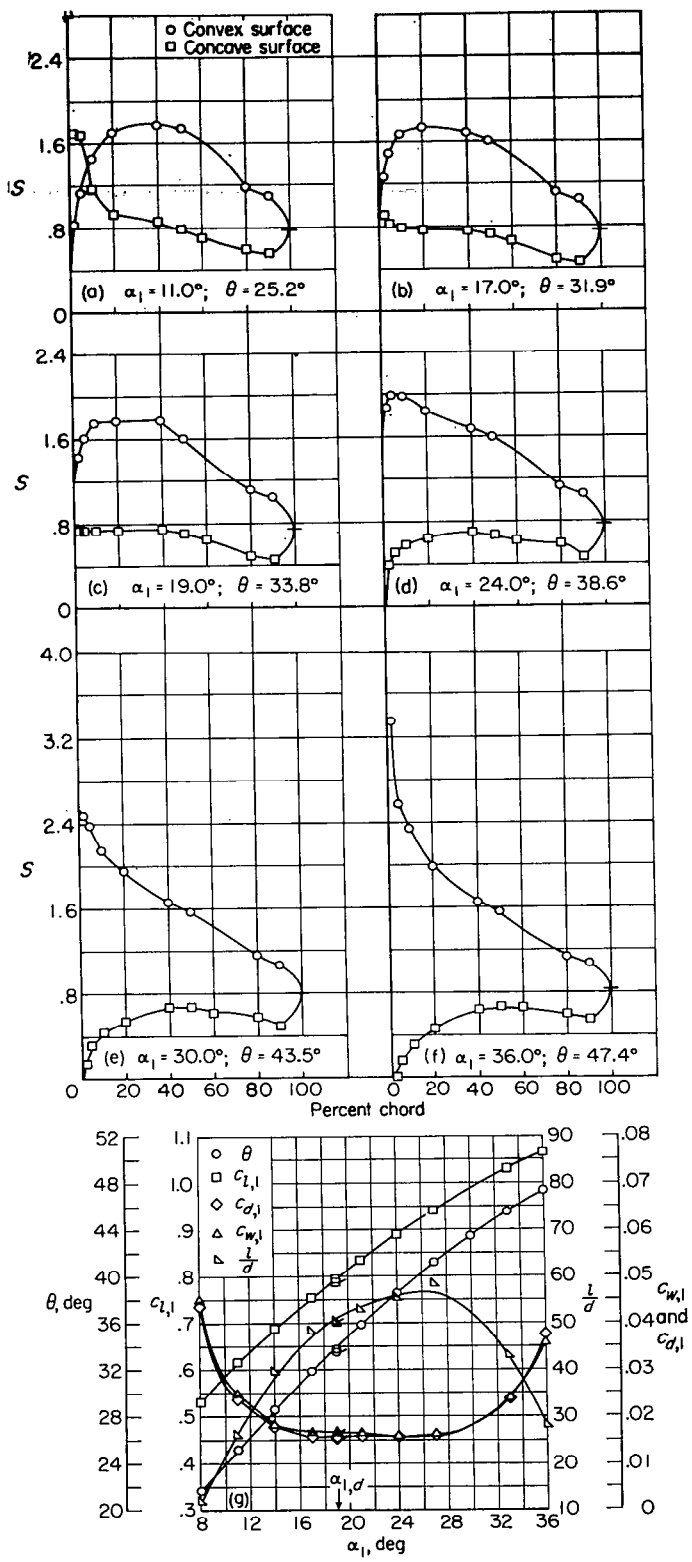

(g) Section characteristics; flagged symbol indicates leading-edge roughness.

FIGURE 14.—Blade-surface pressure distributions and blade section characteristics for the cascade combination, $\beta_1=30°$, $\sigma=1.25$, and blade section, NACA 65–(18)10.

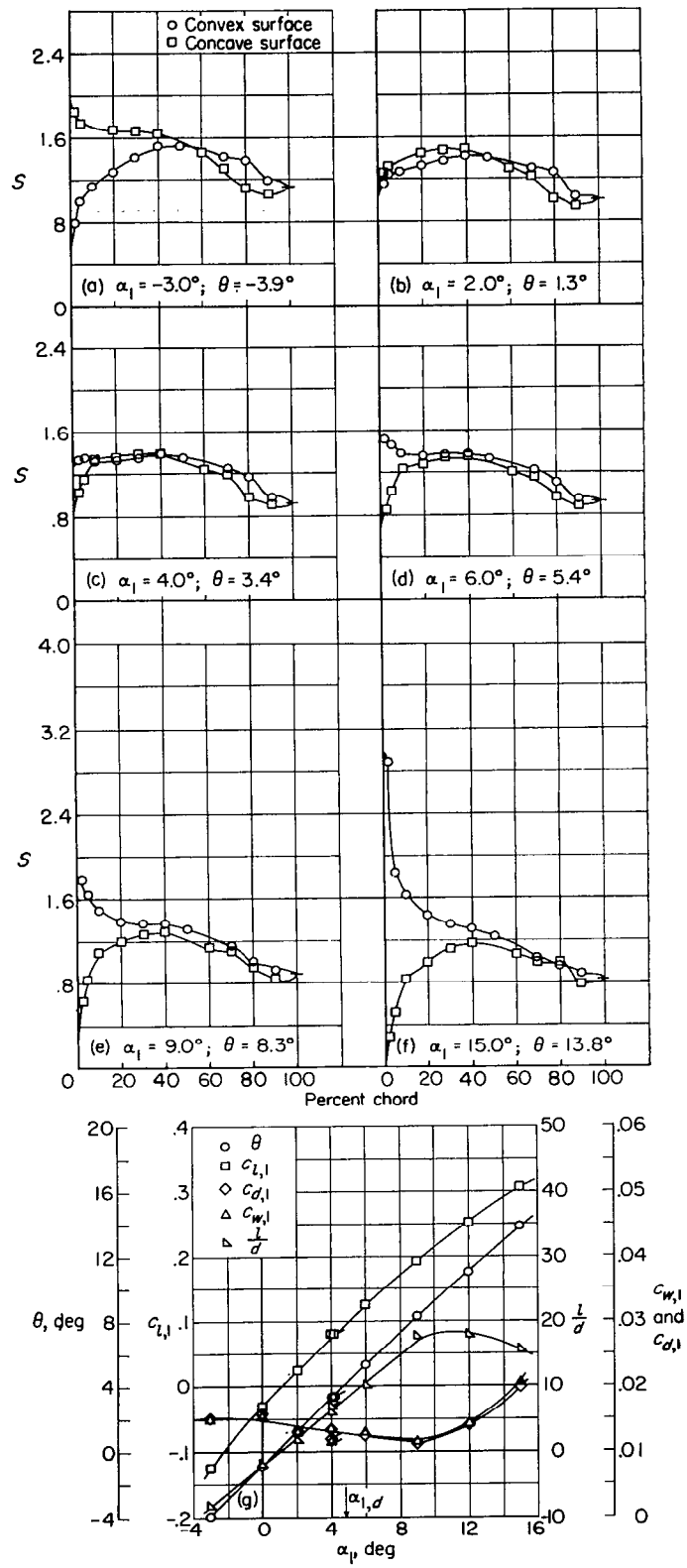

(g) Section characteristics; flagged symbol indicates leading-edge roughness.

FIGURE 15.—Blade-surface pressure distributions and blade section characteristics for the cascade combination, $\beta_1=30°$, $\sigma=1.50$, and blade section, NACA 65–010.

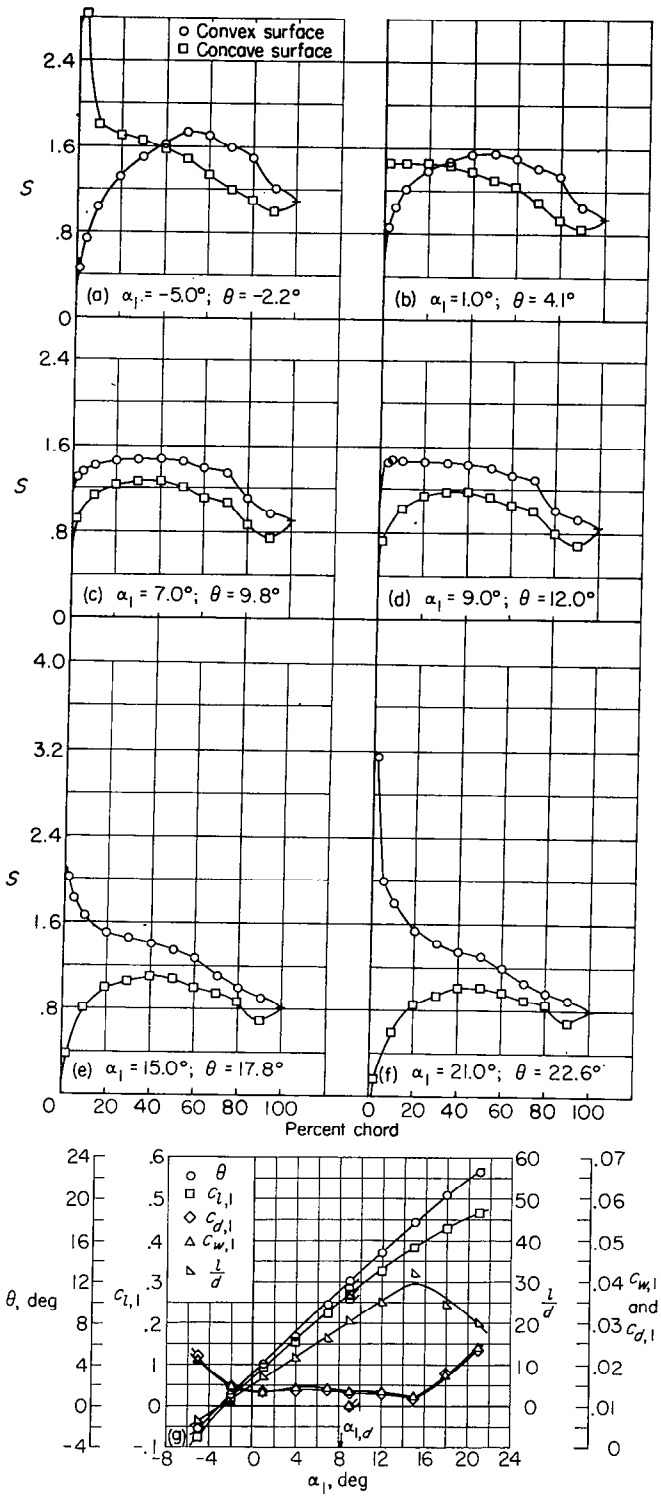

(g) Section characteristics; flagged symbol indicates leading-edge roughness.

FIGURE 16.—Blade-surface pressure distributions and blade section characteristics for the cascade combination, $\beta_1=30°$, $\sigma=1.50$, and blade section, NACA 65–410.

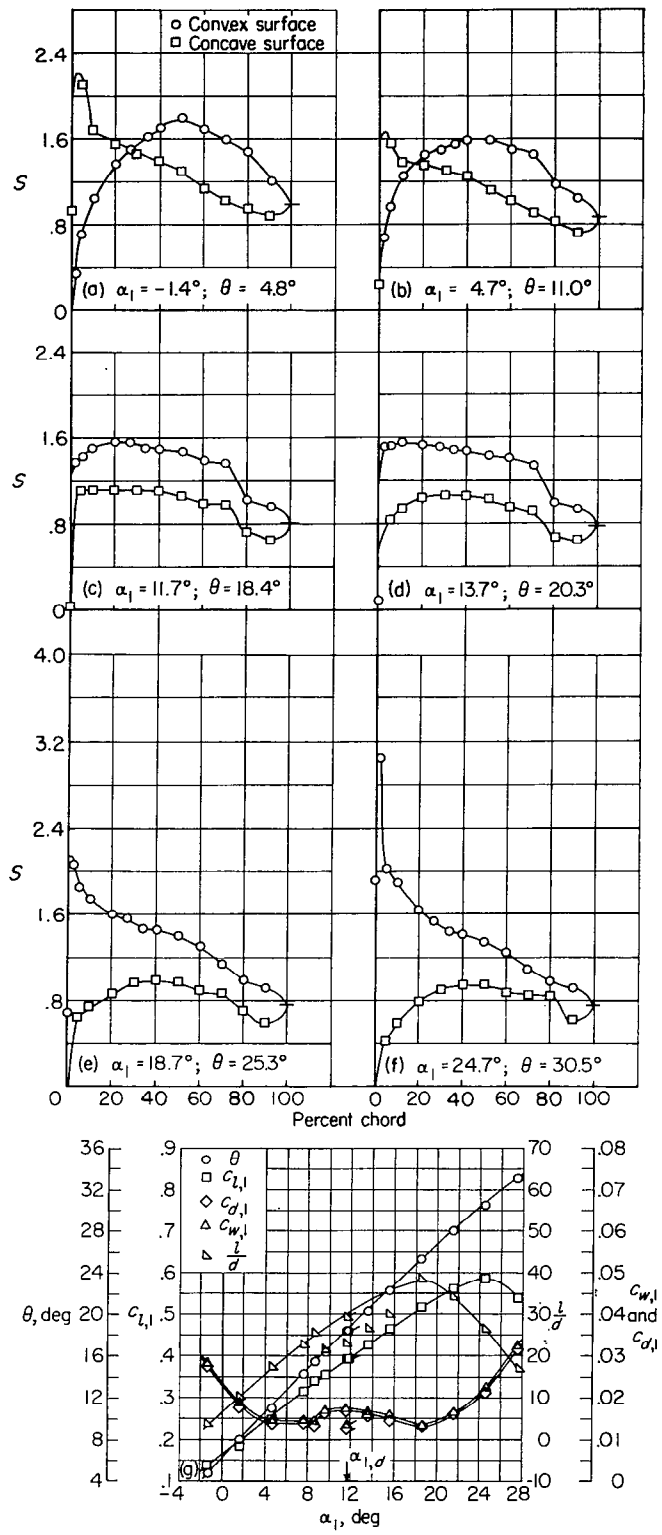

(g) Section characteristics; flagged symbol indicates leading-edge roughness.

FIGURE 17.—Blade-surface pressure distributions and blade section characteristics for the cascade combination, $\beta_1=30°$, $\sigma=1.50$, and blade section, NACA 65–810.

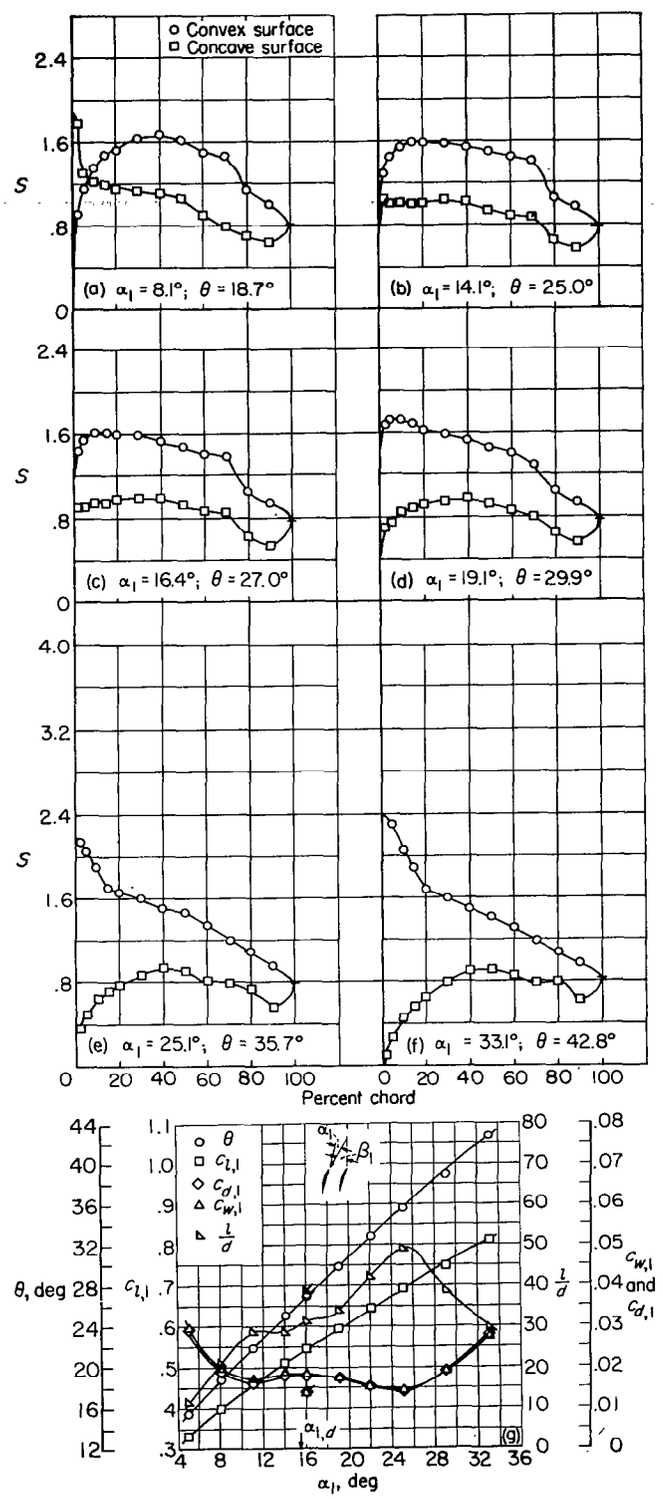

(g) Section characteristics; flagged symbol indicates leading-edge roughness.

FIGURE 18.—Blade-surface pressure distributions and blade section characteristics for the cascade combination, $\beta_1=30°$, $\sigma=1.50$, and blade section, NACA 65-(12)10.

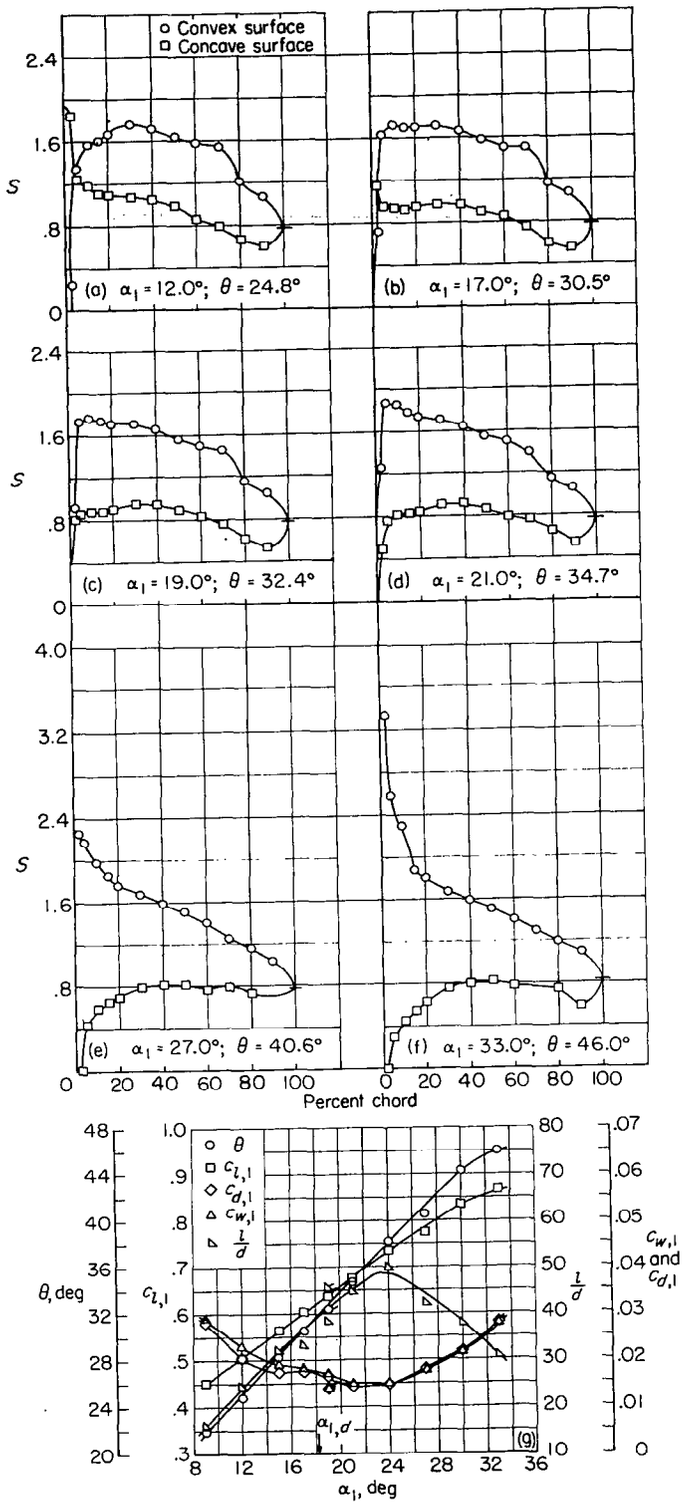

(g) Section characteristics; flagged symbol indicates leading-edge roughness.

FIGURE 19.—Blade-surface pressure distributions and blade section characteristics for the cascade combination, $\beta_1=30°$, $\sigma=1.50$, and blade section, NACA 65-(15)10.

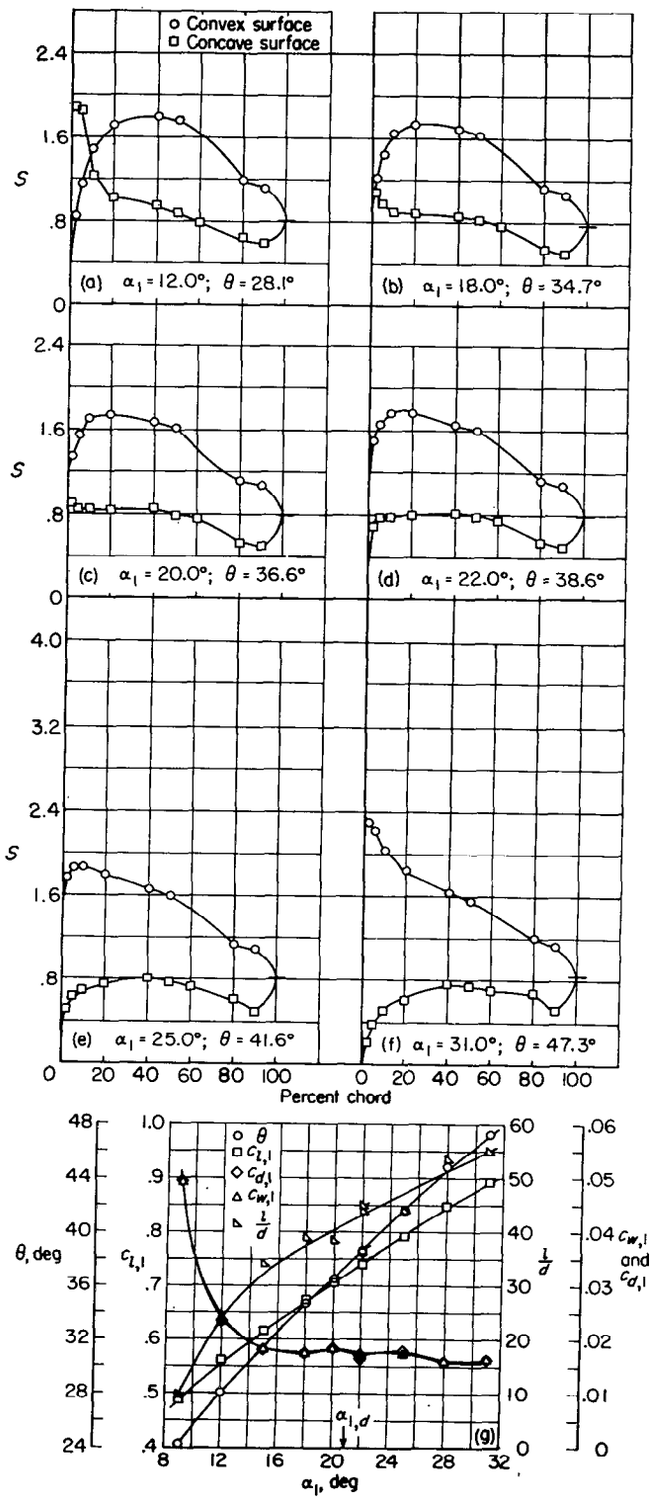

(g) Section characteristics; flagged symbol indicates leading-edge roughness.

FIGURE 20.—Blade-surface pressure distributions and blade section characteristics for the cascade combination, $\beta_1=30°$, $\sigma=1.50$, and blade section, NACA 65-(18)10.

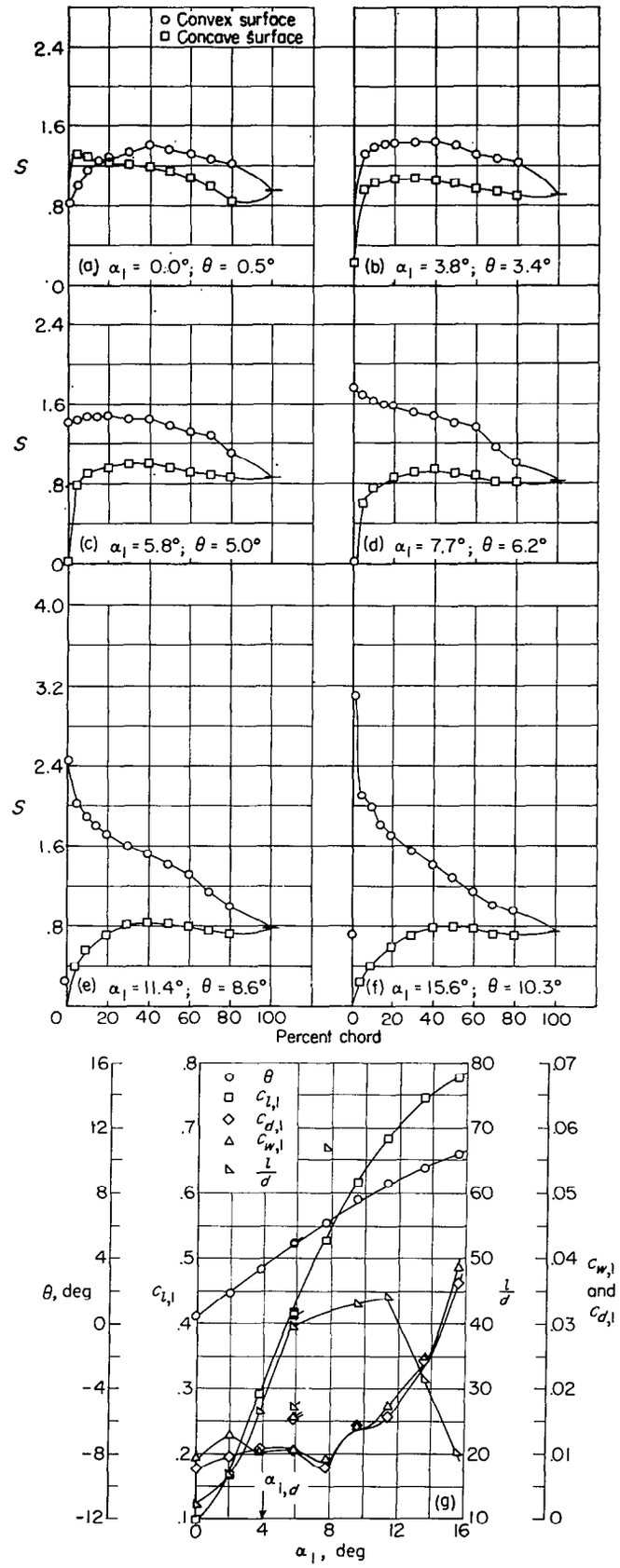

(g) Section characteristics; flagged symbol indicates leading-edge roughness.

FIGURE 21.—Blade-surface pressure distributions and blade section characteristics for the cascade combination, $\beta_1=45°$, $\sigma=0.50$, and blade section, NACA 65-410.

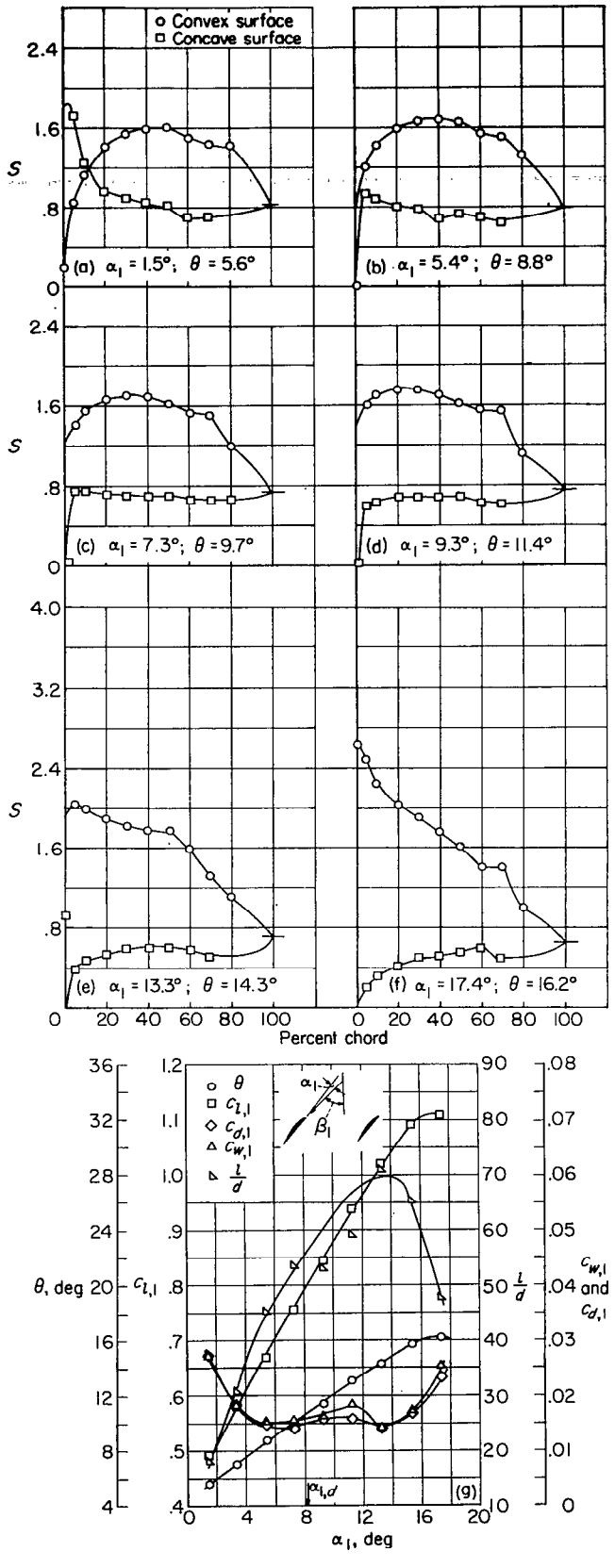

(g) Section characteristics.

FIGURE 22.—Blade-surface pressure distributions and blade section characteristics for the cascade combination, $\beta_1=45°$, $\sigma=0.50$, and blade section, NACA 65–(12)10.

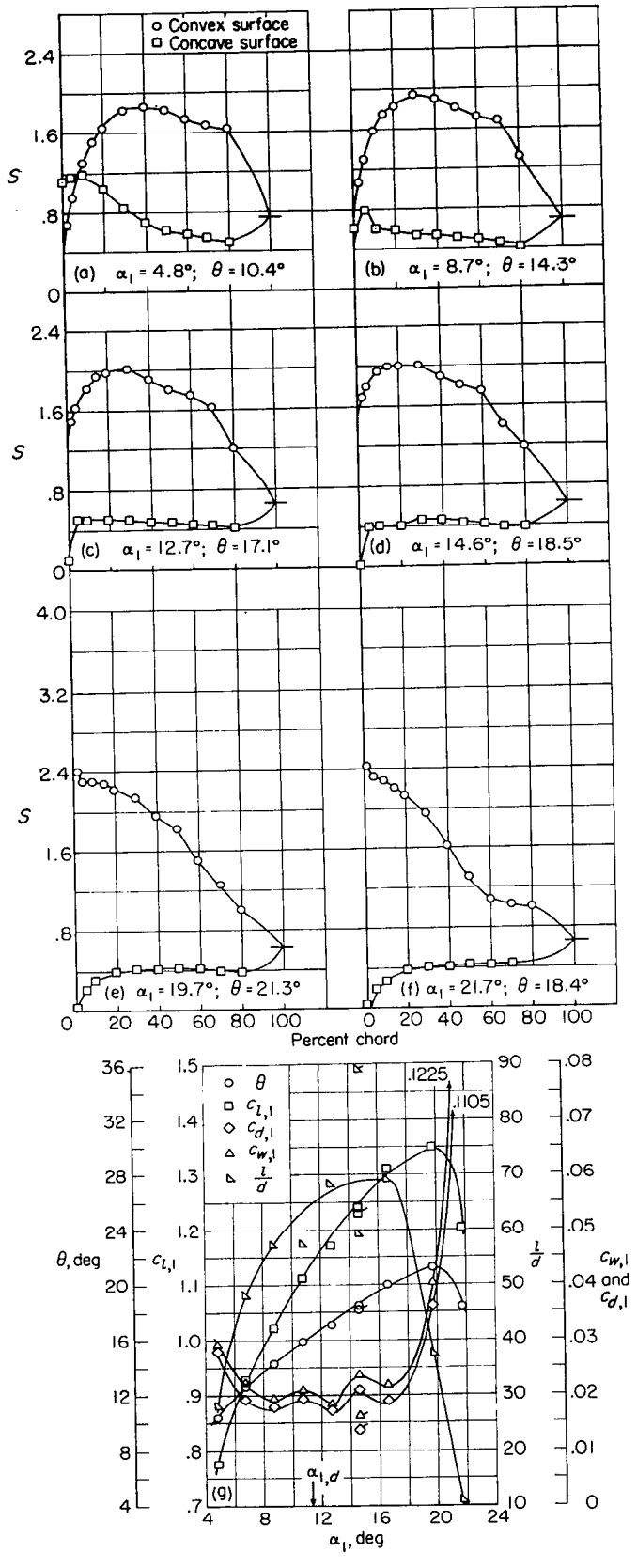

(g) Section characteristics; flagged symbol indicates leading-edge roughness.

FIGURE 23.—Blade-surface pressure distributions and blade section characteristics for the cascade combination, $\beta_1=45°$, $\sigma=0.50$, and blade section, NACA 65–(18)10.

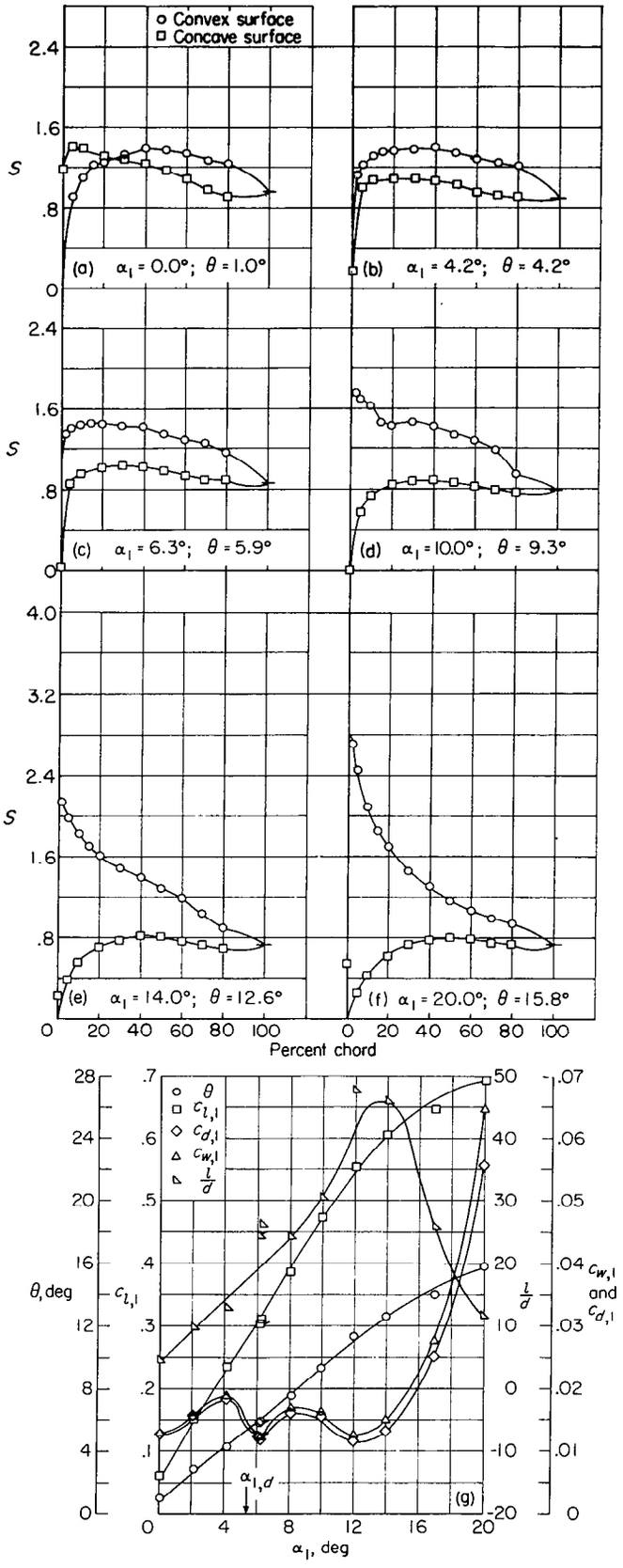

(g) Section characteristics; flagged symbol indicates leading-edge roughness.

FIGURE 24.—Blade-surface pressure distributions and blade section characteristics for the cascade combination, $\beta_1=45°$, $\sigma=0.75$, and blade section, NACA 65-410.

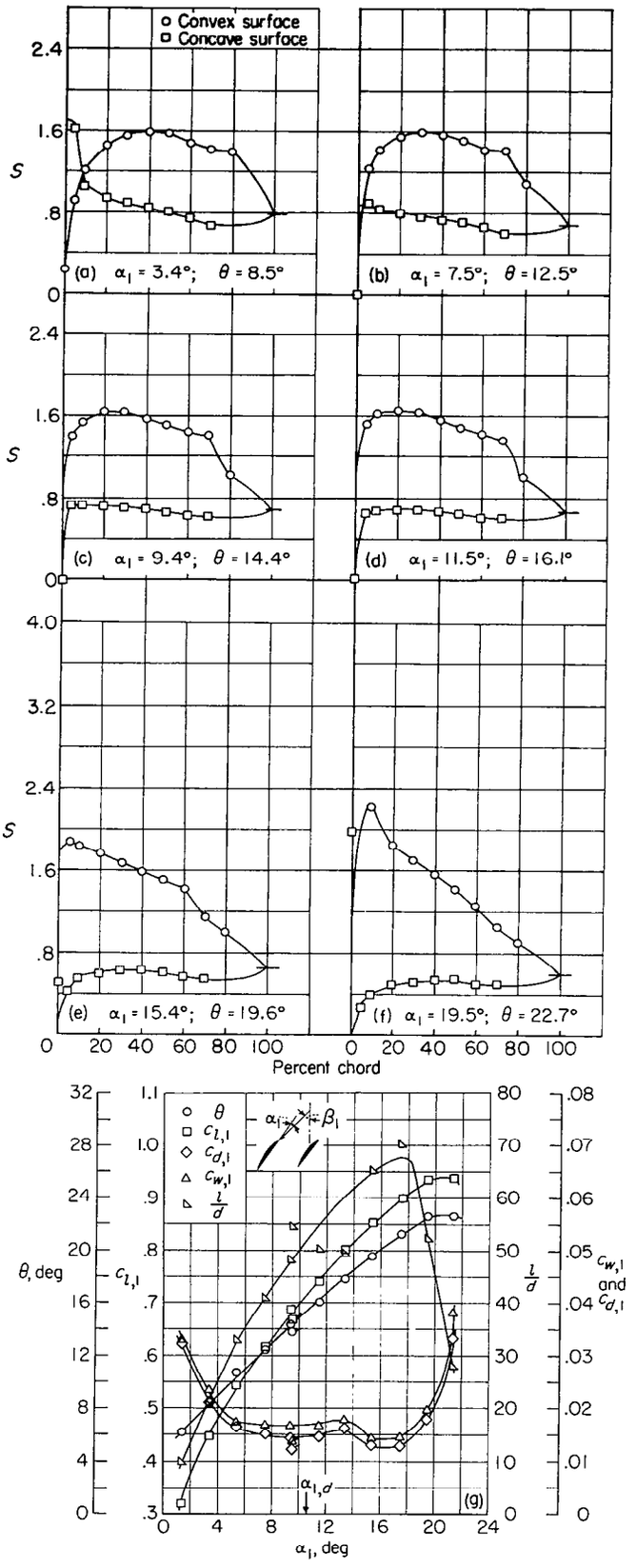

(g) Section characteristics; flagged symbol indicates leading-edge roughness.

FIGURE 25.—Blade-surface pressure distributions and blade section characteristics for the cascade combination, $\beta_1=45°$, $\sigma=0.75$, and blade section, NACA 65-(12)10.

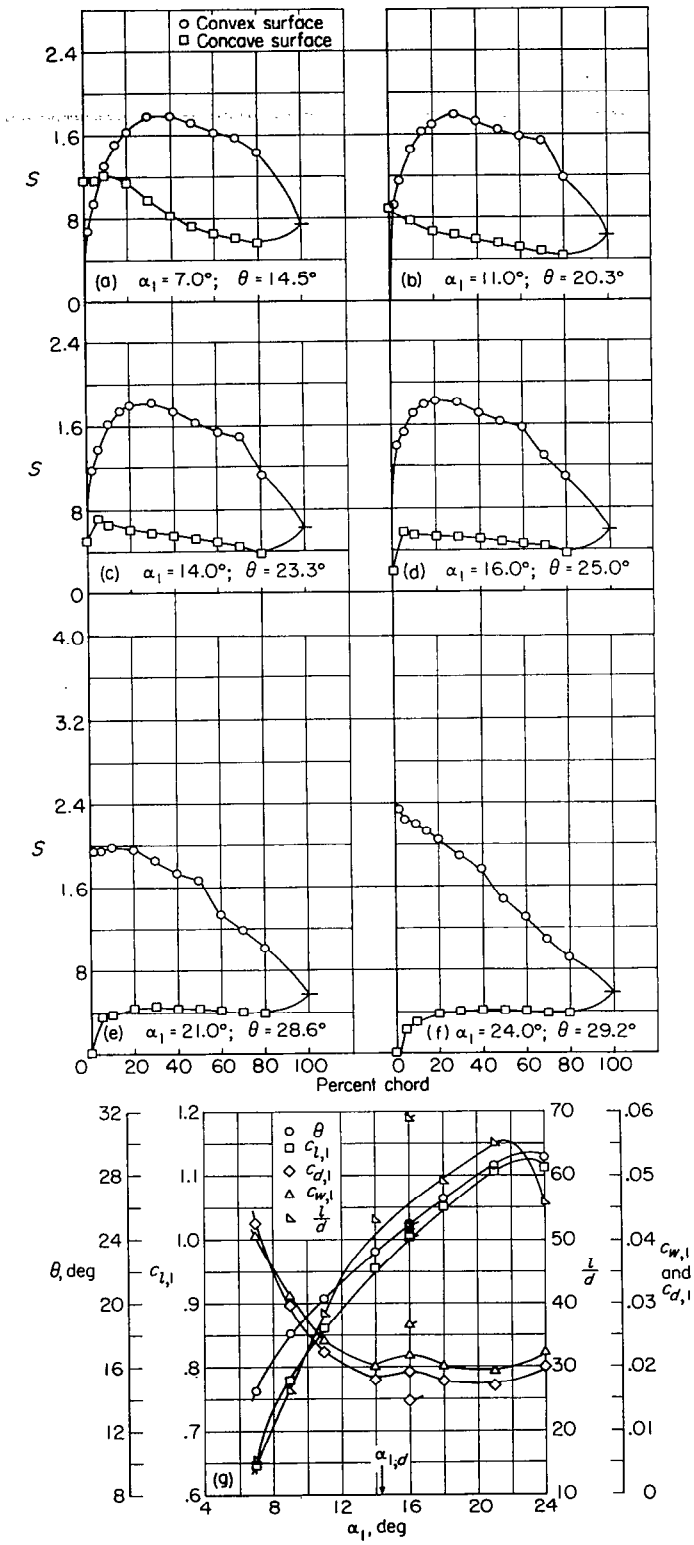

(g) Section characteristics; flagged symbol indicates leading-edge roughness.

FIGURE 26.—Blade-surface pressure distributions and blade section characteristics for the cascade combination, $\beta_1=45°$, $\sigma=0.75$, and blade section, NACA 65-(18)10.

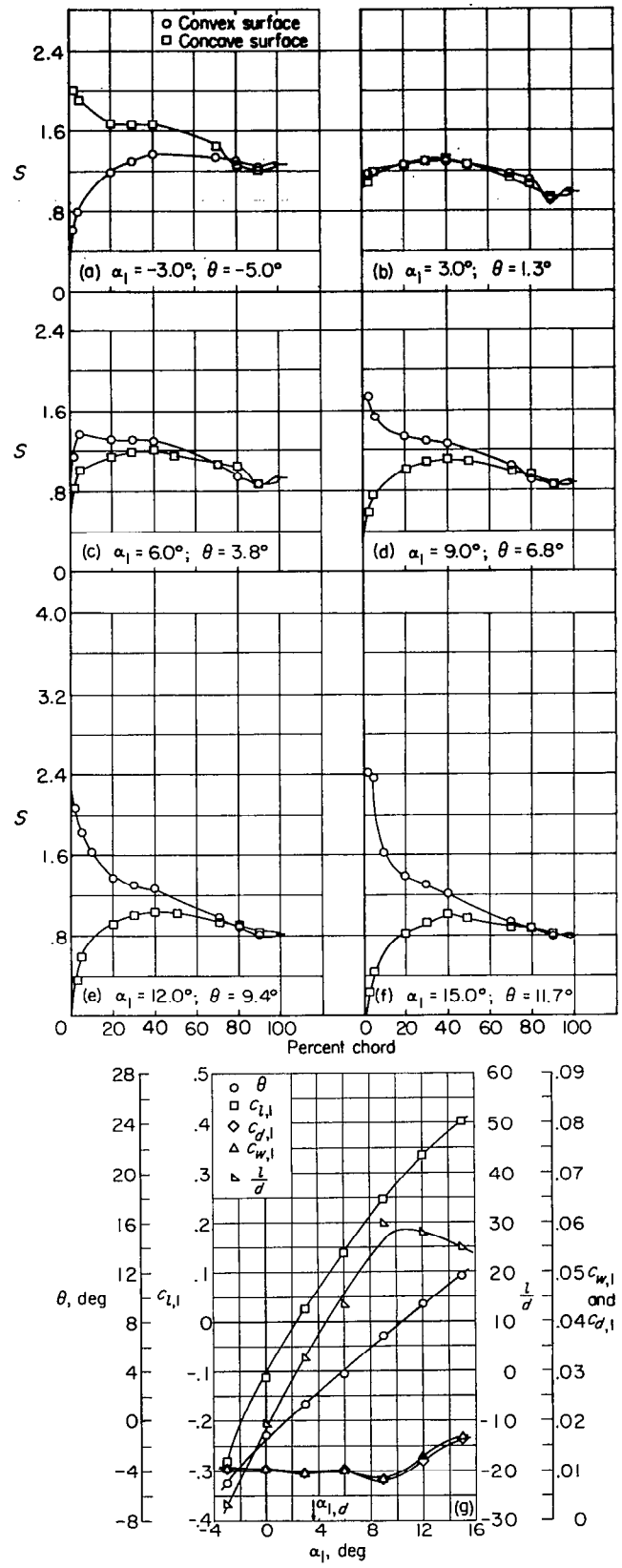

(g) Section characteristics.

FIGURE 27.—Blade-surface pressure distributions and blade section characteristics for the cascade combination, $\beta_1=45°$, $\sigma=1.00$, and blade section, NACA 65-010.

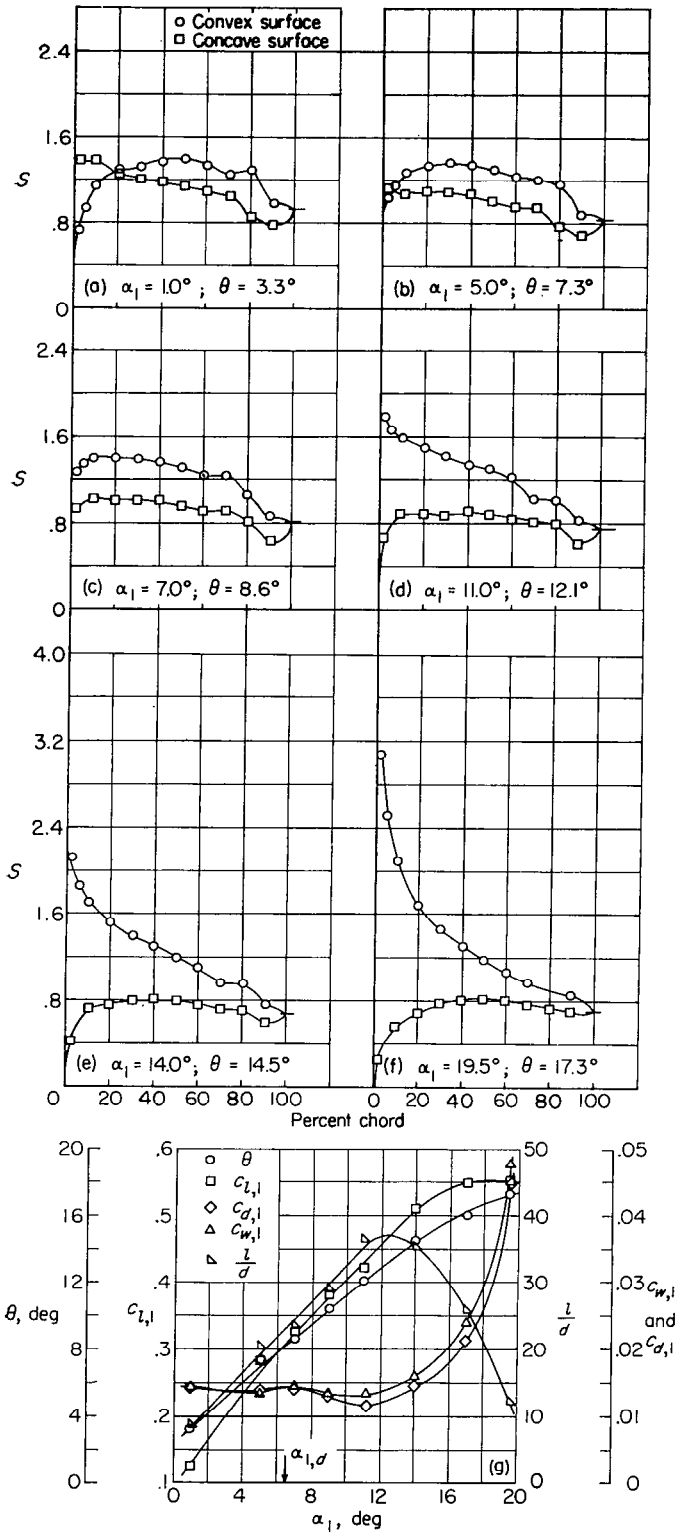

(g) Section characteristics.

FIGURE 28.—Blade-surface pressure distributions and blade section characteristics for the cascade combination, $\beta_1=45°$, $\sigma=1.00$, and blade section, NACA 65–410.

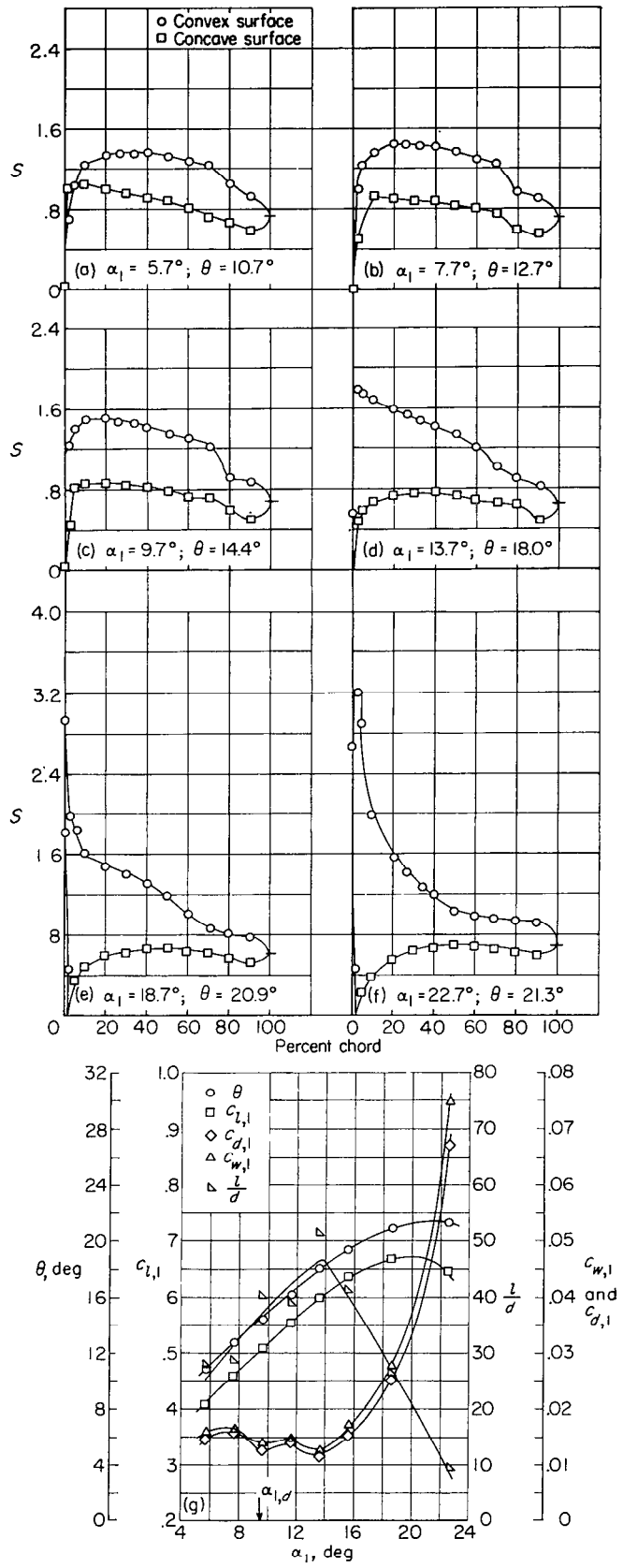

(g) Section characteristics.

FIGURE 29.—Blade-surface pressure distributions and blade section characteristics for the cascade combination, $\beta_1=45°$, $\sigma=1.00$, and blade section, NACA 65–810.

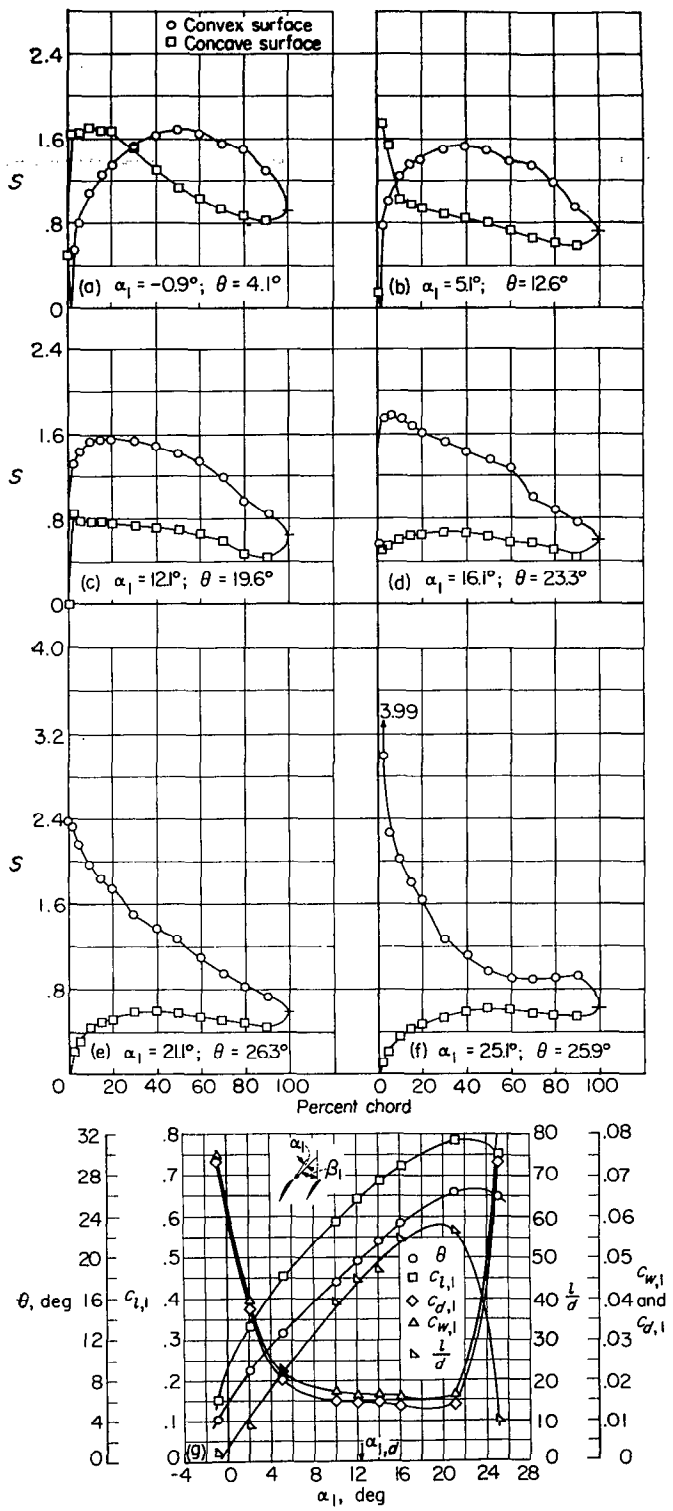

(g) Section characteristics.

FIGURE 30.—Blade-surface pressure distributions and blade section characteristics for the cascade combination, $\beta_1=45°$, $\sigma=1.00$, and blade section, NACA 65-(12)10.

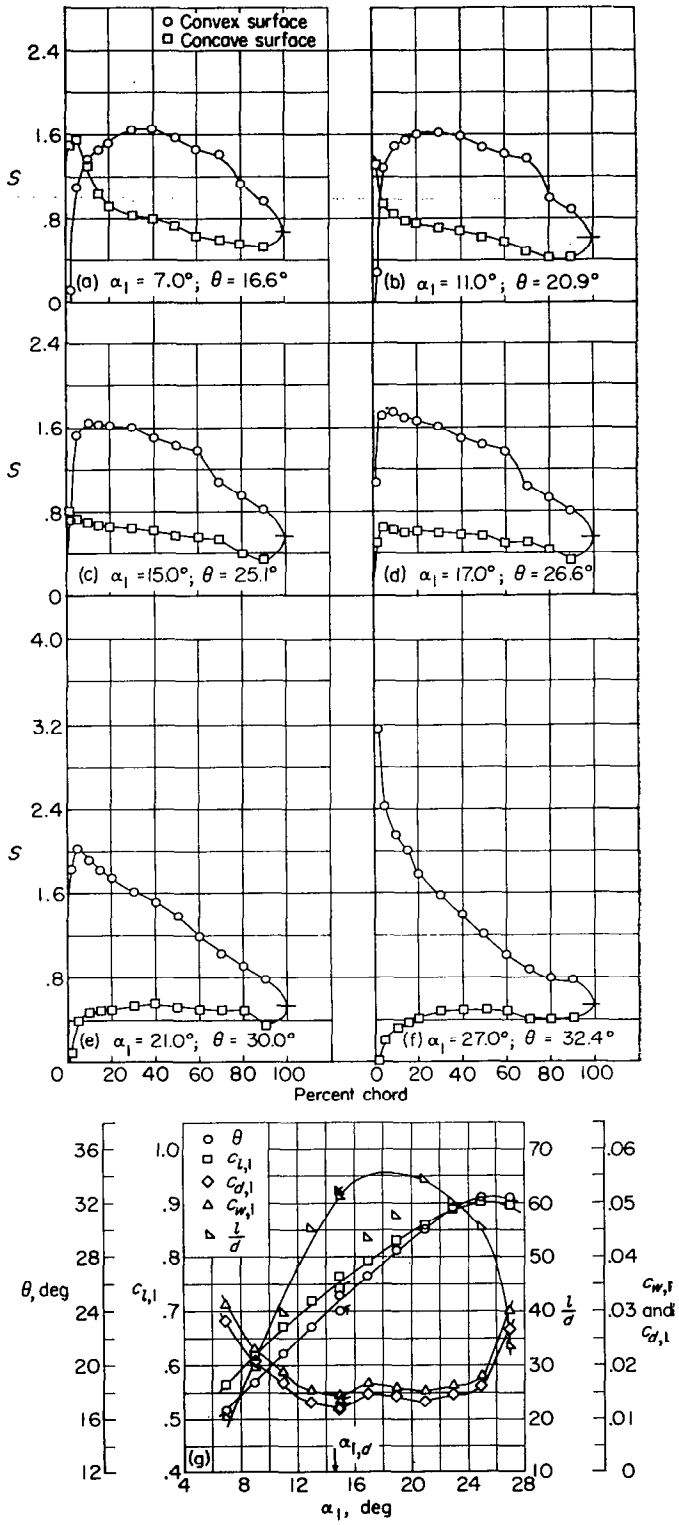

(g) Section characteristics; flagged symbol indicates leading-edge roughness.

FIGURE 31.—Blade-surface pressure distributions and blade section characteristics for the cascade combination, $\beta_1=45°$, $\sigma=1.00$, and blade section, NACA 65-(15)10.

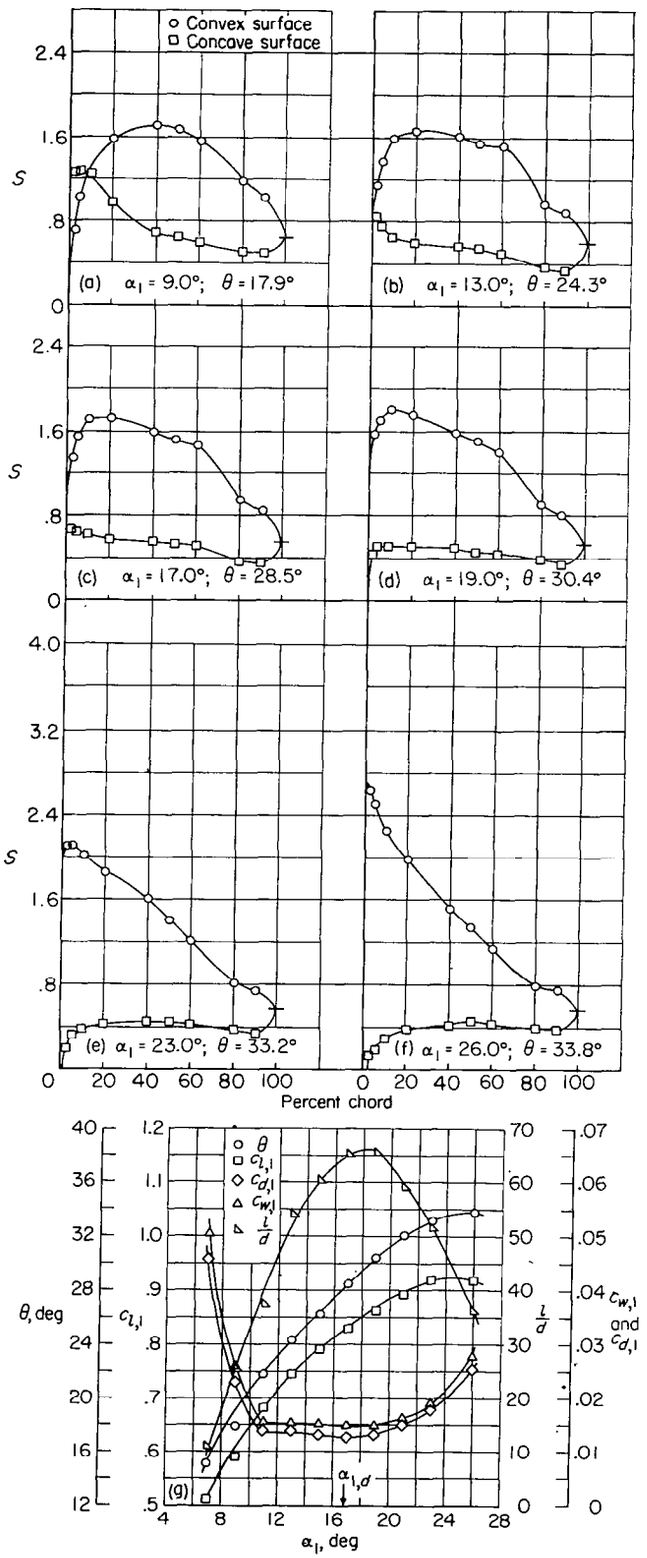

(g) Section characteristics.

FIGURE 32.—Blade-surface pressure distributions and blade section characteristics for the cascade combination, $\beta_1=45°$, $\sigma=1.00$, and blade section, NACA 65-(18)10.

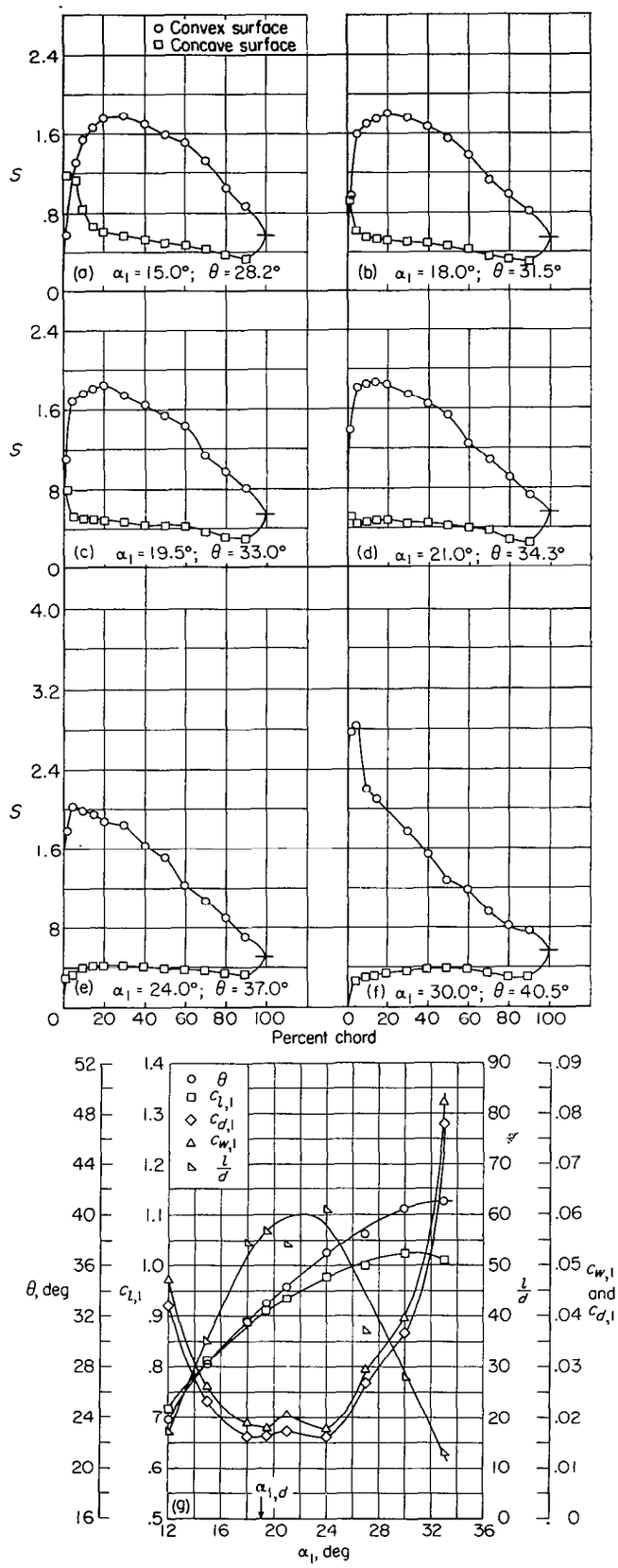

(g) Section characteristics.

FIGURE 33.—Blade-surface pressure distributions and blade section characteristics for the cascade combination, $\beta_1=45°$, $\sigma=1.00$, and blade section, NACA 65-(21)10.

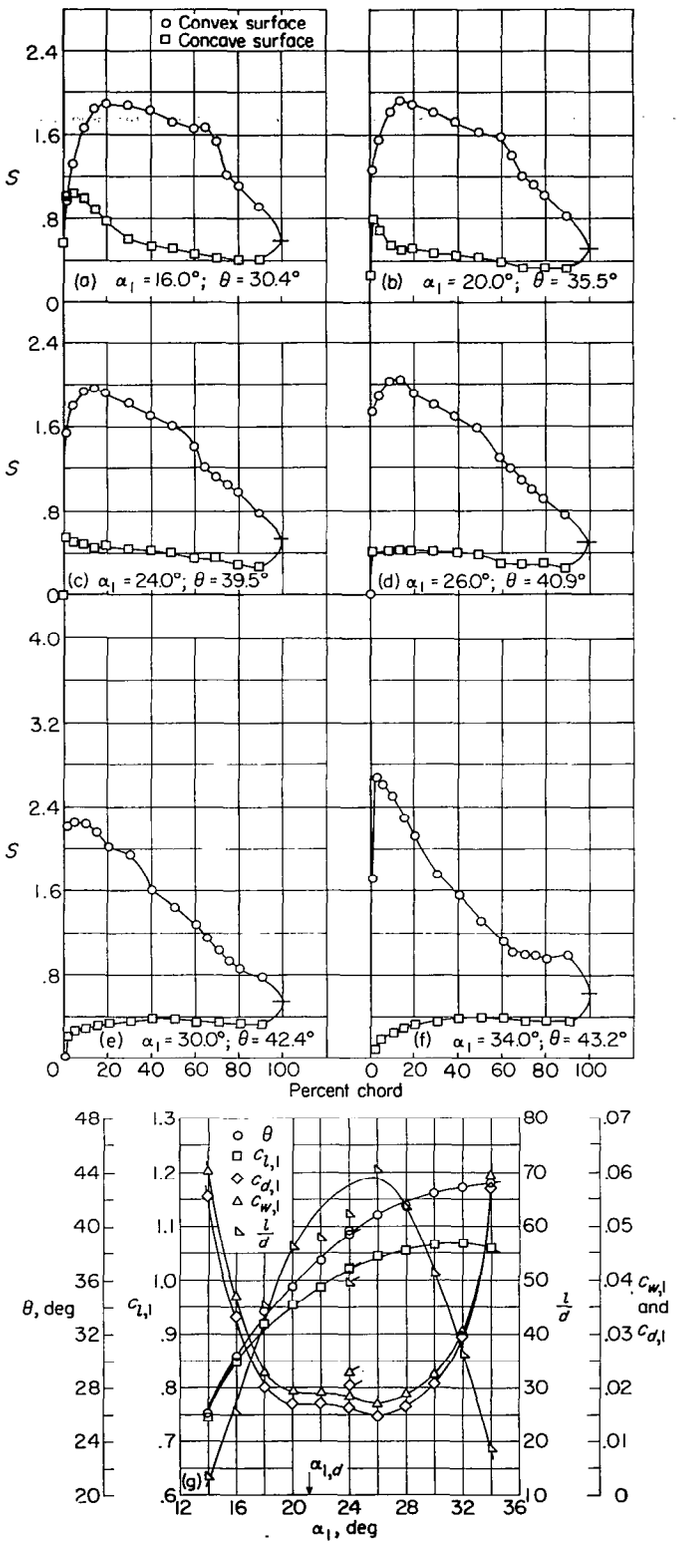

(g) Section characteristics; flagged symbol indicates leading-edge roughness.

FIGURE 34.—Blade-surface pressure distributions and blade section characteristics for the cascade combination, $\beta_1=45°$, $\sigma=1.00$, and blade section, NACA 65-(24)10.

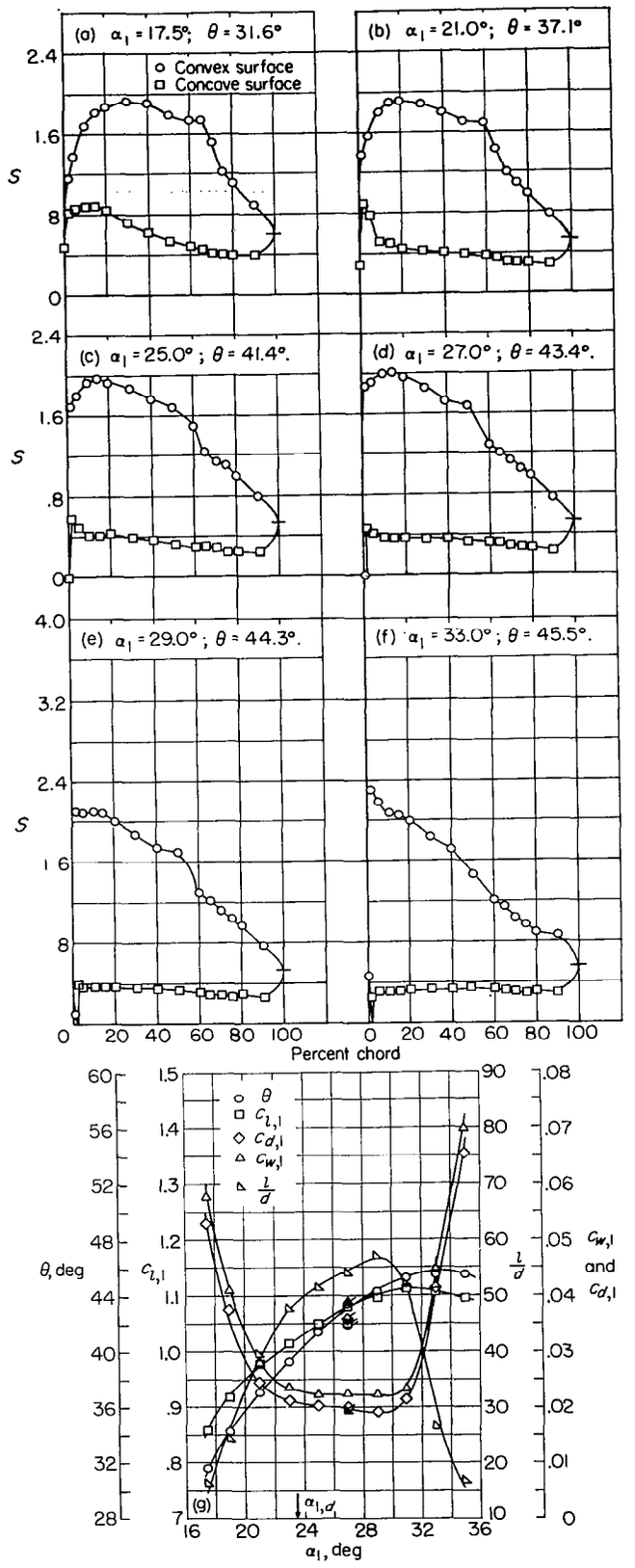

(g) Section characteristics; flagged symbol indicates leading-edge roughness.

FIGURE 35.—Blade-surface pressure distributions and blade section characteristics for the cascade combination, $\beta_1=45°$, $\sigma=1.00$, and blade section, NACA 65-(27)10.

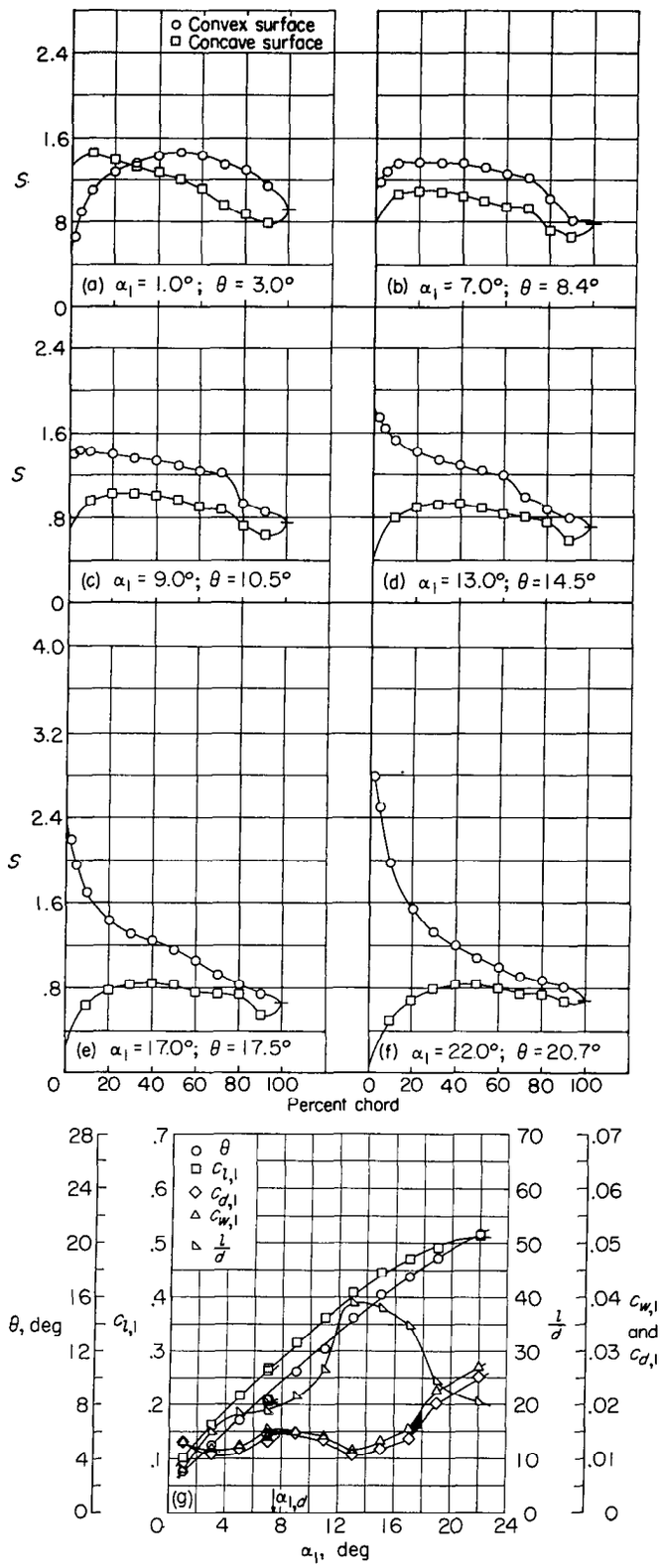

(g) Section characteristics; flagged symbol indicates leading-edge roughness.

FIGURE 36.—Blade-surface pressure distributions and blade section characteristics for the cascade combination, $\beta_1=45°$, $\sigma=1.25$, and blade section, NACA 65–410.

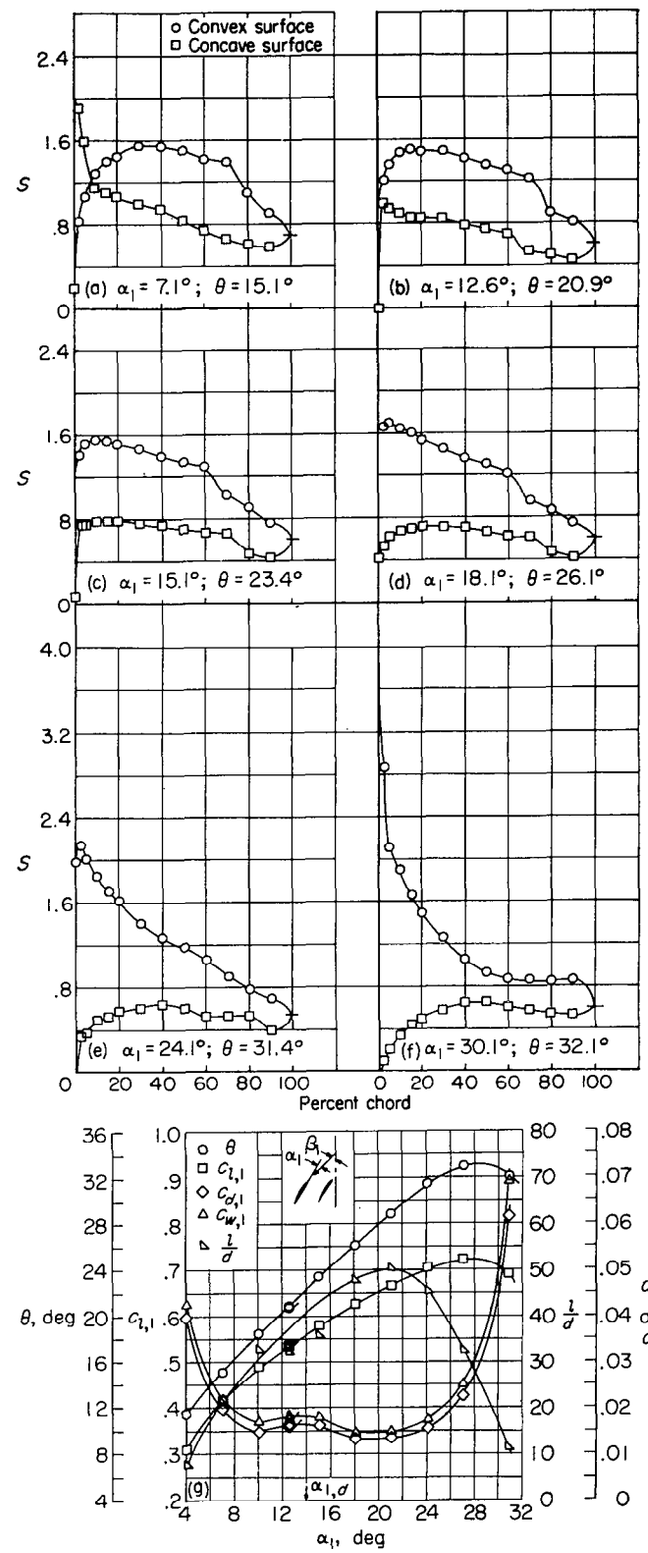

(g) Section characteristics; flagged symbol indicates leading-edge roughness.

FIGURE 37.—Blade-surface pressure distributions and blade section characteristics for the cascade combination, $\beta_1=45°$, $\sigma=1.25$, and blade section, NACA 65–(12)10.

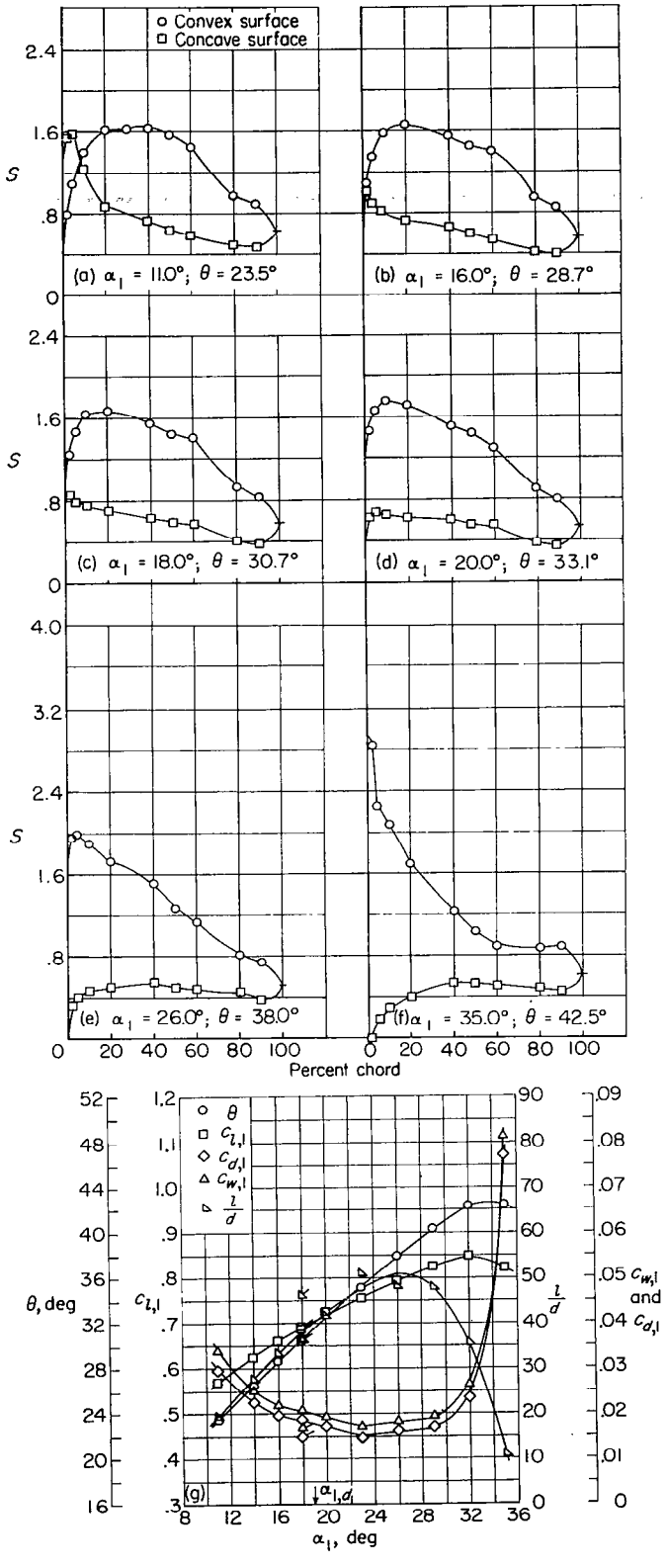

(g) Section characteristics; flagged symbol indicates leading-edge roughness.

FIGURE 38.—Blade-surface pressure distributions and blade section characteristics for the cascade combination, $\beta_1=45°$, $\sigma=1.25$, and blade section, NACA 65-(18)10.

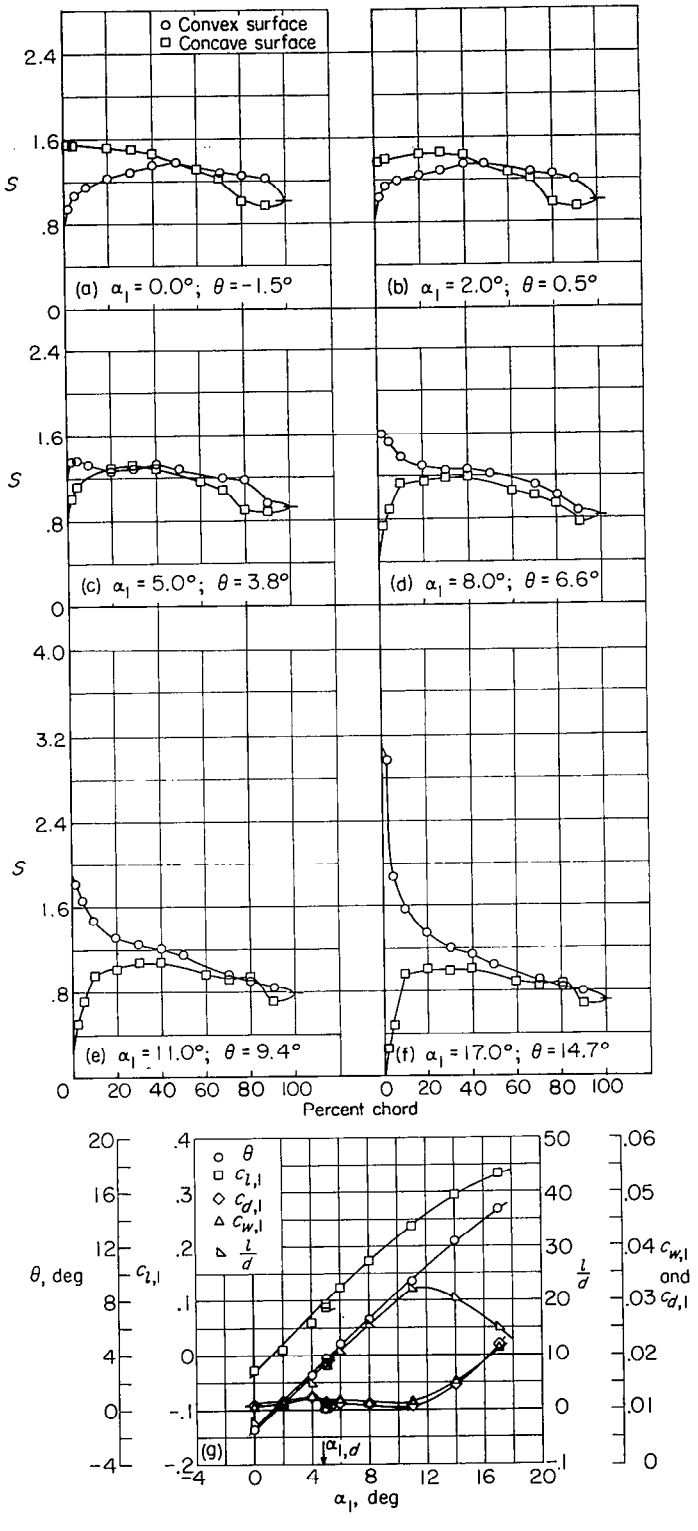

(g) Section characteristics; flagged symbol indicates leading-edge roughness.

FIGURE 39.—Blade-surface pressure distributions and blade section characteristics for the cascade combination, $\beta_1=45°$, $\sigma=1.50$, and blade section, NACA 65-010.

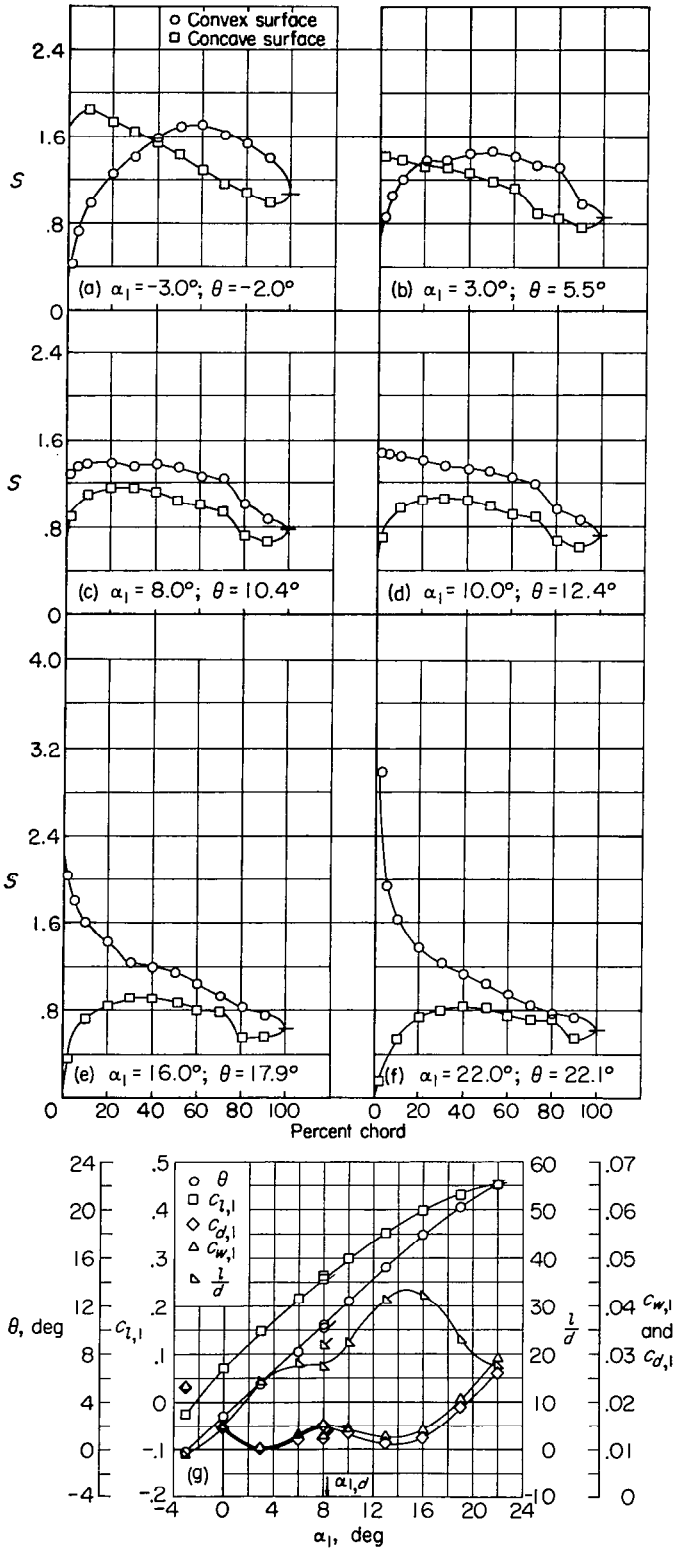

(g) Section characteristics; flagged symbol indicates leading-edge roughness.

FIGURE 40.—Blade-surface pressure distributions and blade section characteristics for the cascade combination, $\beta_1=45°$, $\sigma=1.50$, and blade section, NACA 65–410.

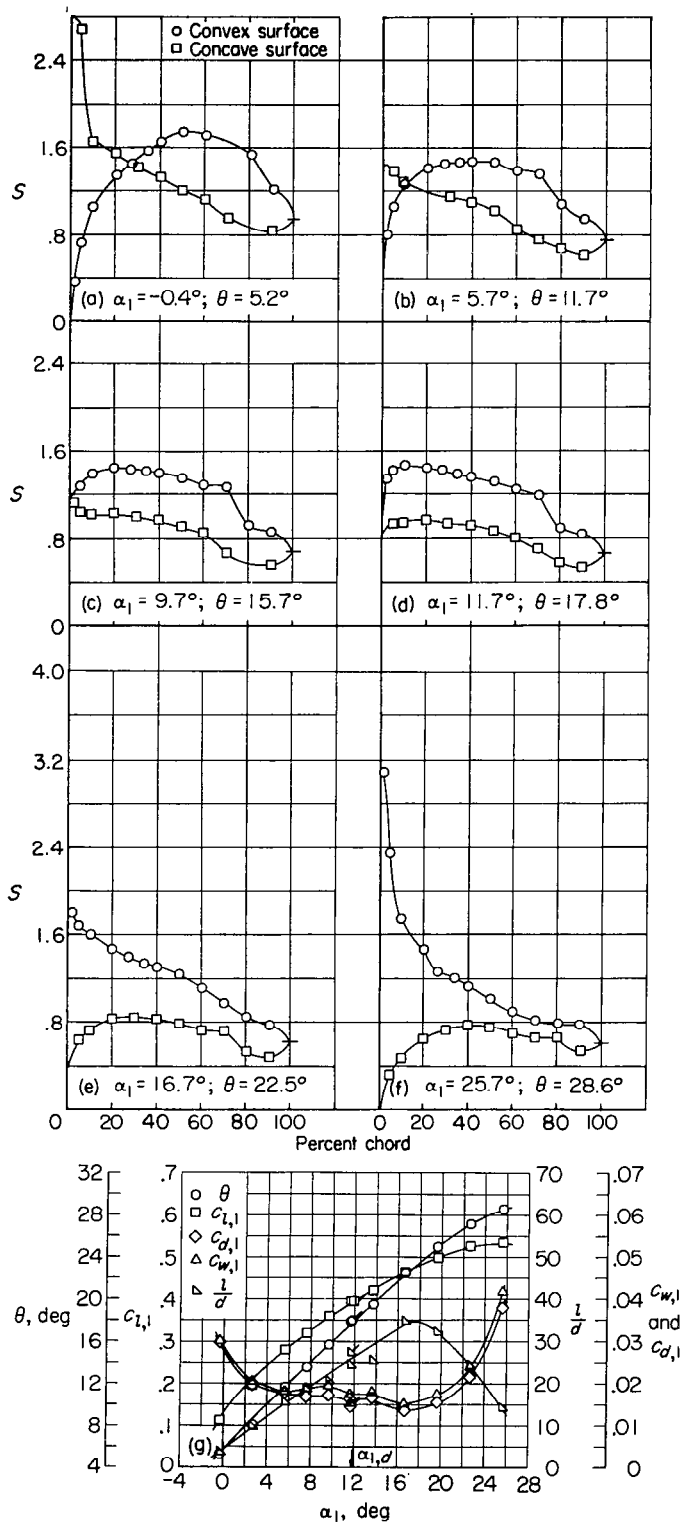

(g) Section characteristics; flagged symbol indicates leading-edge roughness.

FIGURE 41.—Blade-surface pressure distributions and blade section characteristics for the cascade combination, $\beta_1=45°$, $\sigma=1.50$, and blade section, NACA 65–810.

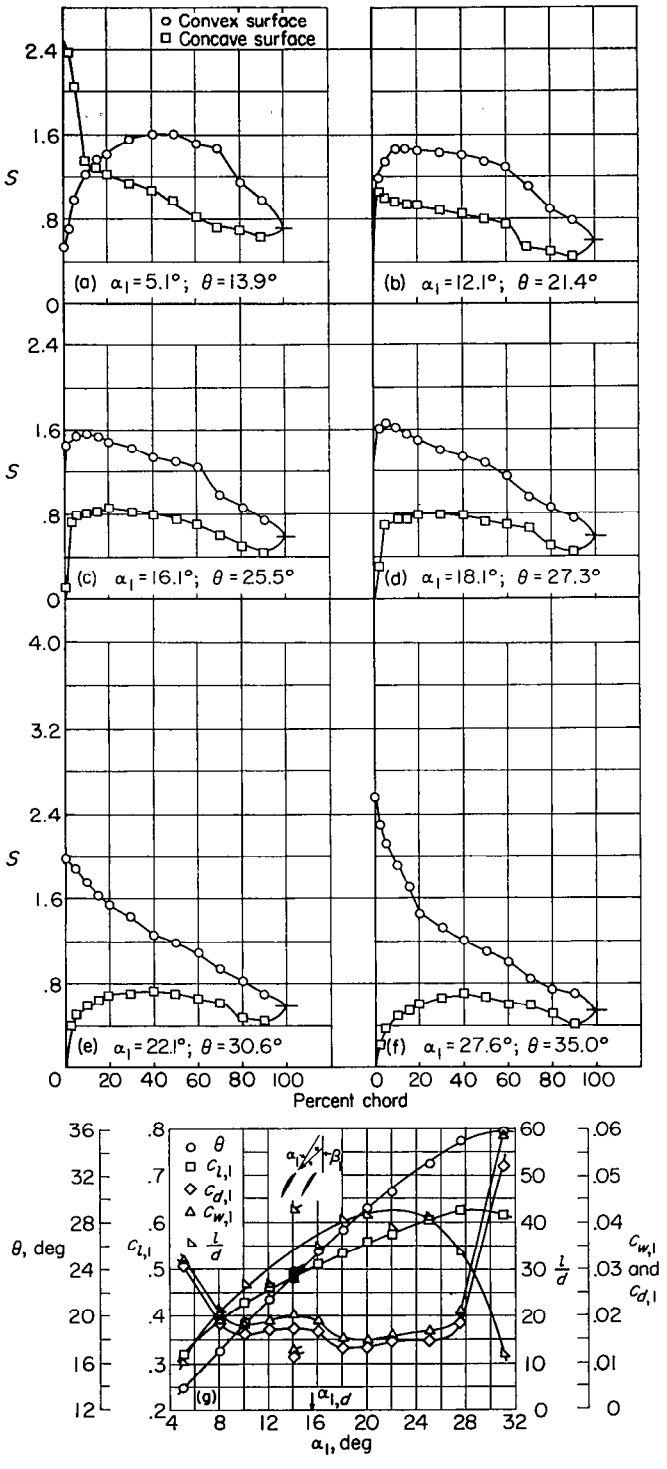

(g) Section characteristics; flagged symbol indicates leading-edge roughness.

FIGURE 42.—Blade-surface pressure distributions and blade section characteristics for the cascade combination, β_1=45°, σ=1.50, and blade section, NACA 65-(12)10.

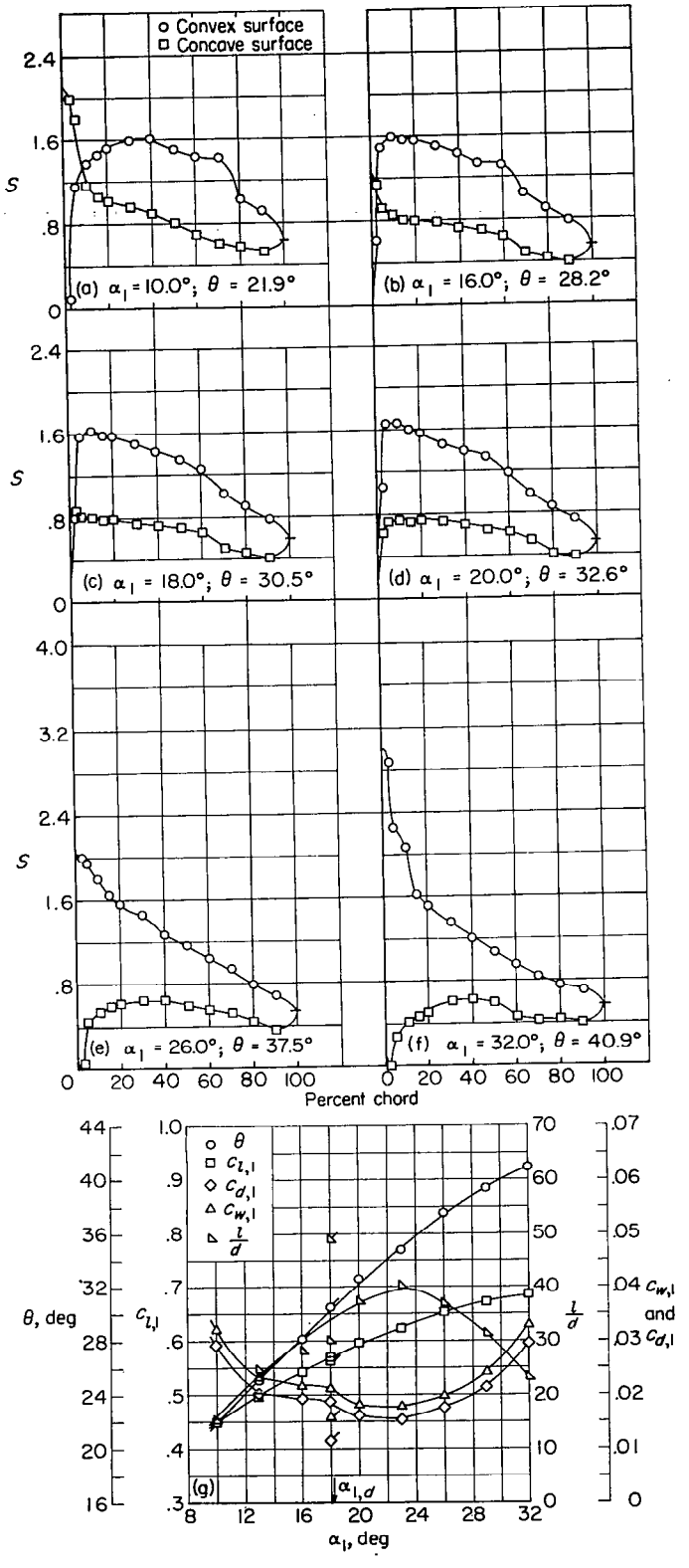

(g) Section characteristics; flagged symbol indicates leading-edge roughness.

FIGURE 43.—Blade-surface pressure distributions and blade section characteristics for the cascade combination, β_1=45°, σ=1.50, and blade section, NACA 65-(15)10.

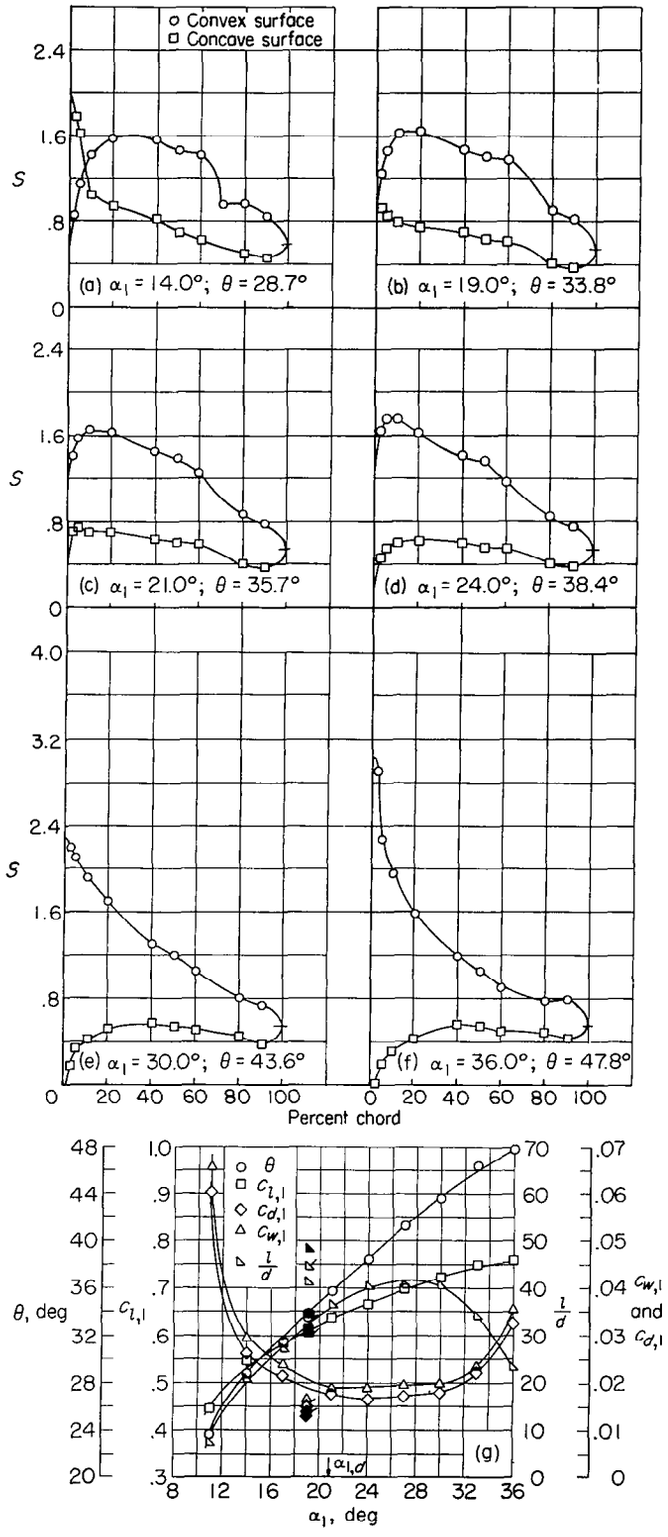

(g) Section characteristics; flagged symbol indicates leading-edge roughness; solid symbol indicates high Reynolds number.

FIGURE 44.—Blade-surface pressure distributions and blade section characteristics for the cascade combination, $\beta_1=45°$, $\sigma=1.50$, and blade section, NACA 65-(18)10.

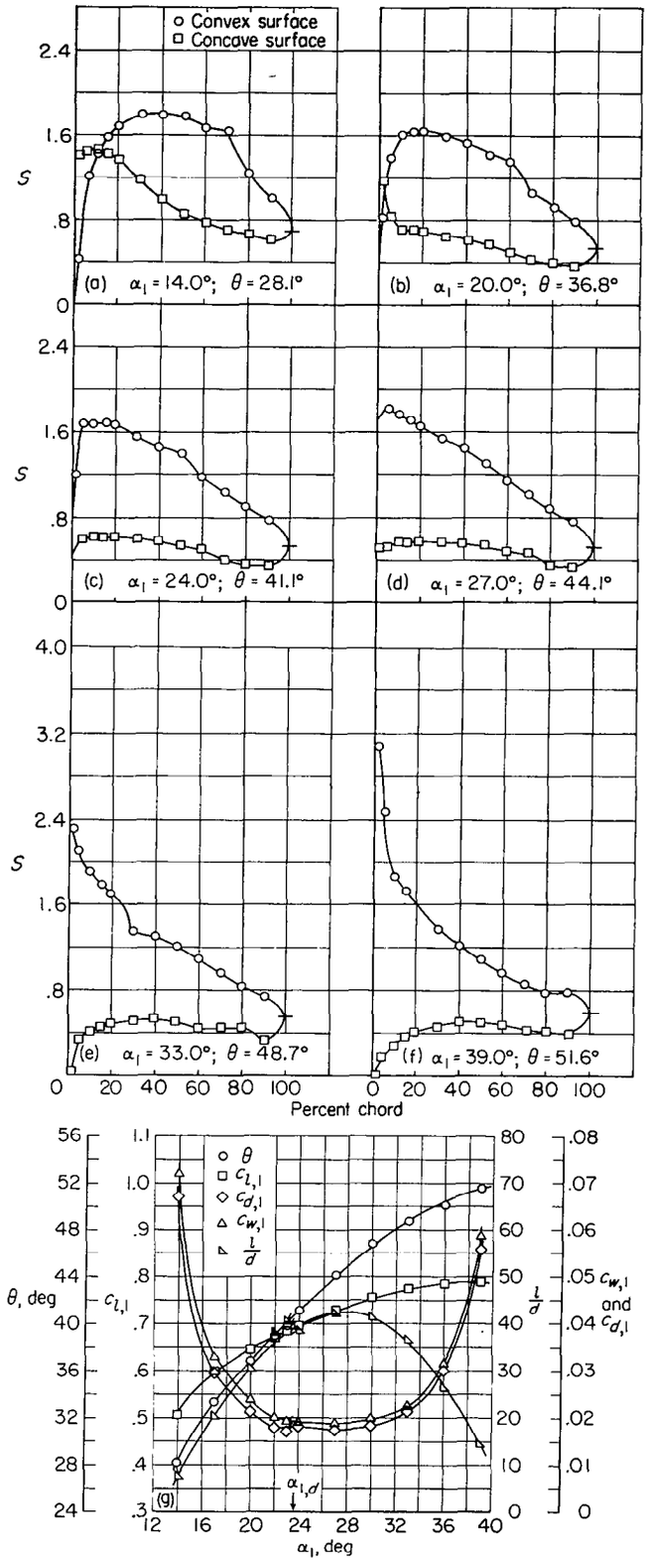

(g) Section characteristics; flagged symbol indicates leading-edge roughness.

FIGURE 45.—Blade-surface pressure distributions and blade section characteristics for the cascade combination, $\beta_1=45°$, $\sigma=1.50$, and blade section, NACA 65-(21)10.

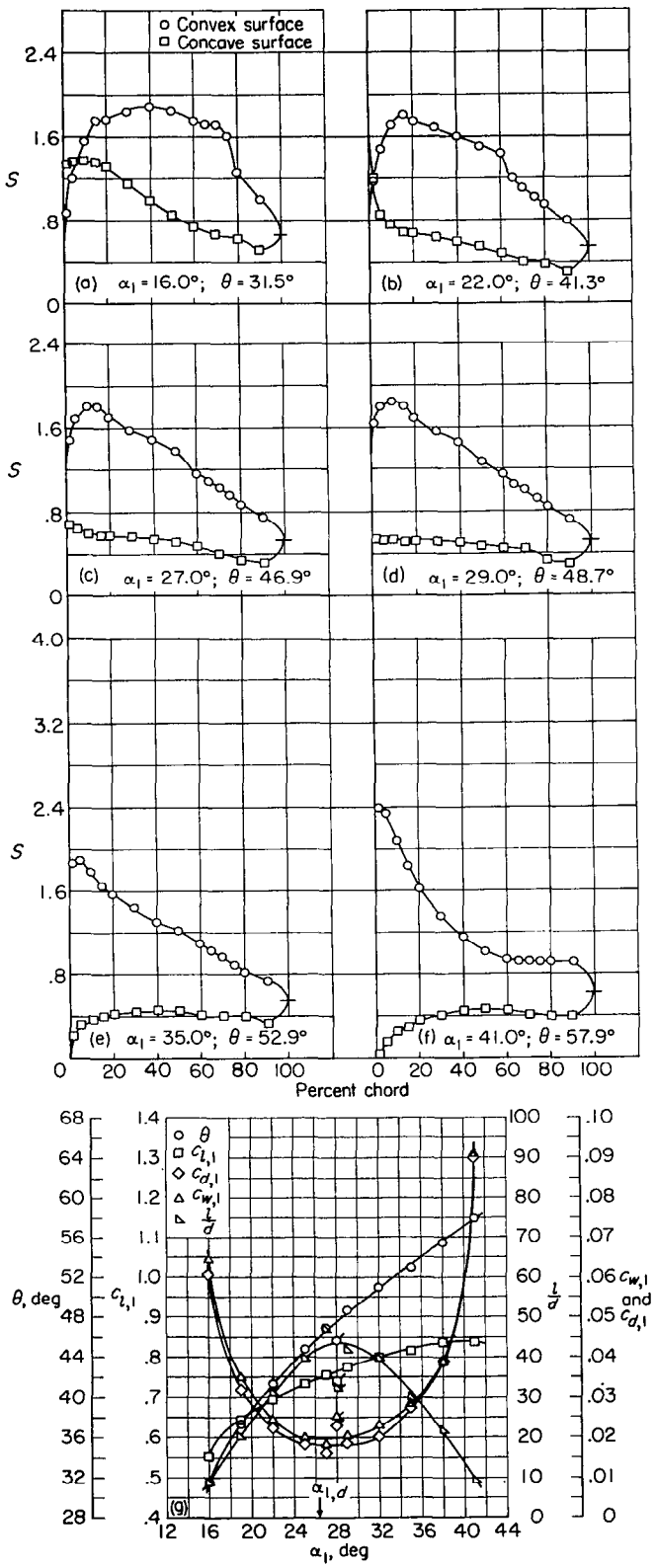

(g) Section characteristics; flagged symbol indicates leading-edge roughness.

FIGURE 46.—Blade-surface pressure distributions and blade section characteristics for the cascade combination, $\beta_1=45°$, $\sigma=1.50$, and blade section, NACA 65-(24)10.

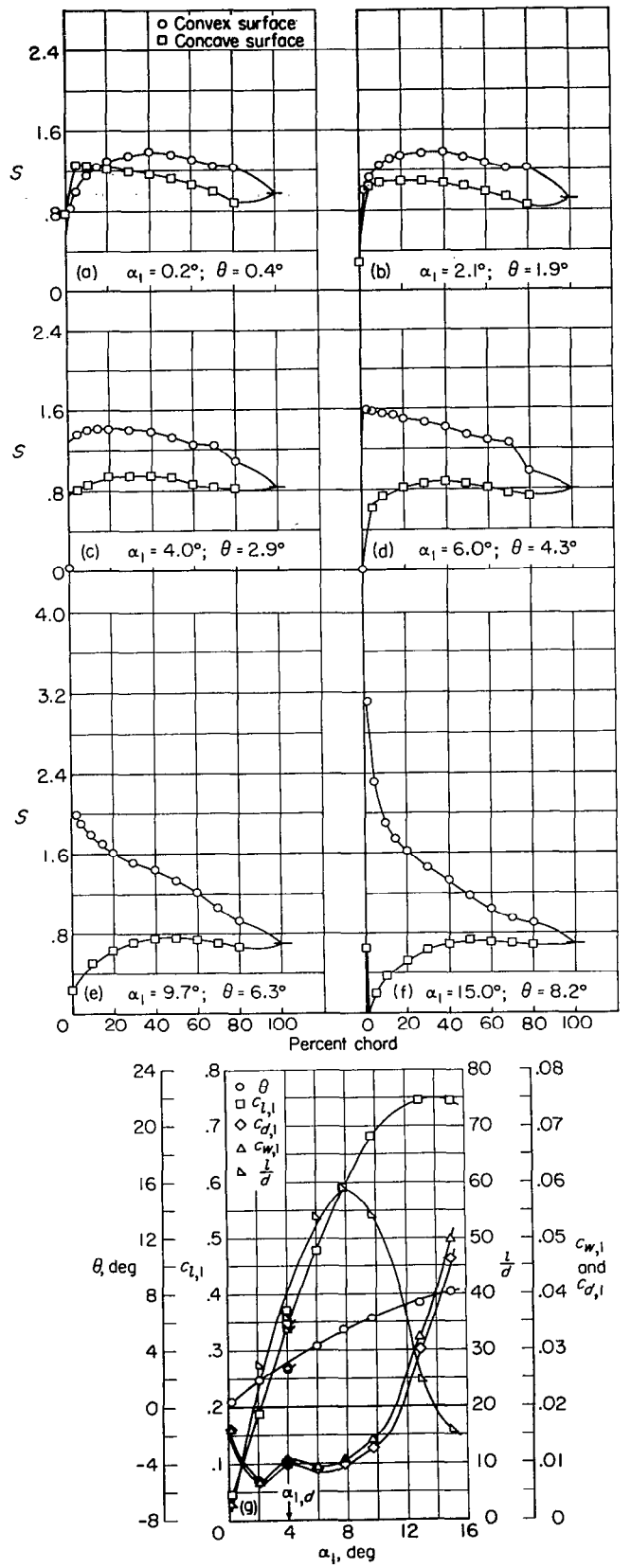

(g) Section characteristics; flagged symbol indicates leading-edge roughness.

FIGURE 47.—Blade-surface pressure distributions and blade section characteristics for the cascade combination, $\beta_1=60°$, $\sigma=0.50$, and blade section, NACA 65-410.

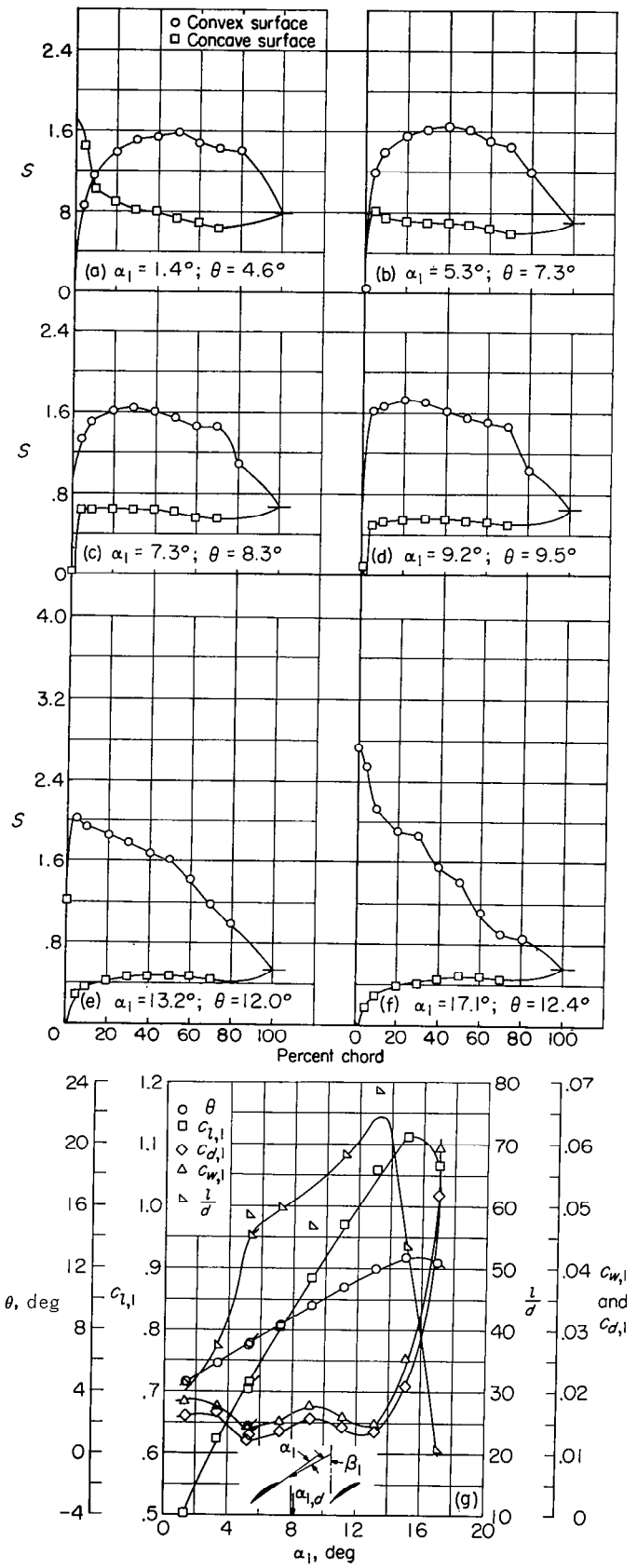

(g) Section characteristics; flagged symbol indicates leading-edge roughness.

FIGURE 48.—Blade-surface pressure distributions and blade section characteristics for the cascade combination, $\beta_1=60°$, $\sigma=0.50$, and blade section, NACA 65–(12)10.

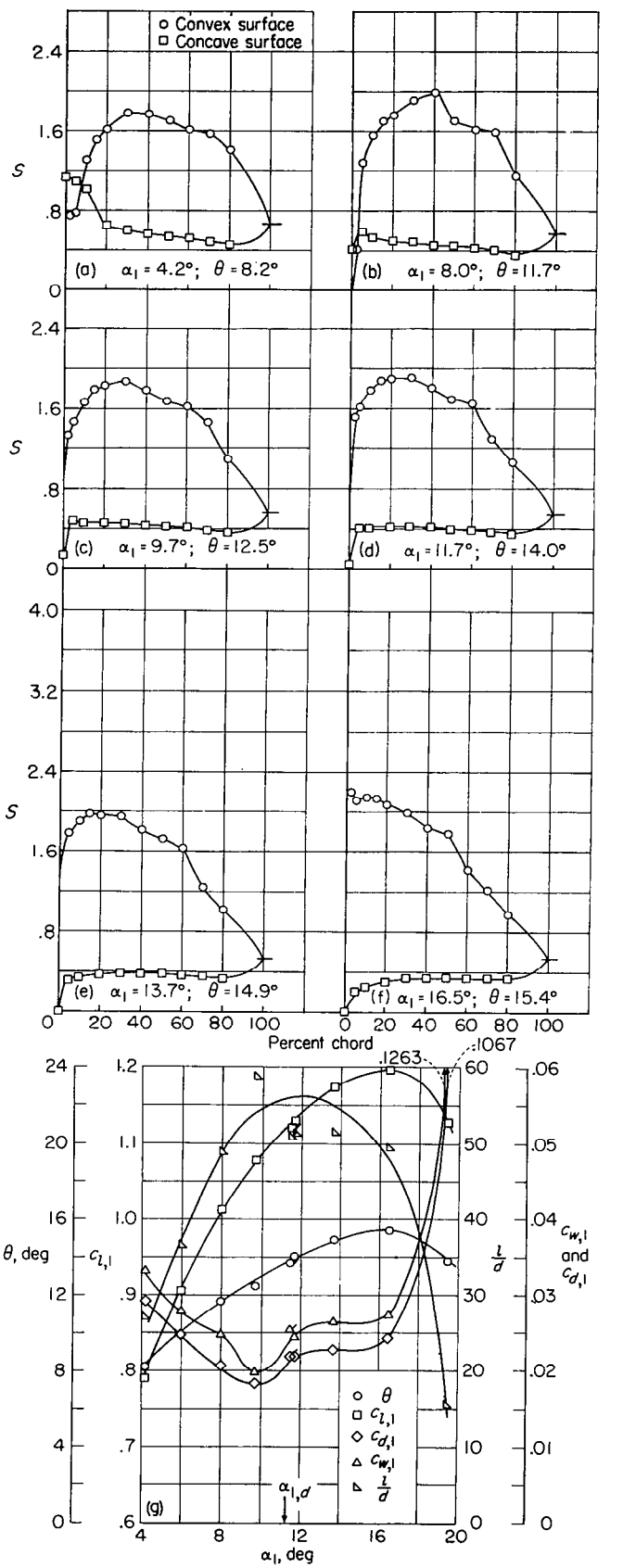

(g) Section characteristics; flagged symbol indicates leading-edge roughness.

FIGURE 49.—Blade-surface pressure distributions and blade section characteristics for the cascade combination, $\beta_1=60°$, $\sigma=0.50$, and blade section, NACA 65–(18)10.

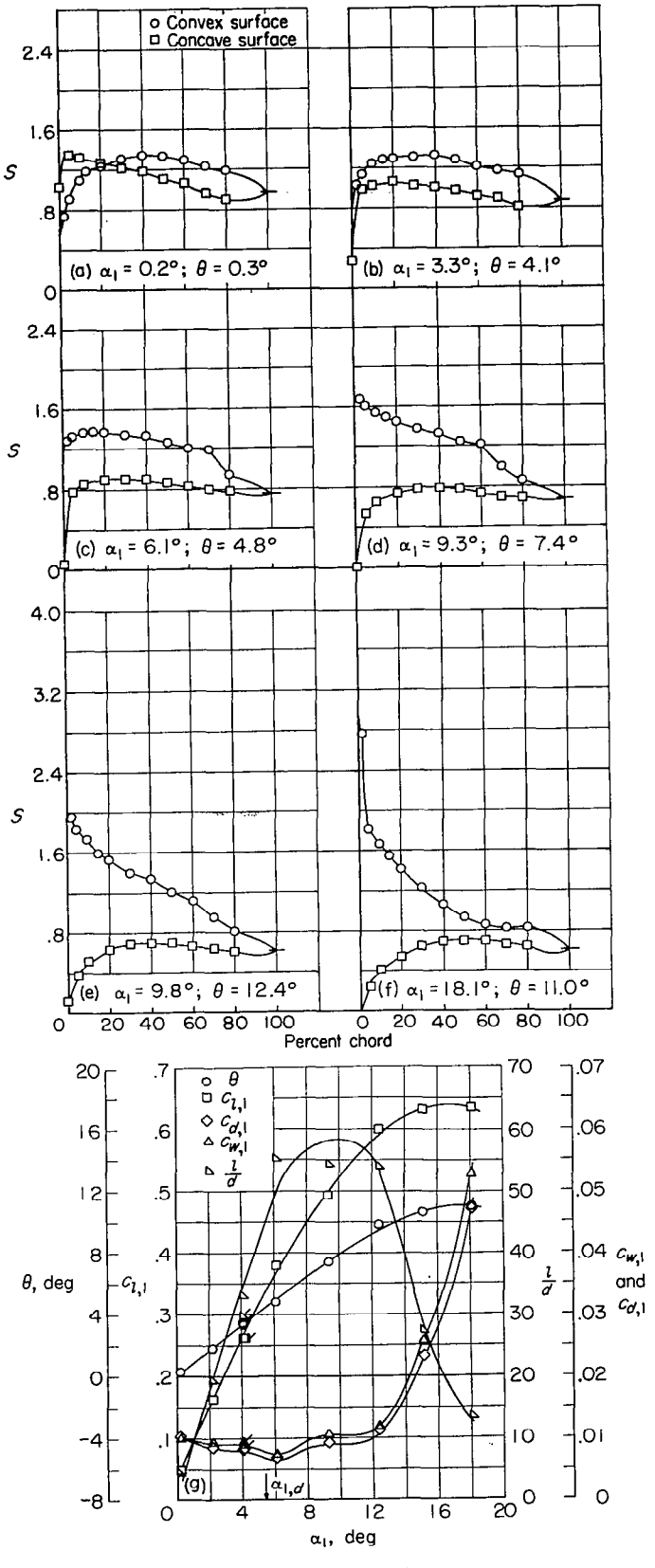

(g) Section characteristics; flagged symbol indicates leading-edge roughness.

FIGURE 50.—Blade-surface pressure distributions and blade section characteristics for the cascade combination, $\beta_1=60°$, $\sigma=0.75$, and blade section, NACA 65–410.

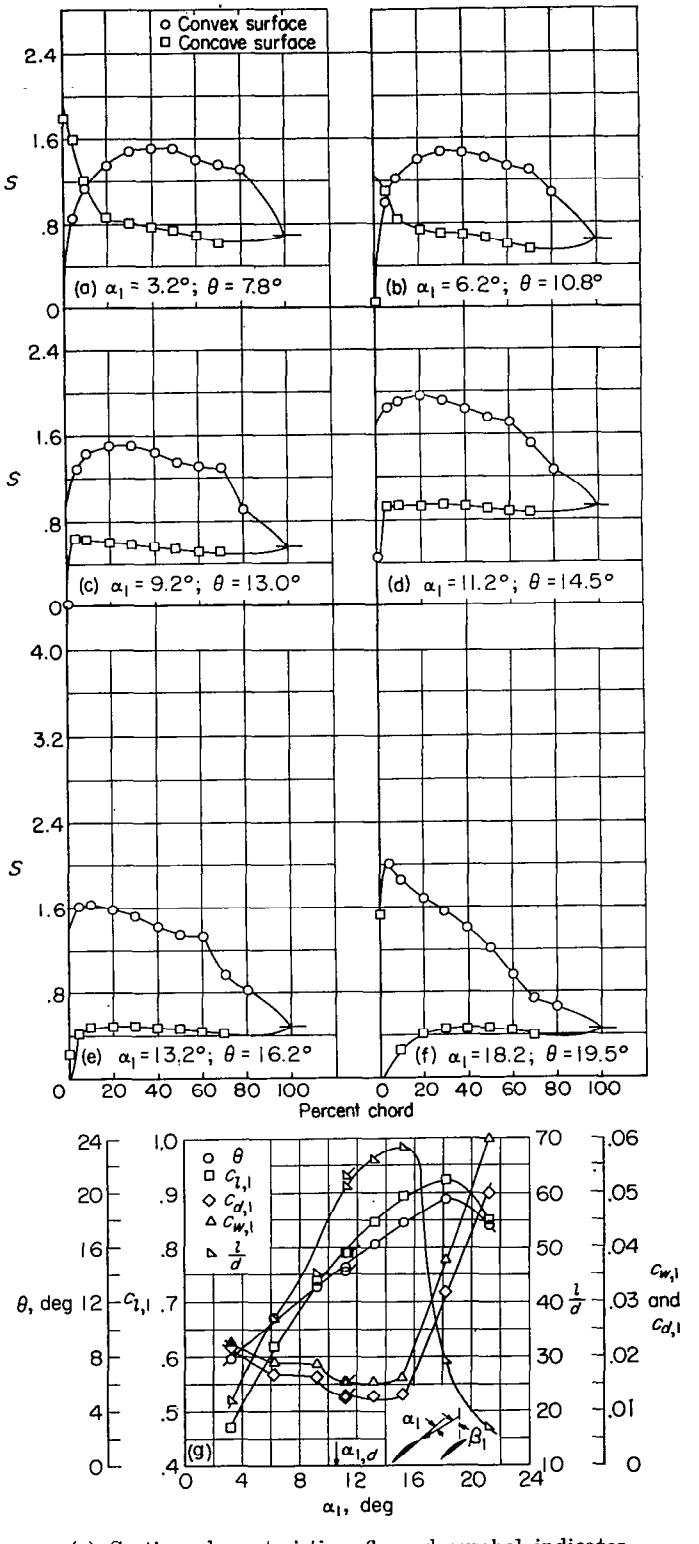

(g) Section characteristics; flagged symbol indicates leading-edge roughness.

FIGURE 51.—Blade-surface pressure distributions and blade section characteristics for the cascade combination, $\beta_1=60°$, $\sigma=0.75$, and blade section, NACA 65–(12)10.

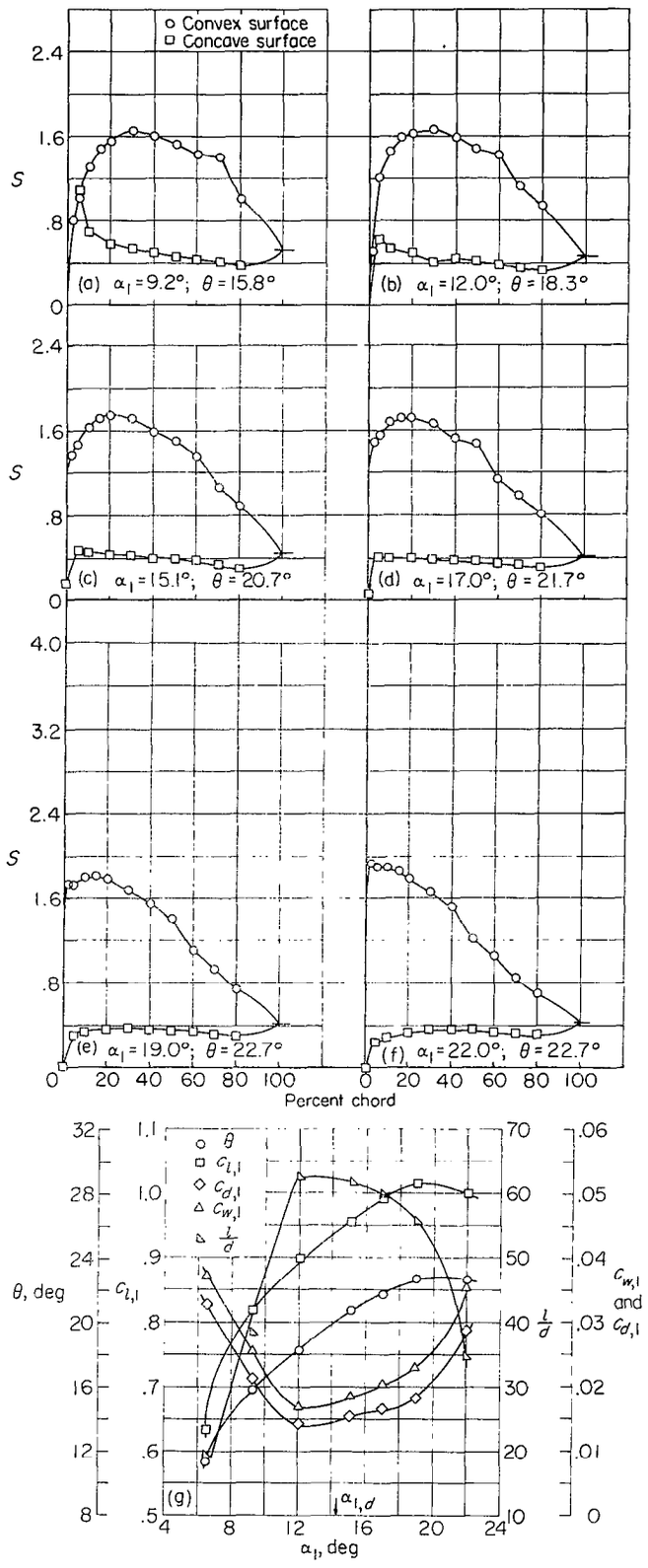

(g) Section characteristics.

FIGURE 52.—Blade-surface pressure distributions and blade section characteristics for the cascade combination, $\beta_1 = 60°$, $\sigma = 0.75$, and blade section, NACA 65-(18)10.

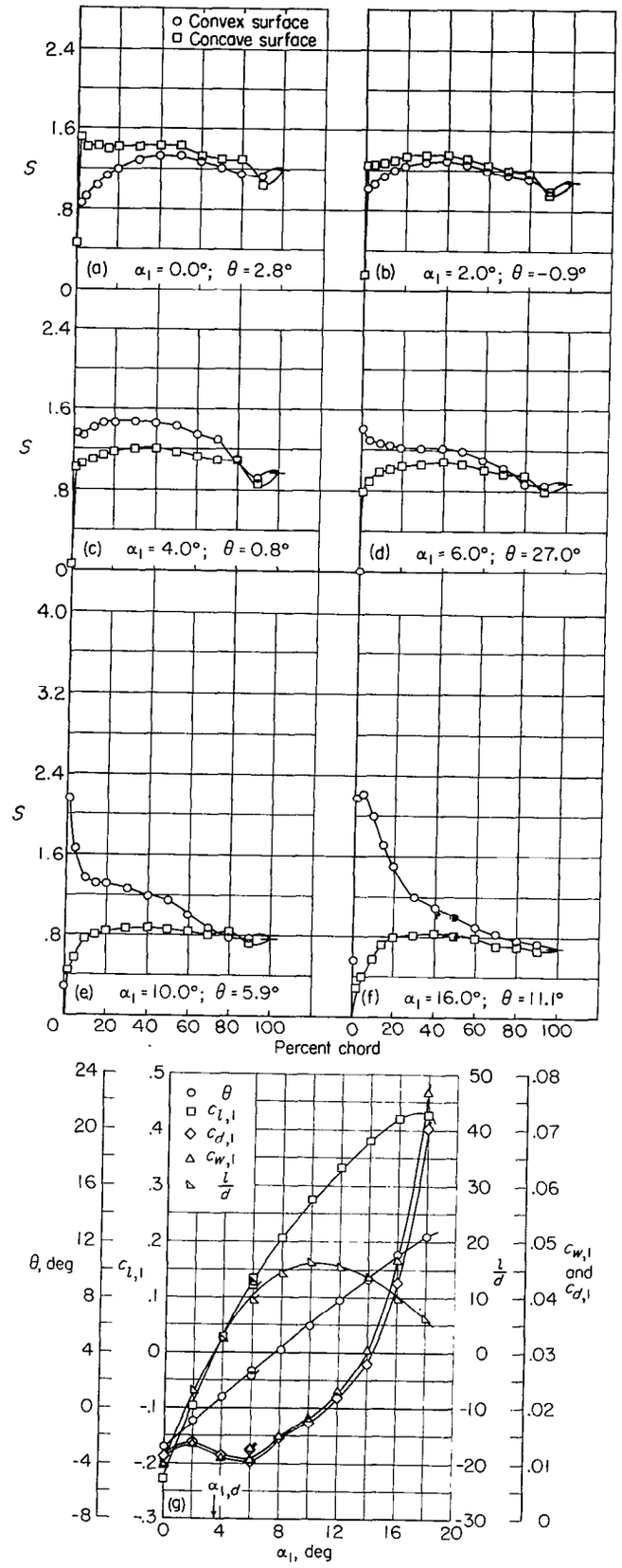

(g) Section characteristics; flagged symbol indicates leading-edge roughness.

FIGURE 53.—Blade-surface pressure distributions and blade section characteristics for the cascade combination, $\beta_1 = 60°$, $\sigma = 1.00$, and blade section, NACA 65-010.

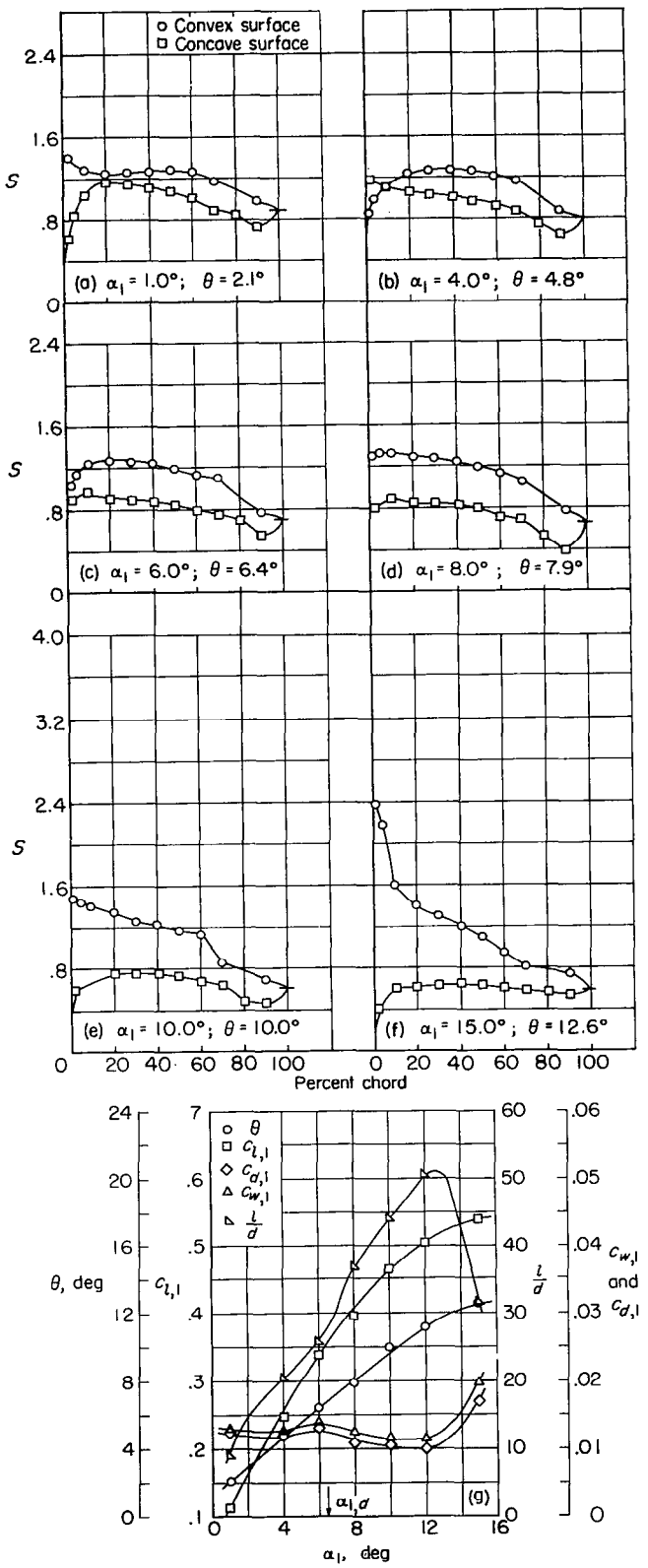

(g) Section characteristics.

FIGURE 54.—Blade-surface pressure distributions and blade section characteristics for the cascade combination, $\beta_1=60°$, $\sigma=1.00$, and blade section, NACA 65-410.

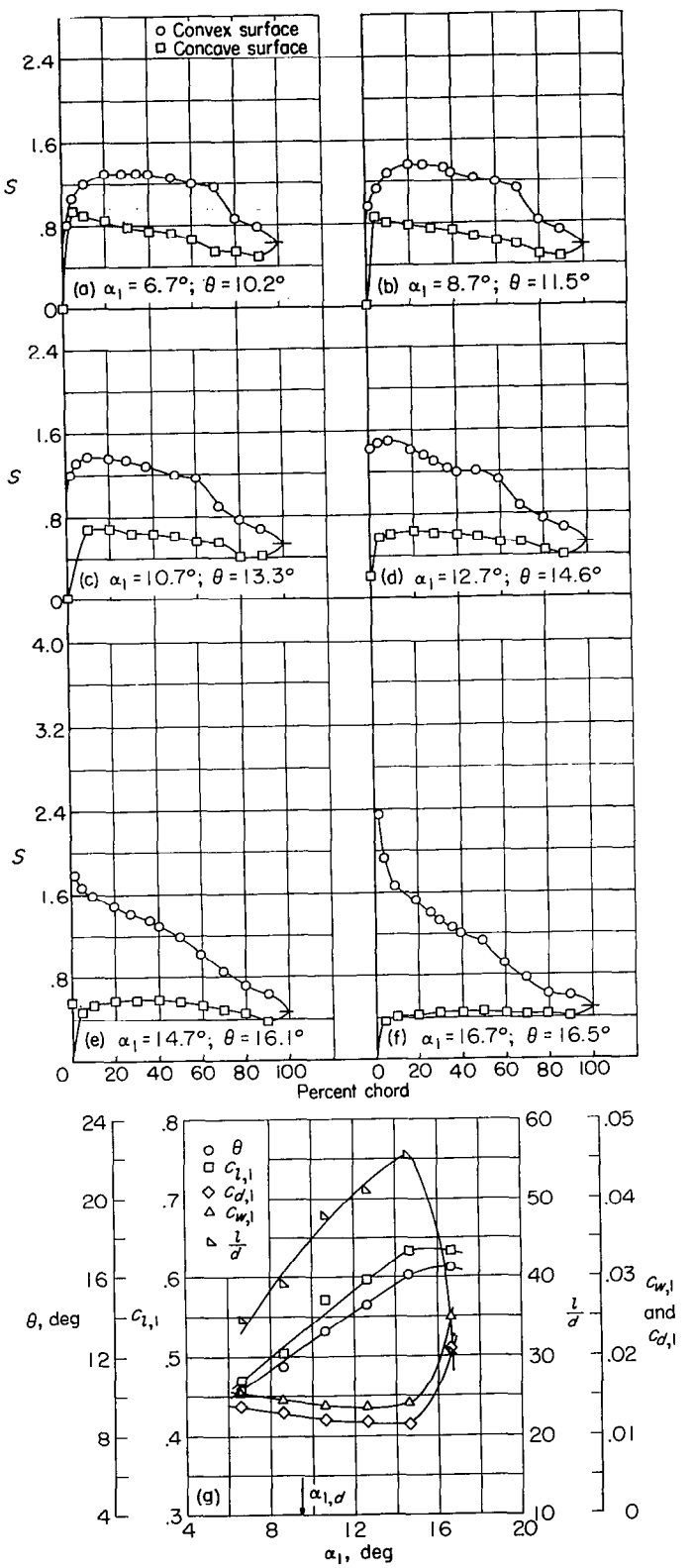

(g) Section characteristics.

FIGURE 55.—Blade-surface pressure distributions and blade section characteristics for the cascade combination, $\beta_1=60°$, $\sigma=1.00$, and blade section, NACA 65-810.

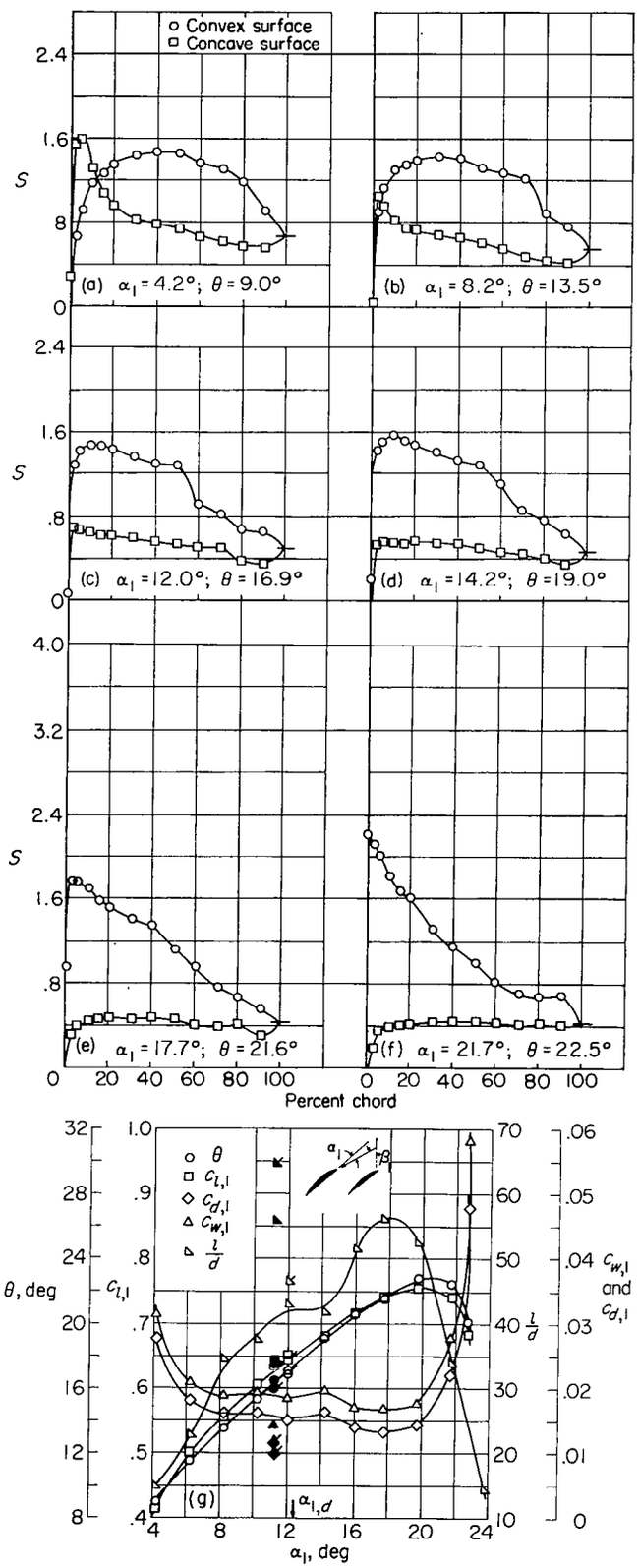

(g) Section characteristics; flagged symbol indicates leading-edge roughness; solid symbol indicates high Reynolds number.

FIGURE 56.—Blade-surface pressure distributions and blade section characteristics for the cascade combination, $\beta_1=60°$, $\sigma=1.00$, and blade section, NACA 65-(12)10.

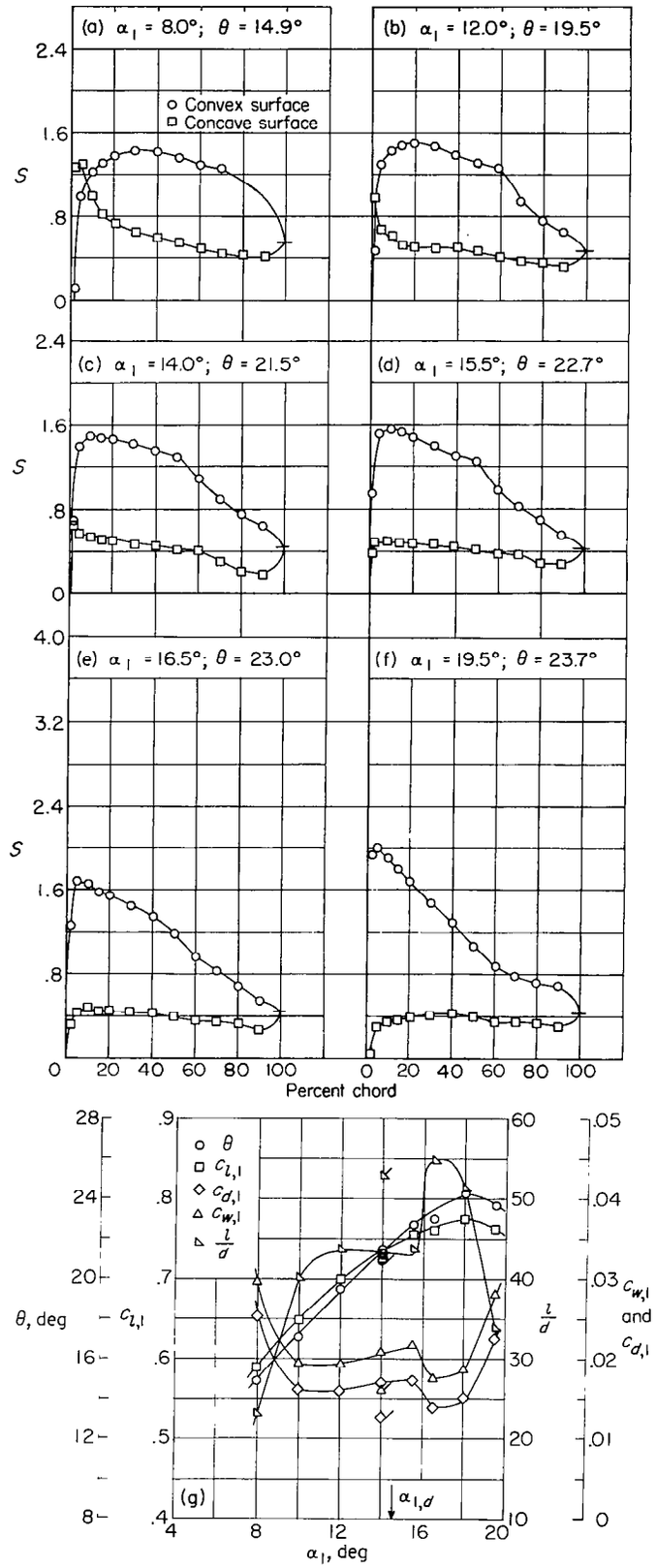

(g) Section characteristics; flagged symbol indicates leading-edge roughness.

FIGURE 57.—Blade-surface pressure distributions and blade section characteristics for the cascade combination, $\beta_1=60°$, $\sigma=1.00$, and blade section, NACA 65-(15)10.

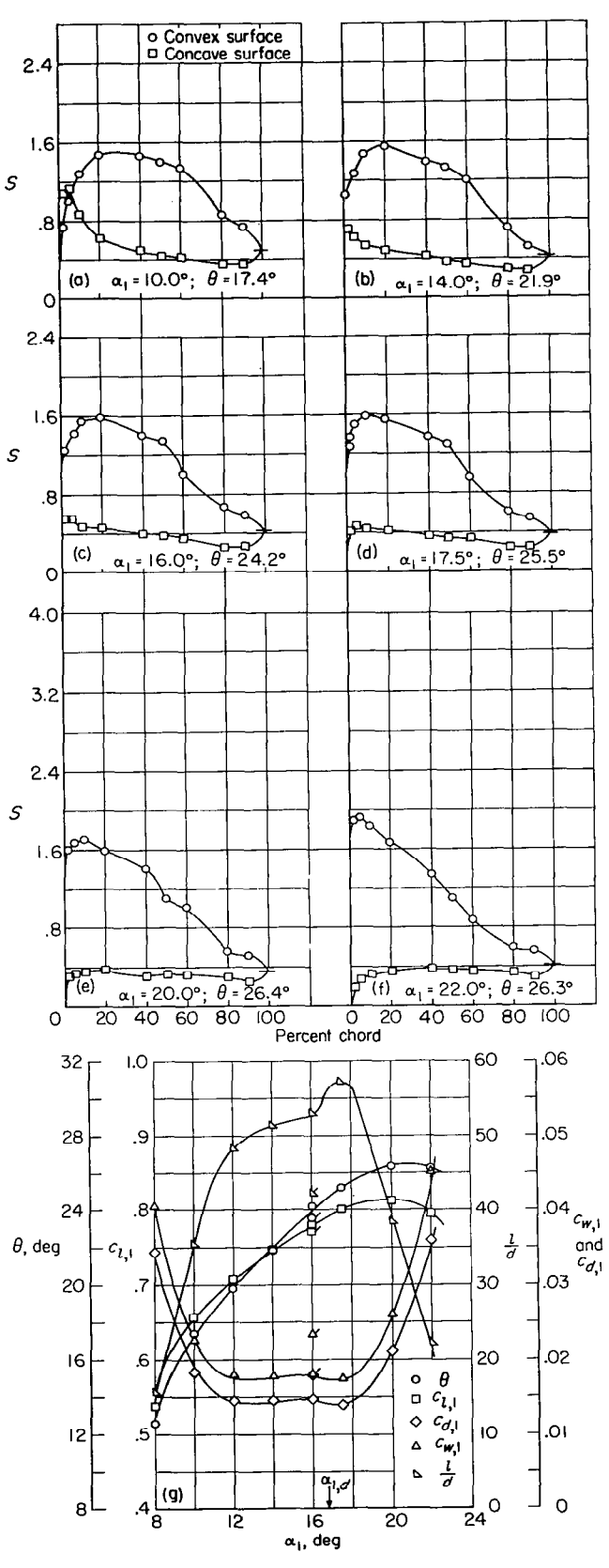

(g) Section characteristics; flagged symbol indicates leading-edge roughness.

FIGURE 58.—Blade-surface pressure distributions and blade section characteristics for the cascade combination, $\beta_1=60°$, $\sigma=1.00$, and blade section, NACA 65-(18)10.

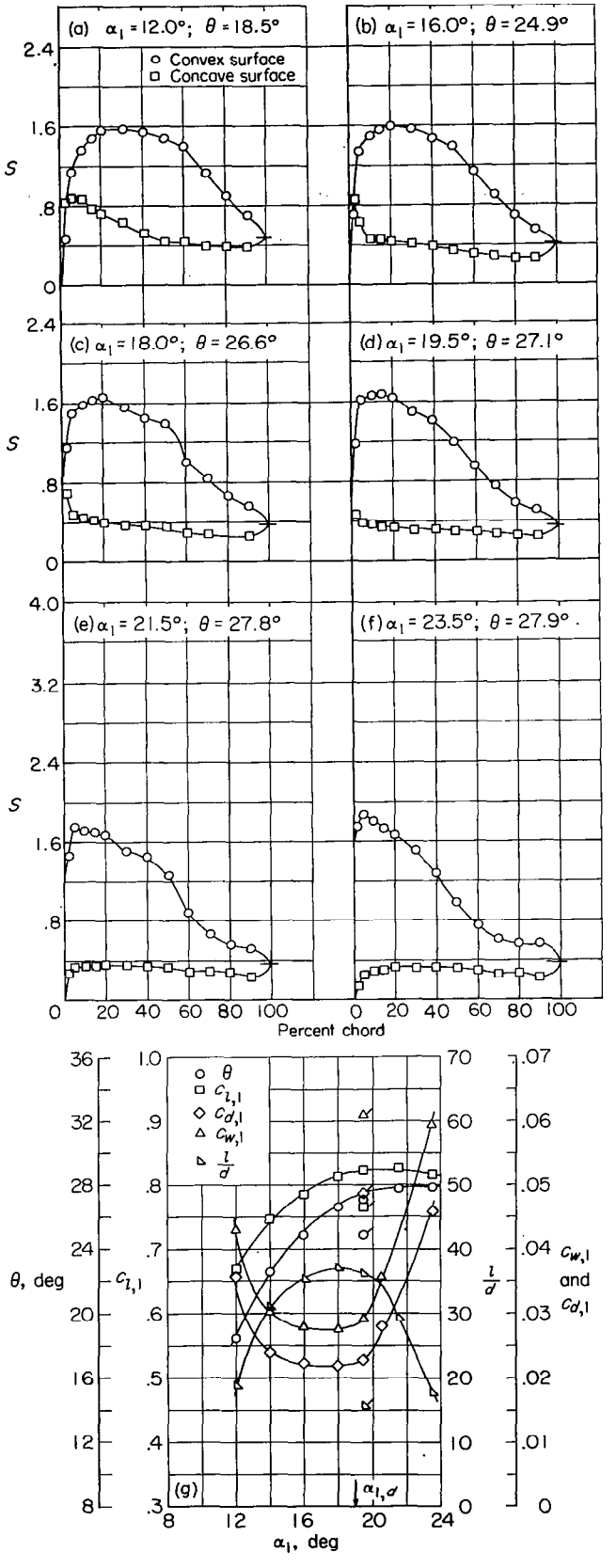

(g) Section characteristics; flagged symbol indicates leading-edge roughness.

FIGURE 59.—Blade-surface pressure distributions and blade section characteristics for the cascade combination, $\beta_1=60°$, $\sigma=1.00$, and blade section, NACA 65-(21)10.

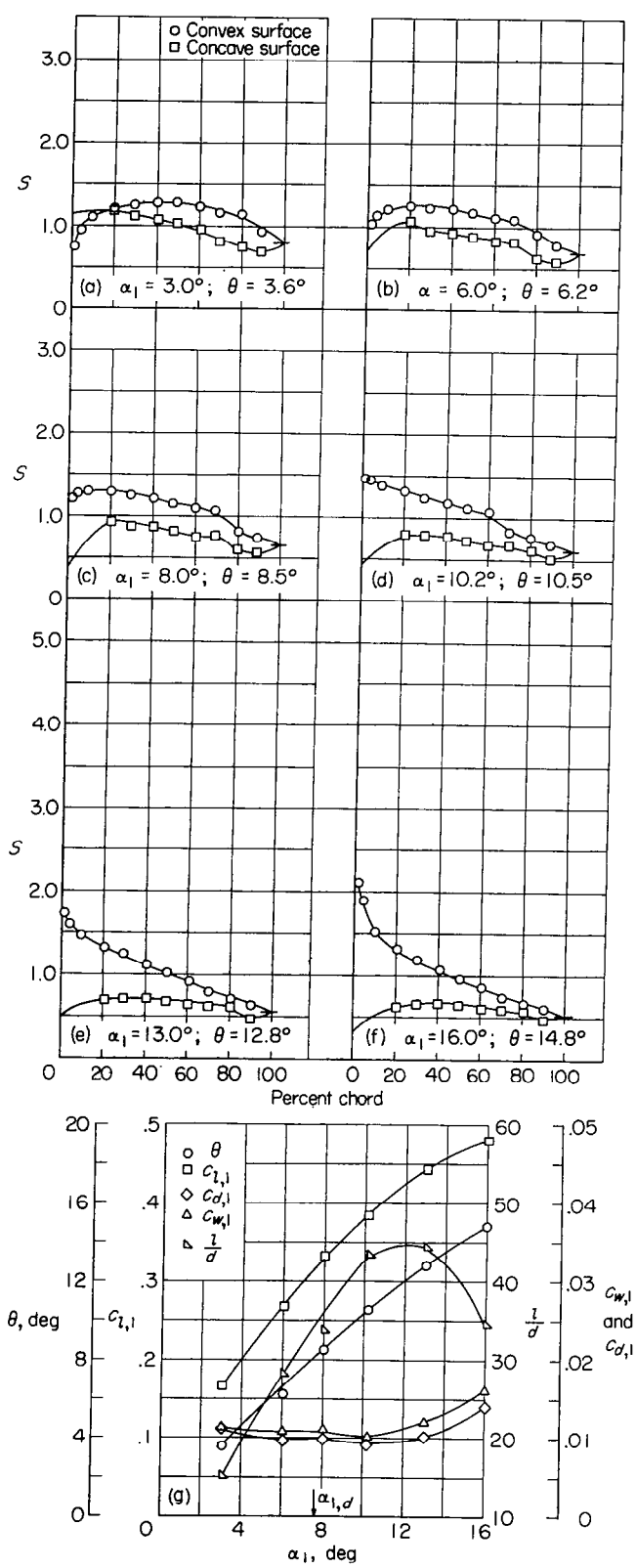

(g) Section characteristics; flagged symbol indicates leading-edge roughness.

FIGURE 60.—Blade-surface pressure distributions and blade section characteristics for the cascade combination, $\beta_1=60°$, $\sigma=1.25$, and blade section, NACA 65–410.

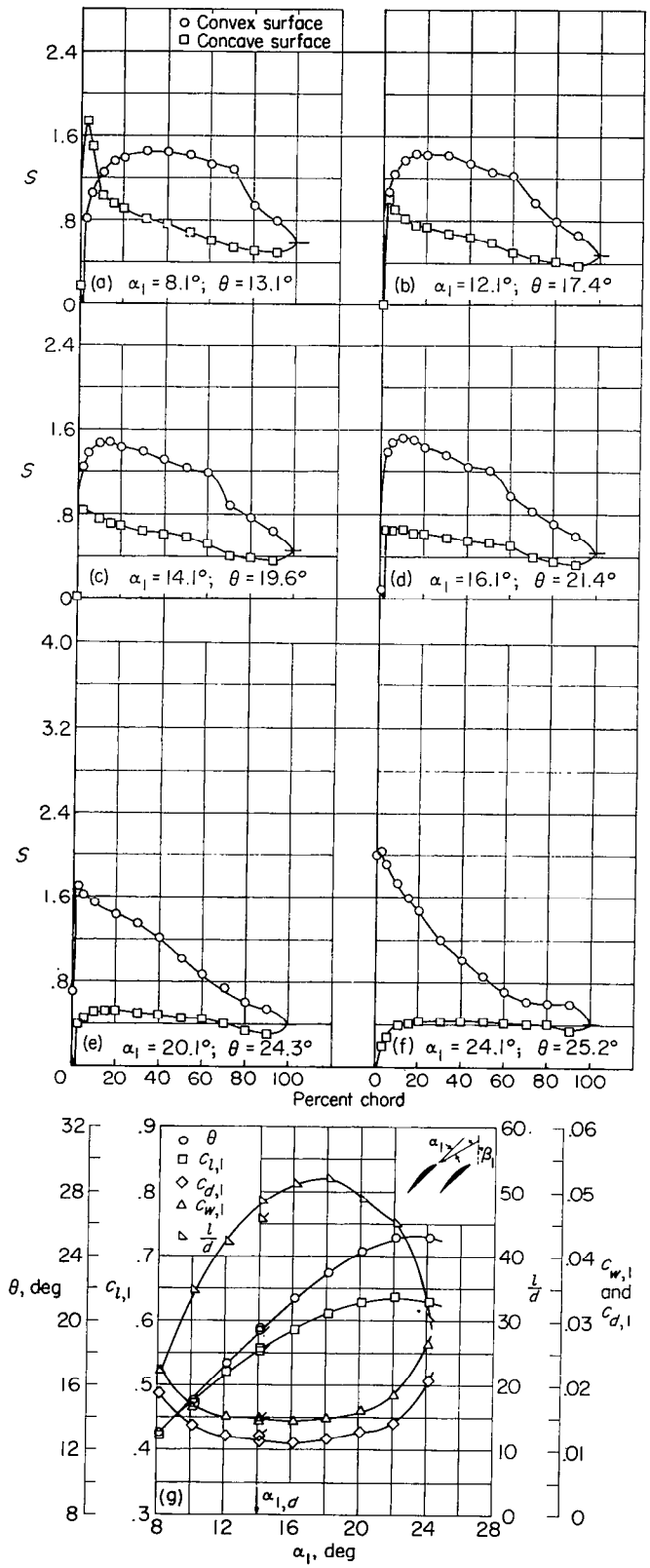

(g) Section characteristics; flagged symbol indicates leading-edge roughness.

FIGURE 61.—Blade-surface pressure distributions and blade section characteristics for the cascade combination, $\beta_1=60°$, $\sigma=1.25$, and blade section, NACA 65–(12)10.

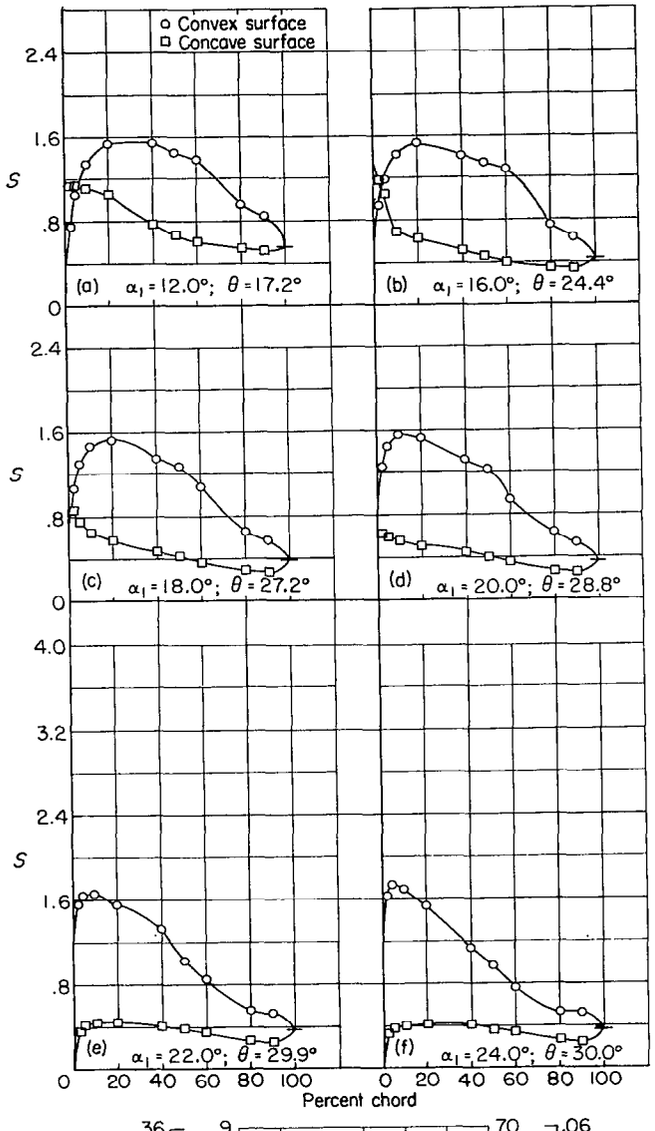

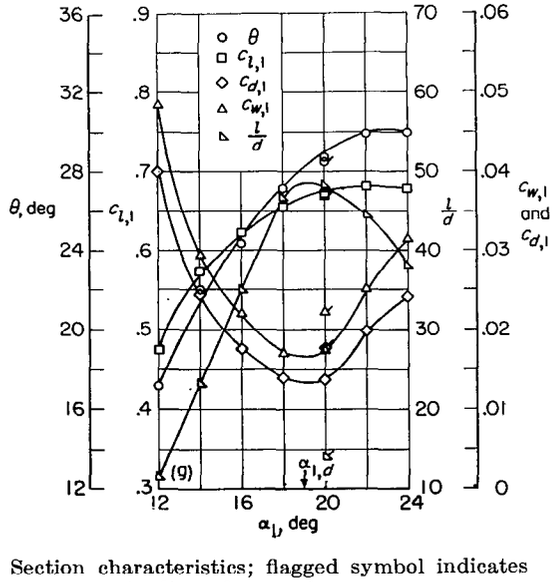

(g) Section characteristics; flagged symbol indicates leading-edge roughness.

FIGURE 62.—Blade-surface pressure distributions and blade section characteristics for the cascade combination, $\beta_1=60°$, $\sigma=1.25$, and blade section, NACA 65-(18)10.

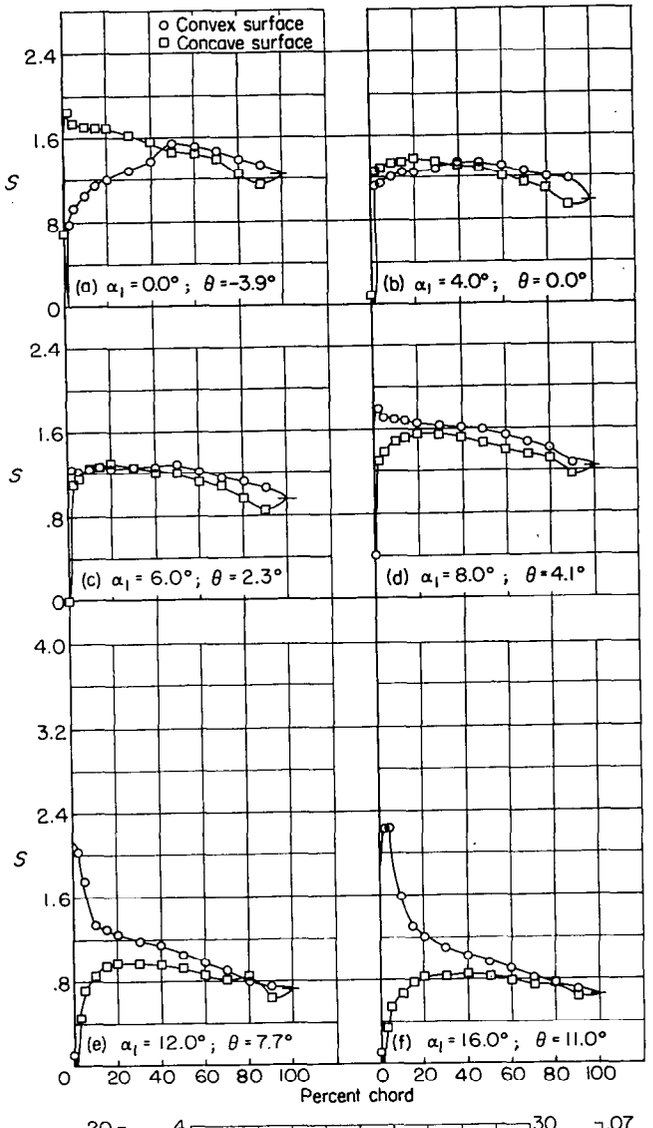

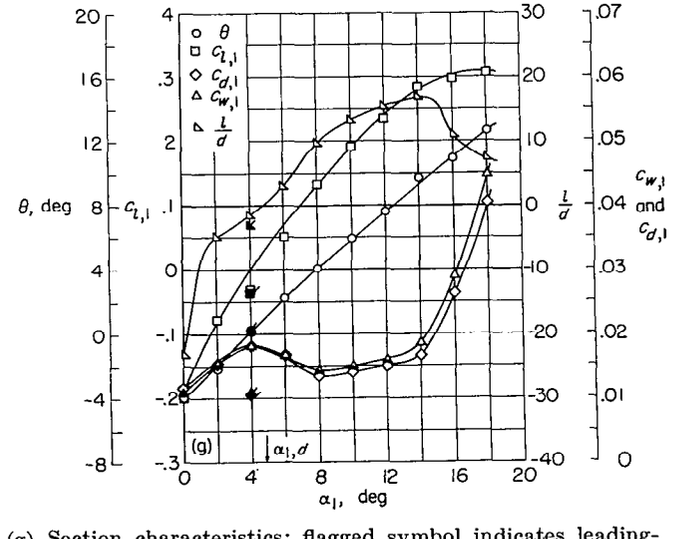

(g) Section characteristics; flagged symbol indicates leading-edge roughness; solid symbol indicates high Reynolds number.

FIGURE 63.—Blade-surface pressure distributions and blade section characteristics for the cascade combination, $\beta_1=60°$, $\sigma=1.50$, and blade section, NACA 65-010.

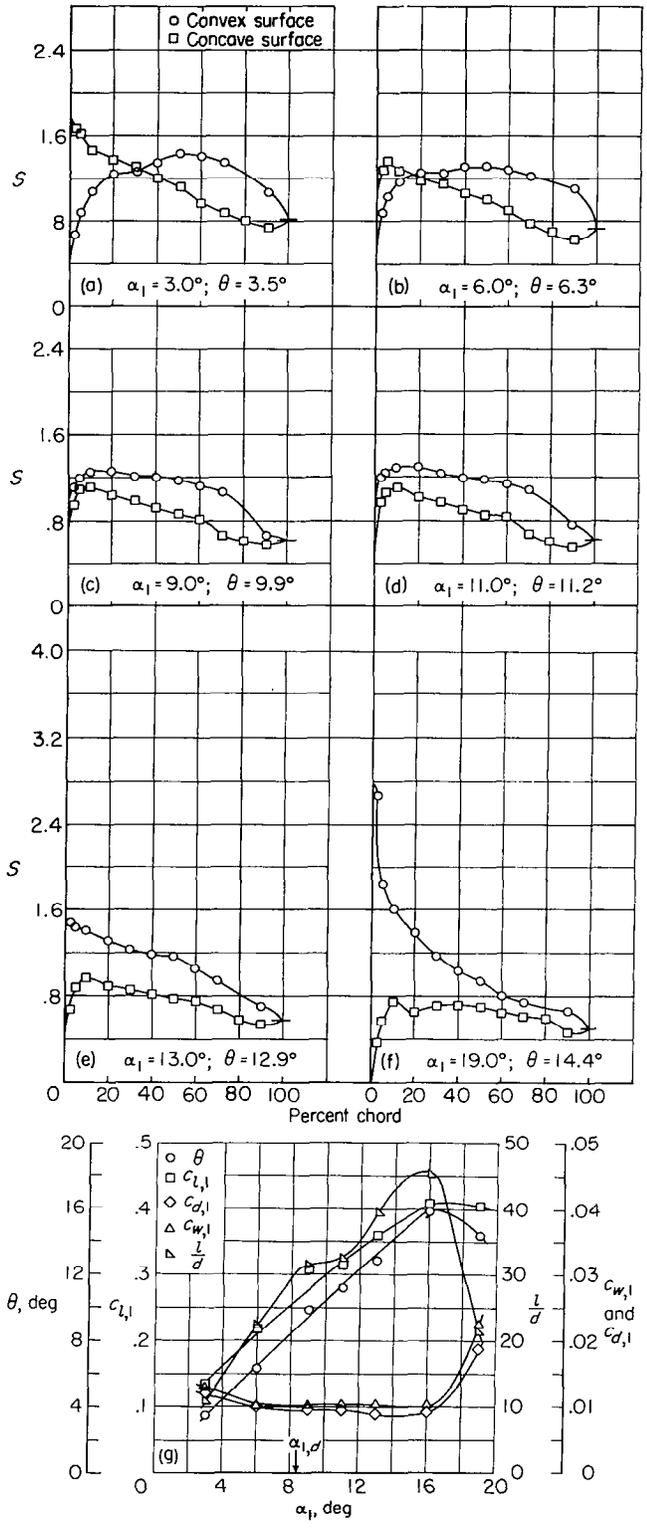

(g) Section characteristics.

FIGURE 64.—Blade-surface pressure distributions and blade section characteristics for the cascade combination, $\beta_1=60°$, $\sigma=1.50$, and blade section, NACA 65-410.

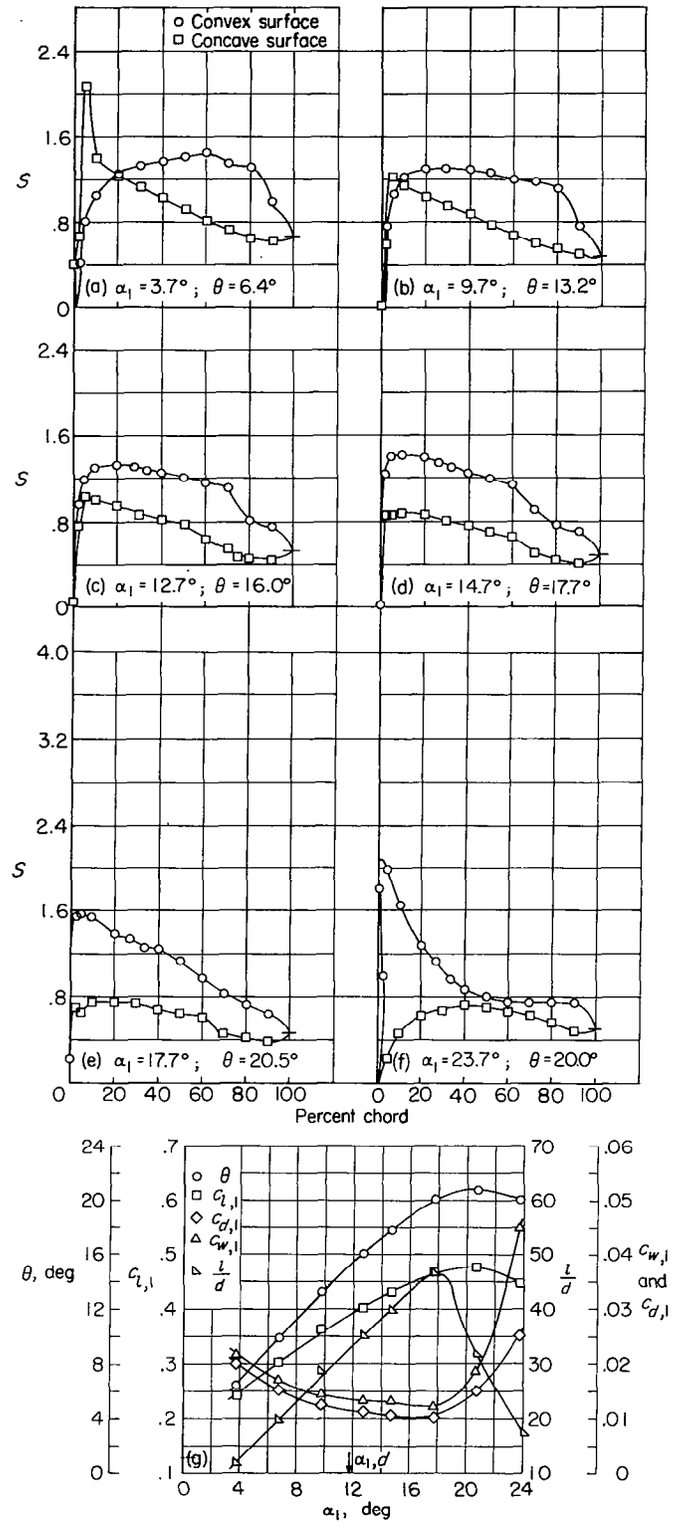

(g) Section characteristics.

FIGURE 65.—Blade-surface pressure distributions and blade section characteristics for the cascade combination, $\beta_1=60°$, $\sigma=1.50$, and blade section, NACA 65-810.

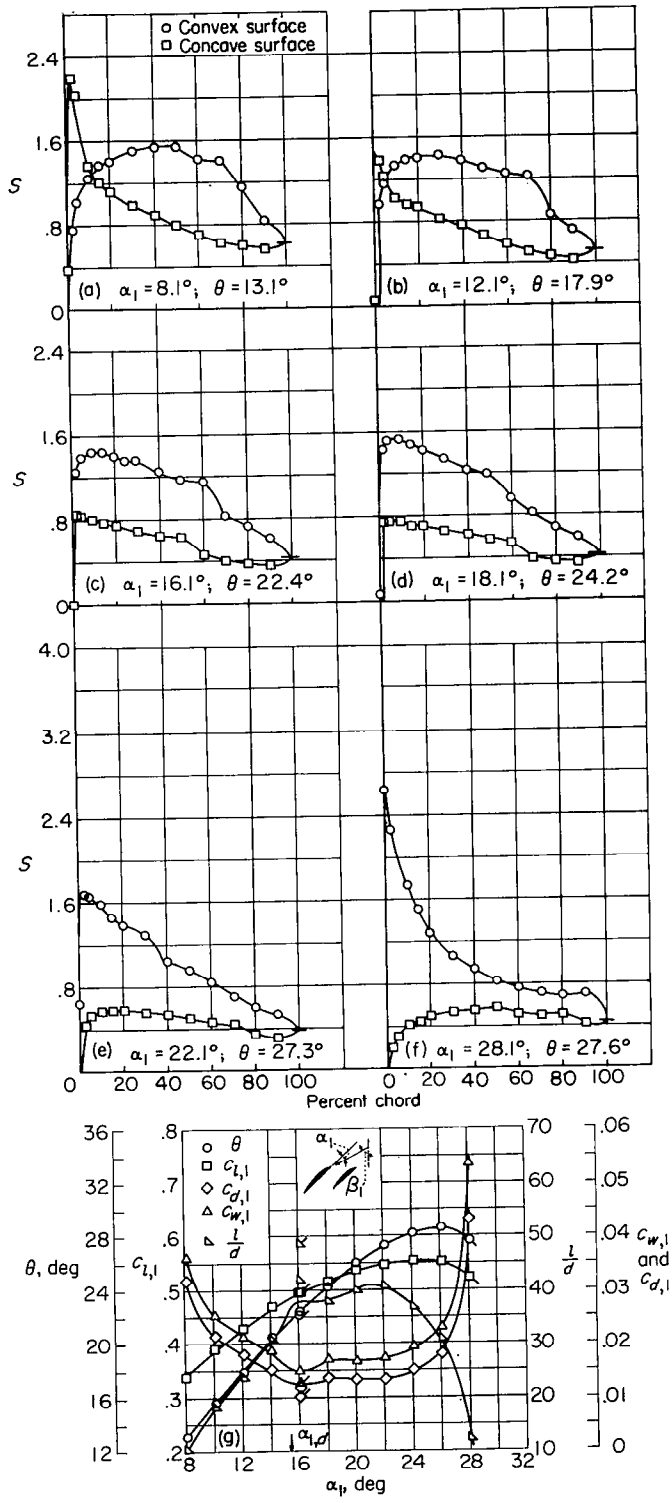

(g) Section characteristics; flagged symbol indicates leading-edge roughness.

FIGURE 66.—Blade-surface pressure distributions and blade section characteristics for the cascade combination, $\beta_1=60°$, $\sigma=1.50$, and blade section, NACA 65-(12)10.

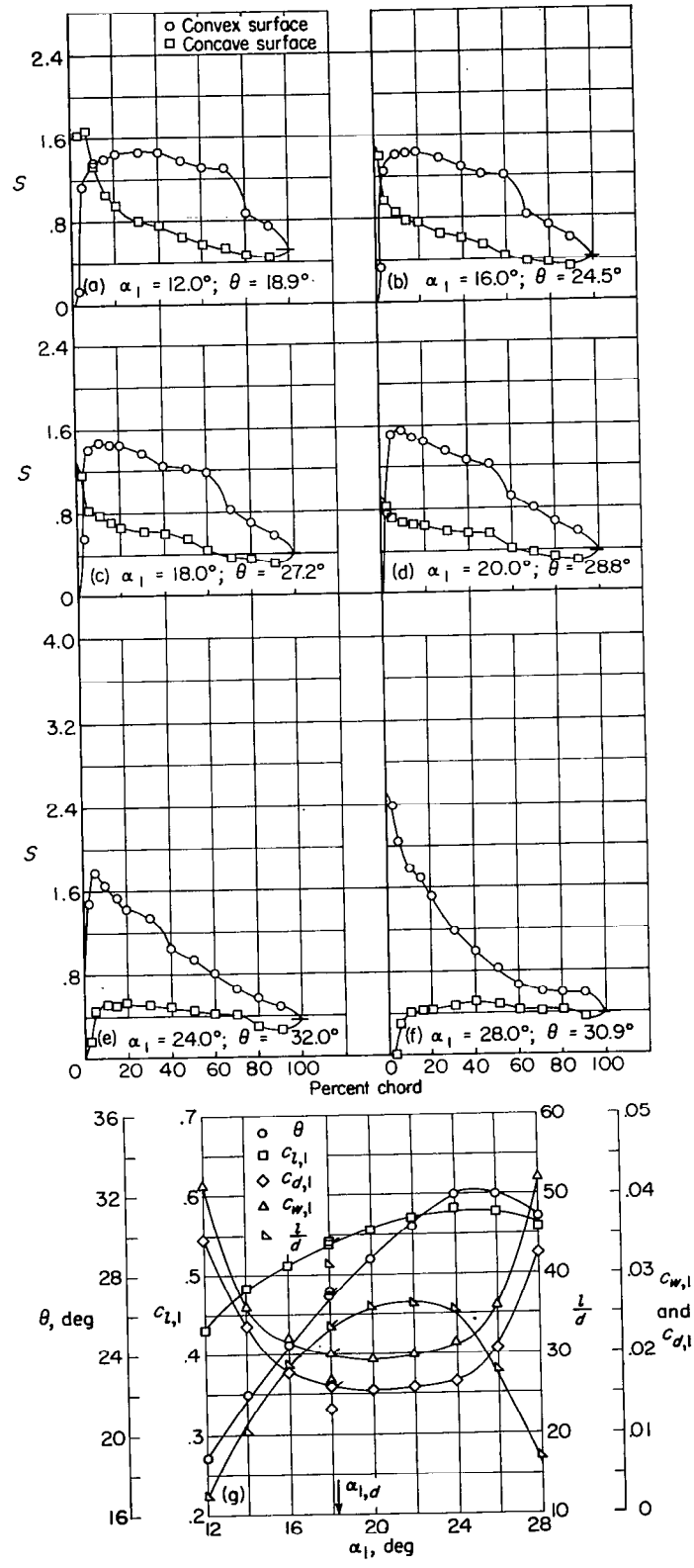

(g) Section characteristics; flagged symbol indicates leading-edge roughness.

FIGURE 67.—Blade-surface pressure distributions and blade section characteristics for the cascade combination, $\beta_1=60°$, $\sigma=1.50$, and blade section, NACA 65-(15)10.

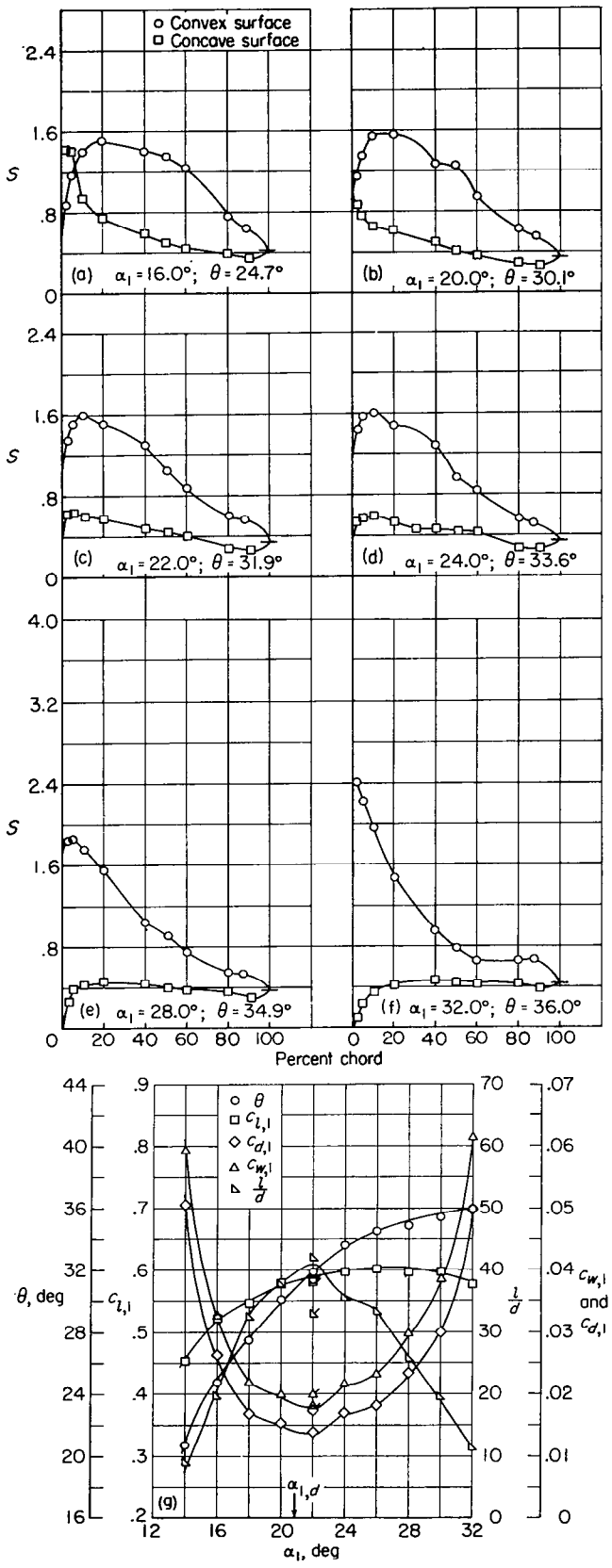

(g) Section characteristics; flagged symbol indicates leading-edge roughness.

FIGURE 68.—Blade-surface pressure distributions and blade section characteristics for the cascade combination, $\beta_1=60°$, $\sigma=1.50$, and blade section, NACA 65–(18)10.

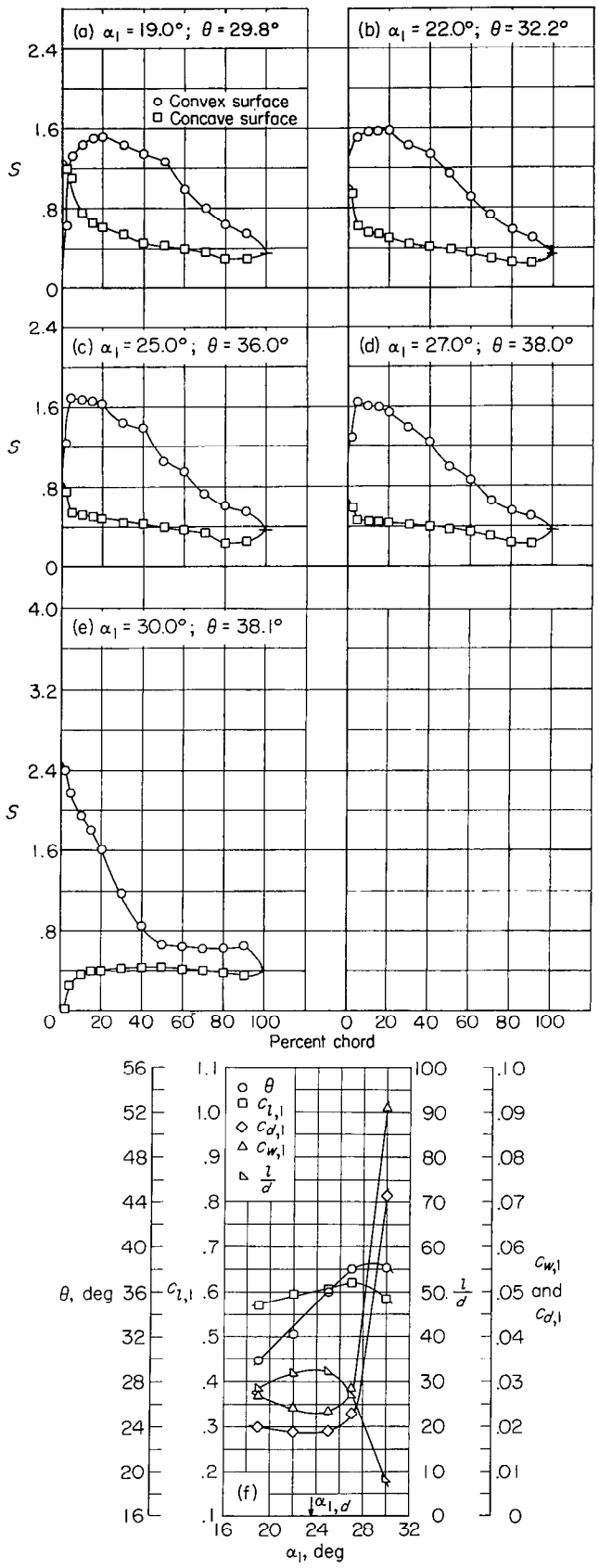

(f) Section characteristics.

FIGURE 69.—Blade-surface pressure distributions and blade section characteristics for the cascade combination, $\beta_1=60°$, $\sigma=1.50$, and blade section, NACA 65–(21)10.

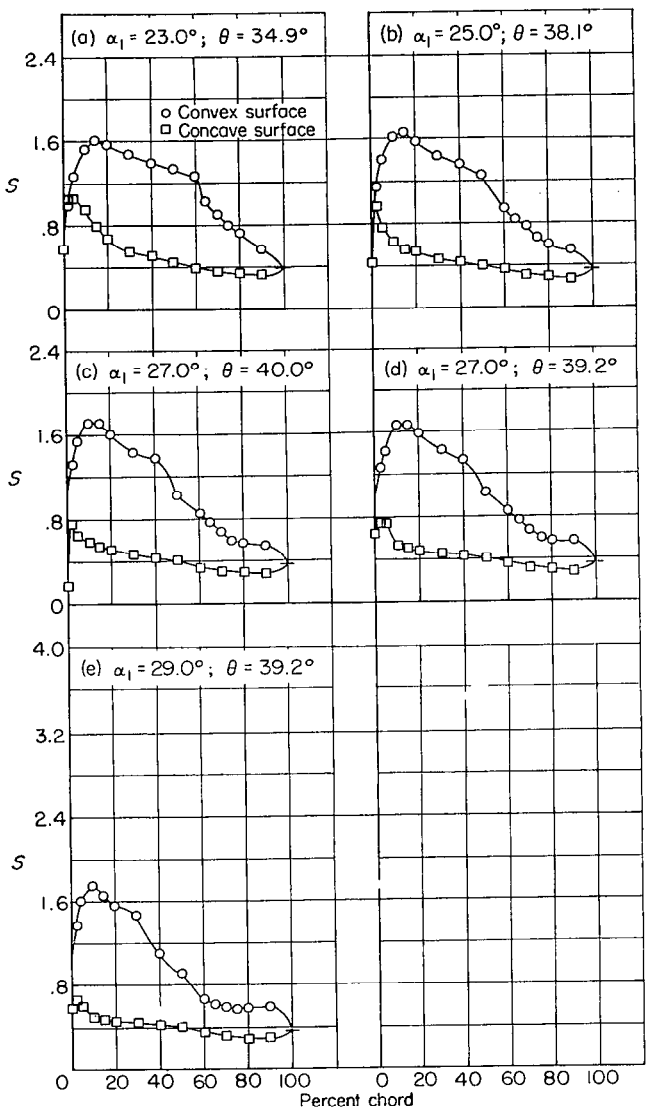

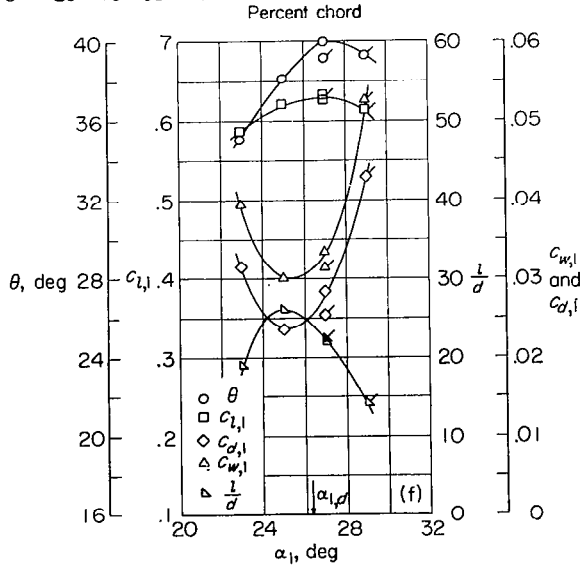

(f) Section characteristics; flagged symbol indicates leading-edge roughness.

FIGURE 70.—Blade-surface pressure distributions and blade section characteristics for the cascade combination, $\beta_1=60°$, $\sigma=1.50$, and blade section, NACA 65-(24)10.

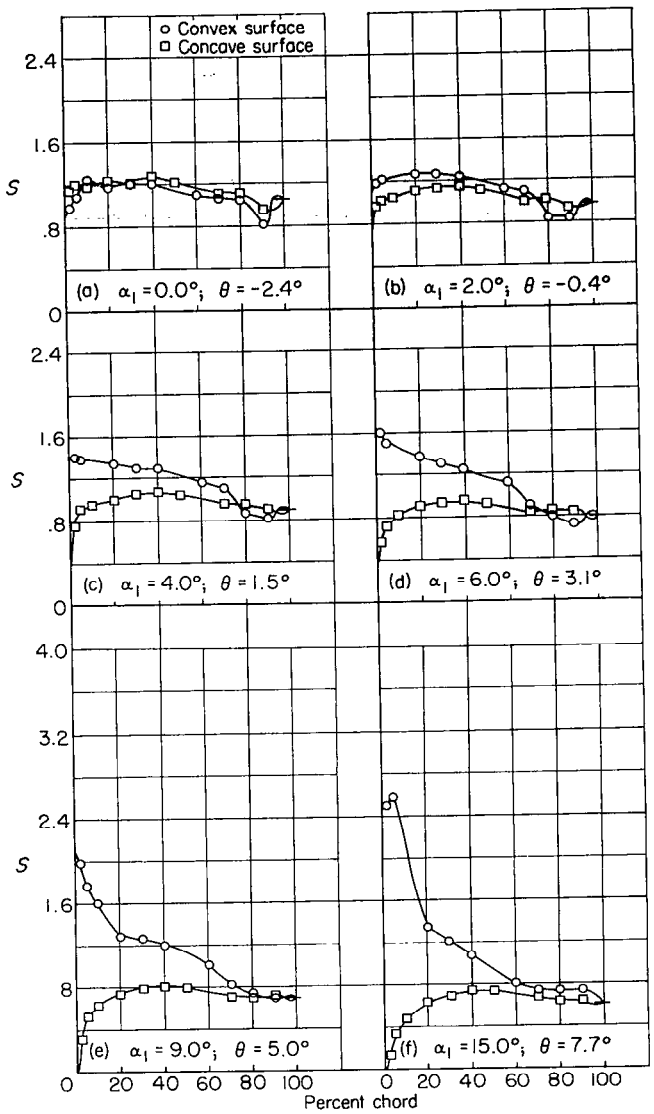

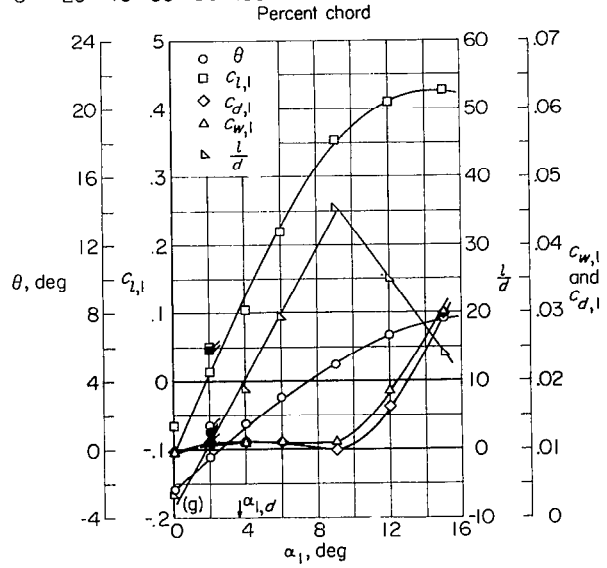

(g) Section characteristics; flagged symbol indicates leading-edge roughness; solid symbol indicates high Reynolds number.

FIGURE 71.—Blade-surface pressure distributions and blade section characteristics for the cascade combination, $\beta_1=70°$, $\sigma=1.00$, and blade section, NACA 65-010.

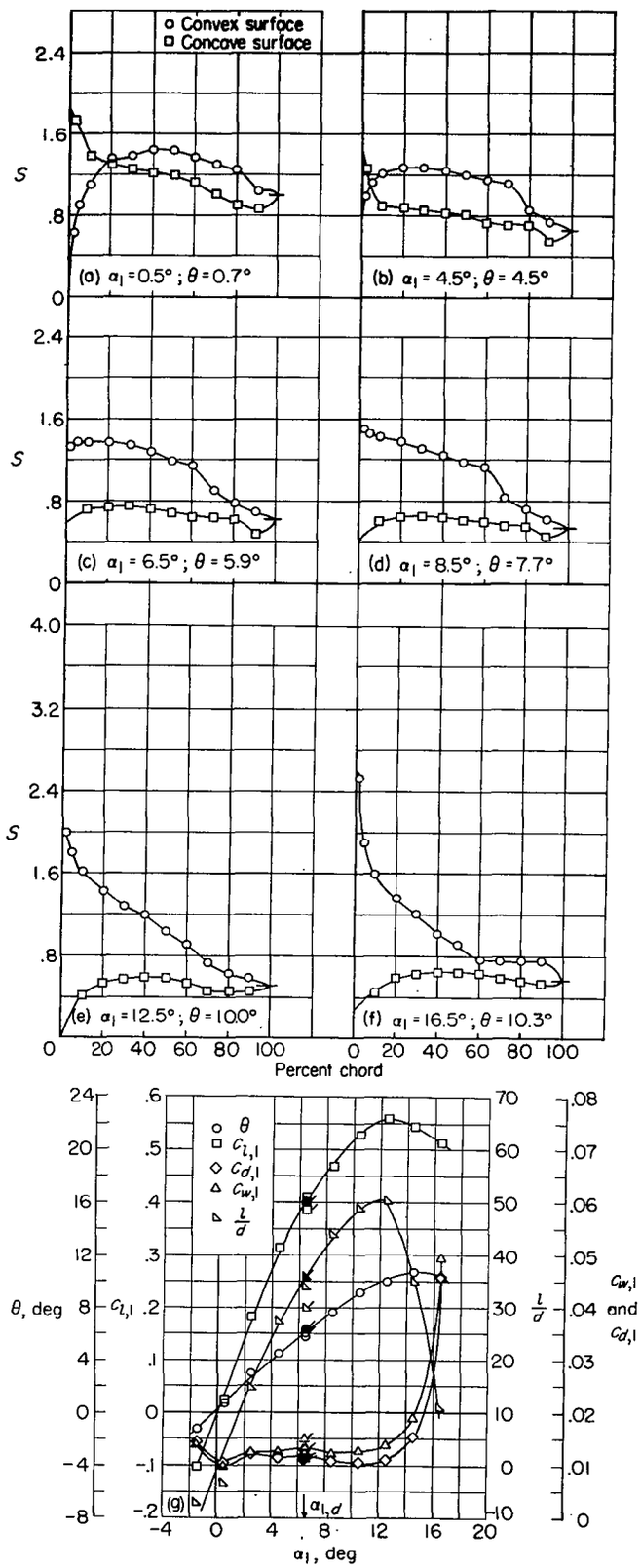

(g) Section characteristics; flagged symbol indicates leading-edge roughness; solid symbol indicates high Reynolds number.

FIGURE 72.—Blade-surface pressure distributions and blade section characteristics for the cascade combination, $\beta_1 = 70°$, $\sigma = 1.00$, and blade section, NACA 65–410.

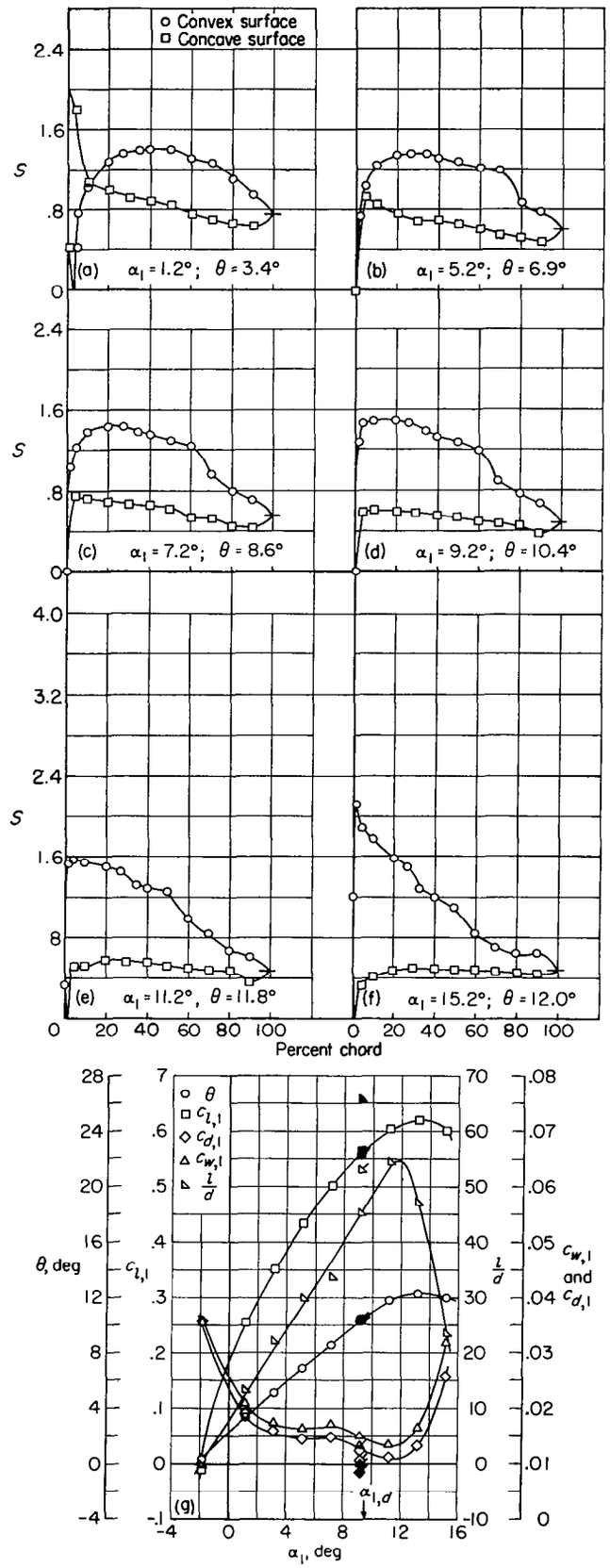

(g) Section characteristics; flagged symbol indicates leading-edge roughness; solid symbol indicates high Reynolds number.

FIGURE 73.—Blade-surface pressure distributions and blade section characteristics for the cascade combination, $\beta_1 = 70°$, $\sigma = 1.00$, and blade section, NACA 65–810.

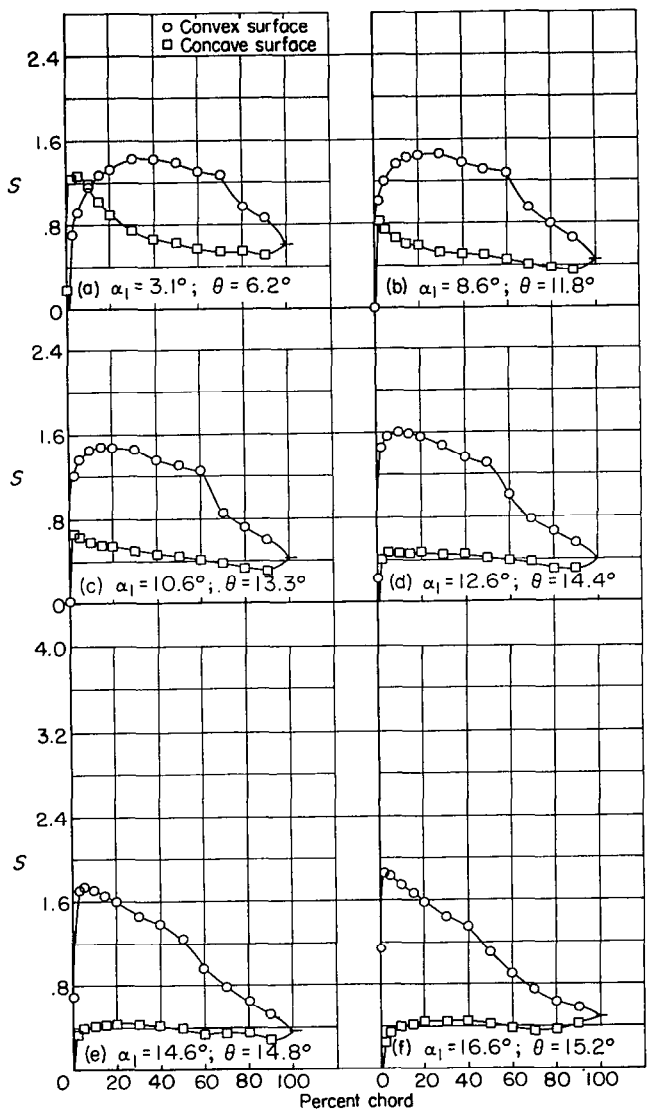

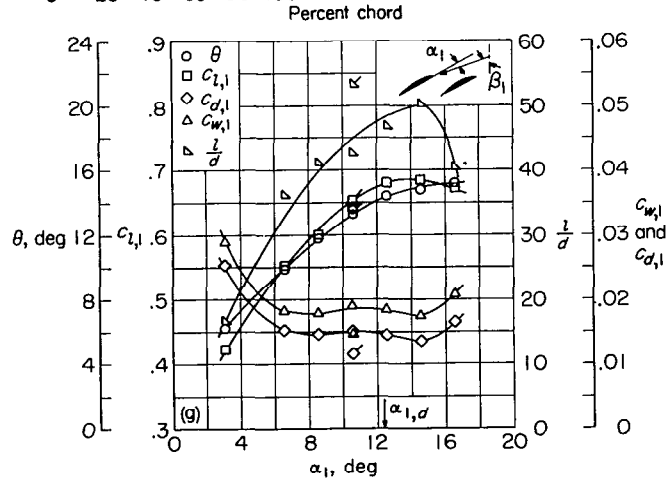

(g) Section characteristics; flagged symbol indicates leading-edge roughness.

FIGURE 74.—Blade-surface pressure distributions and blade section characteristics for the cascade combination, $\beta_1=70°$, $\sigma=1.00$, and blade section, NACA 65-(12)10.

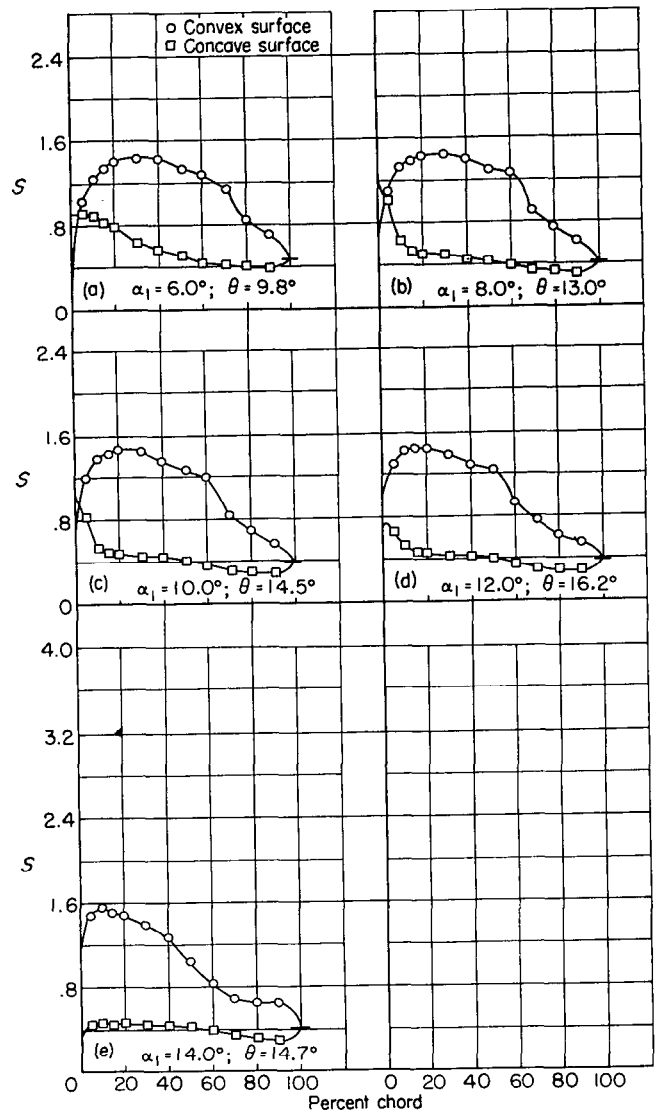

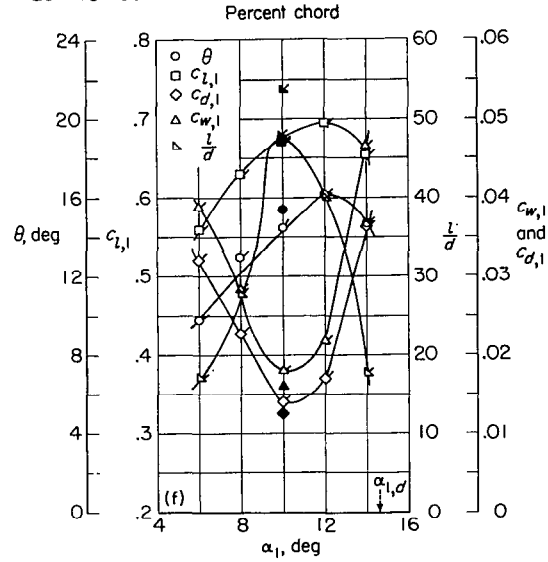

(f) Section characteristics; no design point was obtained; flagged symbol indicates leading-edge roughness; solid symbol indicates high Reynolds number.

FIGURE 75.—Blade-surface pressure distributions and blade section charactertistics for the cascade combination, $\beta_1=70°$, $\sigma=1.00$, and blade section, NACA 65-(15)10.

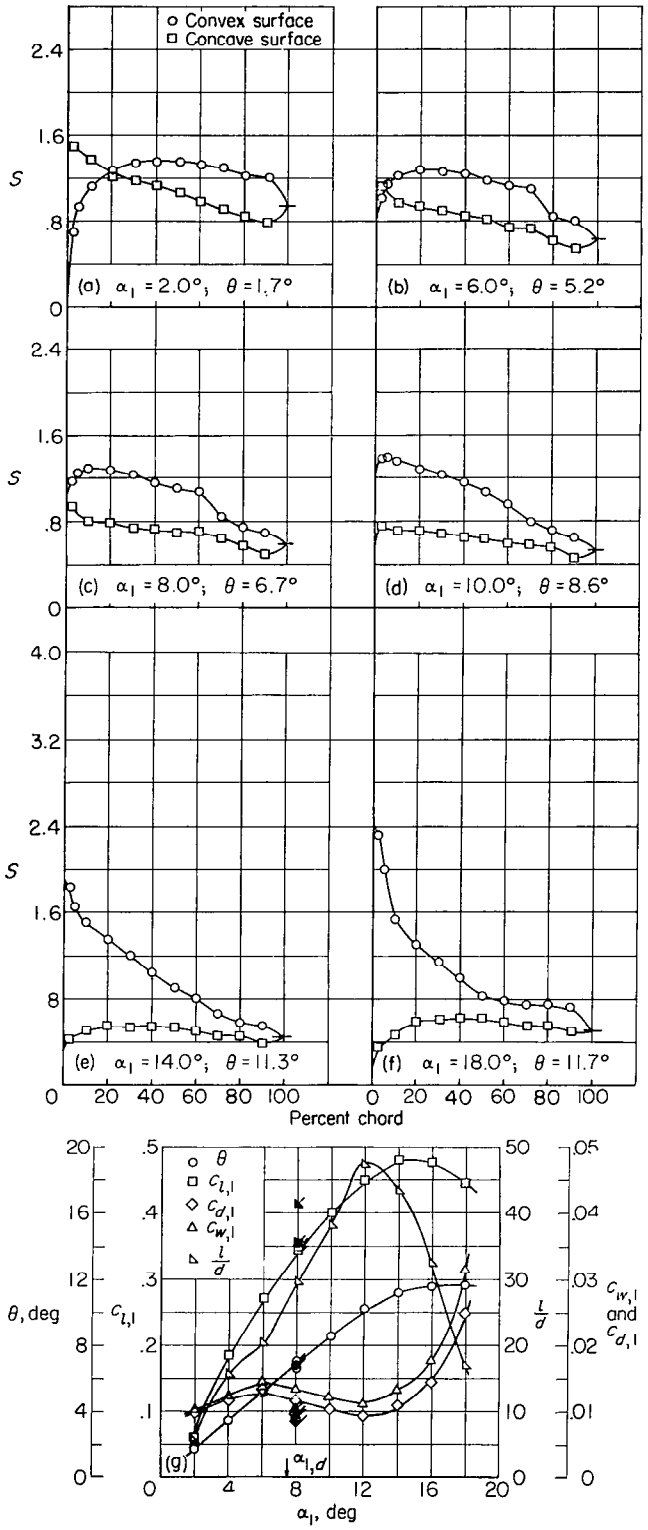

(g) Section characteristics; flagged symbol indicates leading-edge roughness; solid symbol indicates high Reynolds number.

FIGURE 76.—Blade-surface pressure distributions and blade section characteristics for the cascade combination, $\beta_1=70°$, $\sigma=1.25$, and blade section, NACA 65-410.

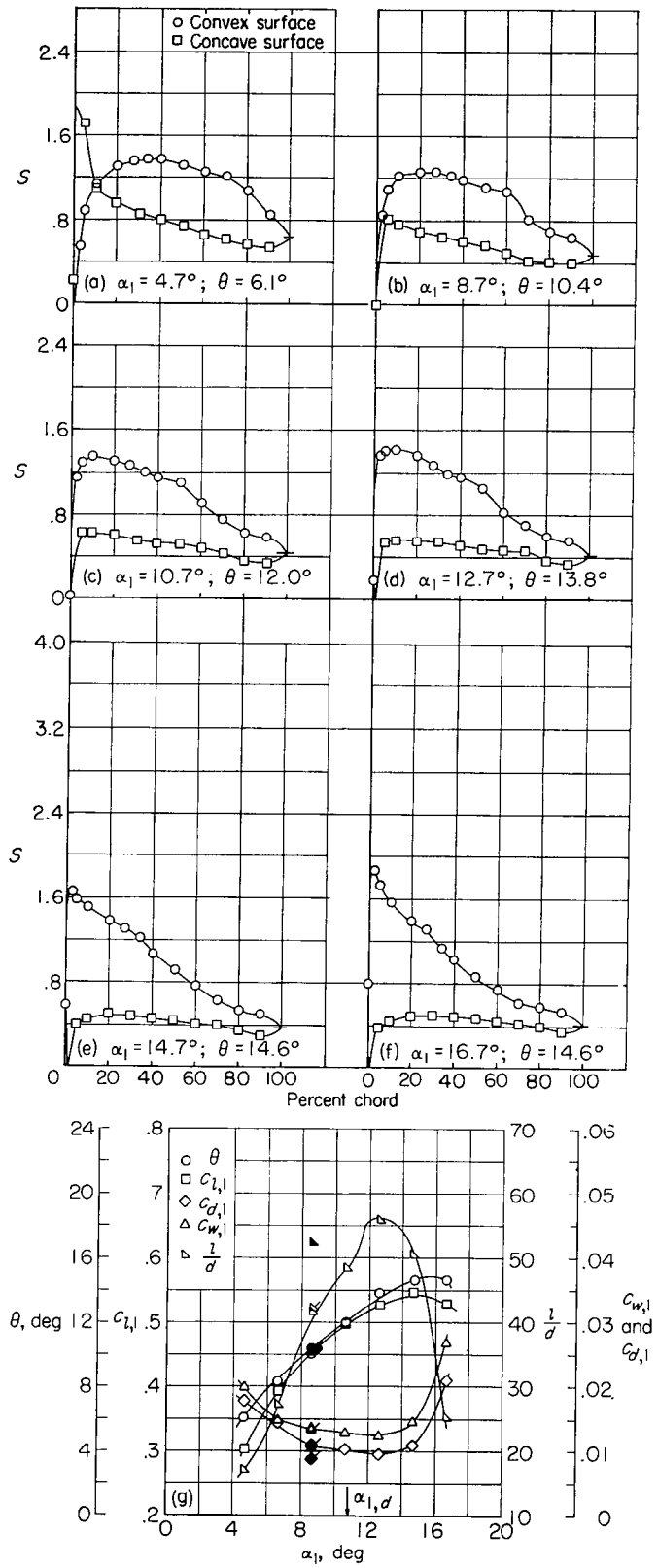

(g) Section characteristics; flagged symbol indicates leading-edge roughness; solid symbol indicates high Reynolds number.

FIGURE 77.—Blade-surface pressure distributions and blade section characteristics for the cascade combination, $\beta_1=70°$, $\sigma=1.25$, and blade section, NACA 65-810.

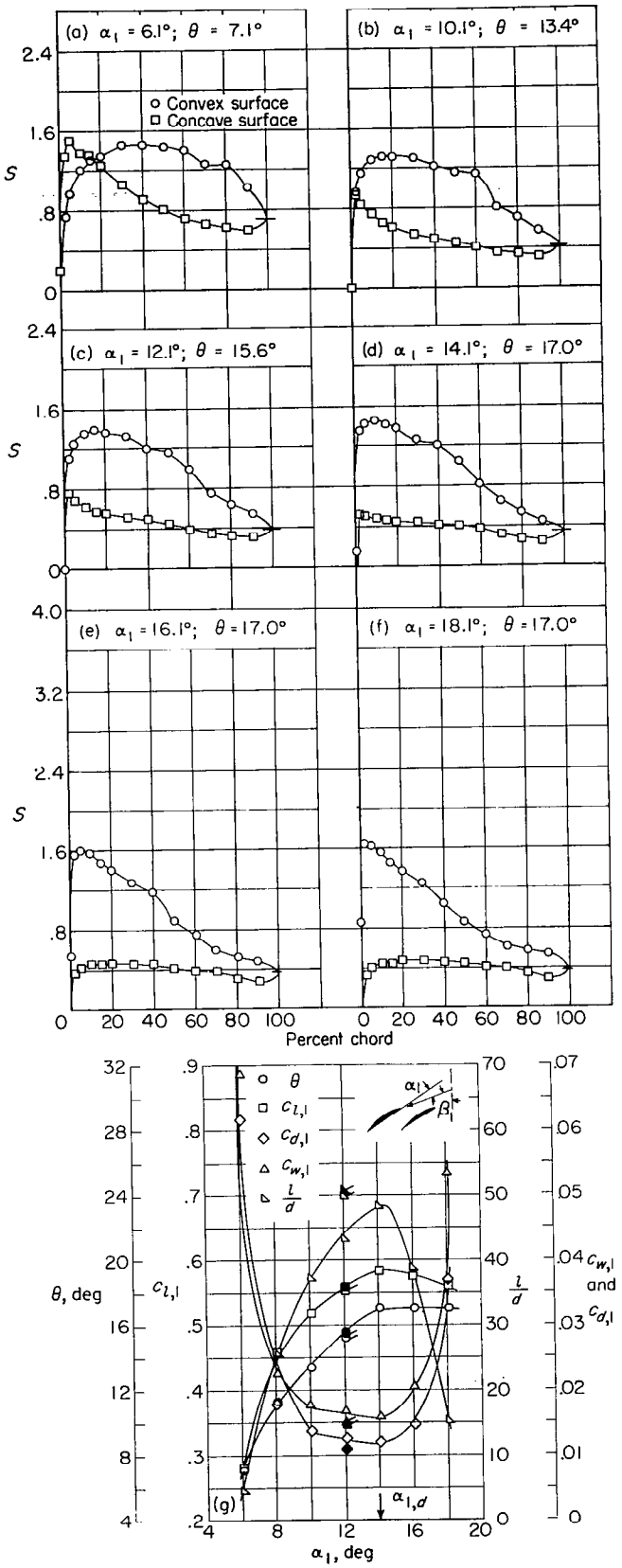

(g) Section characteristics; flagged symbol indicates leading-edge roughness; solid symbol indicates high Reynolds number.

FIGURE 78.—Blade-surface pressure distributions and blade section characteristics for the cascade combination, $\beta_1=70°$, $\sigma=1.25$, and blade section, NACA 65-(12)10.

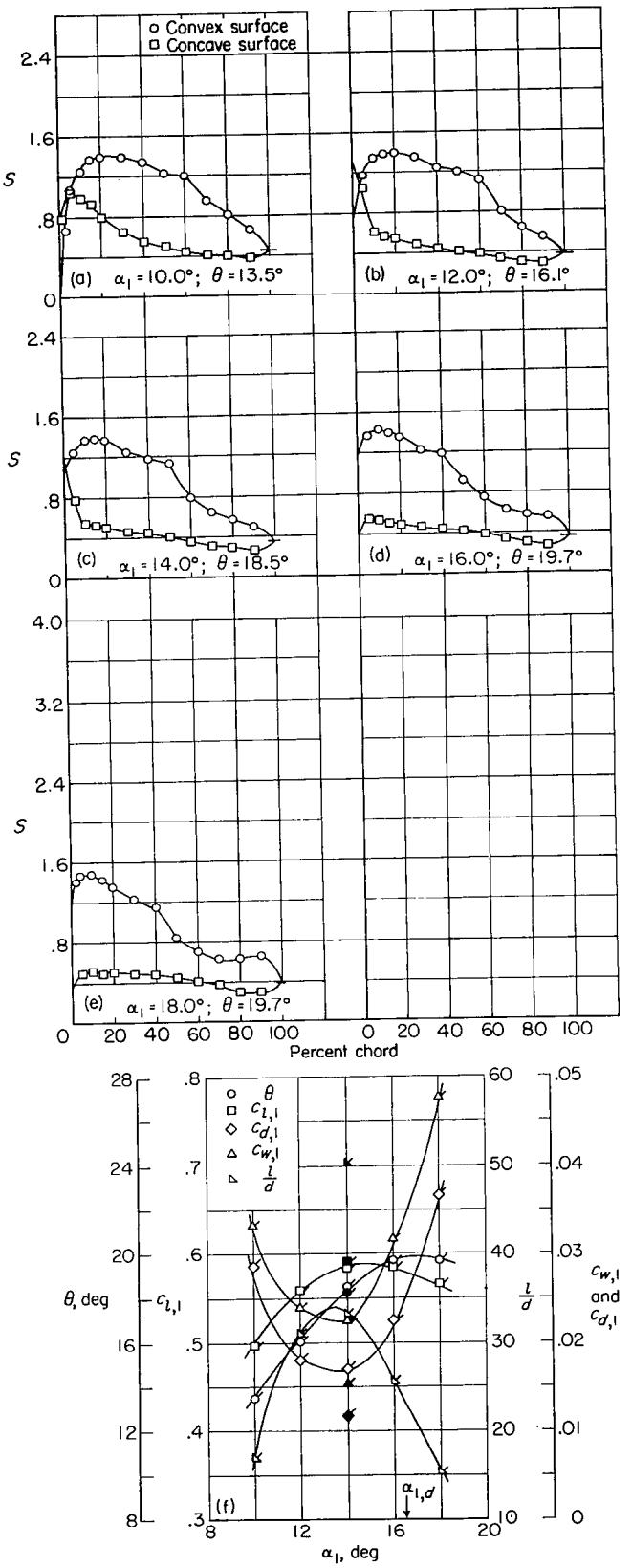

(f) Section characteristics; flagged symbol indicates leading-edge roughness; solid symbol indicates high Reynolds number.

FIGURE 79.—Blade-surface pressure distributions and blade section characteristics for the cascade combination, $\beta_1=70°$, $\sigma=1.25$, and blade section, NACA 65-(15)10.

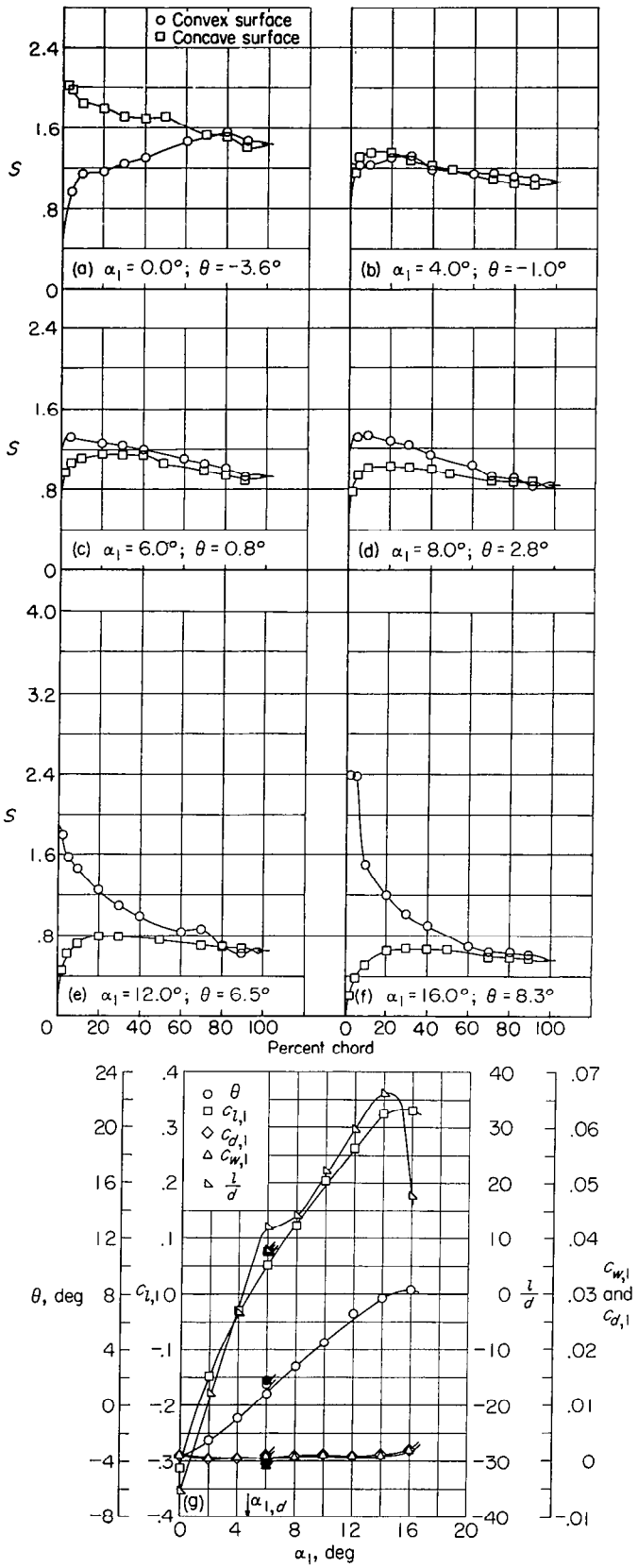

(g) Section characteristics; flagged symbol indicates leading-edge roughness; solid symbol indicates high Reynolds number.

FIGURE 80.—Blade-surface pressure distributions and blade section characteristics for the cascade combination, $\beta_1=70°$, $\sigma=1.50$, and blade section, NACA 65–010.

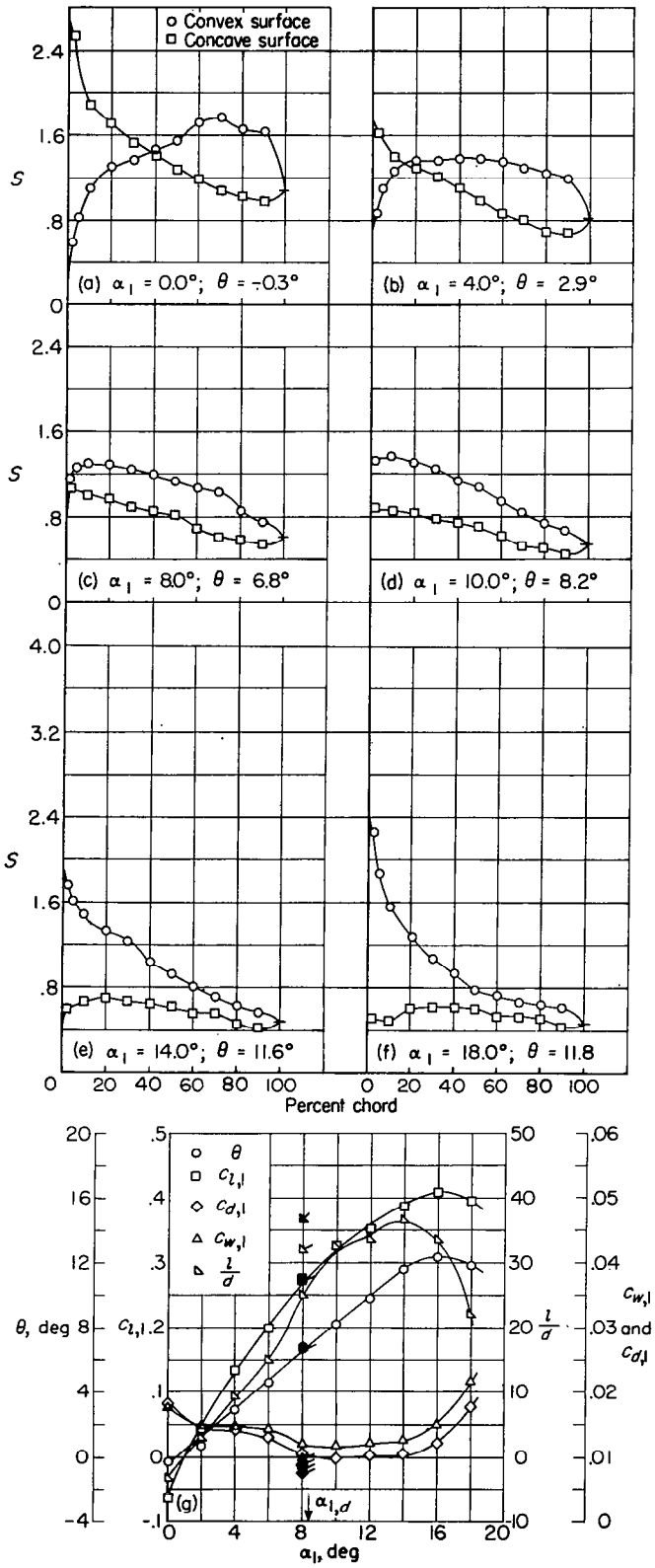

(g) Section characteristics; flagged symbol indicates leading-edge roughness; solid symbol indicates high Reynolds number.

FIGURE 81.—Blade-surface pressure distributions and blade section characteristics for the cascade combination, $\beta_1=70°$, $\sigma=1.50$, and blade section, NACA 65–410.

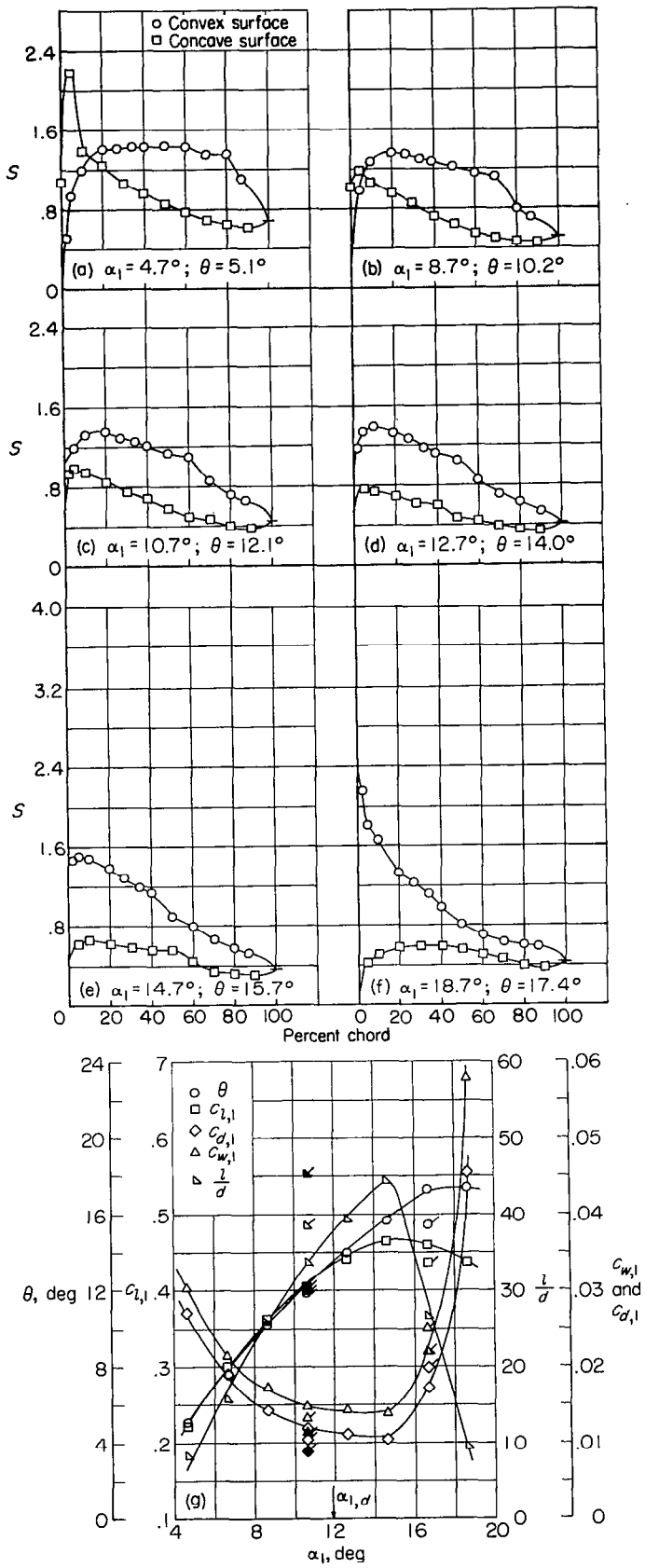

(g) Section characteristics; flagged symbol indicates leading-edge roughness; solid symbol indicates high Reynolds number.

FIGURE 82.—Blade-surface pressure distributions and blade section characteristics for the cascade combination, $\beta_1=70°$, $\sigma=1.50$, and blade section, NACA 65-810.

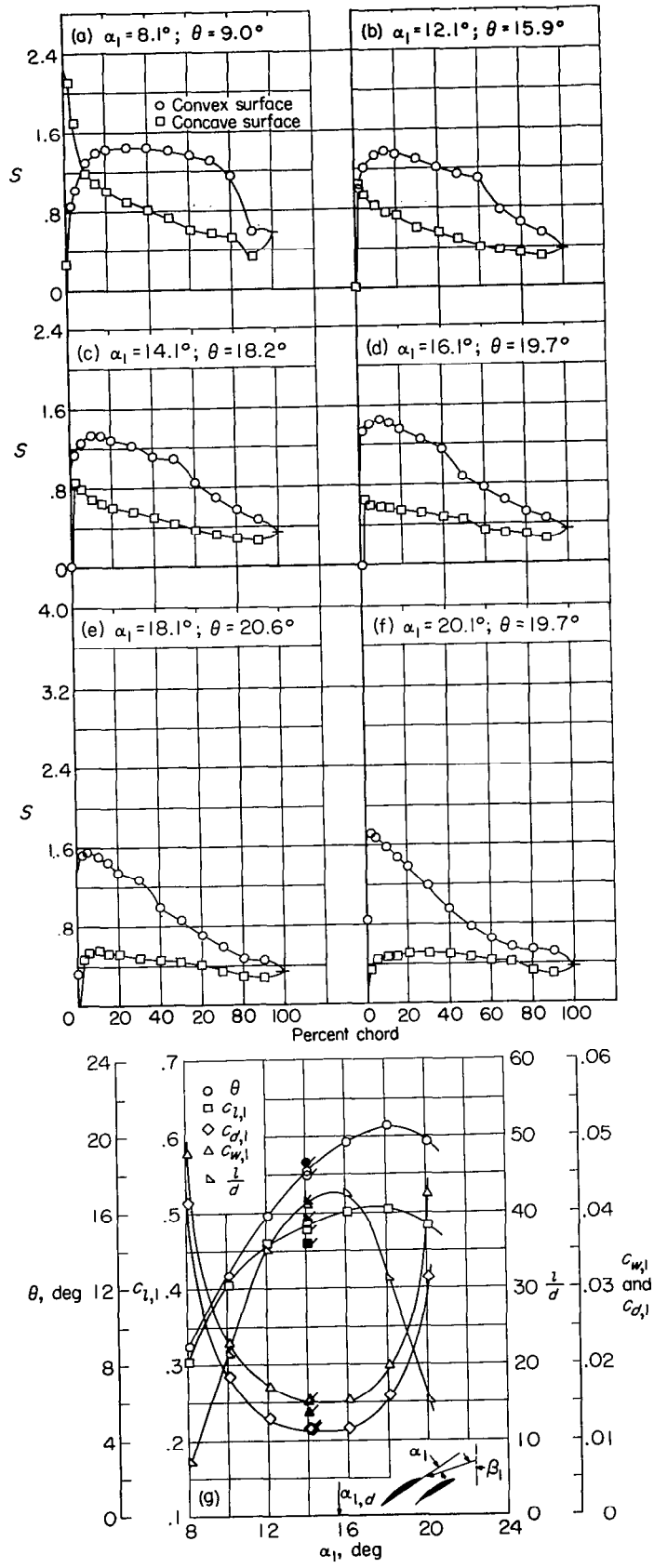

(g) Section characteristics; flagged symbol indicates leading-edge roughness; solid symbol indicates high Reynolds number.

FIGURE 83.—Blade-surface pressure distributions and blade section characteristics for the cascade combination, $\beta_1=70°$, $\sigma=1.50$, and blade section, NACA 65-(12)10.

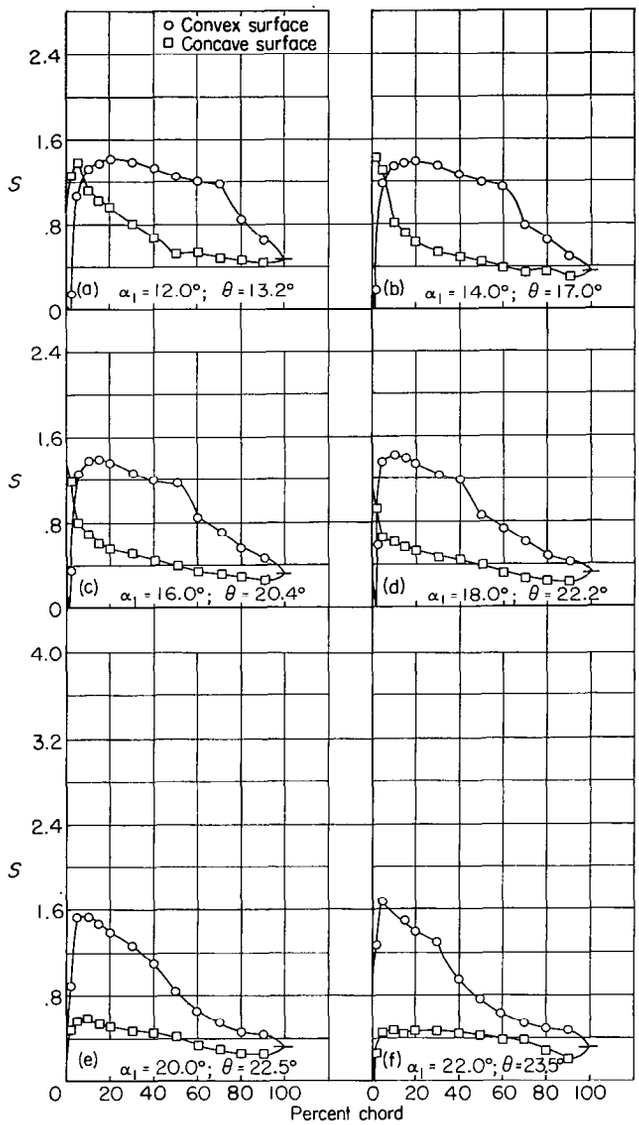

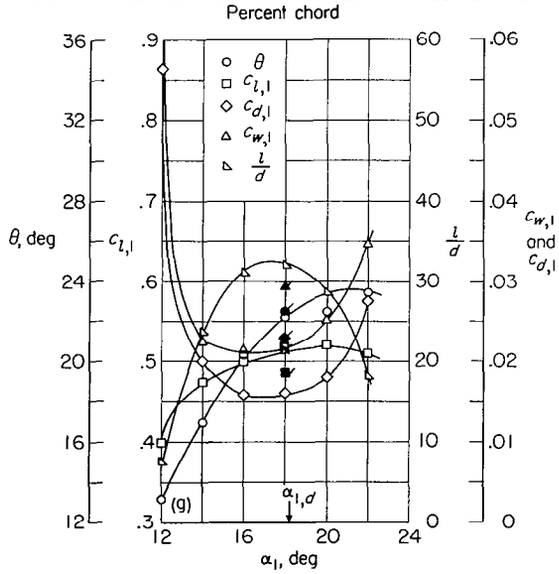

(g) Section characteristics; flagged symbol indicates leading-edge roughness; solid symbol indicates high Reynolds number.

FIGURE 84.—Blade-surface pressure distributions and blade section characteristics for the cascade combination, $\beta_1 = 70°$, $\sigma = 1.50$, and blade section, NACA 65-(15)10.

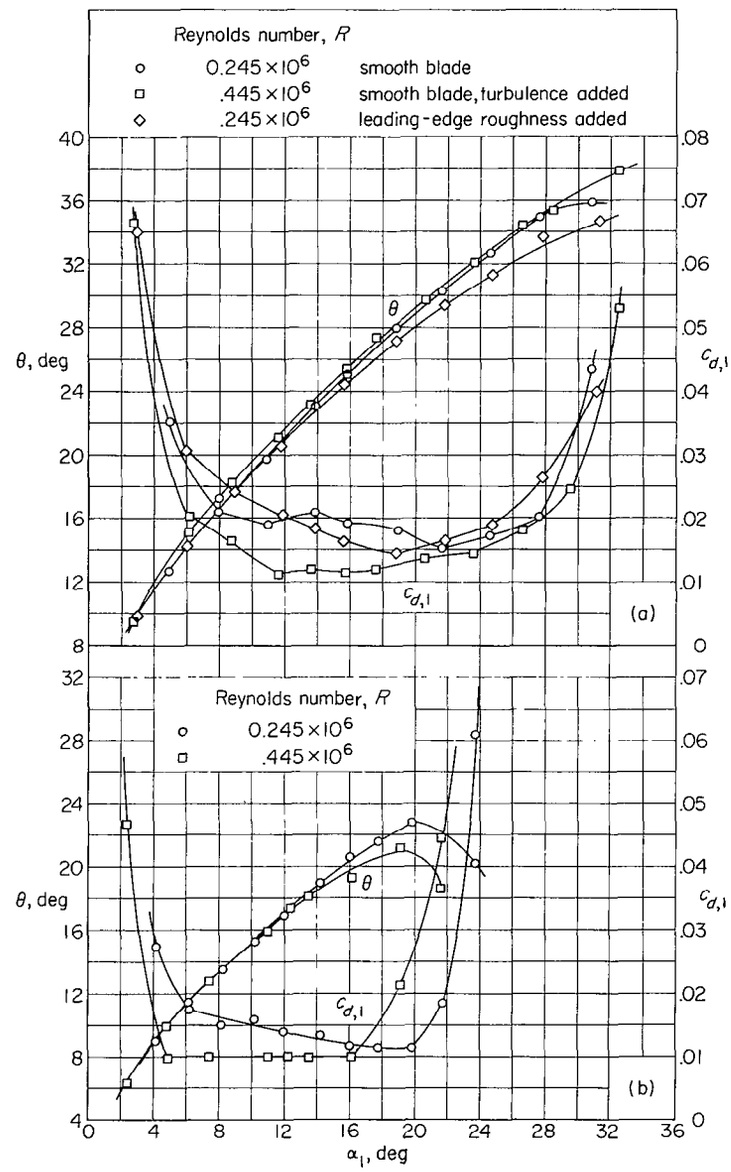

(a) Comparison for the angle-of-attack range for $\beta_1 = 45°$, $\sigma = 1.50$.
(b) Comparison for the angle-of-attack range for $\beta_1 = 60°$, $\sigma = 1.00$. Smooth blade.

FIGURE 85.—Effect of Reynolds number on turning angle and drag coefficient of the NACA 65-(12)10 blade section for typical cascade combinations.

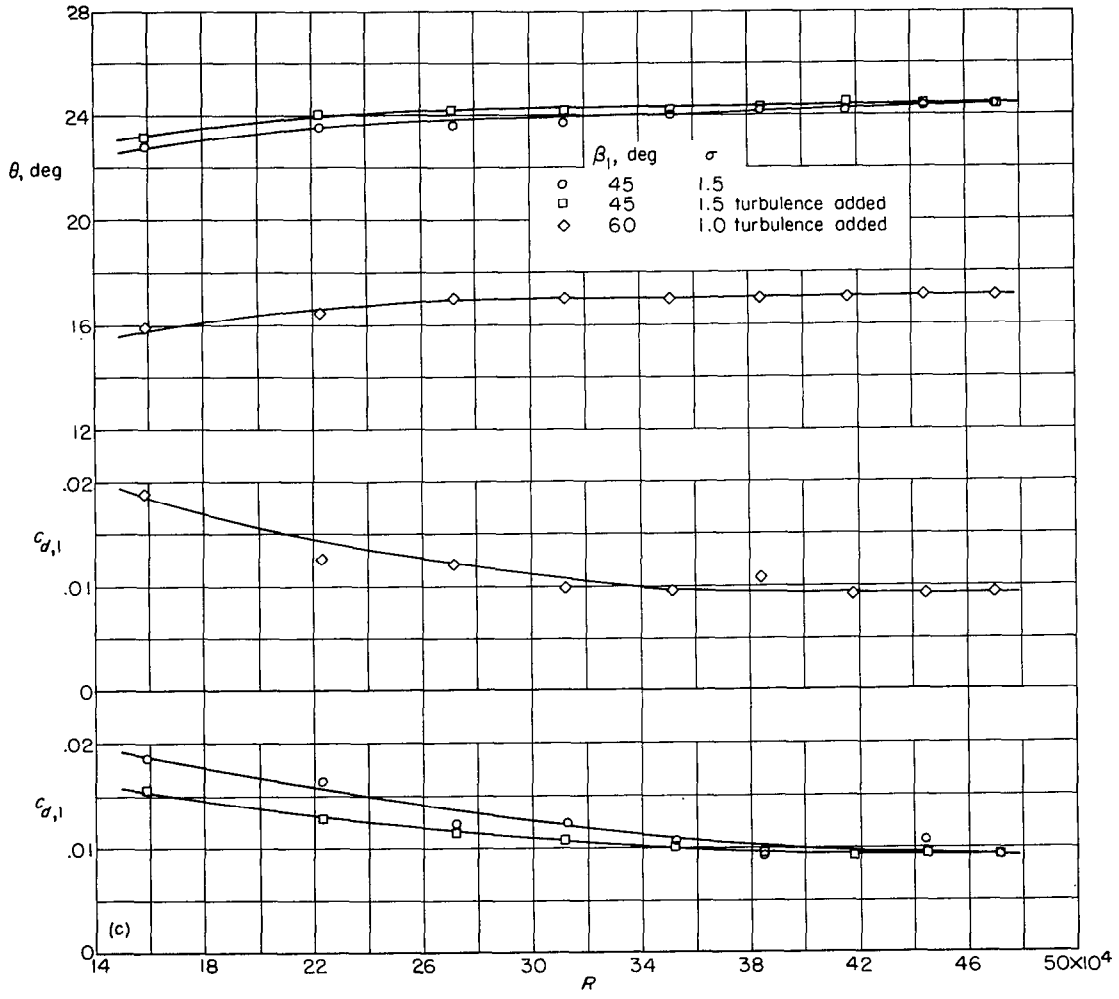

(c) Variation with R near design angle of attack.
FIGURE 85.—Concluded.

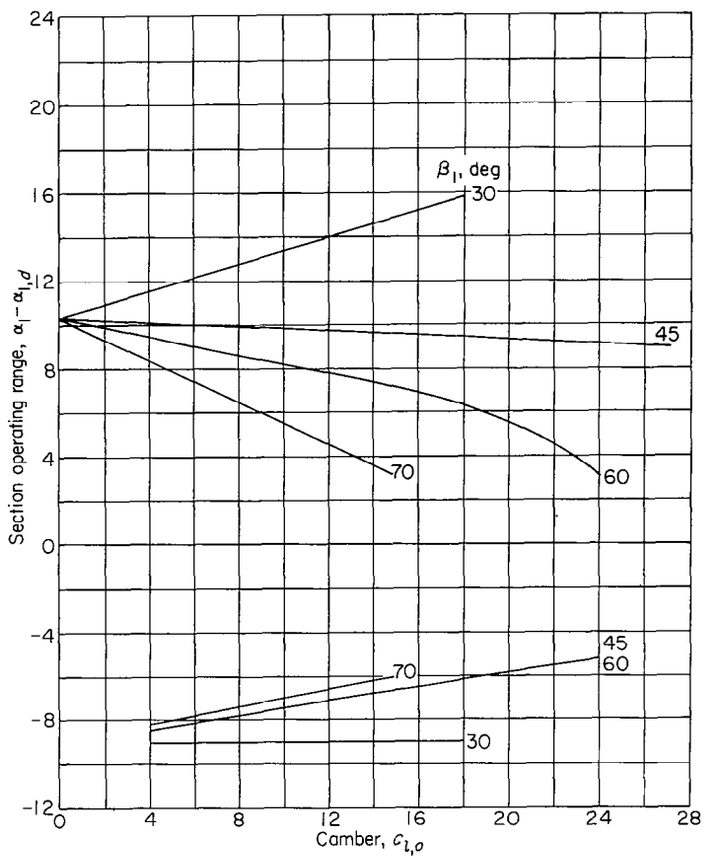

FIGURE 86.—Variation of estimated operating angle-of-attack range with camber for the inlet angles of the tests.

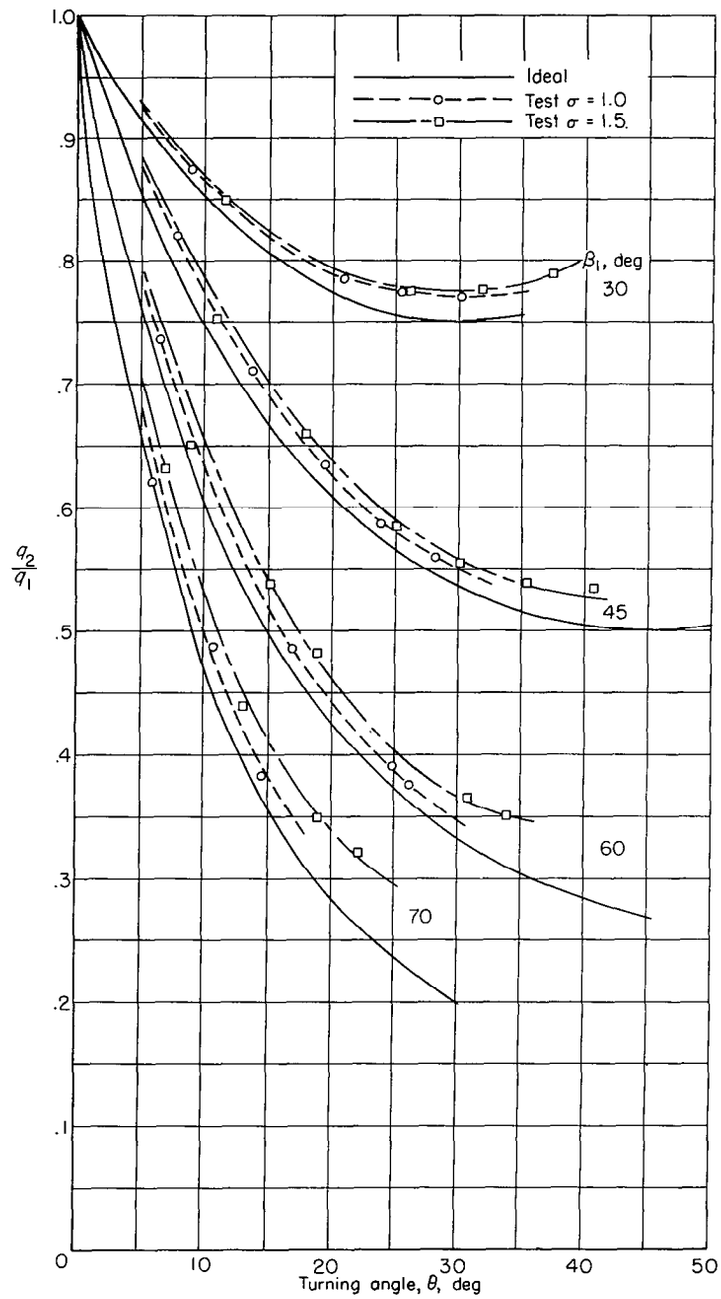

FIGURE 87.—Variation of ideal and test dynamic-pressure ratio across the cascade.

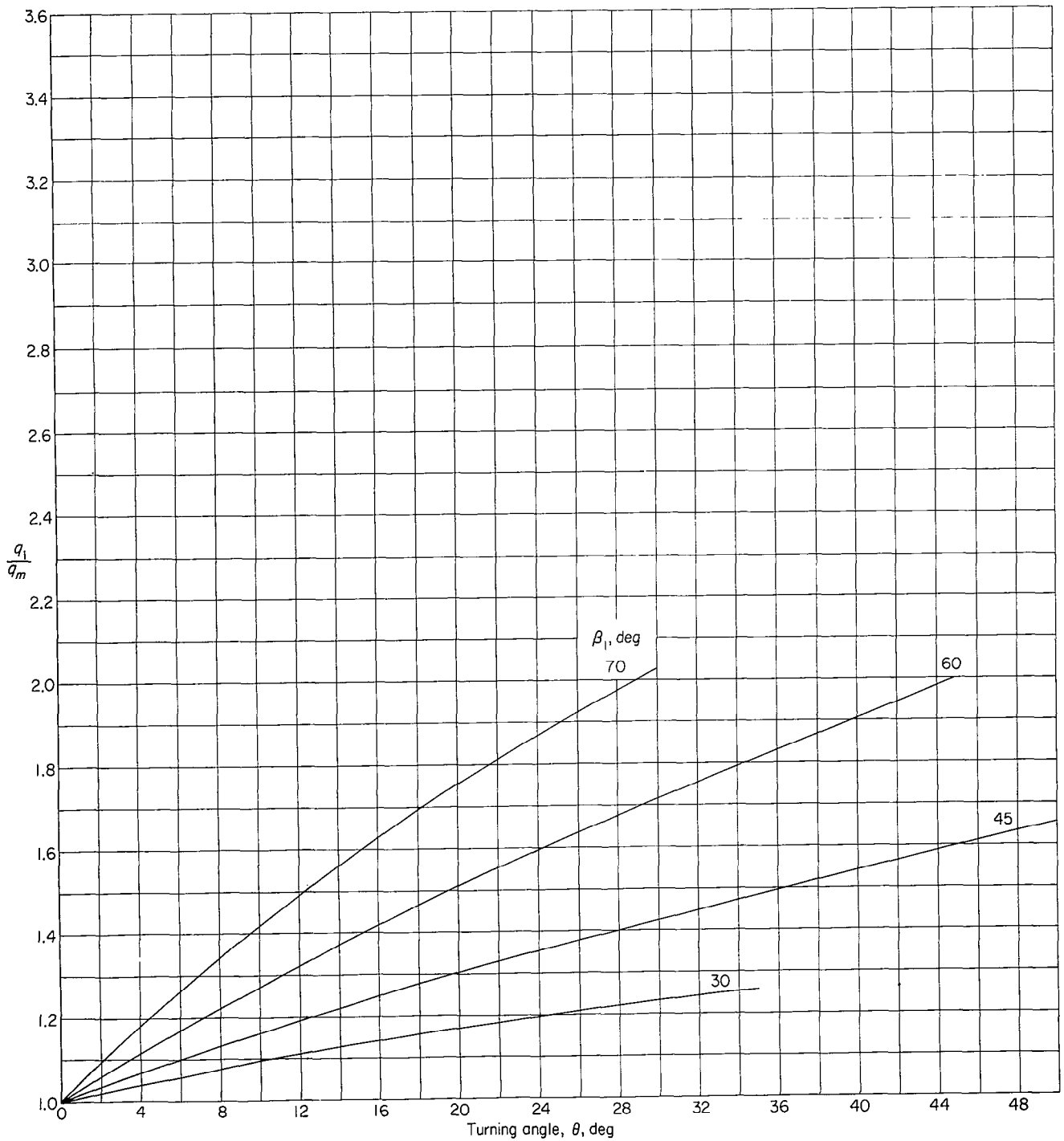

FIGURE 88.—Conversion chart showing the relation between entering and mean dynamic pressure as a function of turning angle and inlet angle.

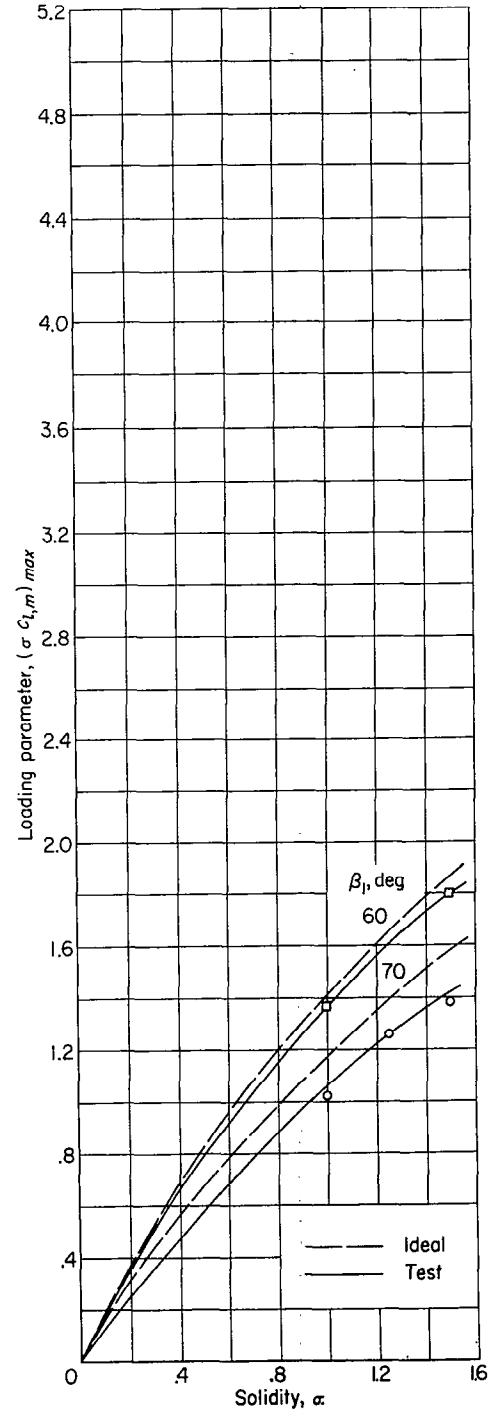

FIGURE 89.—Variation of the limit loading parameter, $(\sigma c_{l,m})_{max}$ with solidity for inlet angles of 60° and 70°.

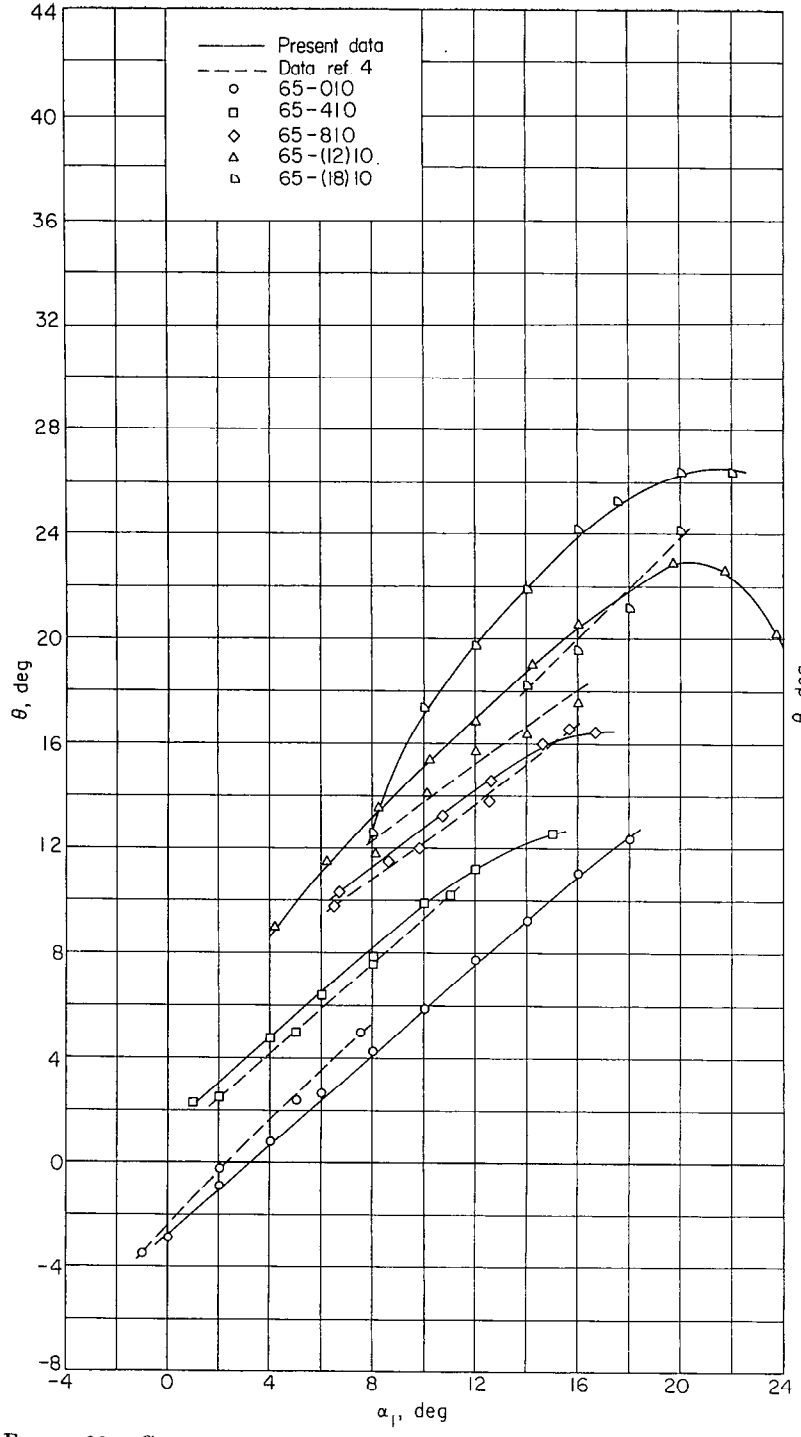

FIGURE 90.—Comparison of relationships between turning angle and angle of attack for the present porous-wall cascade results with those for the solid-wall cascade of reference 4 for a typical combination. $\beta_1=60°$; $\sigma=1.00$.

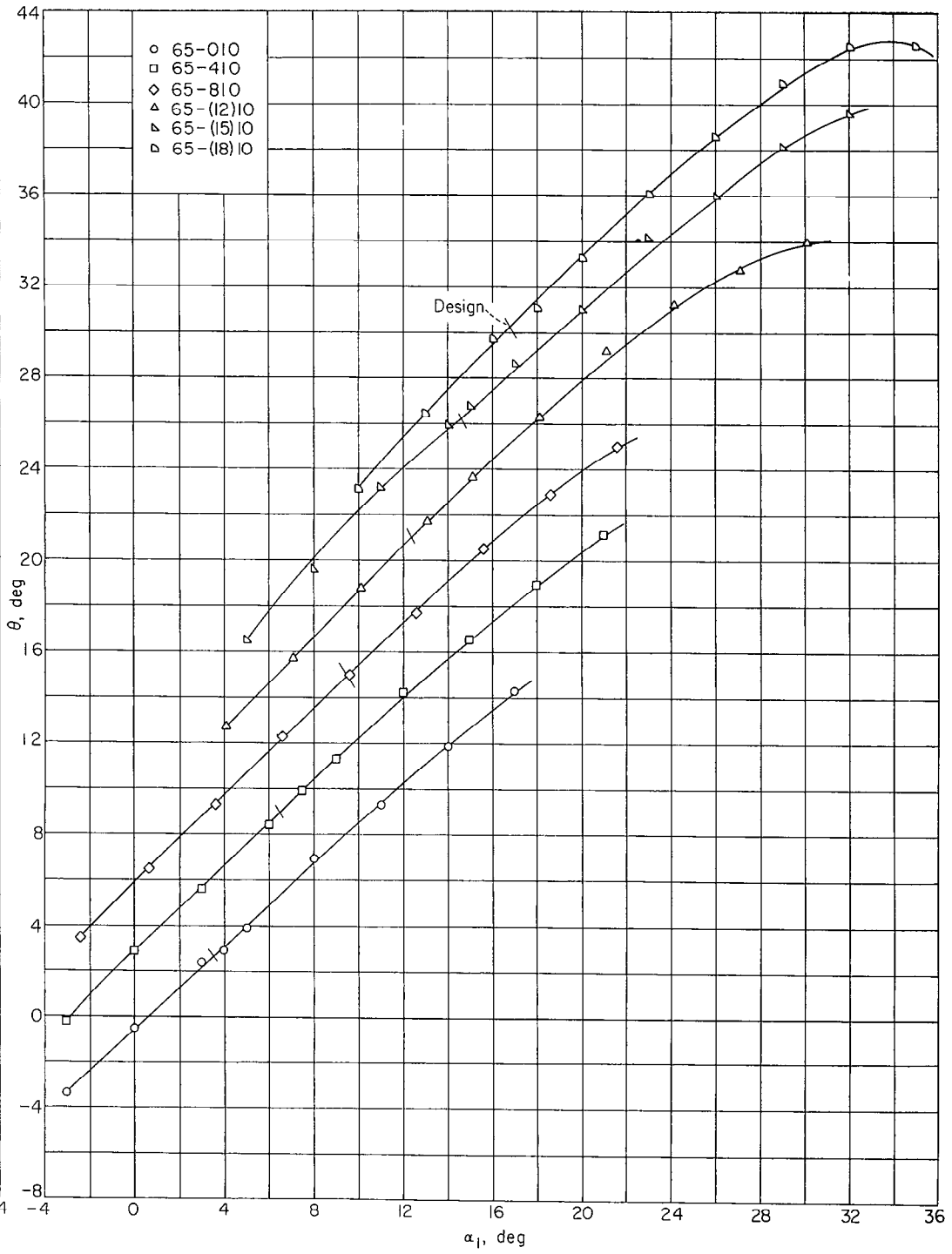

FIGURE 91.—Summary of relationship between turning angle θ and angle of attack α_1 for the blade sections tested at $\beta_1=30°$, $\sigma=1.00$.

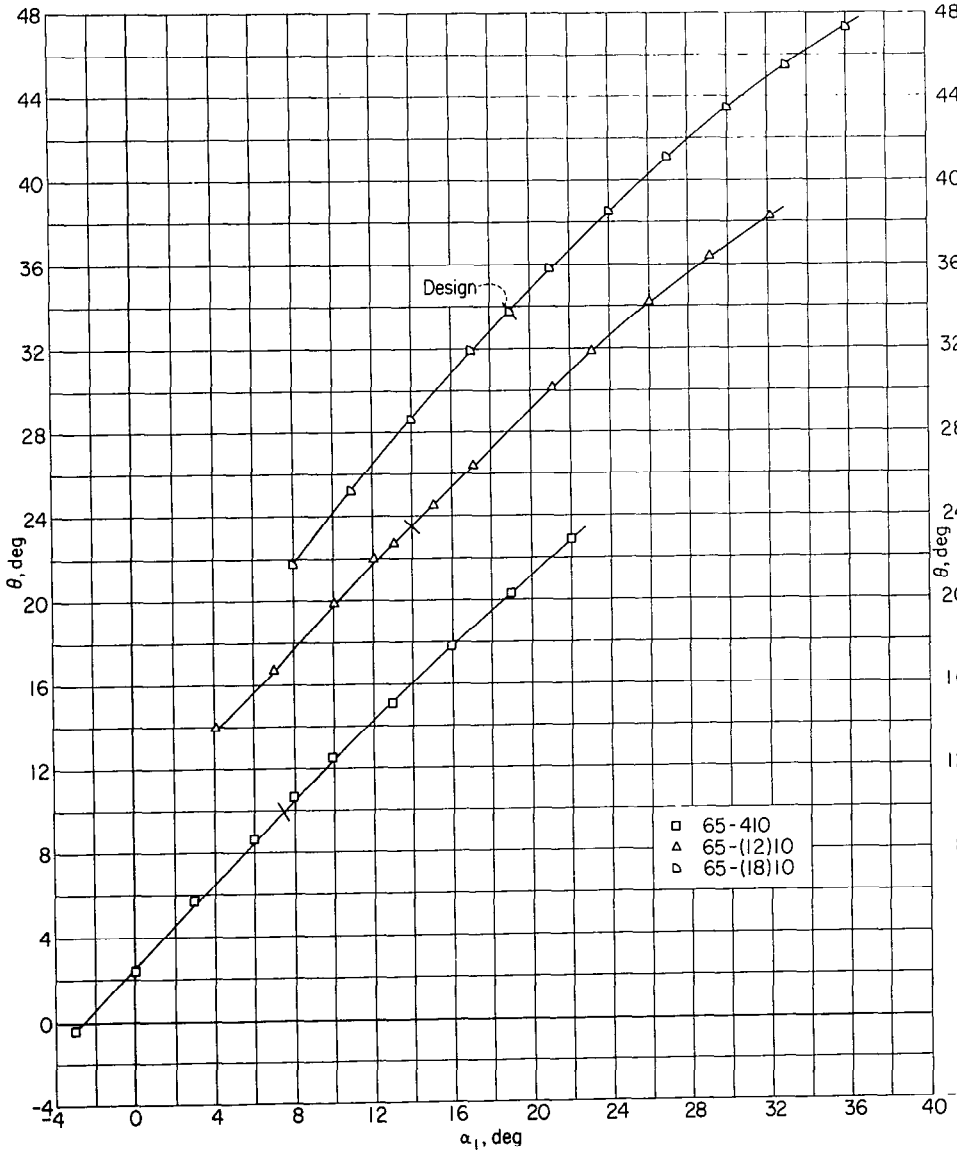

FIGURE 92.—Summary of relationship between turning angle θ and angle of attack α_1 for the blade sections tested at $\beta_1=30°$, $\sigma=1.25$.

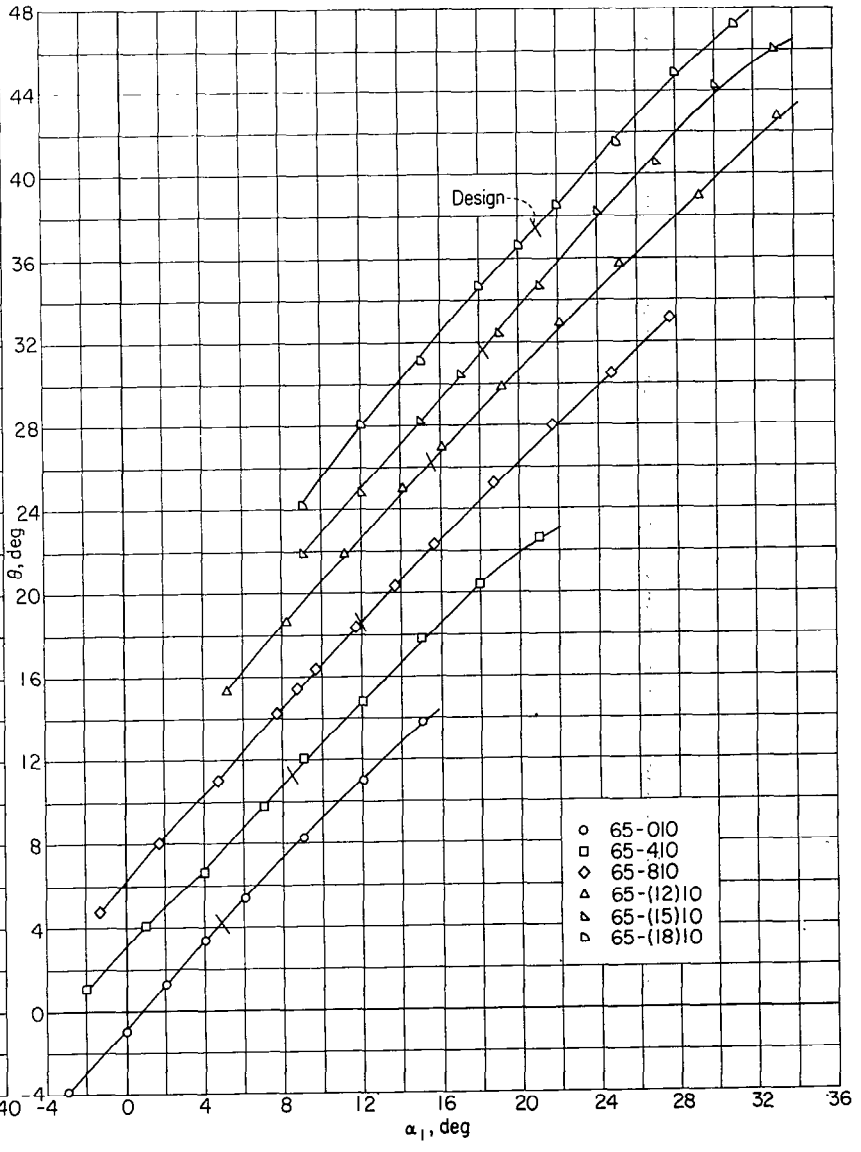

FIGURE 93.—Summary of relationship between turning angle θ and angle of attack α_1 for the blade sections tested at $\beta_1=30°$, $\sigma=1.50$.

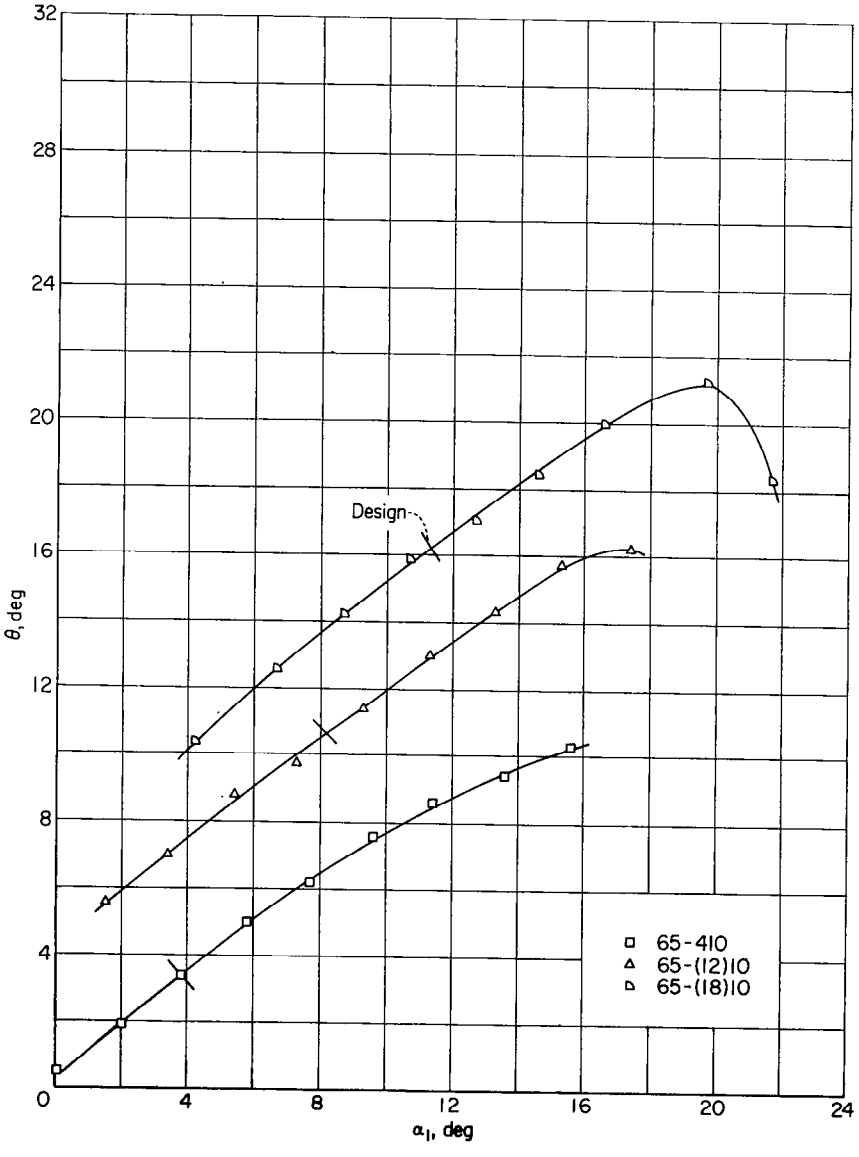

FIGURE 94.—Summary of relationship between turning angle θ and angle of attack α_1 for the blade sections tested at $\beta_1=45°$, $\sigma=0.50$.

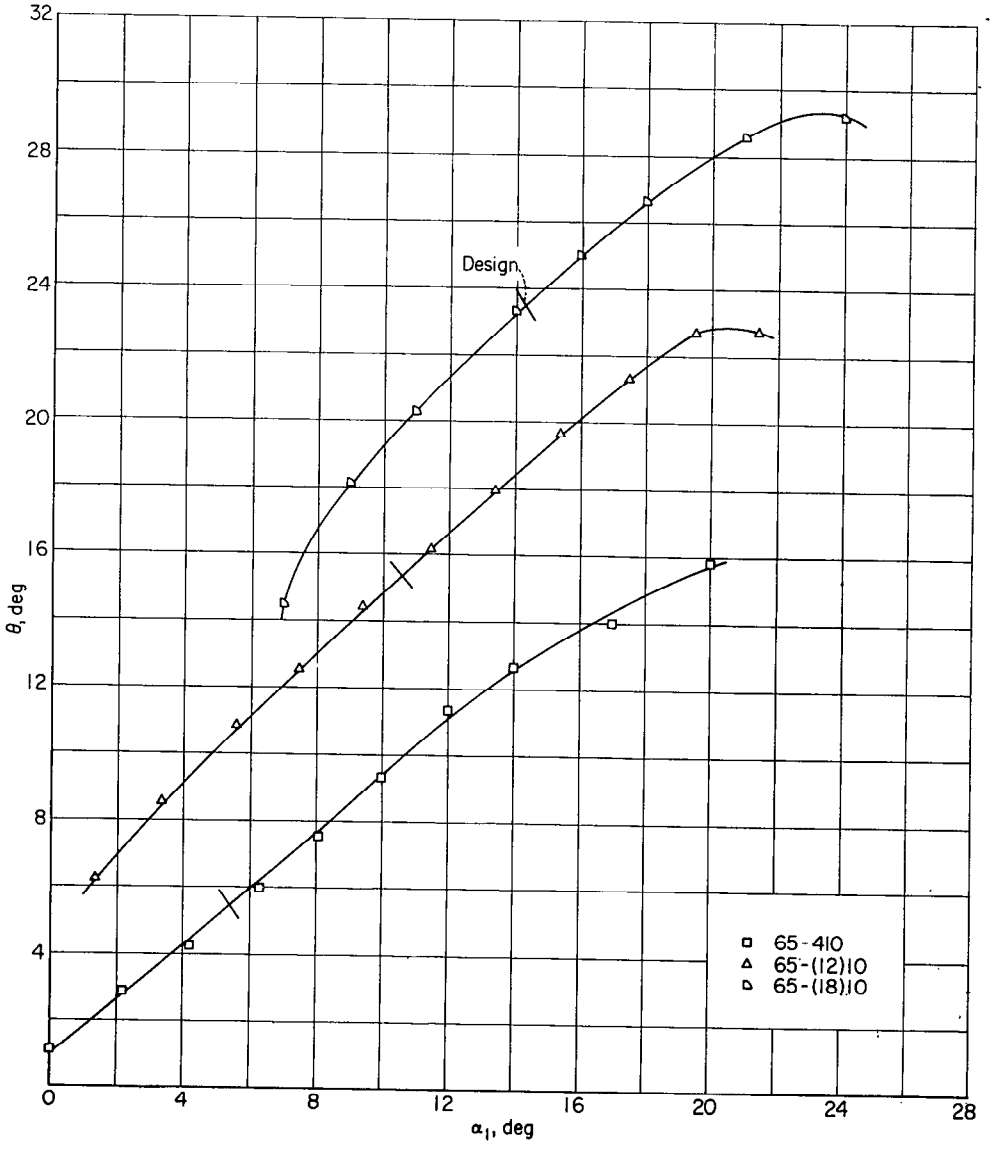

FIGURE 95.—Summary of relationship between turning angle θ and angle of attack α_1 for the blade sections tested at $\beta_1=45°$, $\sigma=0.75$.

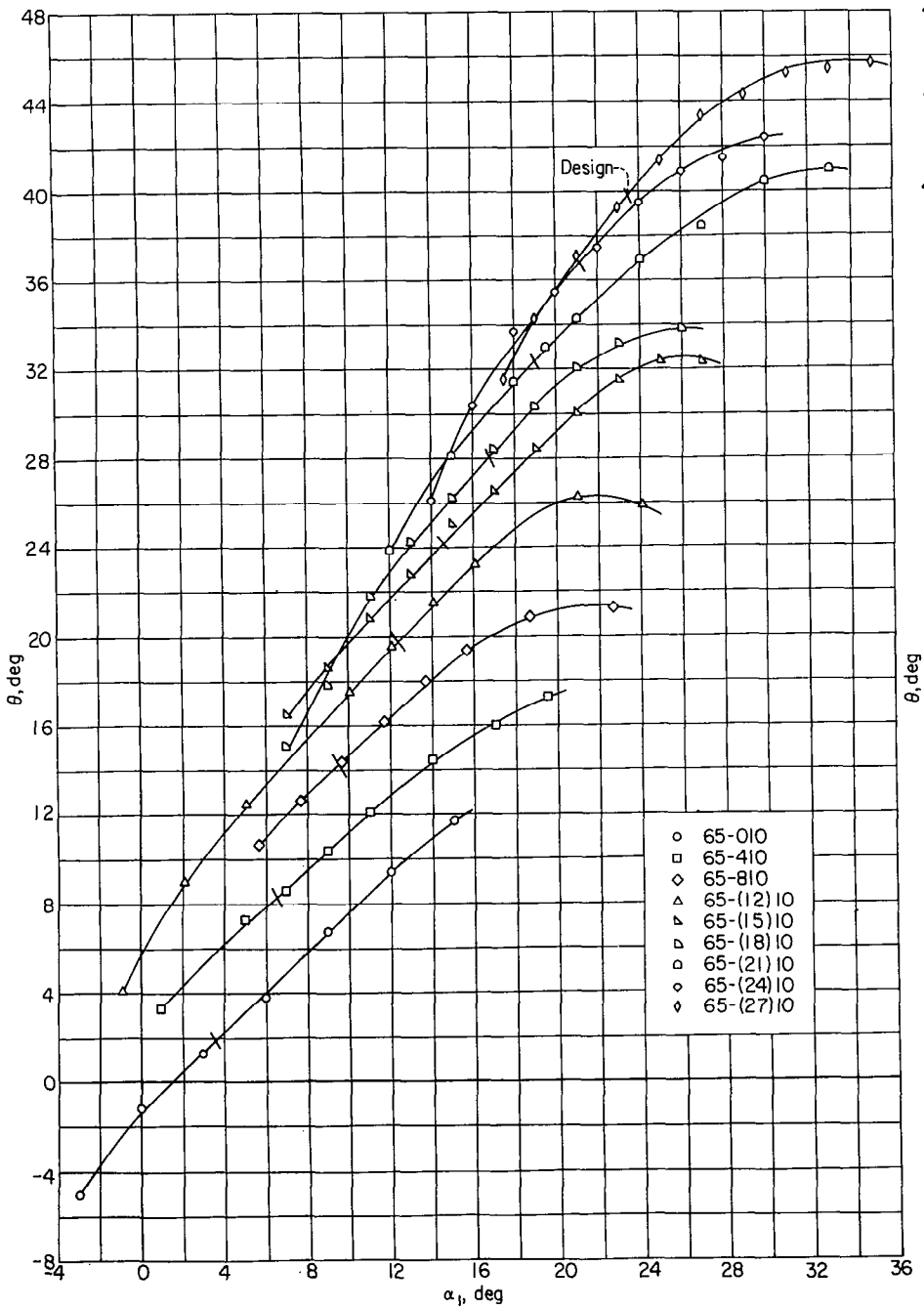

FIGURE 96.—Summary of relationship between turning angle θ and angle of attack α_1 for the blade sections tested at $\beta_1=45°$, $\sigma=1.00$.

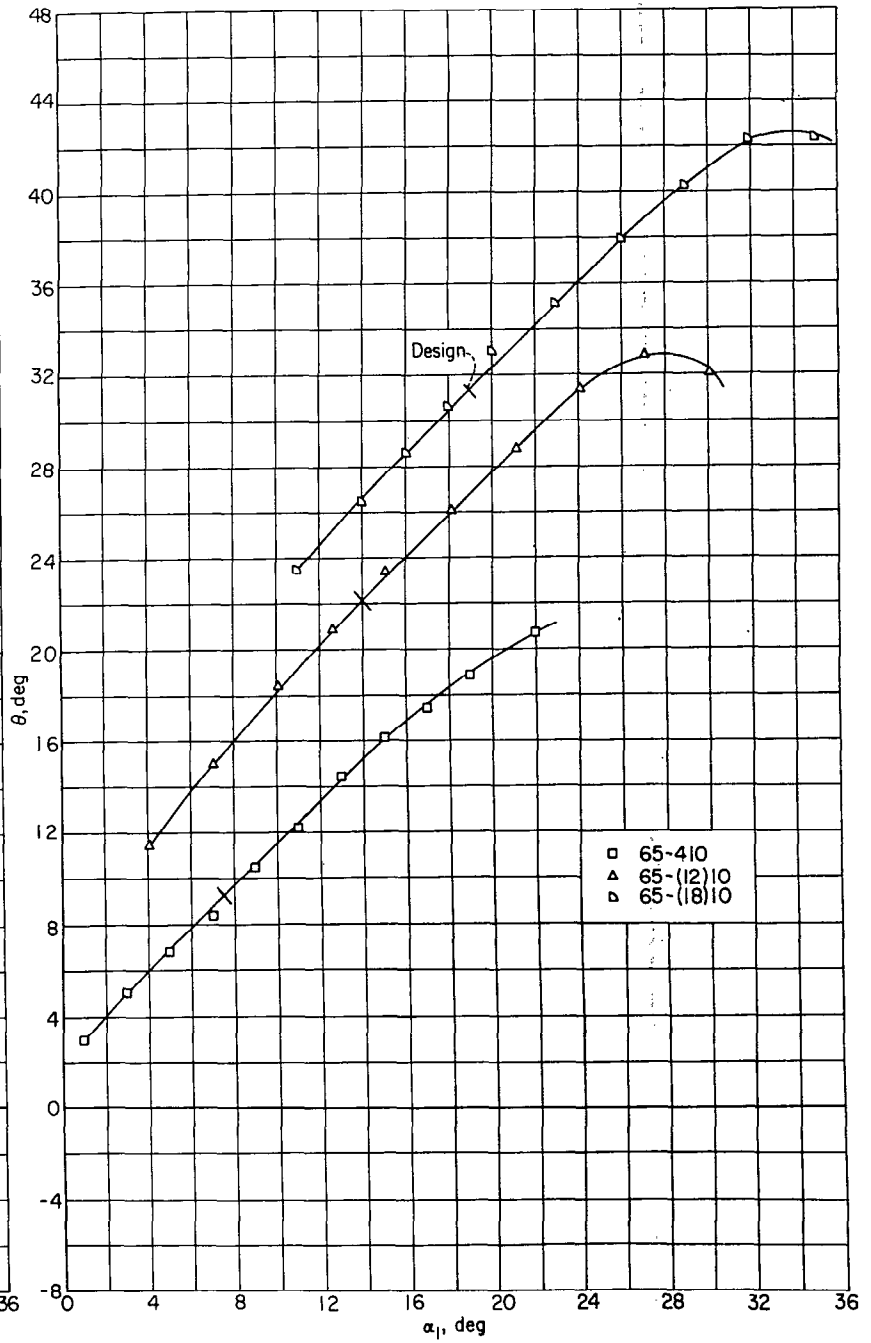

FIGURE 97.—Summary of relationship between turning angle θ and angle of attack α_1 for the blade sections tested at $\beta_1=45°$, $\sigma=1.25$.

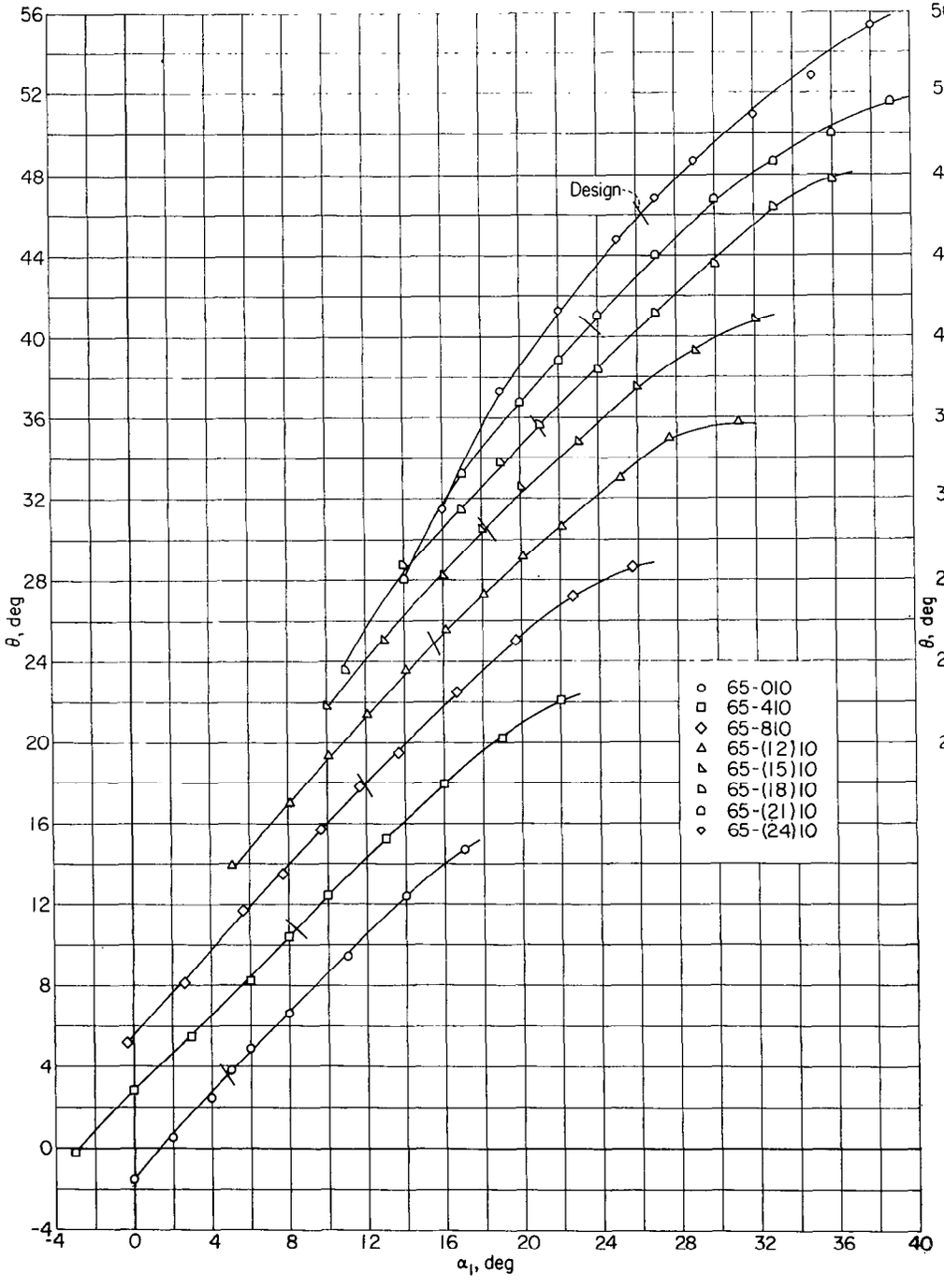

FIGURE 98.—Summary of relationship between turning angle θ and angle of attack α_1 for the blade sections tested at $\beta_1=45°$, $\sigma=1.50$.

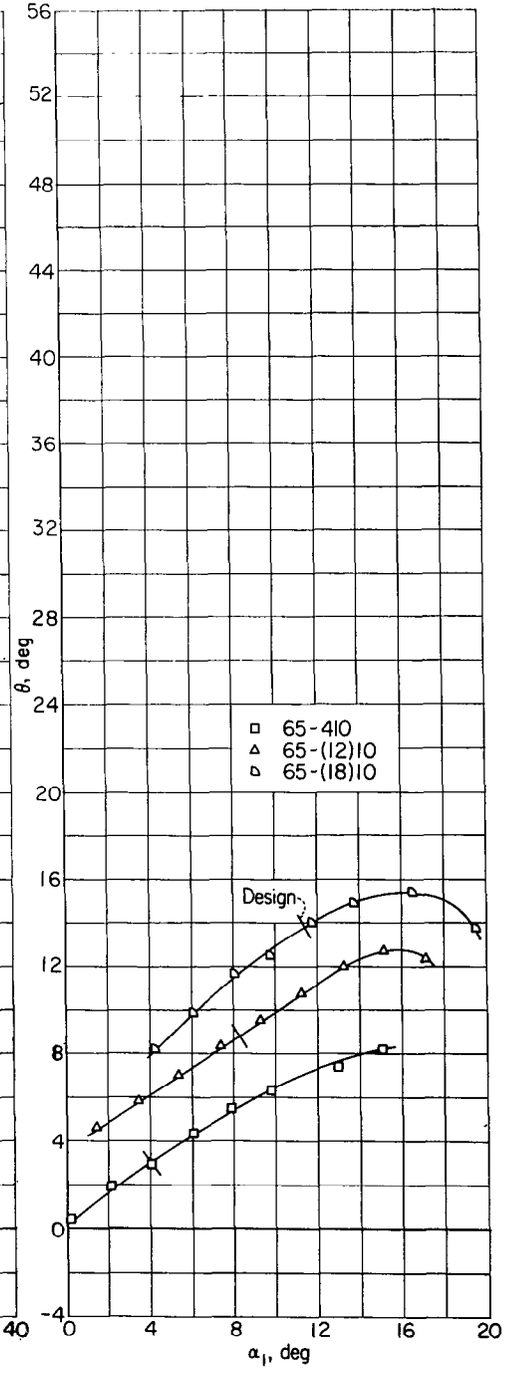

FIGURE 99.—Summary of relationship between turning angle θ and angle of attack α_1 for the blade sections tested at $\beta_1=60°$, $\sigma=0.50$.

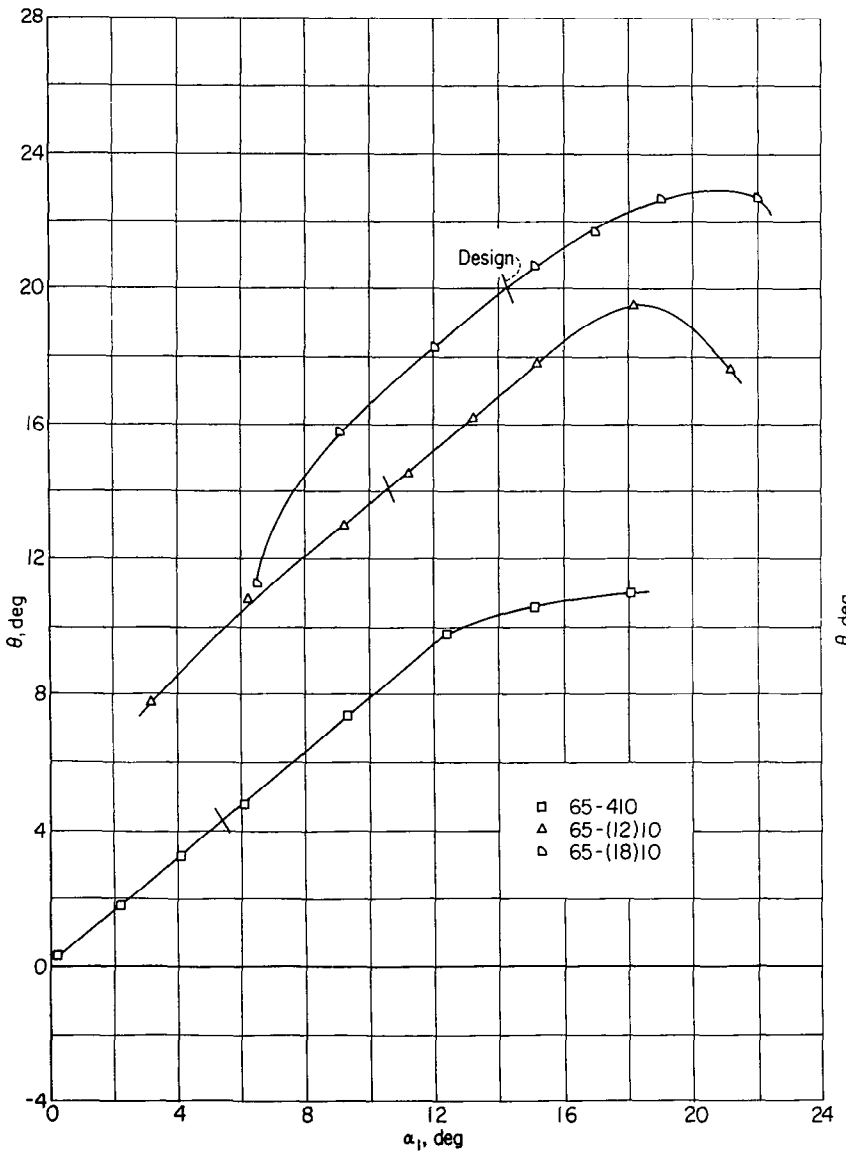

FIGURE 100.—Summary of relationship between turning angle θ and angle of attack α_1 for the blade sections tested at $\beta_1=60°$, $\sigma=0.75$.

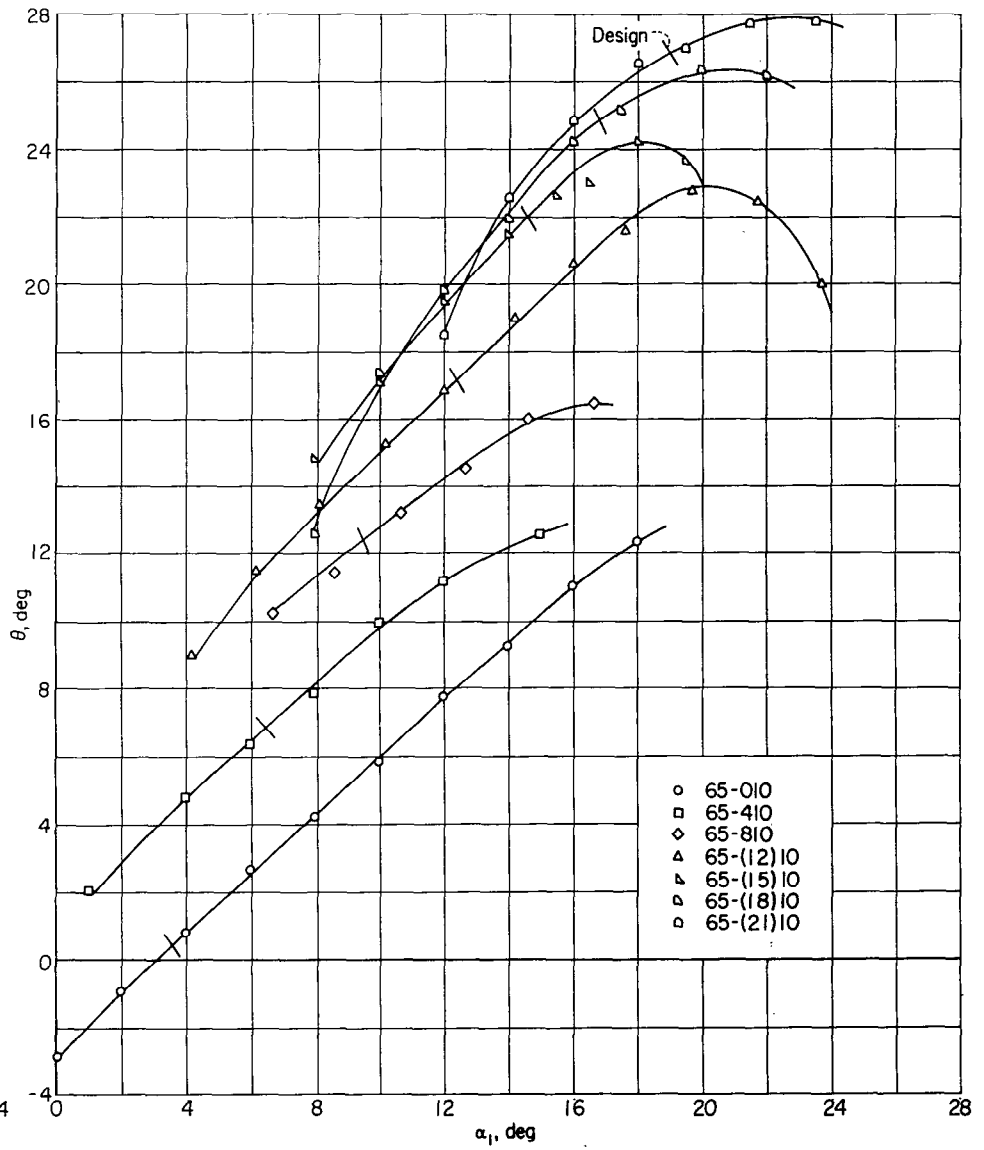

FIGURE 101.—Summary of relationship between turning angle θ and angle of attack α_1 for the blade sections tested at $\beta_1=60°$, $\sigma=1.00$.

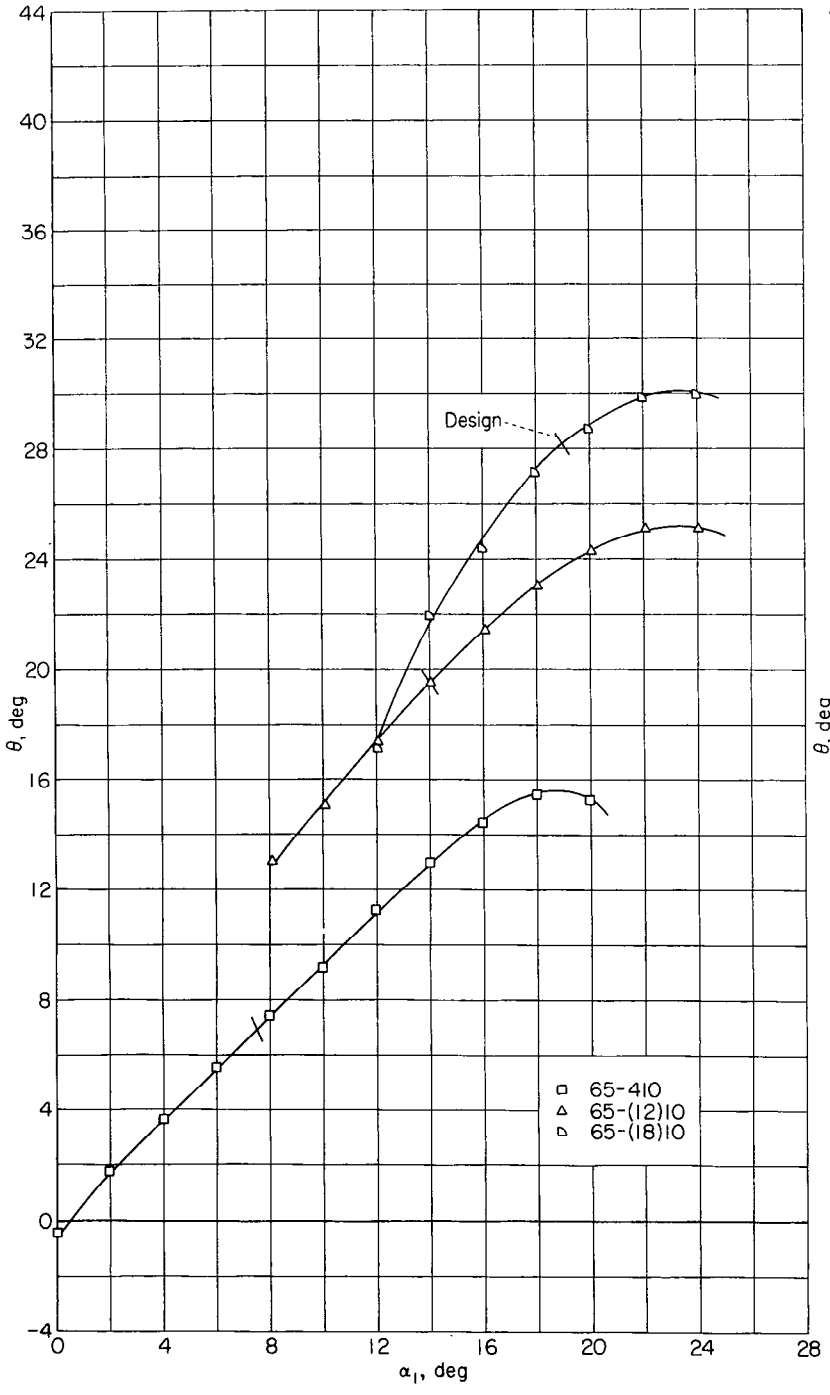

FIGURE 102.—Summary of relationship between turning angle θ and angle of attack α_1 for the blade sections tested at $\beta_1=60°$, $\sigma=1.25$.

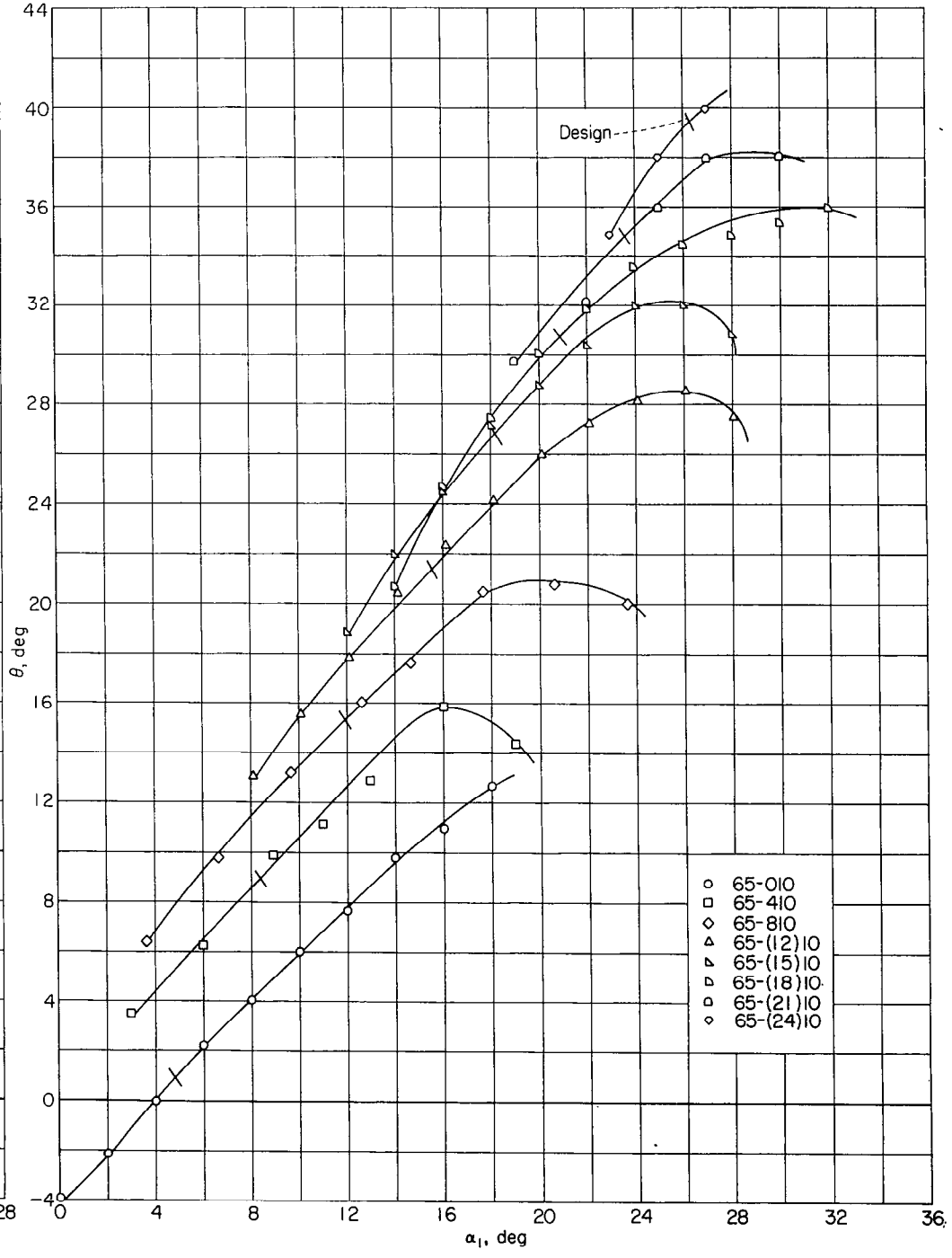

FIGURE 103.—Summary of relationship between turning angle θ and angle of attack α_1 for the blade sections tested at $\beta_1=60°$, $\sigma=1.50$.

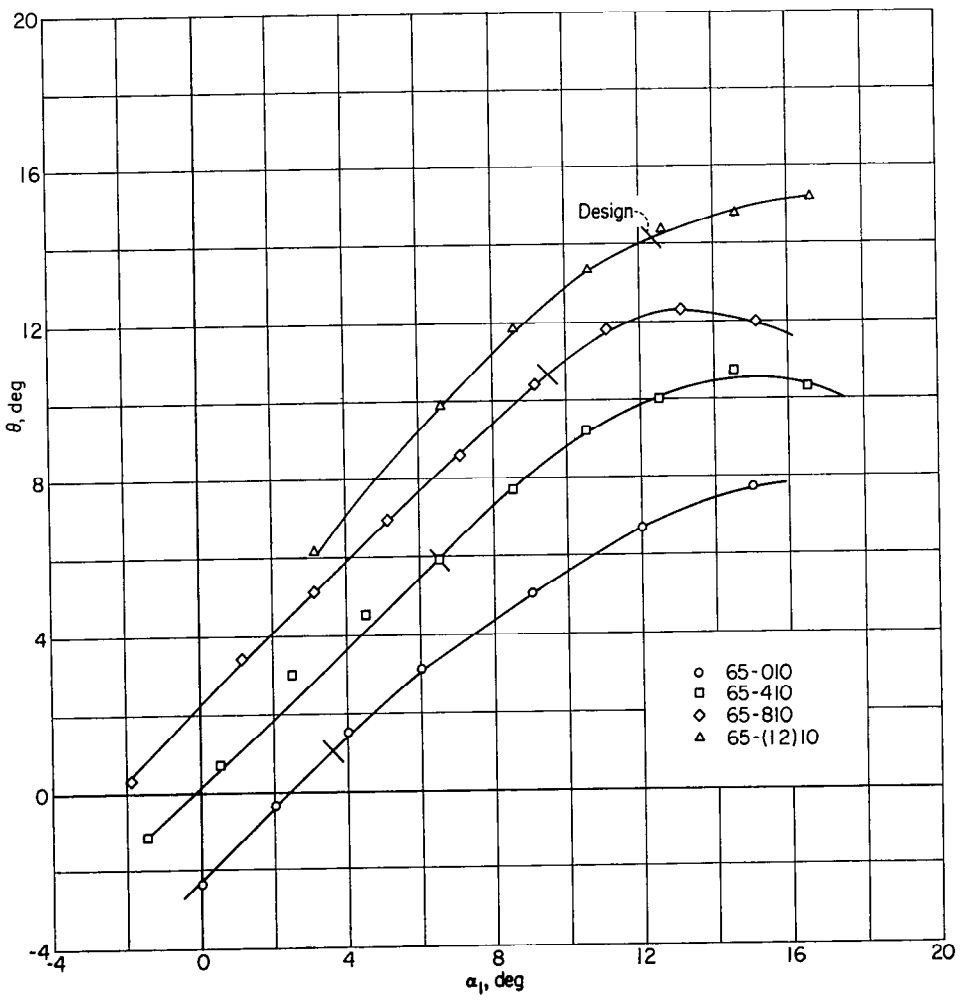

FIGURE 104.—Summary of relationship between turning angle θ and angle of attack α_1 for the blade sections tested at $\beta_1=70°$, $\sigma=1.00$.

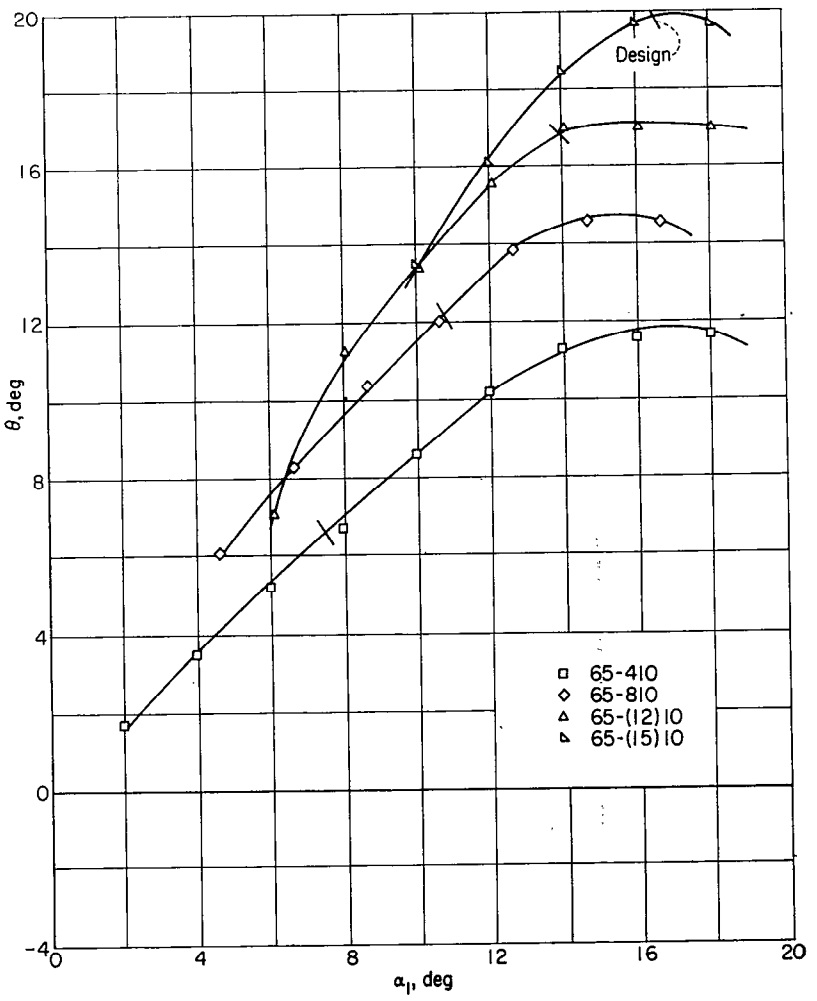

FIGURE 105.—Summary of relationship between turning angle θ and angle of attack α_1 for the blade sections tested at $\beta_1=70°$, $\sigma=1.25$.

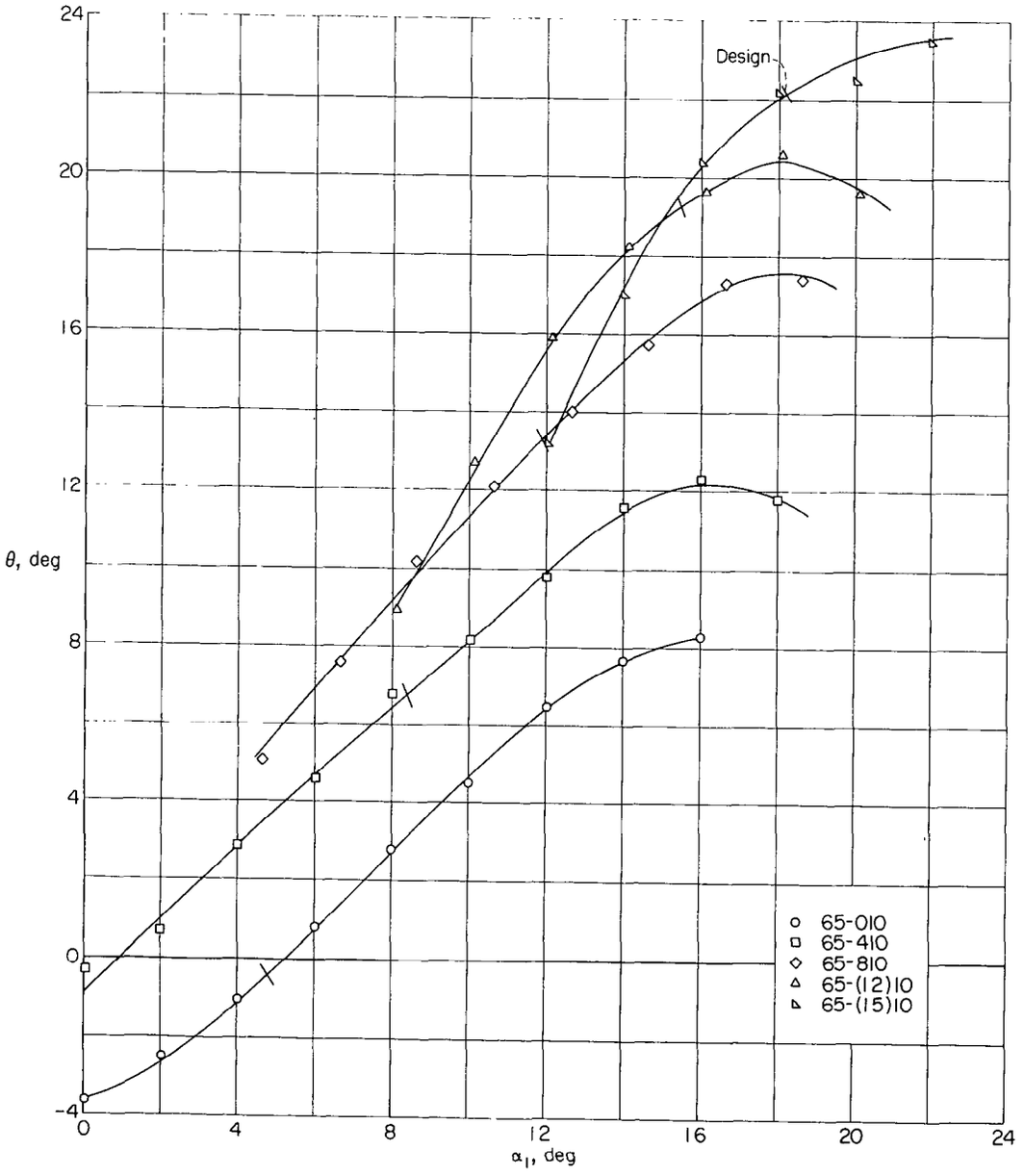

FIGURE 106.—Summary of relationship between turning angle θ and angle of attack α_1 for the blade sections tested at $\beta_1=70°$, $\sigma=1.50$.

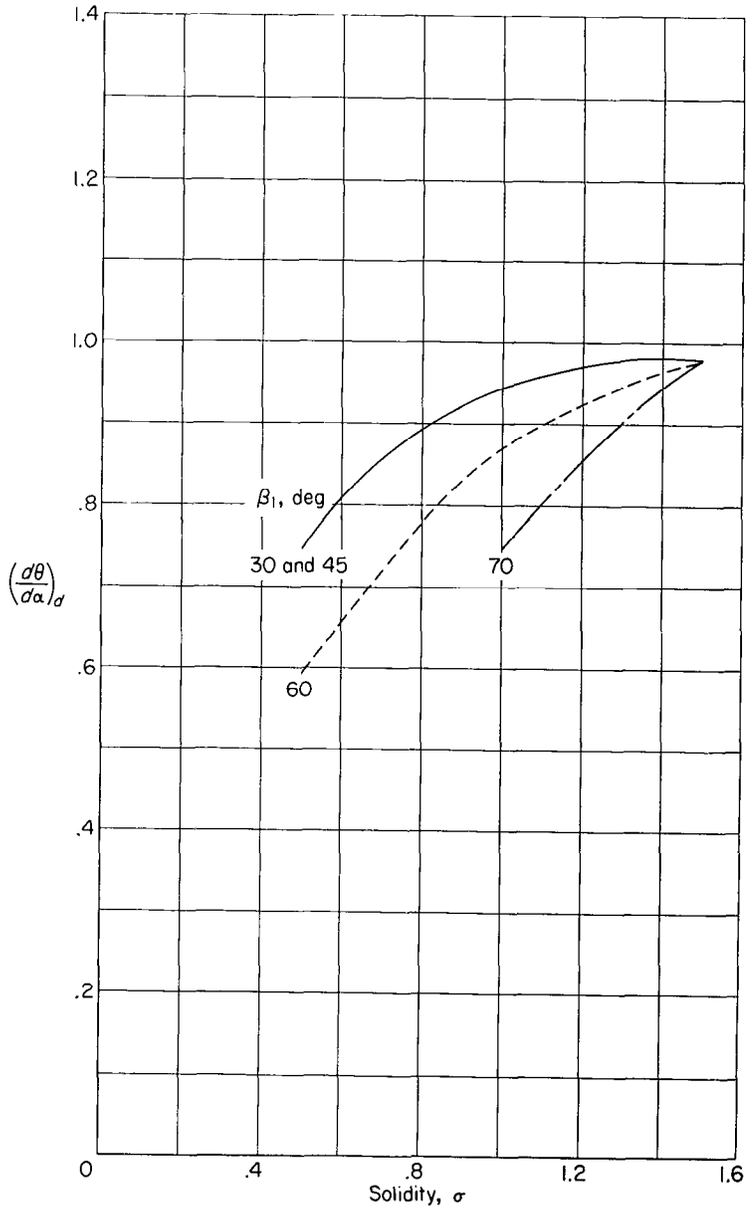

FIGURE 107.—Variation of slope of curves of turning angle against angle of attack at design conditions with solidity and inlet angle. The slopes are averages for the moderate camber range.

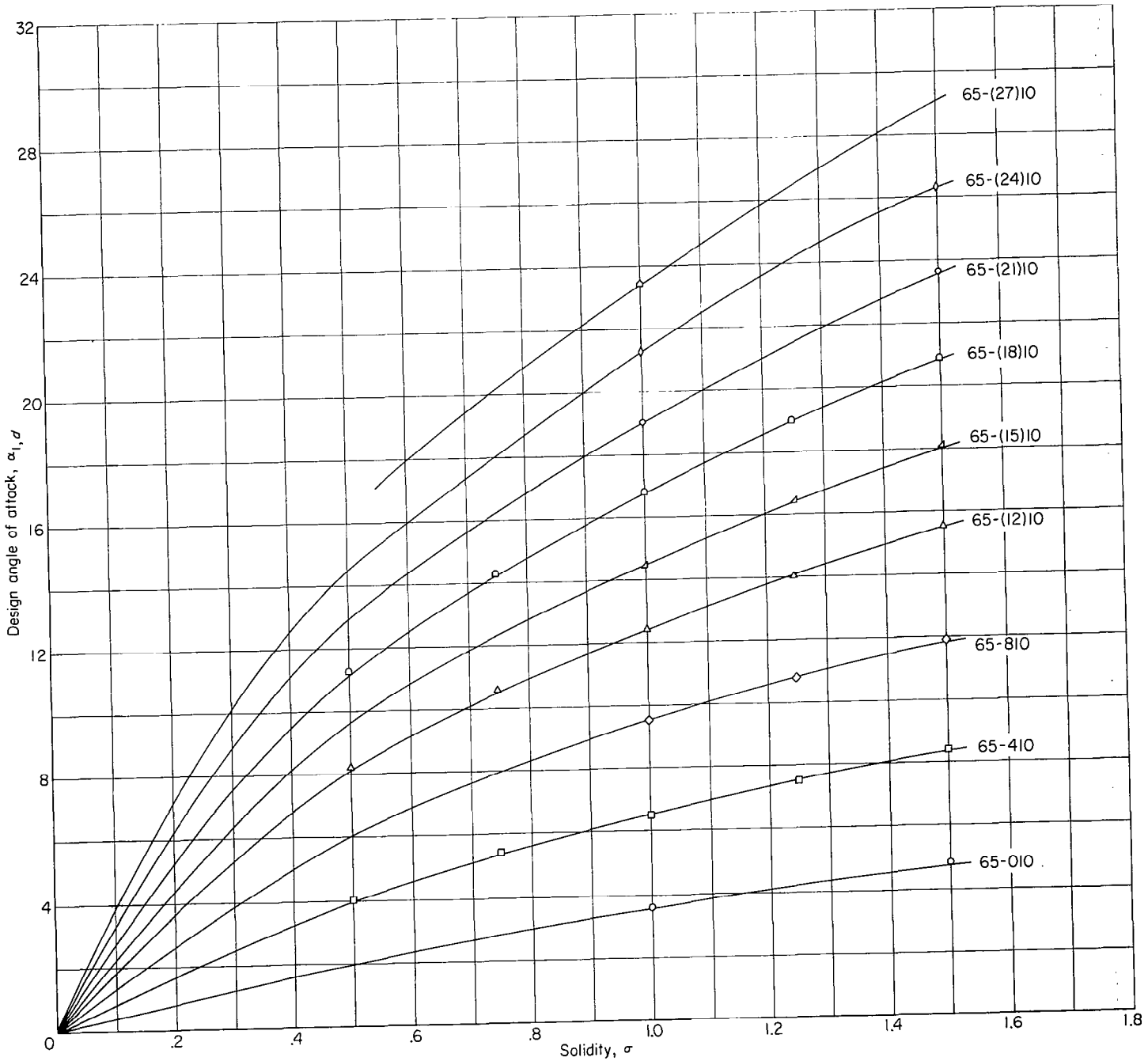

FIGURE 108.—Variation of design angle of attack with solidity for the sections tested.

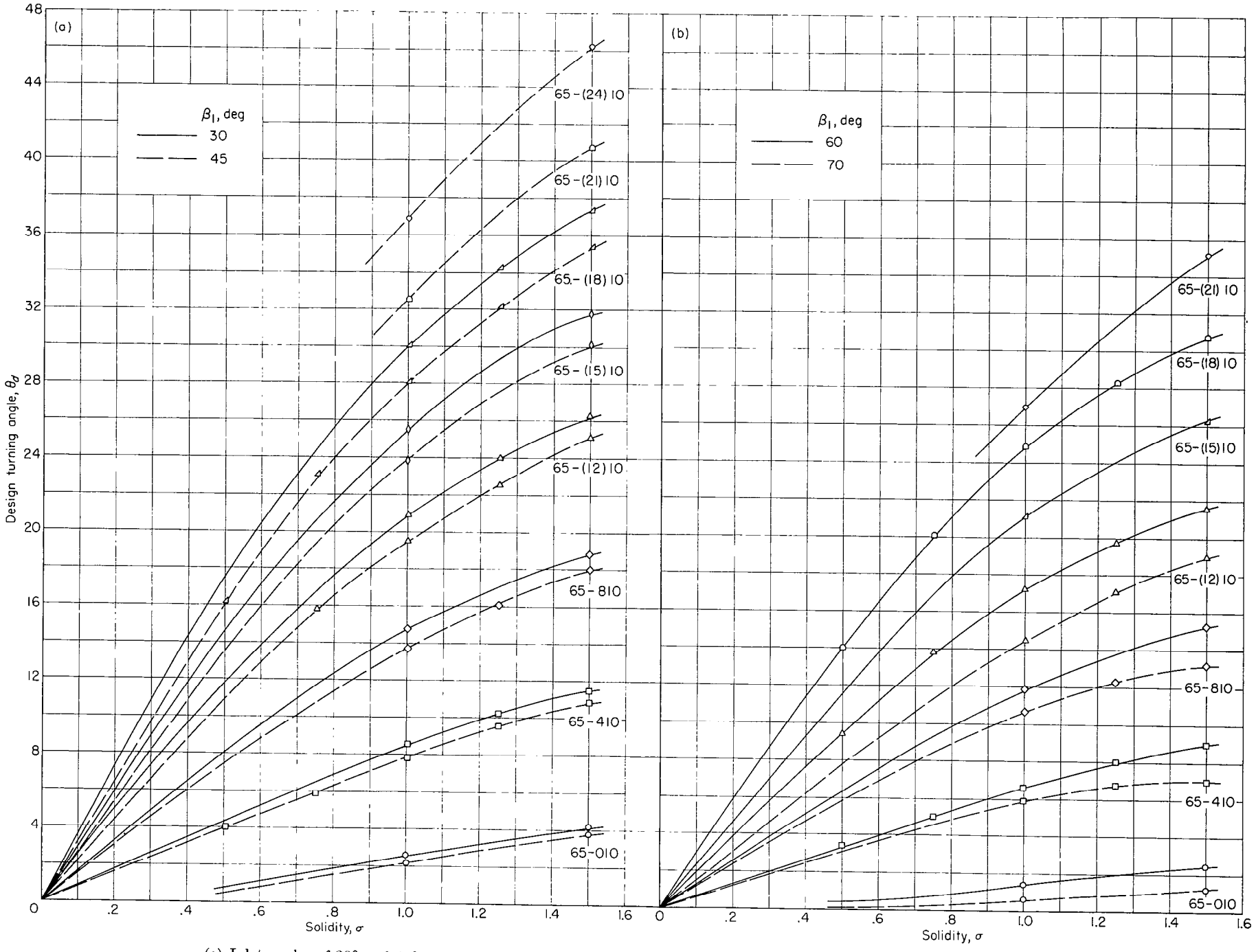

(a) Inlet angles of 30° and 45°.

(b) Inlet angles of 60° and 70°.

FIGURE 109.—Variation of design turning angle with solidity and inlet angle for the sections tested.

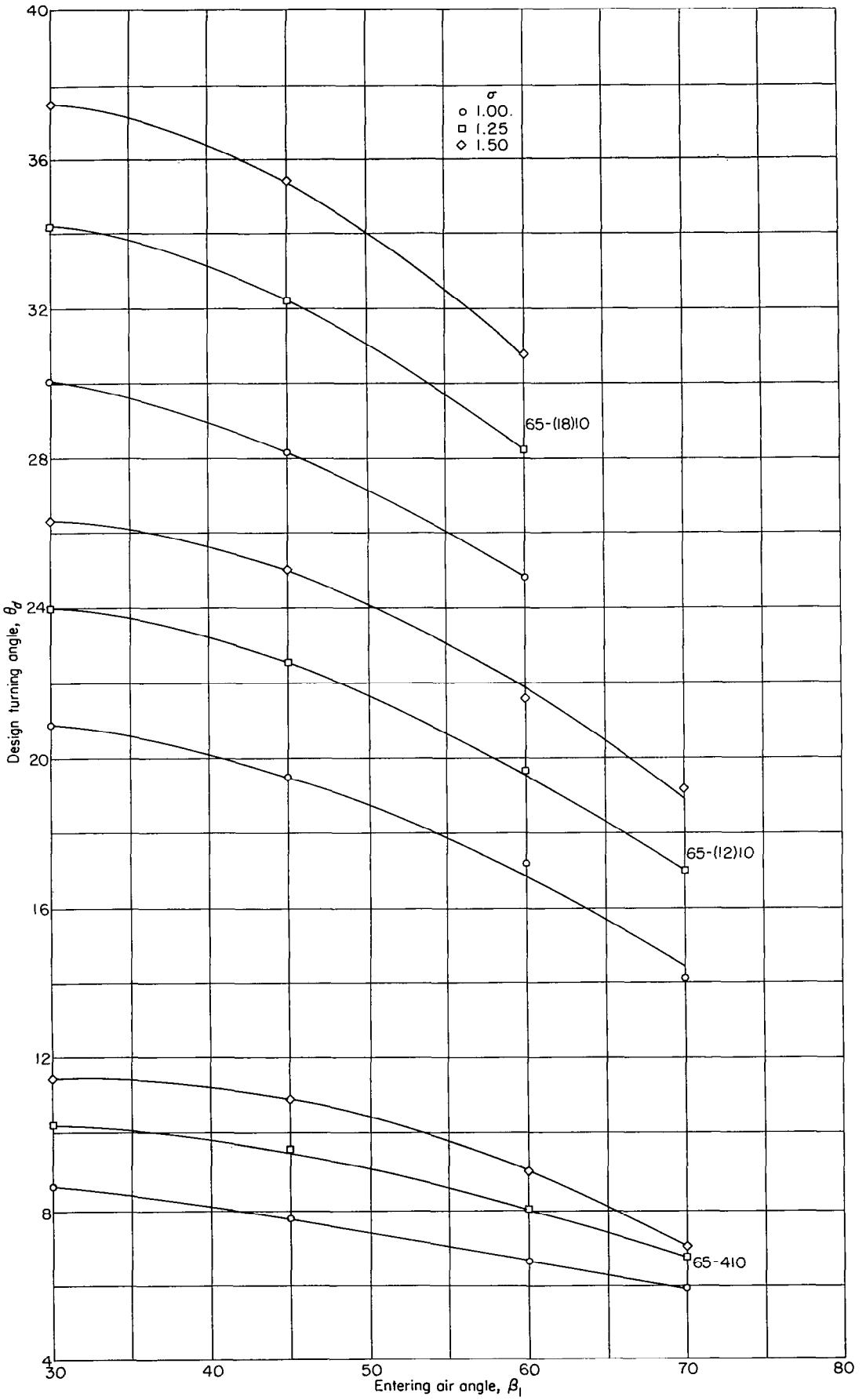

FIGURE 110.—Variation of design turning angle with inlet angle and solidity for typical sections.

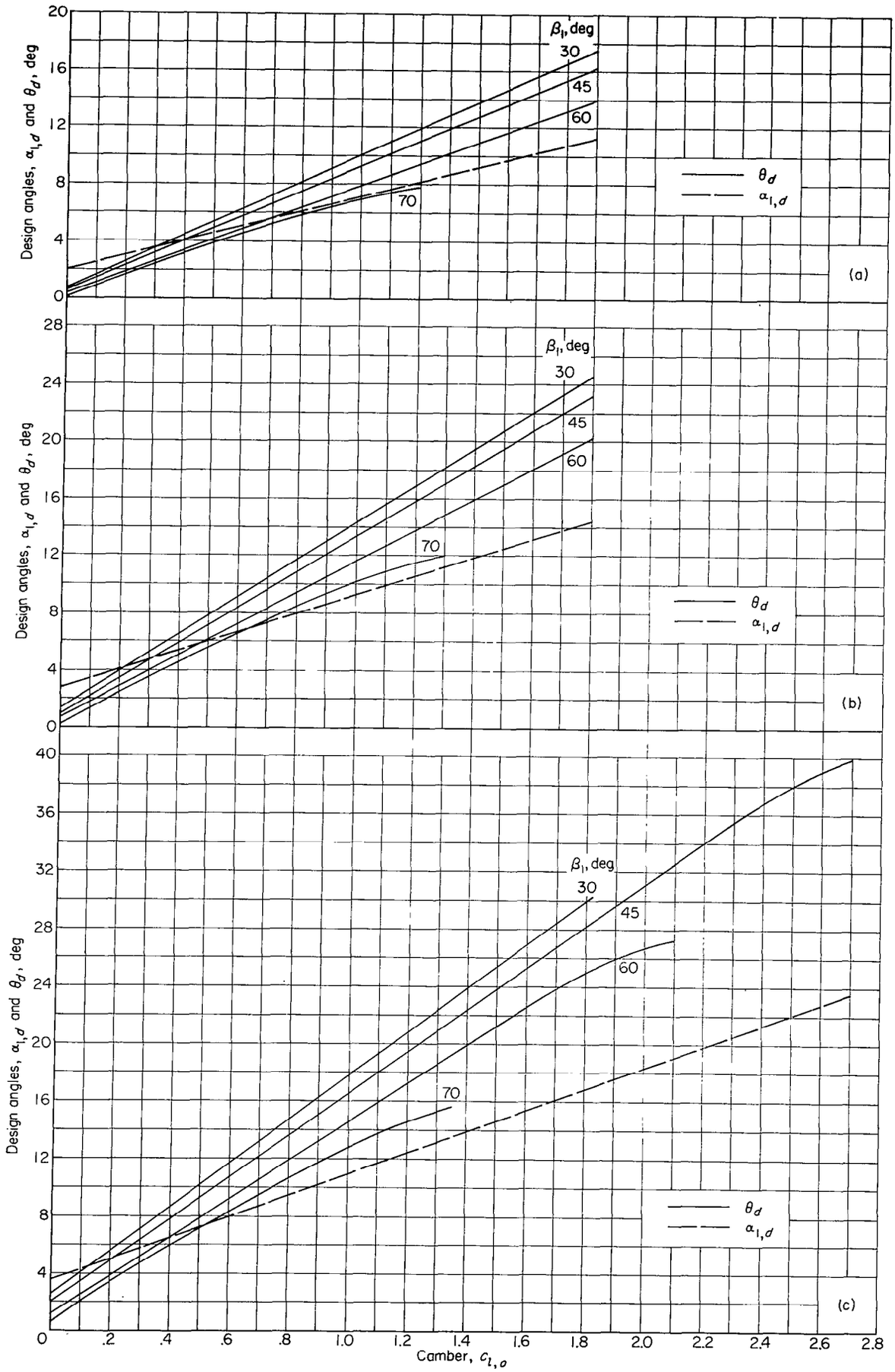

(a) $\sigma=0.50$. (b) $\sigma=0.75$. (c) $\sigma=1.00$.

FIGURE 111.—Variation of design turning angle and design angle of attack with camber and inlet angle.

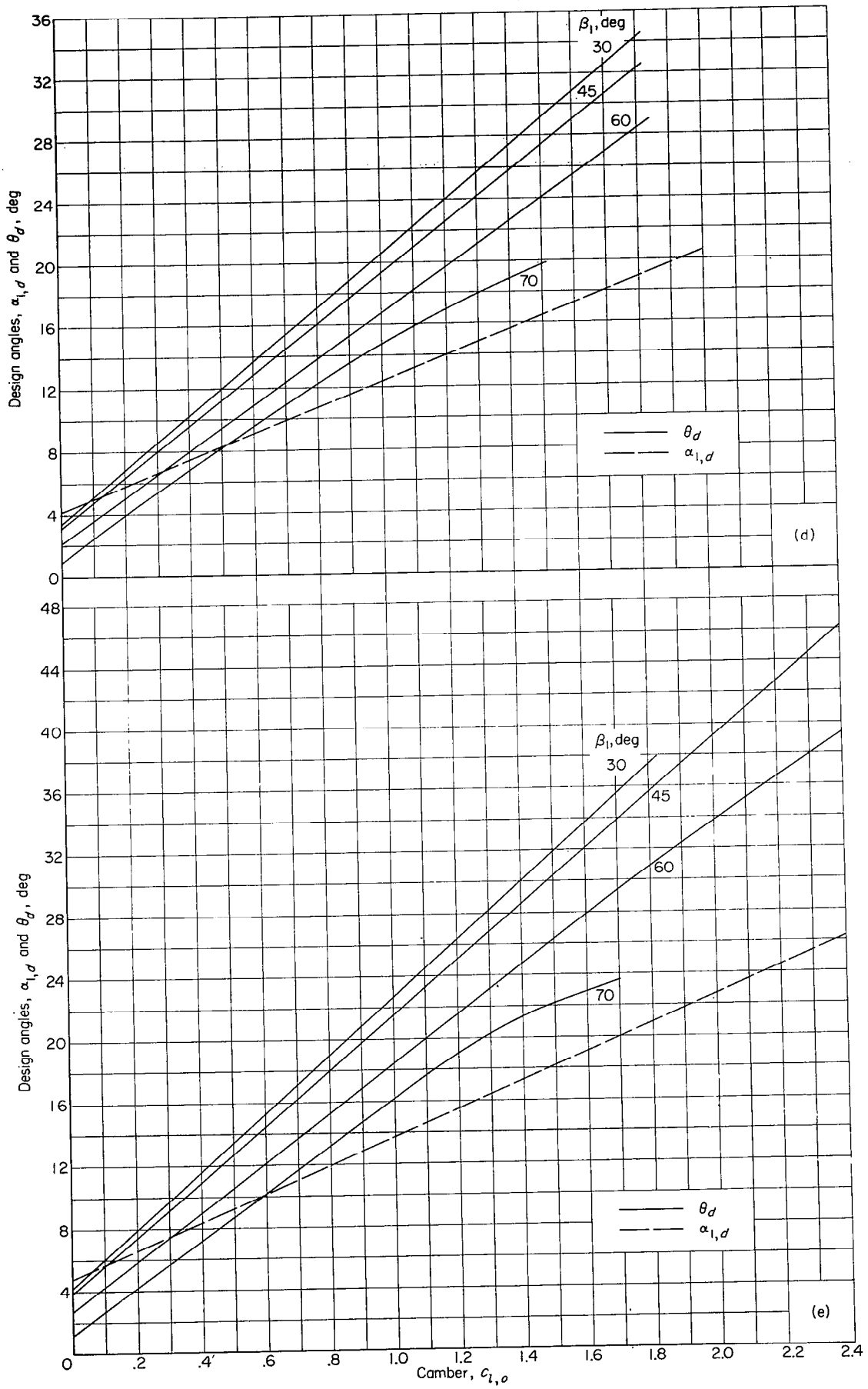

(d) $\sigma=1.25$.

(e) $\sigma=1.50$.

FIGURE 111.—Concluded.

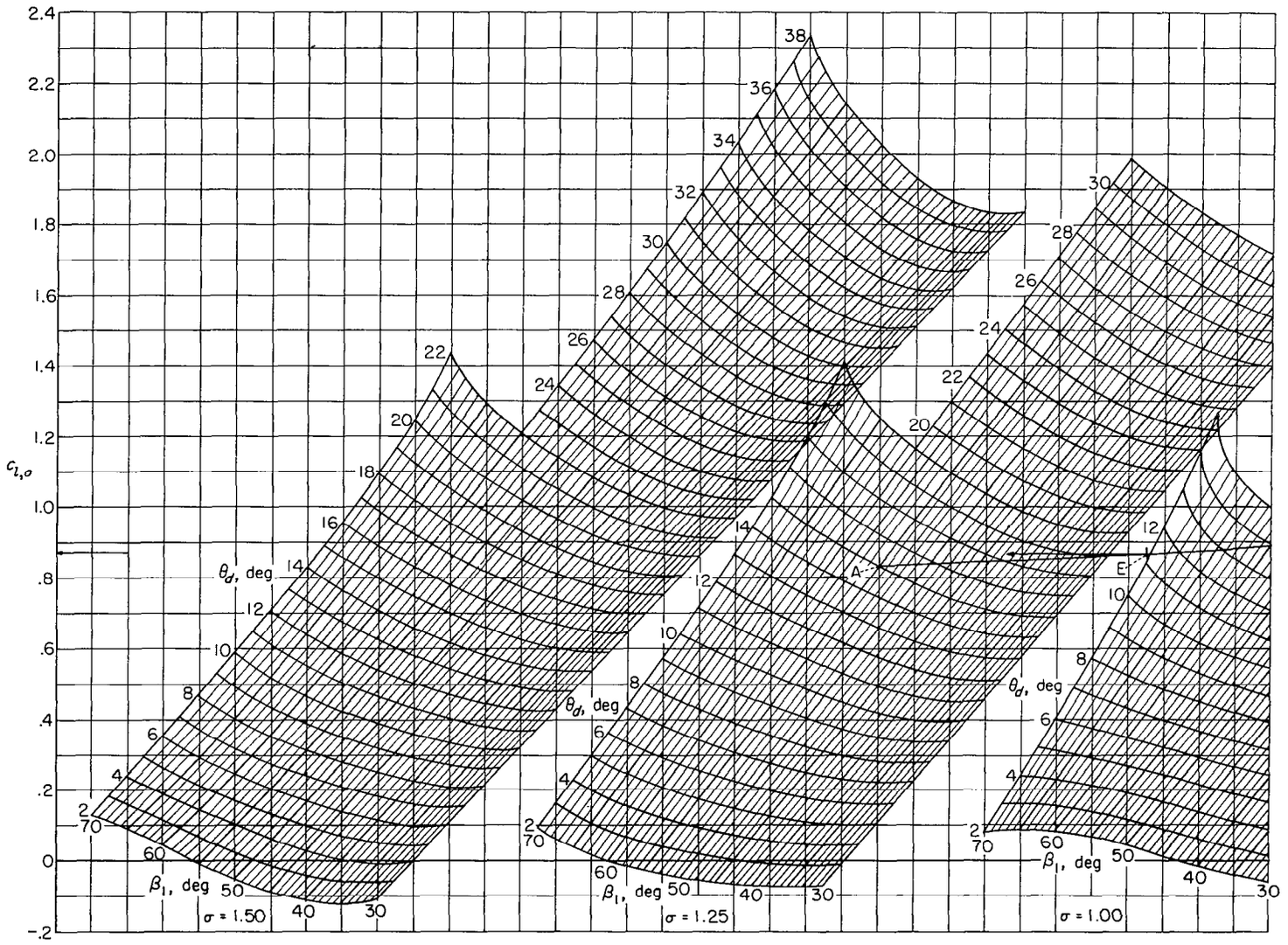

FIGURE 112.—Design-camber selection chart for NACA 65-($c_{l,o}$)10 sections.

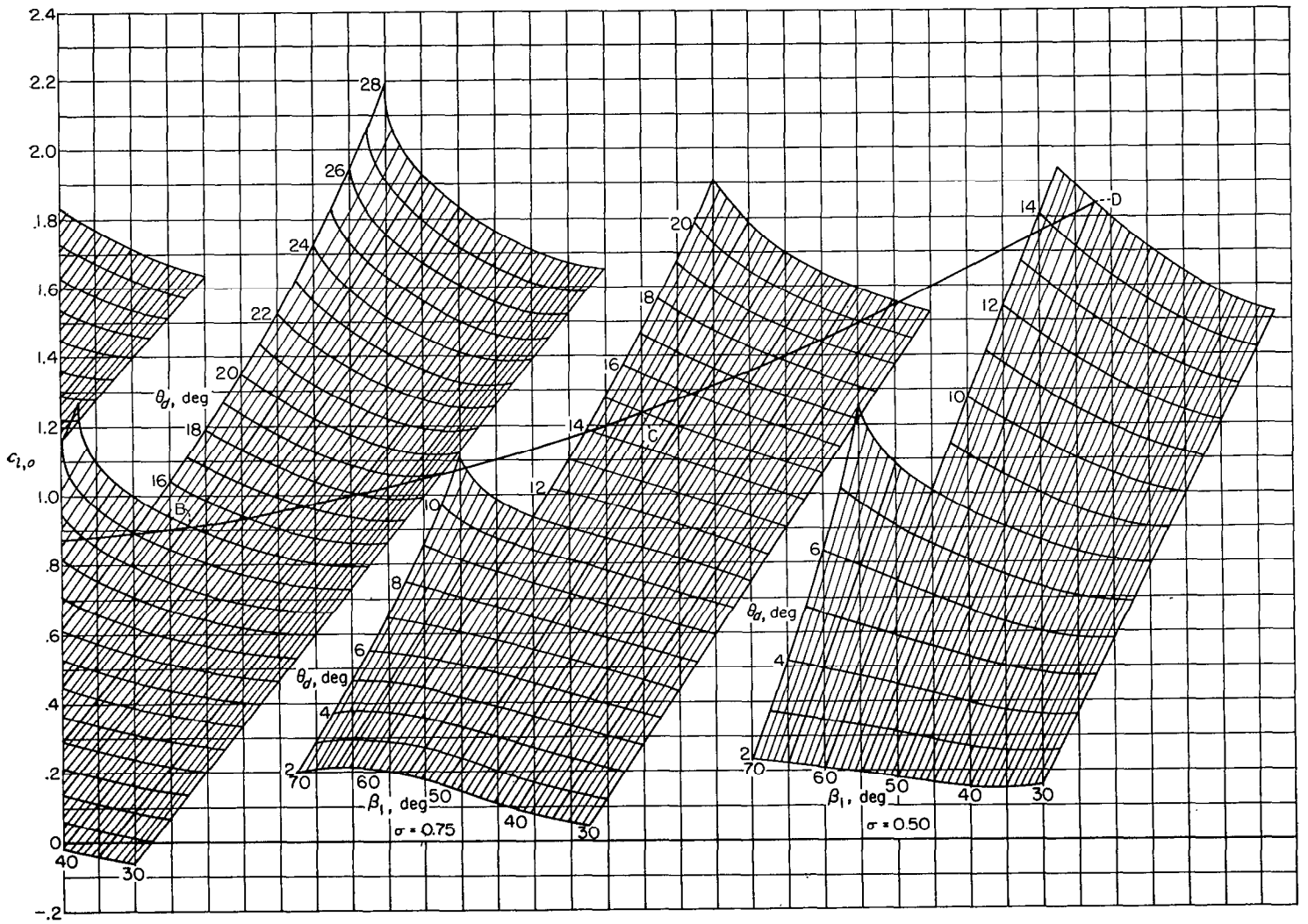

FIGURE 112.—Concluded.

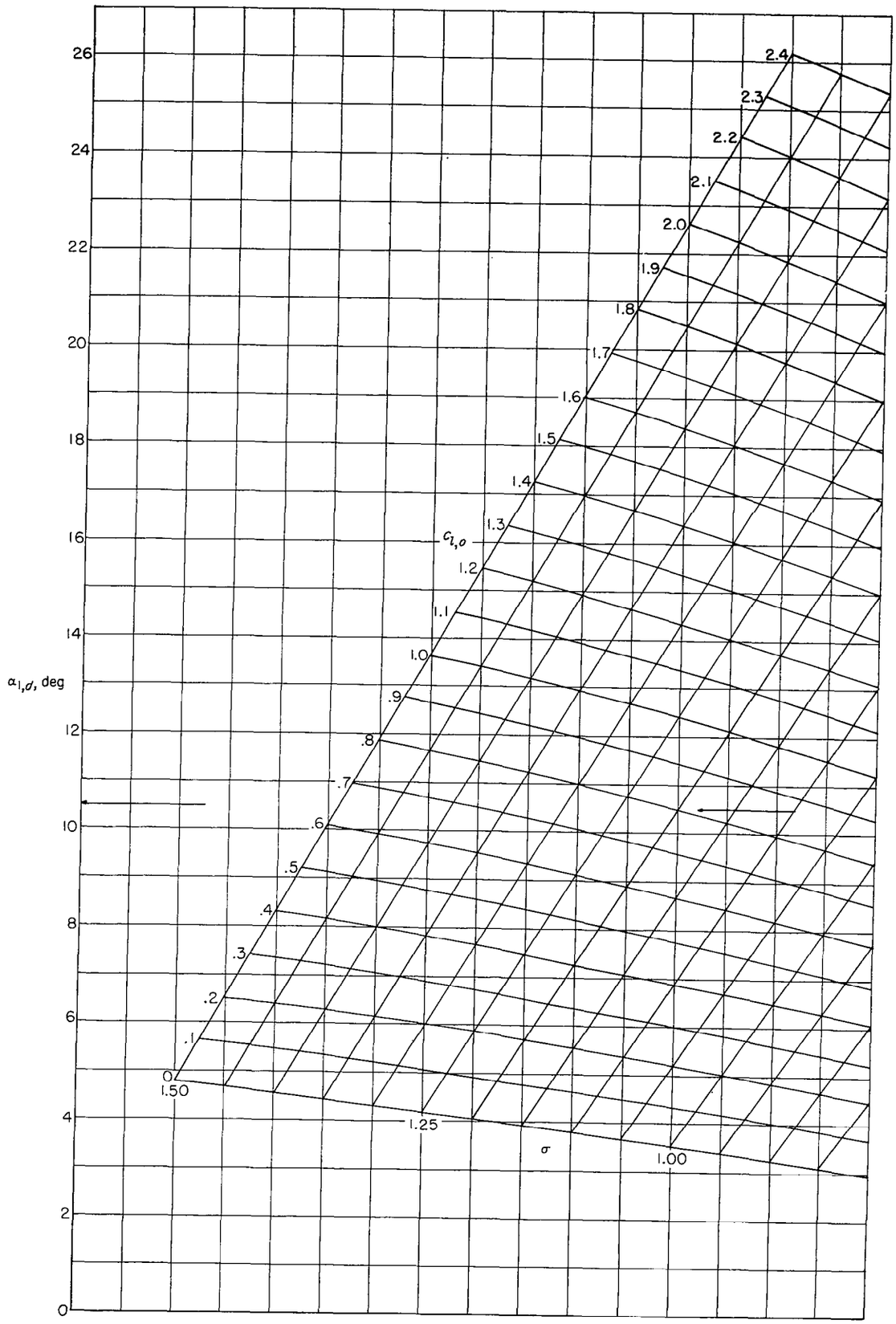

FIGURE 113.—Design angle-of-attack chart for NACA 65-($c_{l,o}$)10 sections.

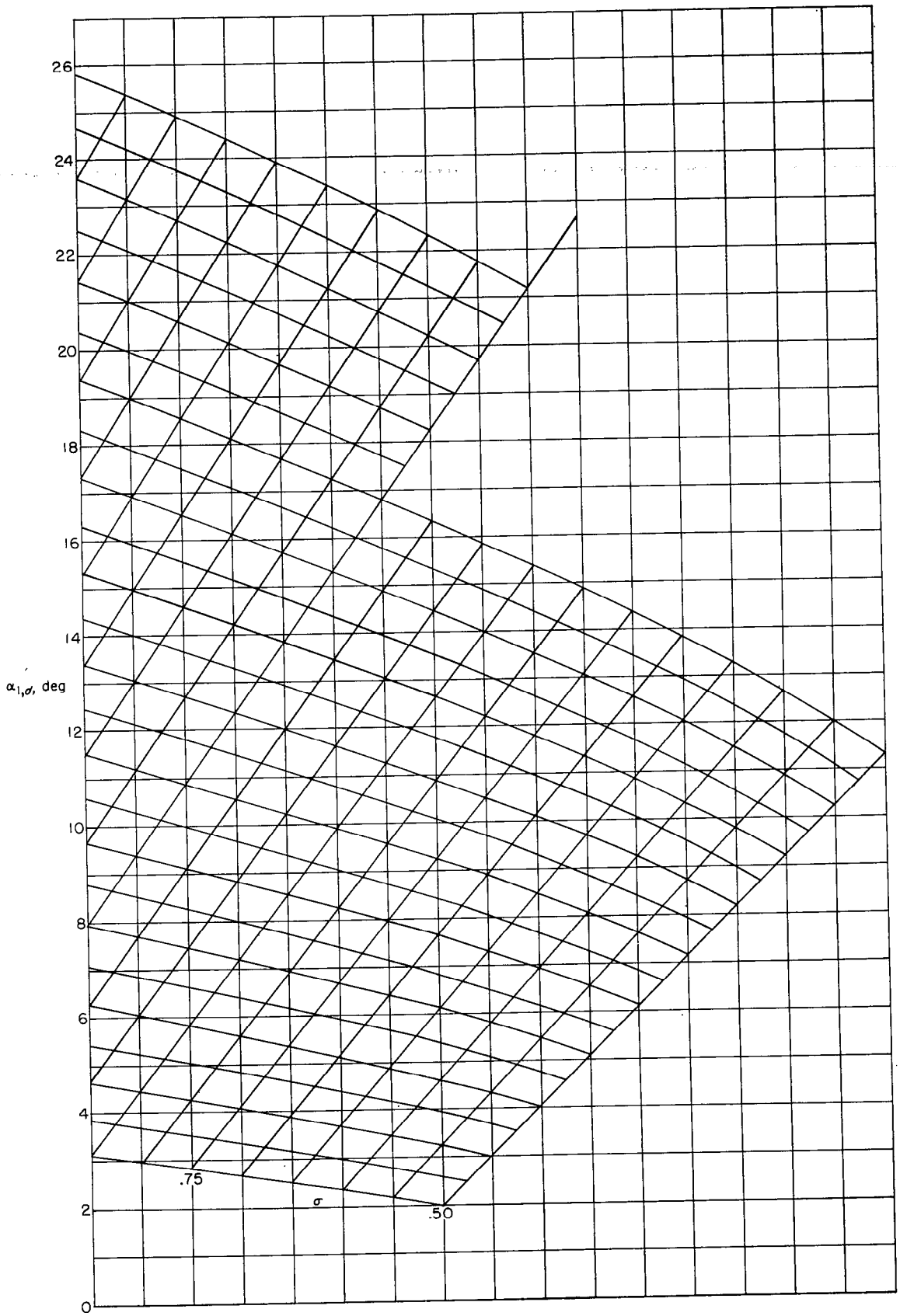

FIGURE 113.—Concluded.

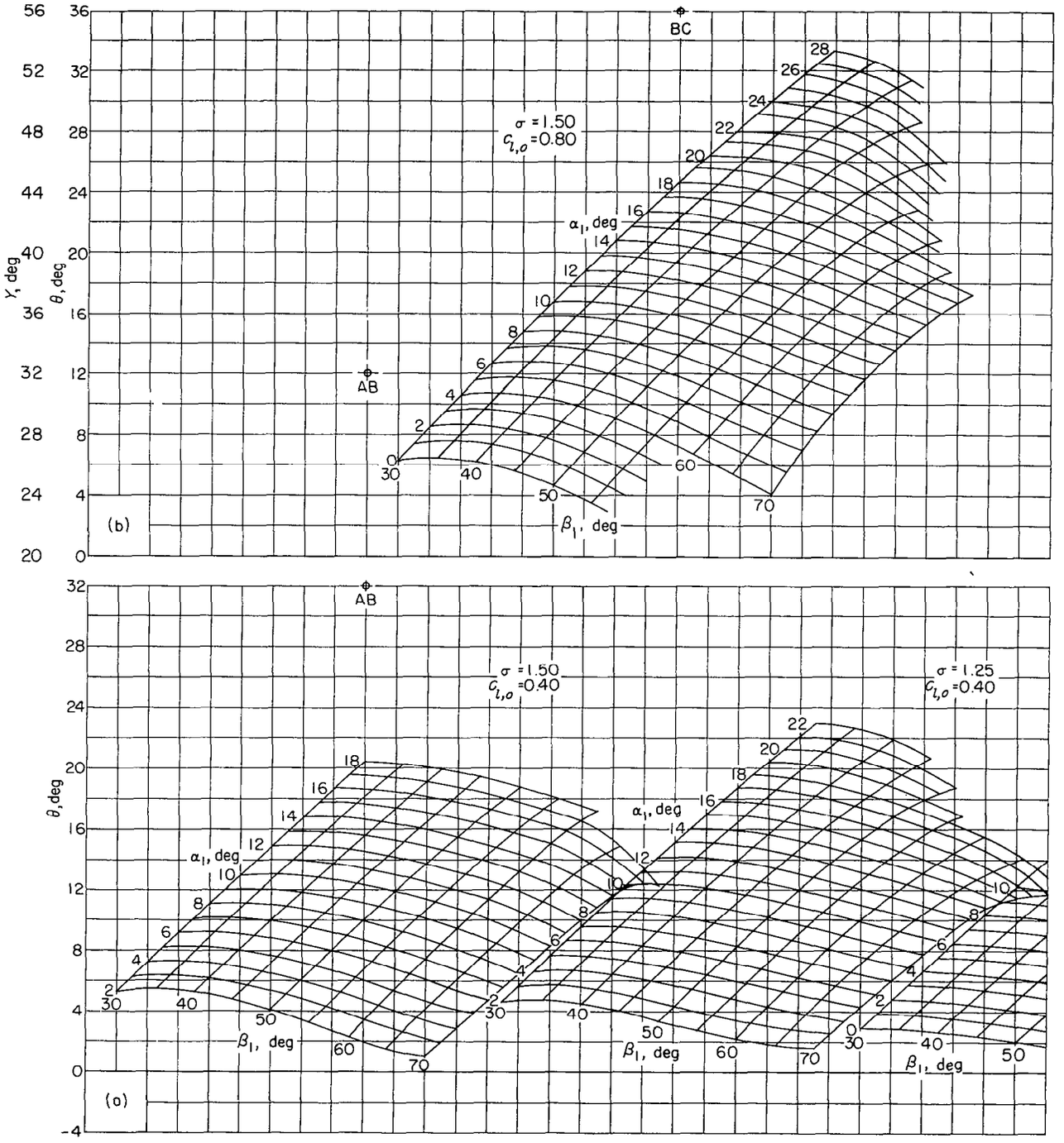

FIGURE 114.—Off-design turning-angle carpets for NACA 65-($c_{l,o}$)10 compressor blades.

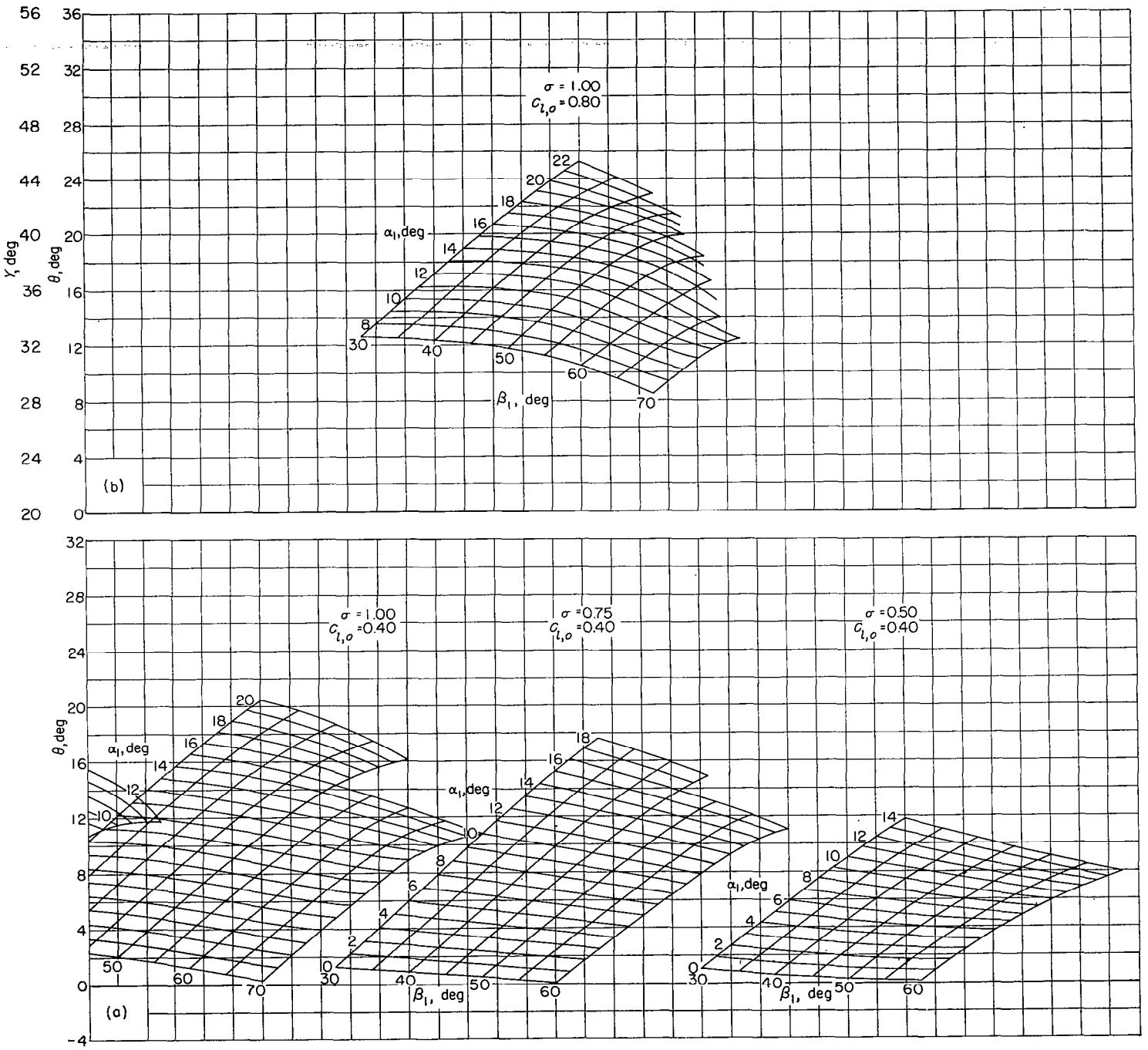

FIGURE 114.—Continued.

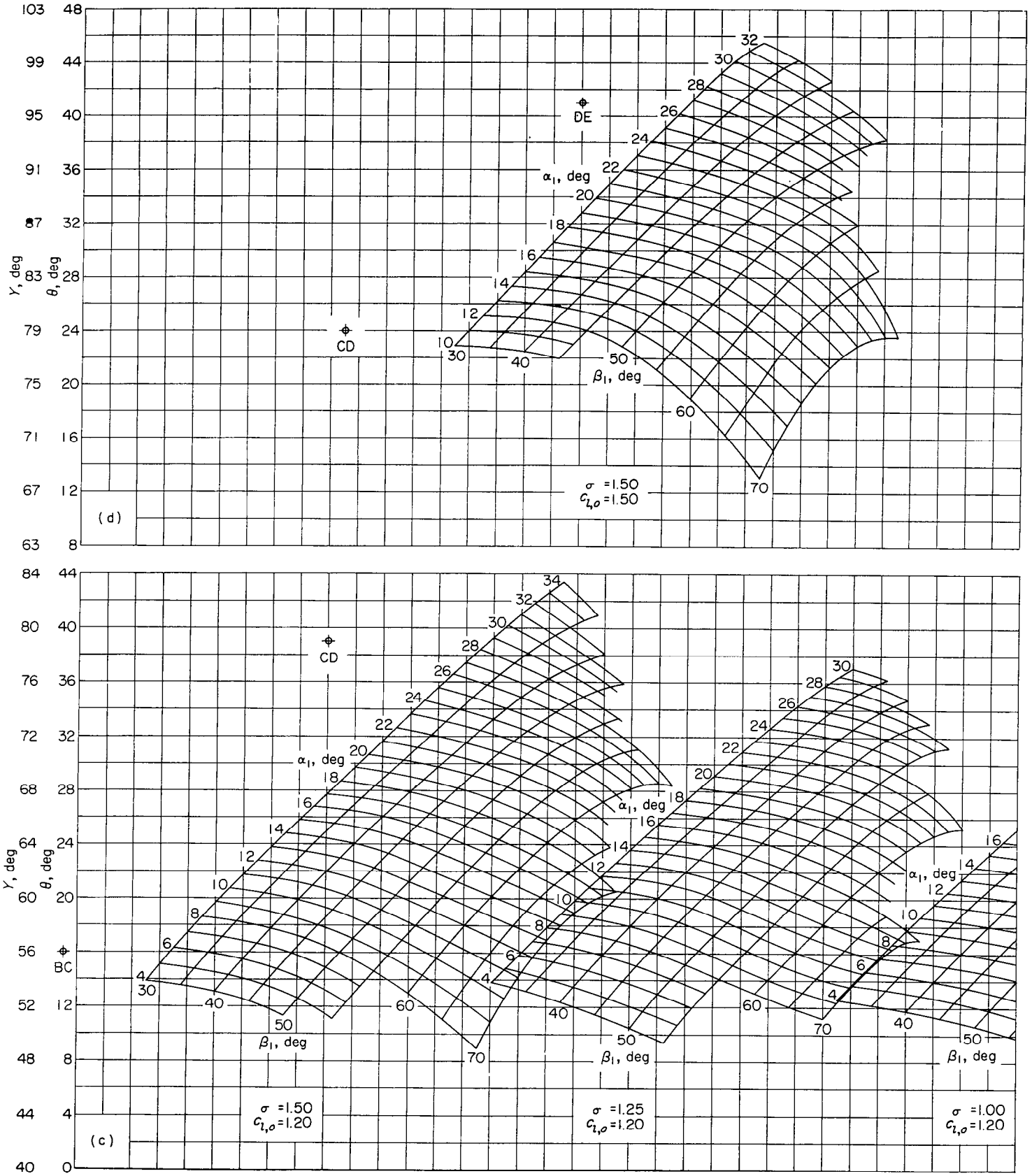

FIGURE 114.—Continued.

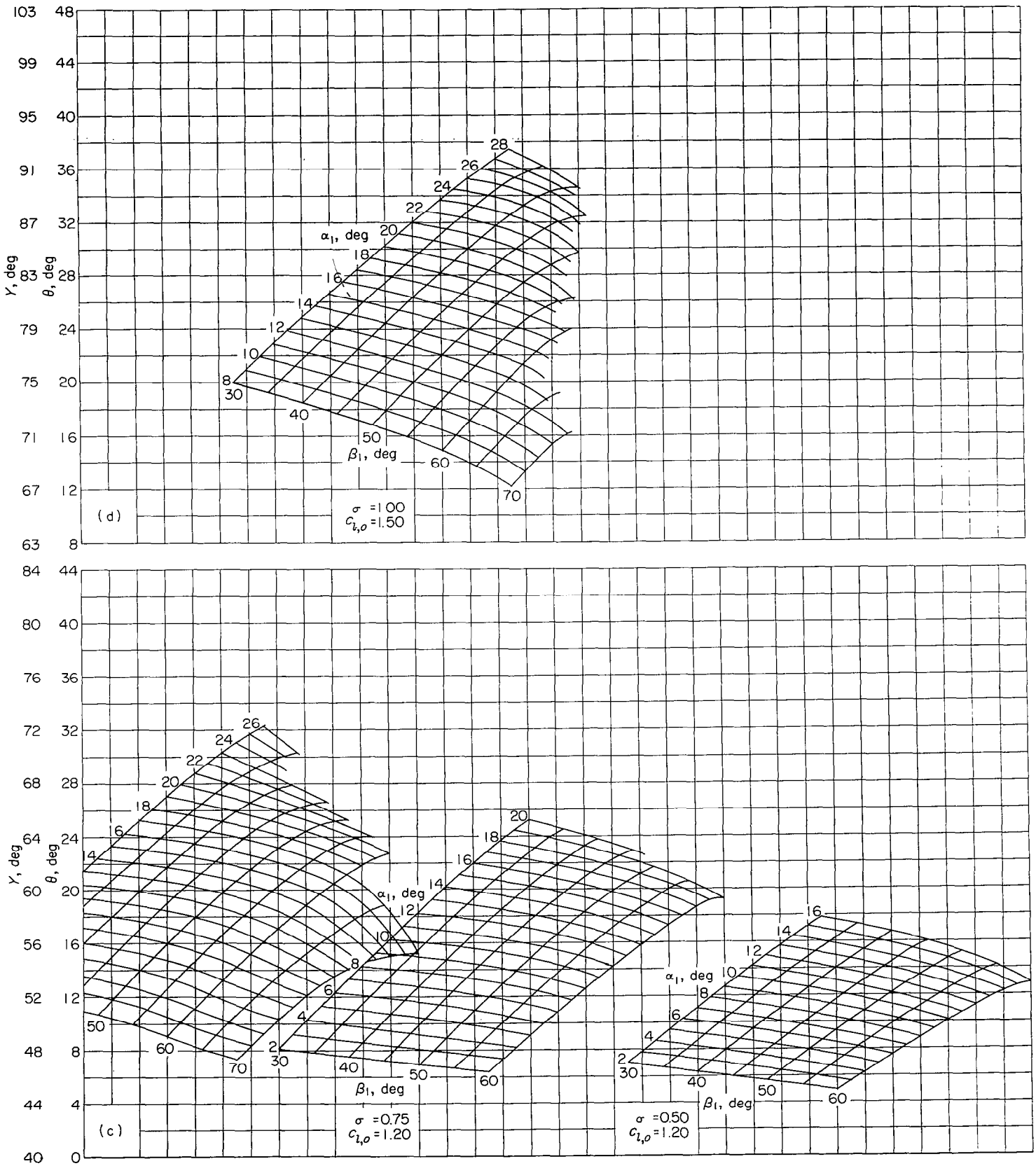

FIGURE 114.—Continued.

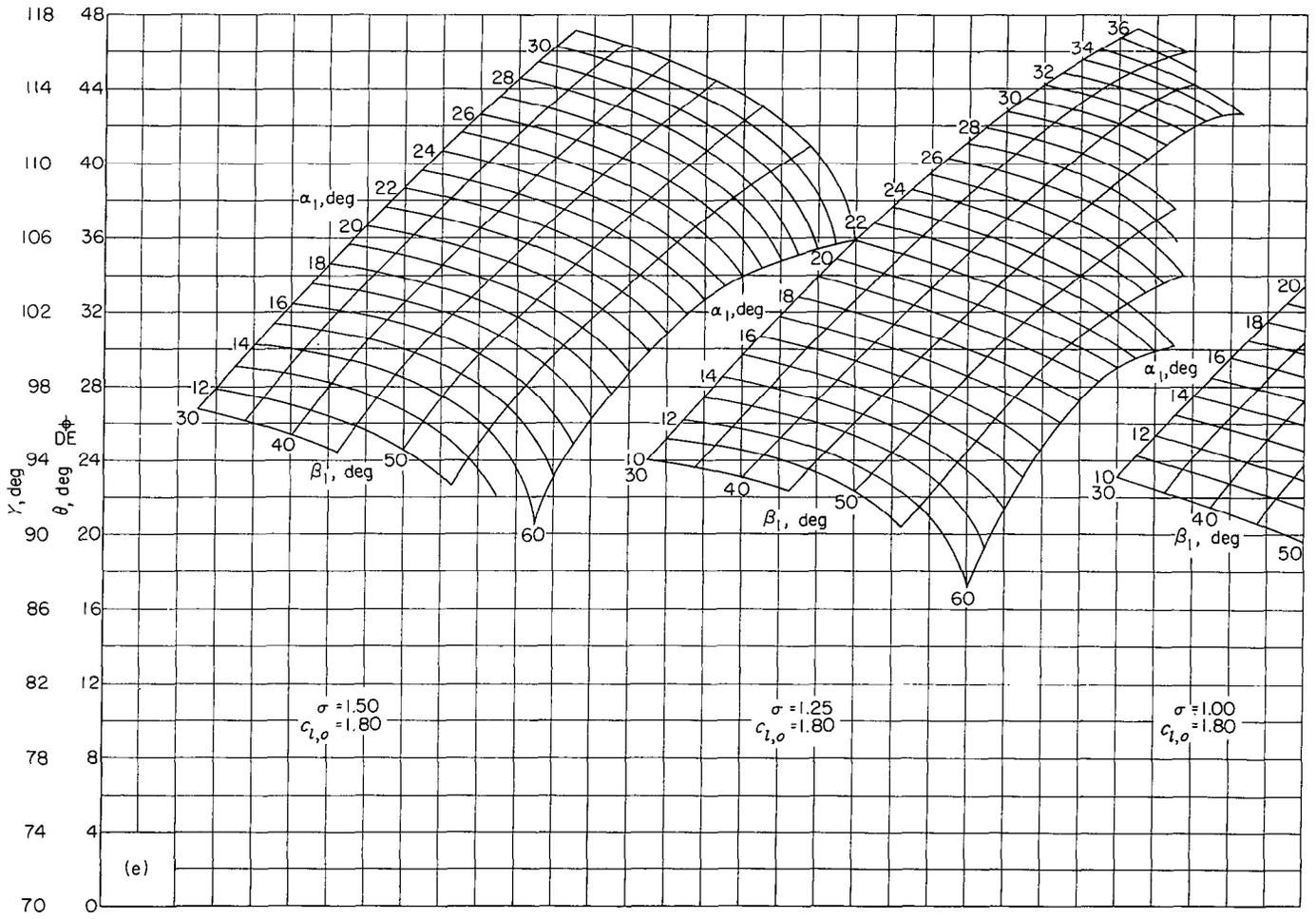

FIGURE 114.—Continued.

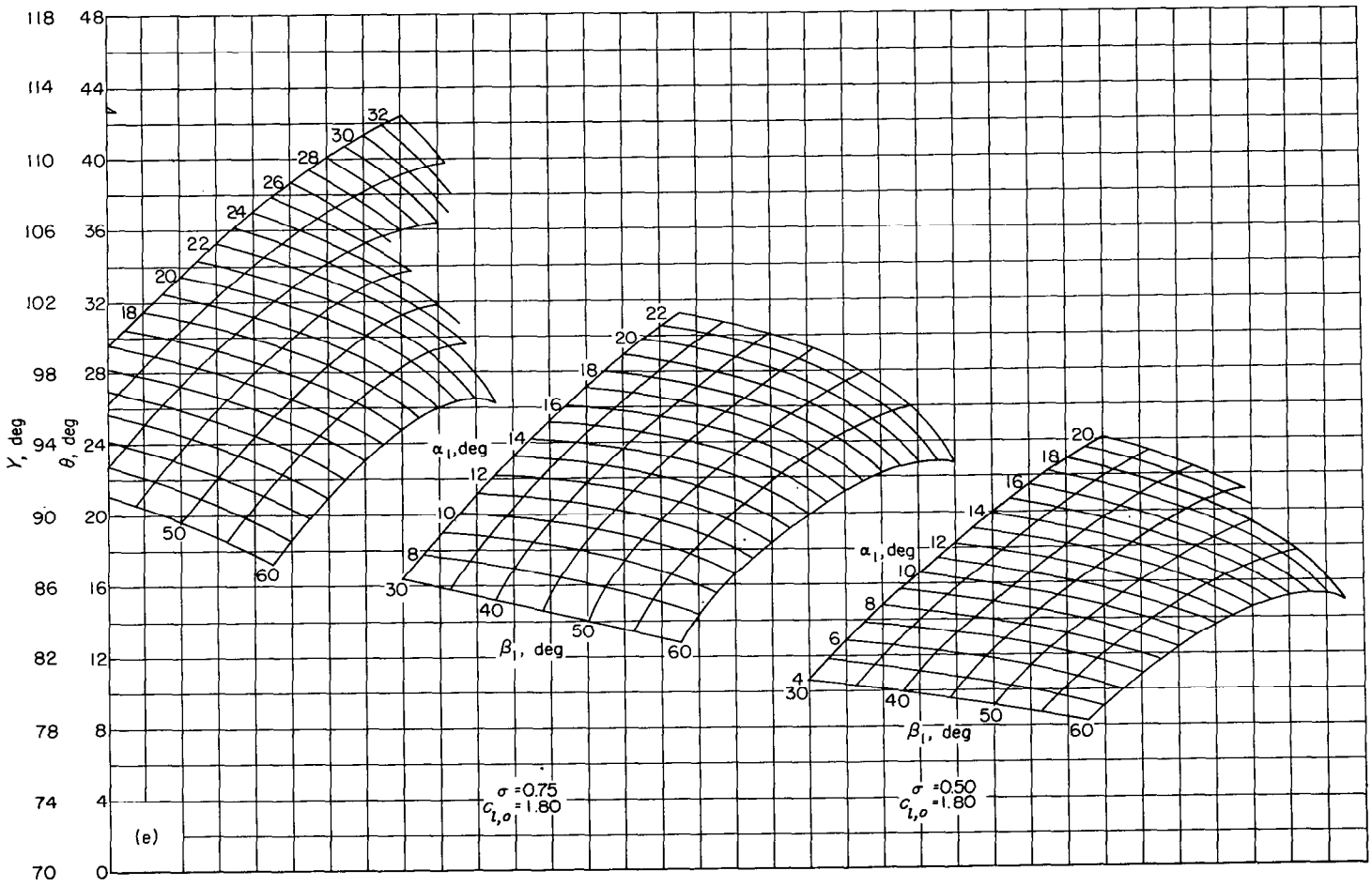

FIGURE 114.—Concluded.

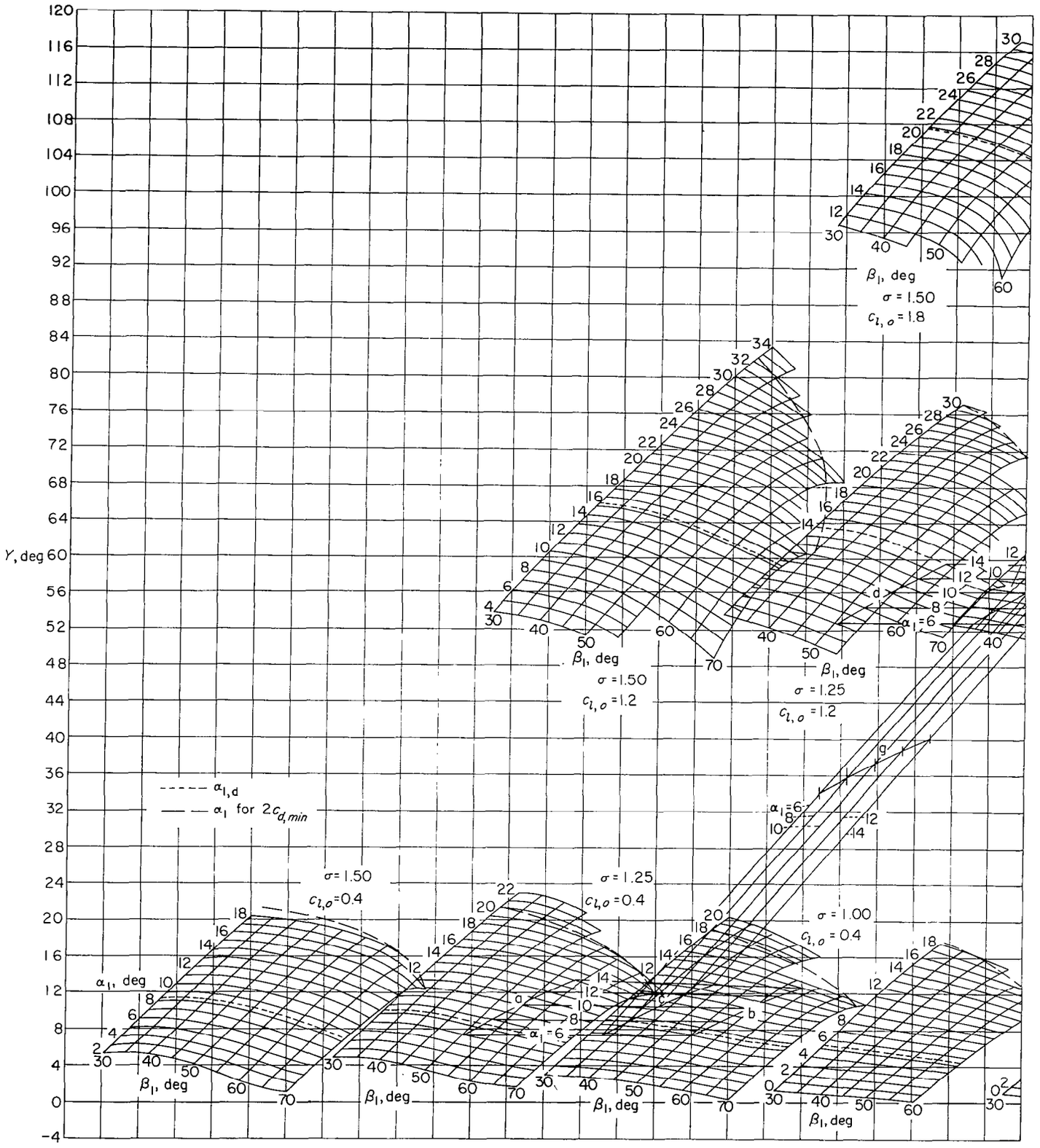

FIGURE 115.—Composite of off-design carpets for NACA 65-series sections for values of $c_{l,o}$ of 0.4, 1.2, and 1.8.

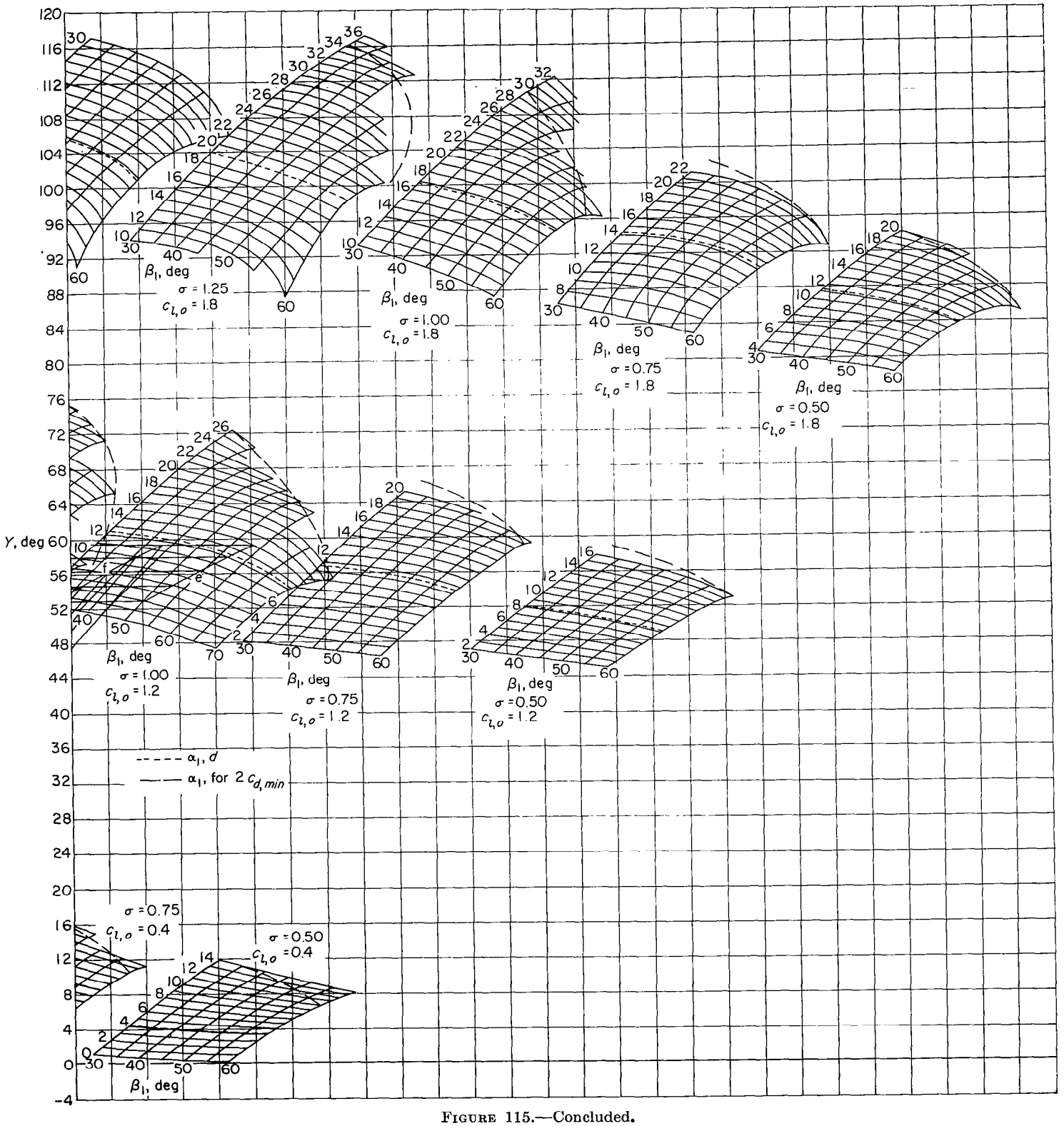

FIGURE 115.—Concluded.

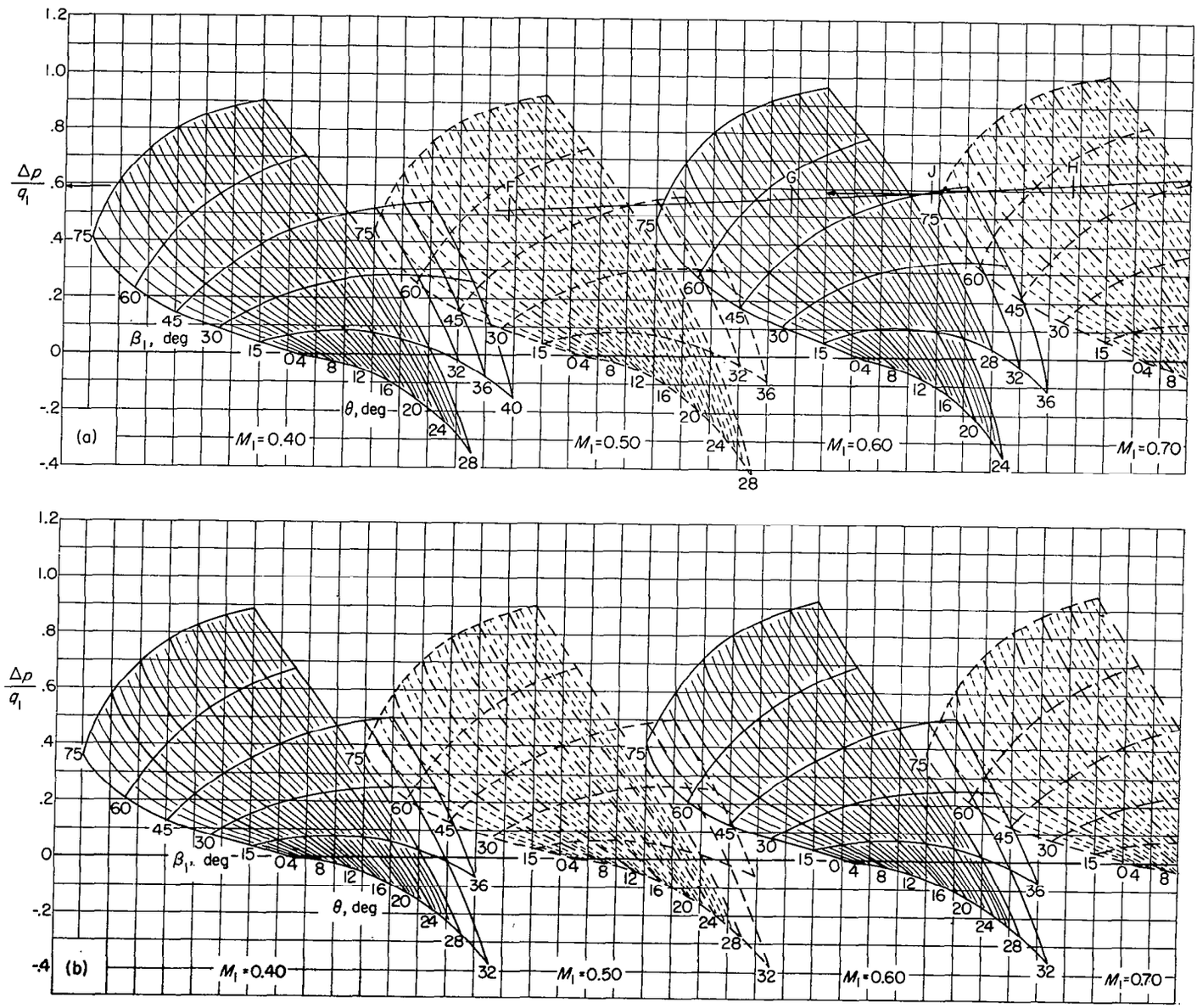

(a) Constant stream-tube area.
(b) Constant axial velocity.

FIGURE 116.—Pressure-rise-coefficient carpets.

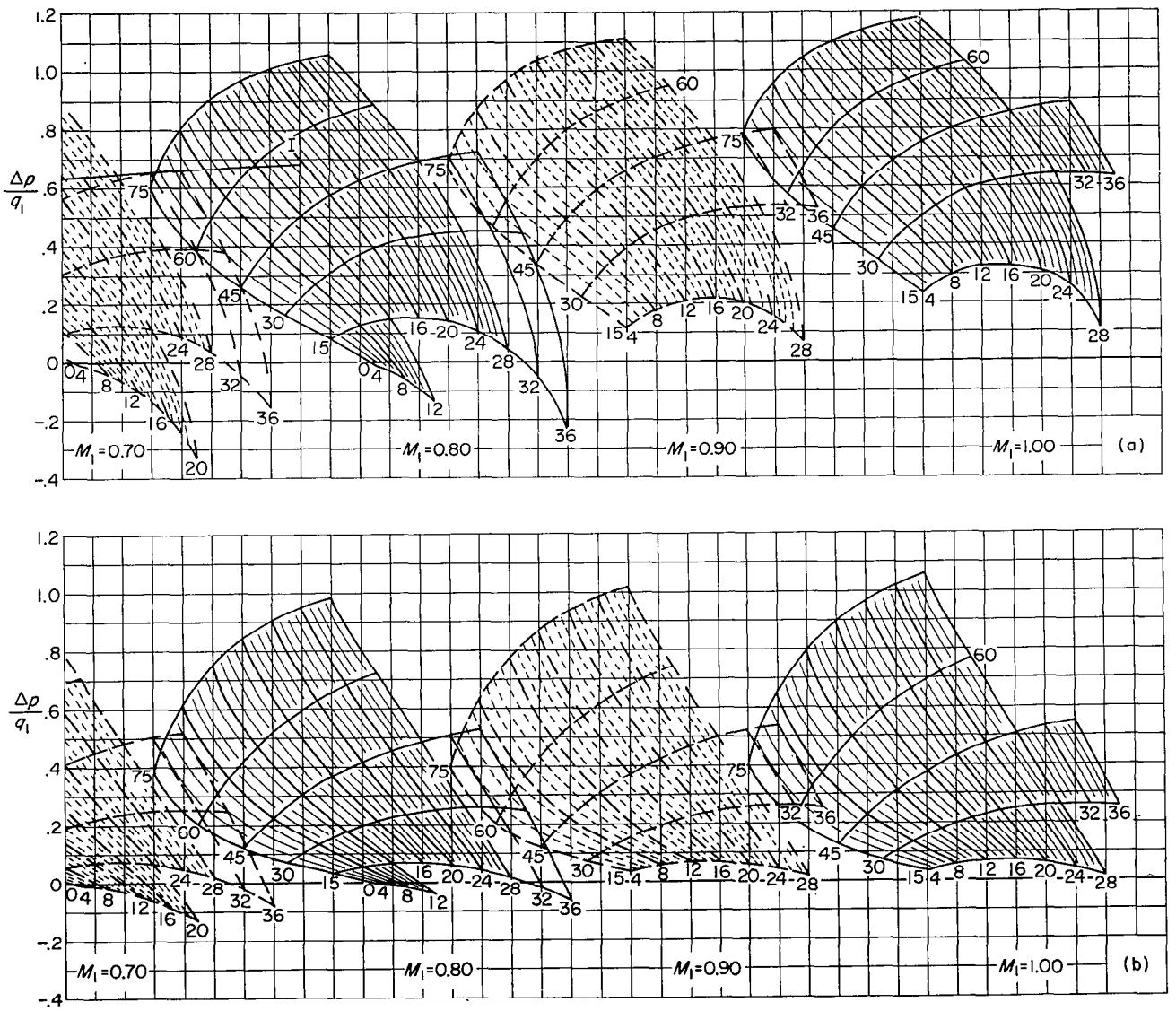

(a) Concluded.
(b) Concluded.

FIGURE 116.—Concluded.

U. S. GOVERNMENT PRINTING OFFICE: 1959